UNIVERSITY OF CALIFORNIA
RIVERSIDE

Design Insights for Eco-Friendly Polymers

A Dissertation submitted in partial satisfaction
of the requirements for the degree of

Doctor of Philosophy

in

Materials Science & Engineering

by

Thomas Dugger

December 2021

Dissertation Committee:
Dr. Kathryn Uhrich, Chairperson
Dr. Cheryl Hayashi
Dr. Christopher Bardeen

The Dissertation of Thomas Dugger is approved:

_____

_____

_____

Committee Chairperson

University of California, Riverside

ACKNOWLEDGEMENTS

The ubiquity of acknowledgements in academic presentations risks underscoring their significance. Every accomplishment comes with support, be it technical, emotional, or professional. Thus, I thank the following faculty, staff, coworkers, friends, and family:

- Prof. Kathryn Uhrich, for taking me in when I needed a change, being patient as I learned how to make polymers and recovered, and putting up with my grumpy, contrary self as I spent far too long in a Ph.D. program
- Dr. Cheryl Hayashi for being a good mentor through thick and thin, and for our nerdy spider moments where we both get excited about some new discovery.
- Doug Brown, Drs. Susan Hackwood, Amy Gilson, and Julianne McCall, for changing my mind about politics and policy and opening up a whole new, exciting career path
- Profs Chris Bardeen, Huinan Liu, Timothy Su, Pablo Zavattieri, and Drs. Josh Speros, Grit Baer, Anna Hoschek, Sonja Kuebelbeck, Mikhail Zhernenkov, Yugang Zhang, Eric Schaible, and Chenhui Zhu for scientific and professional advice during the course of my dissertation
- The past and current UCR GradSuccess and graduate writing center team, who sponsored a training course for fellowship applications that rubbed off on me
- The UCR staff who make sure things actually work and get done: Rachel, Kellie, Rebecca, Alejandra, Kevin, Sabrina, and many others
- My current coworker Shuang, for knowing what she's doing and helping teach me

- Former coworkers Morgan, Jesus, Steven, Ramya, Luz, Fabian, Nick, and Pao for struggling through the trenches together with me
- The undergrads who I've had a privilege to mentor: Kim, Aidan, Diana, Jessica, and Winnie, who I was worried would get her Ph.D. before me.
- Gabe Ceccini, for sharing a drink we call grad school, going just easy enough on me at pool to keep things interesting, and making me feel like part of his family
- Debbie Nelson, for helping me continue to grow as a person and editing one very important fellowship application
- Friends in grad school who helped make things fun: Nick, David, Alex, Sara, Andy, Alyssa, Austin, Chithra, Christian, Devin, Ece, Jill, Josh, Marissa, Max, Sami, Tucker, Wenny, and many more
- Friends from my first quarter of life, for providing other fun escapes: Davis, Chaz, Arjun, Cindy, Morgan, Andrew, Erica, Jenny, Luis, Pete, Tyrell, Wes
- My mom and dad, Debbie and Larry, for always believing in me, helping me make hard decisions, and treating me like an adult.
- Ragnar, Khloe, Gracie, Nala, Murphy, Nali, Lacey, Lobeanhoneysweet and the greyhounds of FastFriends rescue, for sharing the unconditional love only dogs can provide, if only until I went home.
- Finally, the spiders, who may not know how cool they are, what part they play, or that I'm their self-appointed promoter, real estate agent, and ambassador.

My research has been funded by many sources, including AFSOR Multi-University Research Initiative FA# 9550-15-1-0009, AFSOR DURIP W911NF-16-1-0208, NIH/UNIVERSITY OF MICHIGAN subaward SUBK00013048, BASF CORPORATION/UC BERKELEY subaward 10120, and UCR fund 87357 Startup/Initial Complement general funds. This research used beamline 7.3.3 of the Advanced Light Source, which is a DOE Office of Science User Facility under contract no. DE-AC02-05CH11231. I would also like to acknowledge the instrumentation facilities on campus for providing and maintaining equipment essential for my research: the Central Facility for Advanced Microscopy and Microanalysis, Advanced Chemistry Instrumentation Facility, and the Materials Science Program's fee for service instruments. Additional thanks to the Brookhaven and Lawrence Berkeley National labs for approving the beamline proposals which allowed me to conduct certain experiments. This material is based upon work supported by the National Science Foundation Graduate Research Fellowship Program under Grant No. DGE-1326120. Any opinions, findings, and conclusions or recommendations expressed in this material are those of the author(s) and do not necessarily reflect the views of the National Science Foundation.

The text of this dissertation, in part (Chapter 3), is a reprint of the material as it appears in "Ultrastructure and Mechanics of Annealed Nephila clavipes Major Ampullate Silk," *Biomacromolecules* 2020. The co-author David Kisailus listed in that publication directed and supervised the research which forms the basis for parts of this dissertation.

ABSTRACT OF THE DISSERTATION

Design Insights for Eco-Friendly Polymers

by

Thomas Dugger

Doctor of Philosophy, Graduate Program in Materials Science & Engineering
University of California, Riverside, December 2021
Dr. Kathryn Uhrich, Chairperson

Polymers are essential, ubiquitous materials in modern society, and their use has led to many industrial and scientific advances. However, many polymers are made using toxic solvents and precursors or are difficult to naturally degrade. This results in polymer waste accumulating in natural spaces, harming those ecosystems. Much of current polymer research focuses on replacing synthetic polymers with natural ones, creating new biodegradable polymers from natural materials, and using more benign synthesis processes. This dissertation investigated the structure-processing-properties-performance relationships of three polymers to better understand how eco-friendly polymers can be designed as replacements for synthetic polymers in select applications.

Polyacrylonitrile (PAN) is the industry standard precursor for carbon fiber, but its synthesis uses toxic solvents and reactants. The oxidative stabilization step of PAN-based carbon fiber production was studied using Nuclear Magnetic Resonance (NMR) spectroscopy and Wide-Angle X-ray Scattering (WAXS) to identify key structural elements of PAN that natural alternatives should include. Although a direct transition

from PAN crystals to graphite crystals was hypothesized, the data collected suggested a delayed transition but underscored the importance of this transition.

Spider silk was investigated as a natural alternative carbon fiber precursor, and the crystallinity, graphite content, and mechanical properties of spider silk carbon fiber were compared to those of PAN-based carbon fiber. These properties were measured using Fourier Transform Infrared spectroscopy, Raman spectroscopy, Scanning Electron Microscopy, WAXS, and tensile testing. Spider silk carbon fiber had comparable strength and lower stiffness than PAN-based carbon fiber. As hydrogen-bonding elements in the silk proteins were combusted, the crystals within silk lost their alignment, resulting in unaligned graphite crystals. In contrast, graphite crystals in annealed PAN retained their alignment along the long axis of the fiber.

Finally, biodegradable, biocompatible salicylic acid-based poly(anhydride ester)s (SAPAE)s were studied using NMR, UV-Visible Spectroscopy, and controlled degradation experiments for use as coatings for bone implants and drug delivery systems with tunable release rates. SAPAEs with different chemical compositions were used to form microspheres and encapsulate a model protein. Significant protein release occurred within hours or days based on the SAPAE used, offering a variety of potential applications.

Table of Contents

List of Figures

List of Tables

List of Schemes

Chapter 1: Polymer Materials Science

1.1 Personal Motivation

I was drawn to materials science and engineering by how tangible it is. Why does pouring hot water on the lid of the pickle jar make it easier to open? Atoms have more energy at higher temperatures, making them more mobile. Translating this to a tangible scale, materials become more malleable at higher temperatures. Thus, the metal lid is slightly more flexible, doesn't grip the jar as hard, and is more easily removed. Everything we physically interact with is a material, so through materials science I can understand how and why materials behave as they do and through materials engineering I can make them better. Studies in materials science often center on the 'materials science tetrahedron,' (Fig 1.1), which displays the interconnected relationship between a material's structure, how it's processed into its final form, its material properties, and its performance [1].

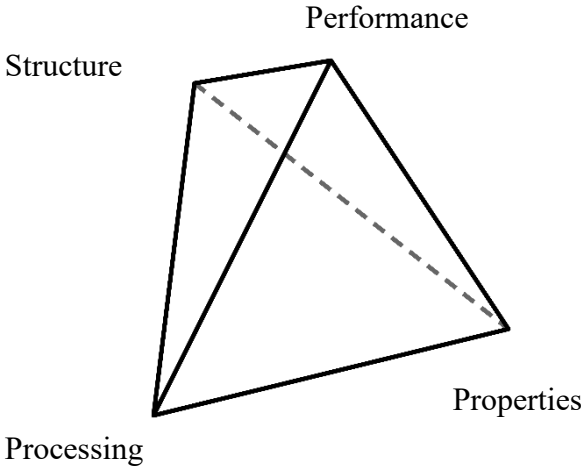

Figure 1.1: The Materials Science Tetrahedron

For example, when purchasing clothing, people consider performance characteristics: will it keep them warm/cool? How easily does it stain? Is it machine washable? How long will it last? The answers to these questions depend on the material properties—like wettability, thermal conductivity, glass transition temperature, and yield strength—of the material the clothing is made from. These properties are determined by the material's structure—polyester, cotton, etc.—and how it is processed from a vat of chemicals to being woven into the final article of clothing. I hope that you learn something new from this dissertation, be it in relation to your own research, fun spider facts, or tips for the design of green polymers.

1.2 Scientific Motivation

This dissertation research focused on polymer materials science. Plastics (synthetic polymers) like polyester and natural materials like cellulose, silk, and DNA, are all polymers. Nature has been making polymers for billions of years, and eventually humanity tried to imitate it. Many early attempts to make plastics were grounded in conservation. As people hunted elephants close to extinction for their ivory horns, entrepreneurs and inventors realized whoever could make synthetic ivory would be rich, famous, and do a little good for the pleasant pachyderms [2]. Synthetic rubbers are another example, motivated by lost access to natural rubber sources during World War II [3]. The military-industrial complex fueled plastics research and manufacturing which exploded postwar into the modern plastics industry, where millions of plastic products are mass-produced to meet almost any demand, from cooking utensils to parachutes.

As humanity gained increasing awareness of how our actions are killing our planet, the daunting permanence of plastics was called into question. Research in ways to recycle plastics began and has transformed into efforts to make eco-friendly, biodegradable plastics. For example, the 12 principles of Green Chemistry can be used to guide the synthesis of biocompatible, biodegradable plastics for medical applications [4,5]. As with any topic, the more fundamental understanding we have of polymer materials science, the better our synthetic polymers will be. In this dissertation, I investigated how the structure of polyacrylonitrile (PAN), the standard carbon fiber precursor, changes during processing to inform the design of greener carbon fiber precursors. I examined the protein structure of spider silk, how spiders make it, and if it was a viable carbon fiber precursor. Finally, I studied the synthesis of salicylic acid-based poly(anhydride esters) (SAPAEs) with different structures, processing, and properties to expand their potential applications.

1.3 Polymer Materials Science

Polymers are macromolecules made of multiple covalently bonded repeat units [6]. There must be sufficient repeat units for the polymer to be considered a macro- (large) molecule, at which point it displays viscoelastic properties. With sufficient molecular weight or chain length, the polymer displays behavior that is consistent with a liquid (i.e., flows at specific temperatures) and also consistent with a solid. Polymers undergo a solid-state phase transition, called the glass transition, at a certain temperature (T_g) depending on the polymer's structure. Below the T_g, the internal motion of polymer chains is limited, embrittling the polymer and decreasing its fracture toughness.

The majority of synthetic and natural polymers are based upon carbon, which forms covalent bonds more readily than ionic or metallic bonds [1]. These three bond types fundamentally separate the three main classes of materials: polymers, ceramics, and metals. Covalent bonds emphasize the permanence of polymers, as they are the strongest bond type, and the C-C bond is especially difficult to break. The fundamental traits ascribed in this definition define polymers' structure-processing-properties-performance relationships (SPPP). Polymers are synthesized from monomers (*structure*), then *processed* to a desired form with specific *properties* for the best *performance* in a given application.

The most fundamental step (by size and workflow) of polymer materials science is the polymer's molecular formula. Monomer choice will define the subsequent processing steps and properties, and copolymers can be synthesized from two or more repeat units. For example, the copolymer poly(3,4-ethylenedioxythiophene) and poly(styrene sulfonate) (PEDOT:PSS, Fig 1.2) is conductive, while most other polymers are insulators. Poly(lactic acid) and poly(glycolic acid) (Fig 1.2) are biodegradable because they contain a hydrolytically labile ester bond, which means they can't be autoclaved, a common sterilization procedure that uses steam to disinfect material surfaces [6].

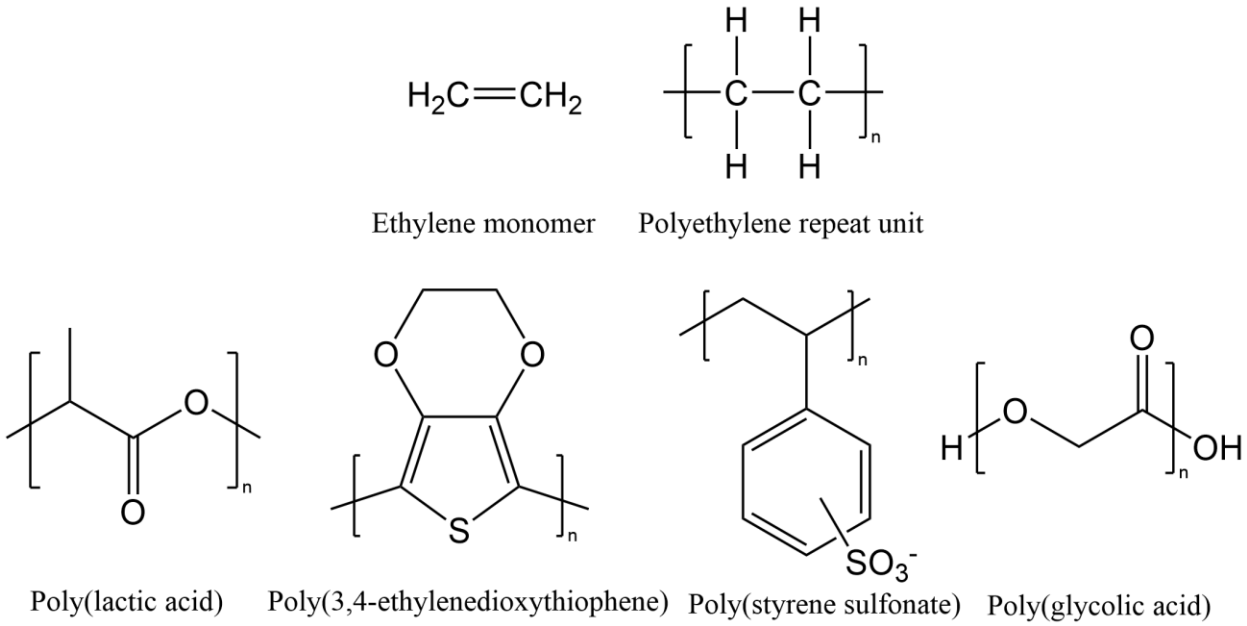

Figure 1.2: Example polymers

Cellulose is a naturally occurring polysaccharide comprised of sugar units; yet is not water soluble because the repeat units are bonded by ether linkages. Silk is a polypeptide made from water soluble proteins, but when processed into a fiber and extruded from the spider, the resulting polymeric material is not water-soluble. All these natural polymers are formed through condensation reactions between monomers. Given the right conditions, they can be hydrolyzed and degraded naturally. By contrast, many synthetic polymers like polyethylene and poly(vinyl alcohol) (PVA) are formed using radical polymerization and have only C-C bonds within and connecting repeat units. C-C bonds are difficult to break naturally, which results in the buildup of discarded synthetic polymer waste in the environment.

The molecular weight of a polymer is key to its properties. Thus, measurement of the polymer molecular weight, or polymer chain length, is a key method of assessment.

Polymer length is characterized by the number-average (M_n) or weight-average (M_w) molecular weight. M_n is a weighted average based on the number of molecules (polymer chains) that have a certain molecular weight, represented as $M_n = \frac{\sum N_i M_i}{\sum N_i}$ [7]. M_w is a weighted average based on the weight fraction of each polymer chain of a certain molecular weight, where $W_i = \frac{N_i M_i}{\sum N_i M_i}$ and $M_w = \sum W_i M_i$. These averages allow comparisons between polymers based on the number of repeat units, regardless of the molar mass of each repeat unit.

After a polymer is synthesized, it is typically processed into its final form through different means. For example, polymers can be melted and molded into specific shapes, extruded through small holes to form fibers, or dissolved in solvents and cast or coated onto a surface. These processing techniques often have a significant effect on a polymer's structure beyond the chemical formula. As an example, consider the primary-quaternary structural order of proteins. Primary structure refers to the amino acid sequence, coded by DNA and analogous to the repeat units of polymers and copolymers. Secondary structure is the arrangement of adjacent peptides into motifs (structures) such as α-helices or β-sheets. Tertiary structure describes the interaction between motifs from different regions of the protein, and quaternary structure is the interaction of multiple protein chains.

While secondary-quaternary structures self-assemble in certain proteins and polymers, processing also drives formation of these higher order structures. Most polymers are semicrystalline, with disordered amorphous regions and ordered crystals, where a crystal is defined as a periodic, repeating arrangement of atoms [8]. Polymers with

high degrees of aromaticity often have crystals which self-assemble as these planar aromatic regions align via pi-pi stacking. Polymer crystals are typically smaller than their metallic or ionic counterparts and are dispersed in an amorphous matrix of polymer chains. Processing techniques like extrusion, where polymers are stretched and densified in one direction, pack polymer chains more closely together, forming more crystals that are aligned in the extrusion direction. Physicochemical material properties can be measured during and after this processing (Table 1.1) using a variety of techniques.

Table 1.1: Materials Characterization Techniques

Material Property	**Characterization Technique**
Chemical composition	Fourier Transform Infrared Spectroscopy (FTIR) Raman Spectroscopy Nuclear Magnetic Resonance (NMR) Spectroscopy X-Ray Photoelectron Spectroscopy (XPS) Energy Dispersive X-Ray Spectroscopy (EDS/EDX)
Glass Transition Temperature (T_g), Melting Temperature (T_m)	Differential Scanning Calorimetry (DSC) Differential Thermal Analysis (DTA)
Degradation Temperature (T_d)	Thermogravimetric Analysis (TGA)
Surface Morphology	Scanning Electron Microscopy (SEM) Optical Microscopy (OM)
Surface tension	Goniometry
Mechanical Properties: Young's Modulus, Yield Strength, Toughness, Adhesion Strength	Mechanical Test Instrument (e.g. Instron)
Hardness	Hardness Testing
Crystallinity	Wide-Angle and Small-Angle X-Ray Diffraction/Scattering (WAXS, SAXS, XRD) DSC

As with all materials, polymers' performance depends on the structure, processing, and properties described above. In this dissertation, various polymers and their properties were evaluated for a variety of applications. Spider dragline silk and

carbon fiber are used in structures like webs and carbon fiber-reinforced composites, while SAPAEs typically have biomedical applications. In chapter 2, the effects of thermal processing on PAN structure as it is converted into carbon fiber were studied. In chapter 3, the process spiders use to fold silk proteins into fibers was studied to improve synthetic fiber extrusion. In addition, spider silk was evaluated as a greener alternative to PAN in carbon fiber production for structural applications. In chapter 4, a range of SAPAEs were synthesized to optimize processes of polymerization, microsphere synthesis, bioactive encapsulation, and degradation studies in preparation for future application studies. Common themes are SPPP relationships and using natural polymers or synthesizing biodegradable polymers from renewable components to reduce the adverse environmental effects of hazardous polymerizations and polymer waste.

1.4 References

(1) Callister, W. D. *Materials Science and Engineering*, 7th ed.; John Wiley & Sons, Inc: York, PA, 2007.

(2) Frienkel, S. A Brief History of Plastic's Conquest of the World. *Scientific American* **2011**. https://www.scientificamerican.com/article/a-brief-history-of-plastic-world-conquest/.

(3) Bix, H. P. *Hirohito and the Making of Modern Japan*; Perennial: New York, NY, 2001.

(4) Anastas, P.; Eghbali, N. Green Chemistry: Principles and Practice. *Chem Soc Rev* **2010**, *39* (1), 301–312. https://doi.org/10.1039/B918763B.

(5) Song, S.; Ngo, K.; Uhrich, K. E. Green Chemistry Principles in Advancing Hierarchical Functionalization of Polymer-Based Nanomedicines. In *Sustainability & Green Polymer Chemistry Volume 1: Green Products and Processes*; Chen, H. N., Gross, R. A., Eds.; American Chemical Society, 2020; pp 135–157.

(6) Uhrich, K. E. Lecture on Designing Polymers for Biomaterials. Presented at UCR, August 2018.

(7) Stevens, M. *Polymer Chemistry, an Introduction*, 3rd ed.; Addison-Welsey: New York, NY, 1975.

(8) Bozhilov, K. Lecture on Crystal Structures and Bonding. Presented at UCR, October 2015.

Chapter 2: Polyacrylonitrile (PAN) for Carbon Fiber Production

2.1 Introduction

Polymers are rarely used for high-strength structural applications as their strength and Young's modulus are too low to provide adequate impact resistance or structural support. Metals and ceramics are more ideal materials as their high crystallinity and density lead to higher strength and stiffness. However, those traits of metals and ceramics are disadvantageous for applications that require strength but benefit from being light weight, like aircraft, automobiles, cut-resistant gloves, and protective body armor. This need for lightweight, strong materials has spurred development of polymers like Kevlar®, a polyaramid fiber that is denser and more crystalline than most polymers. Combining Kevlar with weaving techniques to further strengthen against cuts and impacts allows for the creation of flexible, strong, and lightweight protective equipment. For more rigid and high strength applications such as parts in automobile and aircraft frames, polymers are typically be incorporated into composite materials.

A simple definition of a composite is "containing two dissimilar parts [1]." Composite materials combine two classes of materials, taking advantage of each material's strengths. Polymers are widely used as a matrix material for fiber-reinforced composites. For example, bone is a composite of protein fibers (a polymer) that provide toughness combined with calcium phosphate (a ceramic) for hardness and strength. For synthetic composites, a relatively ductile and tough polymer matrix, typically an epoxy or

polyurethane, is impregnated with strong, stiff ceramic fibers, typically glass or carbon fiber.

Carbon fiber is synthesized by thermally processing a polymer precursor. Different sources define carbon fiber as having over 92-94 weight % carbon, which exists as graphite crystals or an amorphous carbon matrix, where the amorphous carbon could be aliphatic, cyclic, or aromatic [2].

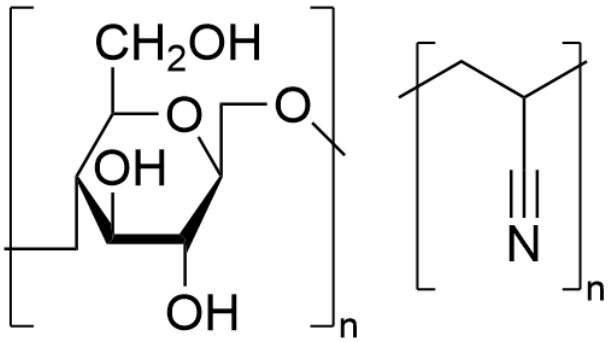

Rayon PAN

Figure 2.1: Molecular structure of polyacrylonitrile (PAN) and Rayon

Carbon fiber production has come a long way, from annealed bamboo filaments in Thomas Edison's 1880 light bulbs [3], to Roger Bacon's carbon filaments in 1958 [4], and now composite panels in modern aircraft and many other applications [5]. Carbon fiber research at the American company Union Carbide in the late 1950s began using similar cellulosic materials as Edison, ultimately choosing Rayon (a cellulosic fiber, Fig 2.1) for high temperature annealing [6]. Shortly afterward, Akio Shindo at Japan's Government Industrial Research Institute in Osaka began research on polyacrylonitrile (PAN) as a carbon fiber precursor [7–9]. PAN offered a higher percent mass conversion to graphite than

the cellulosic precursors but required additional processing via oxidative stabilization [9]. This process, combined with stretching fibers during annealing (hot stretching), was also adopted by researchers in the United Kingdom [10,11] and the United States [12]. Companies such as Toray, Rolls Royce, and Union Carbide began licensing and developing carbon fiber patents for commercial carbon fiber production, and the industry has since grown substantially with PAN as the ubiquitous precursor [13].

Current carbon fiber manufacturing processes consist of three steps: oxidative stabilization, carbonization, and graphitization (Fig 2.2) [14–17]. First, oxidative stabilization in an oxygen-containing atmosphere at 250-350 ^{o}C converts individual PAN chains to a cyclized, "ladder-like" structure. Then, carbonization in an inert atmosphere with temperatures up to 1000 ^{o}C fuses adjacent cyclized chains and begins to remove non-carbon impurities, forming a turbostratic structure—a mixture of aliphatic and conjugated aromatic regions loosely arranged in a graphitic crystal structure [18,19]. Lastly, during graphitization in an inert atmosphere above 1000 ^{o}C, impurities are further eliminated and true graphite crystals form, with their size proportionate to the graphitization temperature. Tows (non-twisted bundles) of PAN fibers are passed through multiple furnaces where these processes occur continuously before being spooled for transportation or woven into desired forms [16]. Although carbonization and graphitization are the most energy-intensive steps, even the early research on PAN observed that the oxidative stabilization step proved critical to producing strong carbon fibers without detrimental deformation [7–9].

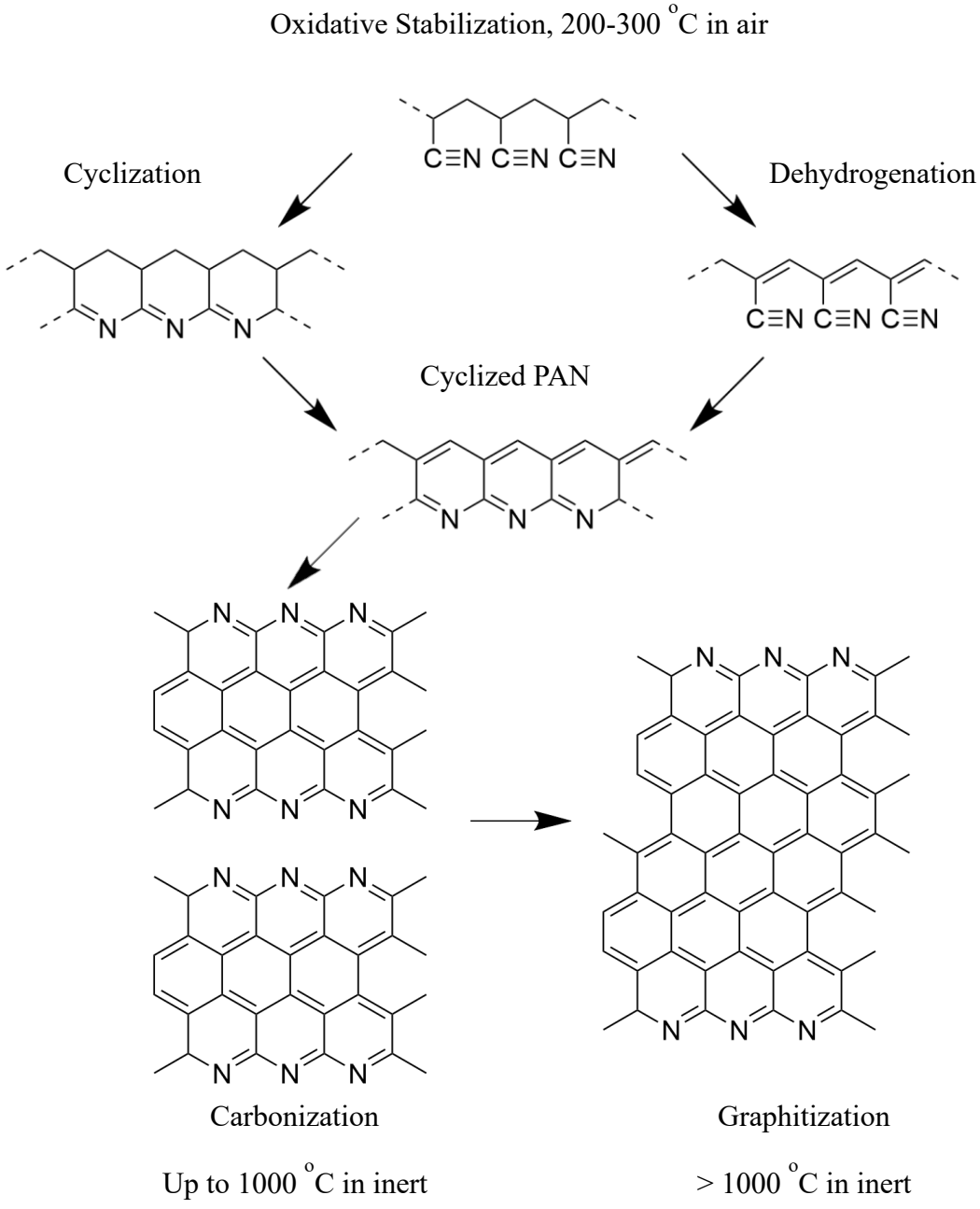

Figure 2.2: Simplified reaction steps during thermal processing of PAN to make carbon fiber

Oxidative stabilization is not required in cellulosic fibers, making them a simple precursor for producing carbon fiber and thus amongst the first materials successfully

commercialized [6]. This difference between PAN and Rayon can be explained by their chemical compositions (Fig 2.1). PAN has a linear, aliphatic backbone with nitrile functional groups, while Rayon is a polysaccharide, with glycosidically linked rings with alcohol functional groups. Oxidative stabilization is necessary to cyclize PAN, preparing it for the chain fusion and graphite growth in carbonization and graphitization [11,20]. Conversely, the polymer backbone of Rayon is cyclic and the alcohol groups likely reactive enough to initiate chain fusion [21,22]. However, the cellulosic backbone risks decomposition through oxygen loss, resulting in a low graphite crystal yield [23].

Despite over 60 years of carbon fiber research, there is no definitively proven reaction mechanism for oxidative stabilization in the published literature, as the majority of studies focus on the final carbon fiber. The prevailing theory is that the two main reaction steps are dehydrogenation of the polymer backbone and nitrile group cyclization (Fig 2.2). However, these two steps do not consider the role of oxygen apart from a proton scavenger, when it has been proven necessary to produce the best carbon fiber [7–9]. Existing studies on oxidative stabilization cover a variety of conditions: inert or oxygen-containing gas environments; PAN homopolymer or 1-10 weight % carboxyl-containing copolymers; and PAN powder, films, electrospun nanofibers, or melt-spun fibers with a range of diameters. All these factors have the potential to alter results observed by chemical and thermal characterization methods.

Understanding the stabilization reaction pathway is particularly important as researchers investigate alternative, greener precursors than PAN. PAN is made by free radical polymerization of carcinogenic acrylonitrile and is not biodegradable. PAN fiber

spinning also requires toxic solvents like dimethylformamide. Researchers have primarily investigated polysaccharides, such as lignin, as renewable alternatives. PAN stabilization and annealing is also costly and energy-intensive, so any process improvements can further reduce the ecological footprint of carbon fiber production. The literature on oxidative stabilization has been reviewed to understand how various elements of the stabilization process influences polymer properties. By understanding the fundamental chemistry and crystallography of PAN-based carbon fiber production, process changes can be recommended to reduce cost and provide insight into the design requirements for natural carbon fiber precursors.

2.1.1 Oxidative Stabilization Mechanism

Although dehydrogenation and cyclization are the accepted stabilization reaction mechanisms, the literature shows uncertainty around the order in which they occur and the incorporation of oxygen and other heterogeneities in the cyclized structure. Many potential reaction pathways have been proposed, but they are difficult to verify as PAN fibers are typically characterized *ex-situ* [24]. FTIR is the most common technique used to characterize the structure of cyclized PAN, but its use is limited. The stabilization reactions change the entire molecular structure, leaving no peak with constant intensity to use as a reference for measuring the relative change in peak intensity. Peak deconvolution is also necessary to separate overlapping peaks such as the different C-H stretches and C=C/C=N stretches, yet this process is often overlooked. Other techniques, such as NMR spectroscopy and XPS, have provided more insight into how the molecular structure of PAN changes during stabilization.

Stabilization in inert atmosphere is the simplest case, with only one sharp thermal transition observed in DSC measurements. Wang et al published a thorough study using ^{13}C-labelled PAN and solid-state NMR spectroscopy to track the position of each carbon in the PAN repeat units [25]. The stabilized structure was shown to be more complex than the simple ladder structure, consisting of multiple nitrogen-containing rings often separated by small linear regions, evoking the image of a broken ladder (Fig 2.3). Cyclization is suggested to occur first, as reported by FTIR analysis [15,26,27], and then dehydrogenation or rearrangement reactions begin shortly afterwards.

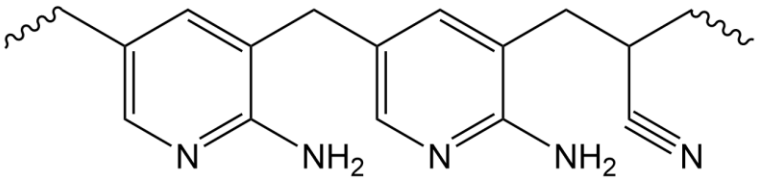

Figure 2.3: Proposed molecular structure of PAN stabilized in inert environment by Wang et al.

Conversely, most studies on PAN homo- and co-polymer stabilization in air report dehydrogenation occurring first [28–37] with a few reports claiming that cyclization occurs first [20,27,38] or that the two processes concurrently occur [39,40]. However, many of these studies were made by analyzing FTIR spectra without rigorous peak deconvolution. Xue et al. performed the most thorough analysis of their FTIR spectra and correlated their conclusions with NMR data. Oxygen is incorporated into the stabilized PAN structure, mostly as alcohols or ketones [15,20,27,41–44]. Oxygen incorporation occurs more rapidly after cyclization and dehydrogenation [15,42–44]. As with stabilization in an inert atmosphere,

XPS- and NMR spectral-based studies showed a variety of cyclic groups in a broken-ladder structure (Fig 2.4) [40,42,45].

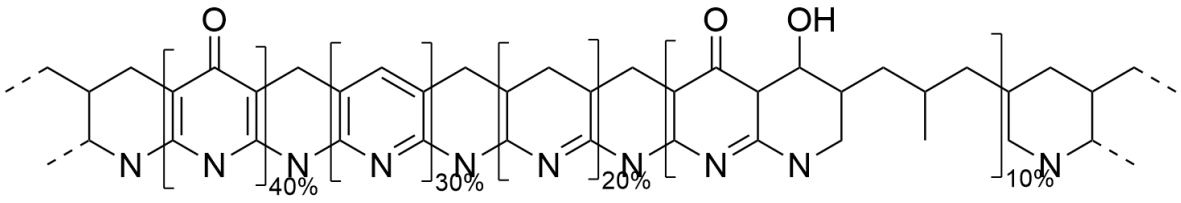

Figure 2.4: Molecular structure of PAN stabilized in air based on work by Takahagi, Usami, and Xue.

2.1.2 Key Factors for Oxidative Stabilization

Most research on PAN-based carbon fiber production has focused on producing carbon fiber with better, controllable mechanical properties and making the process cheaper and more efficient. Studies on oxidative stabilization have similar goals, realized by modifying the precursor fiber or stabilization process. Stabilization atmosphere, copolymers and initiators, crystal alignment, formation of a core-shell structure, and novel techniques for oxidative stabilization have been studied by multiple research groups, resulting in modifications of PAN precursor or oxidative stabilization processes adopted by manufacturers. Variation in PAN form, copolymer content, size, origin, crystallinity, and procedures used in studying oxidative stabilization often make direct comparisons between studies difficult, but themes and trends can be identified.

2.1.2.1 Stabilization Atmosphere

PAN was unique among initial carbon fiber precursors for requiring a stabilization step in air, but further studies suggest oxygen-containing functional groups on cyclized PAN are the true requirement for chain fusion during carbonization [20].

Oxidative stabilization occurs in both inert and oxygen-containing atmospheres for PAN homo- and copolymers (Table 2.1). Stabilization in nitrogen occurs more rapidly, as indicated by one sharp peak in DSC curves from 270-280 ºC and an occasional shoulder around 340 ºC [20,25,27,46–50]. In comparison, DSC measurements in air show two distinct, broader peaks at 260-290 ºC and 300-330 ºC [20,27,33,40,46–48,51–53]. DSC peak position is directly proportional to heating rate. If the DSC heating rate is 10 ºC/min vs 2.5 ºC/min, for example, the DSC peaks will appear at higher temperatures [48,53,54]. Peak onsets in DSC measurements offer more direct comparisons. Stabilization begins at a lower temperature in air than nitrogen but is affected by the amount of copolymer(s) present [25,33,47,49]. Gupta and Belyaev noted that PAN fibers darken more quickly when stabilized in air [47,53]. Stabilization in air is more exothermic, releasing 7.03 kJ/g compared with 0.511 kJ/g for nitrogen [48,53]. Calculated activation energies vary between studies, which results from analyzing one or both of the DSC peaks in air. Despite some disagreement, the activation energy for PAN homopolymer appears to be higher in nitrogen, 153.2 kJ/mol [49] compared with 124 kJ/mol for air [33]. The activation energies for copolymers follows a similar, but less pronounced trend [33,40,48,49,53].

Table 2.1: Summary of references

Reference	PAN Polymer	Stabilization Atmosphere	Characterization Techniques
1968 Ross[22]	Rayon	Air	weight loss, shrinkage, DTA, TGA, SEM, OM
1970 Grassie[41]	homopolymer powder	Nitrogen, air	DTA, TGA, thermal volumetric analysis (TVA), FTIR, weight loss
1971 Bell[55]	homopolymer films	Inert	Micropyrolysis-gas liquid chromatography
1972 (Mar) Grassie[56]	homopolymer and 7 copolymer powders: co-methyl acrylate (MA), -benzyl acrylate, -α-methyl methacrylate (MMA), -styrene, -methyl styrene, -2,5 dimethyl styrene, 2-vinyl pyridine	nitrogen, air, vacuum	DSC, TGA, DTA, TVA, FTIR
1972 (Sep) Grassie[57]	homopolymer and 4 copolymer powders: co-acrylic Acid (AA), -methacrylic Acid (MAA), -itaconic acid (IA), -acrylamide (AM)	nitrogen, air, vacuum	DSC, TGA, DTA, TVA, FTIR
1973 (Sep) Grassie[58]	homopolymer and 4 copolymer powders: co-vinyl acetate (VA), -vinyl formate, -acrolein, -methyl vinyl ketone	nitrogen, air, vacuum	DSC, TGA, DTA, TVA, FTIR
1973 (Dec) Grassie[59]	homopolymer and 4 copolymer powders: co-vinyl chloride, -vinylidene chloride, -α-chloroacrylonitrile, and commercial co-MA (Courtaulds, courtelle brand)	nitrogen, air, vacuum	DSC, TGA, DTA, TVA, FTIR
1975 Fitzer[46]	commercial fibers: Dralon T and Dolan (co-MA)	nitrogen, air	DTA, FTIR

1979 Warner[60]	commercial fibers: Monsato co-VA, Du Pont co-MA, Bayer homopolymer, Courtaulds co-MA-IA	air	Elemental analysis (EA), SEM
1986 Takahagi[45]	homopolymer and co-hydroxyethylacrylonitrile fibers and powder	air	XPS, EA
1988 Ko[61]	Courtelle fibers	air	SEM, transmission electron microscopy (TEM), electron diffraction
1990 Peebles[62]	Industrial homopolymer powder	inert	EA, DSC, FTIR on evolved gases
1990 Usami[42]	Nikkiso co-MMA-IA	air	pyrolysis gas chromatography mass spectroscopy (Py-GC-MS), FTIR, solid state 13C NMR (SSNMR)
1991 Mascia[51]	commercial fibers: Courtelle, Enichem SpA terpolymer	air	UV pretreatment, DSC, FTIR, EA, SEM, swelling in solvents, dynamic mechanical testing
1991 Tsai[63]	homopolymer, co-IA-(2-ethylhexyl acrylate)	air	EA, DSC, FTIR, XRD, mechanical testing
1992 Wang[64]	commercial fibers: Courtaulds special acrylic fiber (SAF) terpolymer	air	mechanical testing, sonic modulus, WAXD, SEM
1994 Cardoso dos Santos[65]	homopolymer films	air	X-ray irradiation, FTIR, XRD, UV-Vis, electron spin resonance (ESR)
1994 Mittal[26]	Courtelle fibers	air, nitrogen	DSC, FTIR
1995 Mukopadhyay[66]	commercially stabilized fibers	air	WAXS, SEM, mechanical testing
1995 Ogawa[28]	commercial fibers: Toho Rayon Co, c-MA, co-sodium acrylate, co-AM, co-(N-methylol acrylamide)	controlled oxygen content	shrinkage stress, mechanical testing, EA, FTIR

1995 Tsai[67]	co-MA-IA fibers	air	XRD, mechanical testing, porosity measurement
1996, 97 Gupta[47,68]	SAF terpolymer fibers	air, argon	DSC, EA, WAXS, SAXS, thermal stress
1996 Kakida[43]	co-MAA fibers	air	DSC, FTIR
1996 Zhu[29]	commercial fibers	air	DSC, FTIR, XRD, mechanical testing
1997 Kakida[69]	homopolymer, co-MAA	air	DSC, FTIR
1997 Lee[70]	Courtaulds fibers	air	Surface area: temperature-programmed desorption and SO_2 adsorption, FTIR, mechanical testing, evolved gas analysis
1997 Xue[30]	homopolymer fibers	air	TGA/FTIR evolved gas analysis, FTIR
1998 Bang[71]	co-MA fibers	air	DSC, XRD, ^{13}C NMR
1998 Surianarayanan[72]	homopolymer powder	He with 10% O_2	TGA-MS
1999 Dalton[73]	commercial fibers: Bayer homopolymer, Courtaulds SAF and films made from these polymers	air	FTIR, EA, SSNMR, WAXS
2003 Bahrami[48]	homopolymer, co-AA, co-MAA, and co-IA fibers	air, nitrogen	DSC, FTIR, TGA
2003 Devasia[49]	co-IA powder	air, nitrogen	DSC
2003 Paiva[74]	co-MA and commercial Mitsubishi copolymer fibers	air	UV irradiation, DSC, FTIR, mechanical testing, optical microscopy, SEM
2005 Naskar[75]	co-AN and co-AN-(acryloyl benzophenone)	nitrogen	UV-irradiation, DSC, FTIR, swelling in solvents
2005 Wu[76]	co-IA fibers	air, nitrogen	DSC, mechanical testing, WAXS
2006 Li[77]	co-MA-(sodium styrenesulfonate) fibers modified with CuCl solution	air	DSC, FTIR, XRD, mechanical testing
2006 Yu[31]	co-IA fibers	air	EA, FTIR, XRD, mechanical testing

2007 Chae[78]	co-MA and co-MA with single-walled carbon nanotubes (SWNT)	air	DSC, FTIR, Raman, WAXS, SEM
2007 Jing[50]	co-IA fibers	air	DSC, FTIR, density measurements, EA, XRD
2007 Yu[79]	co-IA fibers	air	optical microscopy, SEM
2007 Zhang[32]	electrospun homopolymer fibers and homopolymer film	air	DSC, TGA, Raman
2008 Ouyang[33]	homopolymer and co-IA films	air	DSC, FTIR, TGA
2008 Yu[80]	co-IA fibers	air	SEM, TEM, WAXS
2009 Liu[81]	commercial SAF dissolved in solvent and electrospun	air	DSC, FTIR, XRD, SEM
2009 Lv[82]	co-IA fibers	air	FTIR, SEM, TEM, EA, EDS
2009 Yu[20]	co-AI powder	air, argon	DSC, TGA
2010 Belyaev[53]	commercial fibers: Nitron terpolymer	air	DSC
2010 Sun[27]	commercial fibers: Huitong terpolymer	air, nitrogen	DSC, TGA, FTIR, MS, density
2010 Wu[34]	homopolymer and co-AM powder	air, nitrogen	DSC, FTIR
2010 Zhou[83]	electrospun homopolymer treated with phosphoric acid	air	FTIR, SEM, XRD, TGA, Raman, TEM
2011 Yuan[84]	commercial fibers: Jilin Chemical Fiber Co	air	UV pretreatment, FTIR, XRD, SEM, density
2012 Karacan[85]	co-VA fibers treated with guanidine carbonate	air	DSC, FTIR, TGA, XRD, EA, density
2012 Lee[39]	homopolymer fibers	air, nitrogen	DSC, FTIR, TGA, Raman, XRD, mechanical testing
2012 Lian[86]	commercial fibers: SAF terpolymer	air	DSC, FTIR, WAXS, stress during stabilization
2013 Ju[35]	bifunctional copolymer fibers	air	DSC, FTIR, TGA, EA, XRD
2013 Qin[87]	co-AM-MAA fibers	nitrogen, steam, air	density, mechanical testing, XRD

2013 Morales[88]	photoinitiator treated homopolymer fibers	air	UV pretreatment, DSC, GTIR, SEM, WAXS, mechanical testing
2013 Xue (January)[40]	co-IA and commercial SAF fibers	air	DSC, FTIR, SSNMR
2013 Xue (August)[89]	commercial fibers: SAF terpolymer	air, controlled O_2 content	FTIR, Raman, WAXS, mechanical testing
2014 Fu[36]	homopolymer, co-MMA, and co-MMA-IA films	air	DSC, FTIR, 13C NMR, TGA
2014 Wang[25]	13C-labeled homopolymer	argon	TGA, SSNMR
2015 Liu S.[90]	homopolymer fibers	air	FTIR, TGA, XRD, EA, density, SEM
2015 Zhang[91]	films of commercial Exlan co-MA mixed with carbon nanotubes	air	SEM, TEM, WAXS, TGA, Raman
2016 Liu[92]	fibers of commercial Exlan co-MAA mixed with lignin	air, nitrogen	DSC, SEM, WAXS, dynamic mechanical analysis (DMA)
2016 Sabet[93]	commercial fibers: SAF terpolymer	air	DSC, DMA, WAXS,
2016 Zhao[44]	commercial fibers: Zhejiang Zhongcheng Packing Mat. Co., co-MMA	air	DSC, FTIR, TGA, SSNMR (^{13}C and ^{1}H)
2017 Fu[94]	homopolymer films	air, nitrogen	FTIR, Raman, DSC, TGA
2018 Salim[37]	commercial fibers: Jilin Chemical Fiber Co	air	DSC, FTIR, density, optical microscopy, mechanical properties, WAXS
2019 Cho[95]	homopolymer, co-IA, co-MA, co-MMA, co-VA, and co-VAIA films	air	FTIR, DSC
2020 Choi[38]	co-MA-IA fibers	air	FTIR, density, DSC, EA, XRD, mechanical testing, SEM, thermomechanical analysis, Raman, XPS

2.1.2.2 Copolymers and Initiators

Commercial PAN precursor fibers often incorporate comonomers to improve the rheological qualities of fibers during spinning and to catalyze oxidative stabilization, resulting in a reduced peak onset temperature and less heat released [15,20,33,43,48,56,57,69]. While a large variety of comonomers have been used in research of PAN-based carbon fibers [58,59], industrial PAN largely uses acidic, methacrylate, and acrylate comonomers.

PAN is copolymerized with acidic comonomers such as itaconic acid (IA) and methacrylic acid (MAA) to provide an ionic pathway to initiate cyclization and dehydrogenation [20,33,48,57]. This initiation reaction is identified as a shoulder in DSC curves; it causes stabilization to begin at a lower temperature and releases less heat. This process minimizes stabilization-induced defects common in homopolymer PAN [33]. Acidic comonomers also shorten reaction time and increase degree of stabilization [33,36,69,73,95]. However, loading of an acidic comonomer above 5-10 mol% can result in severe weight loss during oxidation and decreased yield [15,48].

PAN copolymerized with acrylate and methacrylate comonomers has a higher degree of polymerization, improved macromolecular regularity and tacticity, improved spinnability, and fewer morphological defects, all improving the resulting carbon fiber mechanical properties [63,90]. These comonomers have little impact on the initiation temperature and heat released during stabilization at low mol %, though with increased loading they slightly increase the stabilization peak onset temperature and heat released, likely by impeding radical cyclization [56,71,95]. Similar to acidic copolymers, overloading

acrylate comonomers reduces PAN crystal size in copolymers, which likely results in weaker carbon fibers [71].

Many PAN precursor fibers incorporate up to 6 mol% acrylate/methacrylate and up to 2 mol% acidic comonomers into terpolymers to leverage the benefits from both types of comonomers. This method introduces new difficulties in polymerization and crystallinity as acidic comonomers have less favorable bonding to acrylonitrile than acrylate/methacrylate comonomers and a larger chance of comonomers terminating ionic or radical stabilization [35,63,90]. To address these issues, recent research focuses on the creation of bifunctional comonomers [35] such as PAN-co-3-aminocarbonyl-3-butenoic acid methyl ester which achieve the same benefits as terpolymers. Other studies have attempted to use various initiators, such as N_2H_4, H_2O_2, PO_4^{3-}, or $KMnO_4$, to decrease the peak onset temperature of stabilization, heat released, or required stabilization time and temperatures [15,77,83,85]. Although they have individually reported mild successes, no comprehensive studies have been performed comparing the many proposed initiators.

2.1.2.3 Stabilization Temperature and Duration

In addition to atmosphere, temperature and duration of oxidative stabilization are key processing parameters directly related to cost. Higher temperatures and longer stabilization times logically result in a higher degree of stabilization and ΔH, and less time is required at higher temperatures [28,32,36,49,69,75,81]. Stabilization time and temperature are expectedly proportional to fiber diameter, with electrospun PAN stabilizing more quickly than gel-spun [81,83].

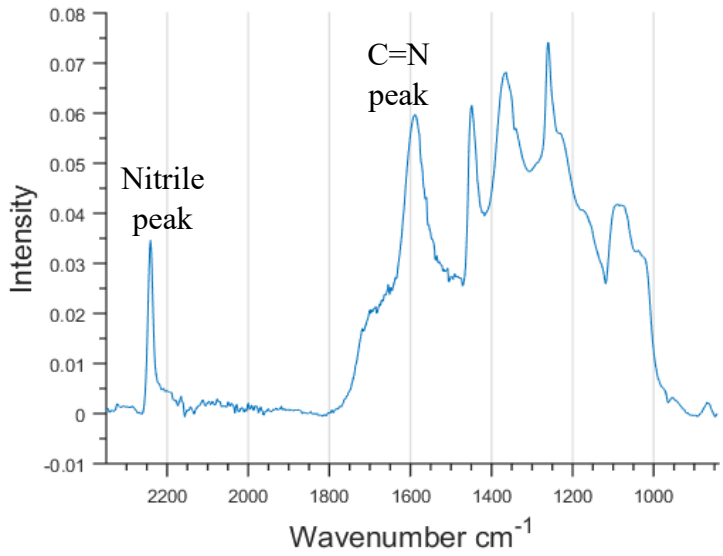

Figure 2.5: Example FTIR spectrum of partially stabilized PAN used to calculate the degree of stabilization.

The degree of stabilization is commonly estimated using the intensity ratio of FTIR peaks, diffraction peaks, or DSC exotherm(s) from the stabilized structure to one of the untreated PAN (Fig 2.5) [28,29,33,36,38,39,51,68,73,81,82]. For example, FTIR-based degree of stabilization is calculated as $\frac{I_{C=N}}{I_{C=N}+I_{nitrile}}$, where $I_{C=N}$ is the intensity of the C=N band around 1600 cm^{-1} and $I_{nitrile}$ is the intensity of the nitrile band around 2250 cm^{-1}. These estimates would be more accurate if a 100% stabilized fiber is used as a control, but it cannot yet be proven that a fiber is 100% stabilized. Diffraction-based estimations are limited as they only reflect the conversion of crystals within PAN, and stabilized PAN has diffraction peaks near those of untreated PAN [29,73] which could interfere with peak fitting required for accurate estimation. FTIR-based estimations require rigorous baseline subtraction and deconvolution of the C=N, C=C, and C=O peaks and a small nitrile peak often remains after stabilization, suggesting some nitrile groups do not react

[29,33,38,39,69,73,82]. DSC measures the amount of unstabilized PAN chains remaining; the DSC peak corresponding to stabilization decreases with the degree of stabilization. PAN fibers shrink during stabilization, stressing their holders if restrained. The change in this tensile stress is correlated to the degree of stabilization, but is not widely studied [28,29].

Degree of stabilization, oxygen content, and tensile strength of carbonized PAN fibers increase asymptotically with time and temperature when stabilized in air, regardless of tension applied to the fibers [15]. An 80-90% degree of stabilization is the threshold above which there is little increase in carbonized fiber tensile strength [28]. Temperatures of 250-300 ^{o}C and durations of 30-120 minutes are best to achieve an >80% degree of stabilization, either through an isothermal or multi-zone process. Stabilization does not occur or takes over 5 hours if the PAN fibers are heated below 240 ^{o}C [33,36,68,69,73]. Degree of stabilization when PAN fibers are held around 250 ^{o}C is 50-70 % after 1 hour, increasing to 80-90% after 2 hours [28,36,39,51,73]. At higher temperatures of 275 and 300 ^{o}C, degree of stabilization can exceed 50% after 30 minutes and reach 80% after an hour [28,73]. Industrially, stabilization is often performed in zoned convection ovens with subsequent zones having higher temperatures. Some studies have imitated this procedure by heating PAN fibers using increasing isotherms which gradually increase in temperature between 190 and 320 ^{o}C for a total of 1-2 hours [82]. Degree of stabilization measured by FTIR increases linearly as it does in constant temperature processes, reaching 80-90% by the end of the process.

2.1.2.4 Crystal Alignment and Tension

Similar to extruded polymer fibers, tension applied during the oxidative stabilization of PAN increases crystallinity, crystal alignment, and consequently the strength and modulus of carbon fiber after graphitization [47,67,68,76,86,87,90]. Applied tension counteracts PAN fiber shrinkage during stabilization, forces PAN chains closer together, reduces the activation energy and heat released for stabilization, yields denser fibers with fewer defects which lose less mass during carbonization, and better aligns the cyclized structure [37,47,67,76,86,90,93,96]. However, too much tension causes detrimental strain in the fibers, losing or reducing these benefits [67,70,96]. During oxidative stabilization, PAN diffraction peaks shrink and broaden while a new peak arises close to the graphite (002) peak, likely from nanocrystalline or turbostratic cyclized regions [31,64,66,71,80,87]. A TEM study performed by Yu et al. shows two regions of PAN crystals of different sizes. The smaller crystalline regions surrounded by amorphous domains disappear first when stabilized, with the larger ones react more slowly [80].

2.1.2.5 Core-Shell Structure

As PAN fibers are stabilized, they develop a core-shell structure (Fig 2.6) [17,19,38,60,61,79,82]. This structure is likely due to diffusion-controlled kinetics of the stabilization reactions. Oxygen reacts with the PAN as it diffuses inward towards the fiber center, with more oxygen incorporated into the shell and less oxygen available to react in the core [38,60,82]. This differentiation could result in different stabilization mechanisms and rates between the core and shell [38]. There is uncertainty on whether stabilization temperature [79] or duration [61] contributes more to the growth rate and size of

either region. After carbonization and graphitization, this process results in a more graphitic fiber shell [17,19,89].

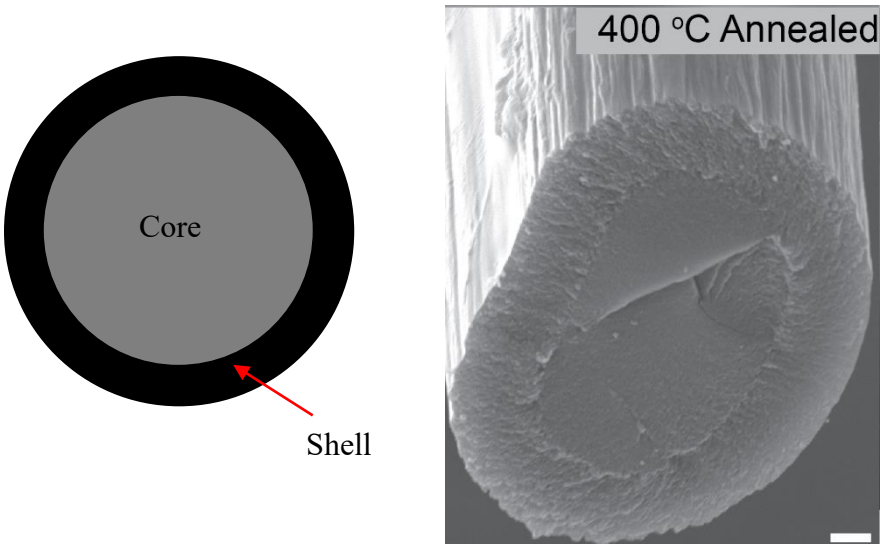

Figure 2.6: Schematic (a) and electron micrograph (b) of core-shell structure that forms during PAN annealing. Scale bar is 1 μm

2.1.2.6 Composite PAN Fibers

Recently, researchers have reinforced PAN fibers with graphite [97] and carbon nanotubes [17,78,91,98–102] to create stronger, higher modulus carbon fiber; the reinforcement leads to larger, better aligned graphite crystals during PAN carbonization [78,91]. Fiber strength increases proportional to CNT alignment along the fiber axis, which is aided by drawing and electrospinning [98]. Single-walled and carboxylate-functionalized CNTs provide better adhesion to the PAN matrix and thus better reinforcement than multi-walled and non-functionalized CNTs [100,102]. Oxidative stabilization occurs at slightly higher temperatures in reinforced PAN, as CNTs and graphite better distribute heat throughout the fiber [91,103]. CNTs slightly disrupt PAN crystallinity [102] and consequently

PAN crystals degrade more quickly during stabilization with CNTs present [91]. Oxidative stabilization for CNT-reinforced fibers has a slightly lower activation energy and is more gradual in a nitrogen atmosphere, but similar in air to unreinforced PAN [103]. The modulus and strength of carbonized fibers increases with stabilization time at 255 ^{o}C in air, but plateaus at 230-260 minutes with a slight decrease afterwards [103]. Although few comprehensive reviews exist on this subject, composite PAN fibers are discussed in reviews of PAN-based carbon fibers [104–106] and extensively studied by Prof. Satish Kumar's group [103].

2.1.2.7 Stabilization Techniques

Heat treatment is not the only way to initiate dehydrogenation and cyclization, though it was the simplest and most widely used when carbon fiber was first made. Electron beam [107], x-ray [65], UV [74,84,88], and gamma ray irradiation reduce the activation energy for the stabilization reactions [108] by generating free radicals within the polymer [109]. Small amounts of radical initiator added to the polymer can promote radiation-induced stabilization [75]. Longer exposures at higher energies can drive stabilization near completion [65] , however this increases the cost of industrial processing. Ion beam, ultraviolet irradiation, and plasma treatment have also been considered [110].

2.2 Experimental

2.2.1 PAN Fibers

Carbon fiber manufacturers did not respond to requests for PAN fibers, and chopped PAN fibers intended as concrete additives were purchased from Smooth On Inc (Macungie, PA). These PAN fibers included a small amount of a carbonyl-containing

comonomer. One benefit of using these fibers was their low cost—$6.90/lb. Given this price, the simplicity of stabilizing and annealing PAN in a tube furnace, and the ease of access to characterization techniques like FTIR, Raman, TGA, DSC, and NMR, studies on these PAN fibers are good projects to introduce undergraduate students to polymer materials science research.

2.2.2 Stabilization and Carbonization

PAN fibers (100 mg) were stabilized in a tube furnace (MTI high temp OTF-1200X-S50-LVT) using a 2.5 ^{o}C/min ramp rate, a constant dry air flow of 100 ccm, stabilization temperatures of 225, 250, 275, and 300 ^{o}C, and isotherms of 0, 1, and 5 h. For comparison, PAN fibers were stabilized using the same ramp and flow rates in nitrogen for 1 h at 250 and 275 ^{o}C. Certain stabilized fibers were carbonized immediately after stabilization using the same furnace, nitrogen flow rate, and ramp rate at 550 or 600 ^{o}C for 1 hour. Using a mass ≤ 100 mg proved essential, as higher masses resulted in a buildup of hydrogen cyanide and other reaction byproducts in the furnace tube. This caused the PAN fibers to shrivel and accelerated mass loss. A similar result was observed when stabilizing the PAN fibers in open air, likely due to the presence of water vapor.

2.2.2.1 Thermal and Spectroscopic Characterization

TGA (Netzsch TG 209 F1 Libra) and DSC (Netzsch DSC 214 Polyma) measurements used a 2.5 ^{o}C/min ramp rate from 25 to 350 ^{o}C under a 100 ccm air flow with a protective nitrogen flow of 100 ccm over the sensors. DSC samples were then cooled under the same conditions to 25 ^{o}C, and the cycle was repeated 2 more times. FTIR was performed on a ThermoFisher Nicolet iS10 using a diamond Attenuated Total

Reflectance (ATR) crystal and accumulating 64 scans, after which the spectrum quality did not improve. Solid state ^{13}C Cross-polarization magic angle spinning (MAS) NMR spectral analysis was performed with assistance from Dr. Lingchao Zhu on a Bruker NEO 600 MHz spectrometer equipped with a double-resonance 4 mm MAS probe. Samples were packed into a 4 mm rotor, which was spun at 10 kHz for more than 5000 scans with a relaxation delay of 3 s.

2.2.2.2 Wide-angle X-ray Scattering (WAXS)

Bundles of ~1,000 PAN fibers were placed in Linkam THMS600 heated stage (Linkam Scientific Instruments, Tadworth, UK), modified to use x-ray transparent Kapton film windows while maintaining the desired temperature and atmosphere. The Linkam stage was pre-calibrated with a thermocouple to determine that a set temperature of 303 ^{o}C was needed to heat the fibers to 275 ^{o}C, as they were not placed in direct contact with the heating element. Fibers were quickly heated to 150 ^{o}C over 4 min, then heated at 2.5 ^{o}C/min to 275 ^{o}C (fiber temperature) using an air flow of 100 ccm. After a 1 h isotherm, the gas was switched to argon and allowed to purge the heated stage for 5 min at 275 ^{o}C. Next, the stabilized fibers were heated at 2.5 ^{o}C/min to 600 ^{o}C (the Linkam stage's maximum temperature) and held at 600 ^{o}C for 1 h.

WAXS was performed on beamline 7.3.3 at Lawrence Berkeley National Laboratory's (LBNL) Advanced Light Source with a 10 keV beam energy and a Pilatus 2M detector [111]. 10 second exposures were collected at a rate of approximately 1.6 exposures/minute. A control bundle of PAN fibers was exposed to the beam at this exposure rate for 10 minutes to ensure no beam damage to the fibers. Diffraction patterns

were analyzed using custom software written by the beamline scientists, ImageJ (National Institutes of Health, NIH), and Datasqueeze (Prof. Paul Hiney, University of Pennsylvania). 1D diffraction plots were obtained by radially averaging diffraction images from ϕ = 85-105^{o} and radial 1D diffraction plots were obtained by averaging a q range of 1.05-1.35 for the PAN (200) peak and 1.4-2 for the graphitic (002) peak. 1D diffraction plots were fitted using Origin Pro (OriginLab Corp., Northampton, MA) with 2-4 gaussian profiles. Crystal sizes were estimated using the Scherrer approximation, $L_a = \frac{K\lambda}{w\cos\theta}$. λ is the X-ray wavelength, K is a constant of 0.9 based on the type of unit cell, θ is the diffracted peak position, and w is the peak full width at half-maximum. Crystal orientation was quantified using Herman's orientation function, $f_c = \frac{3}{2}(< \cos^2\phi > -1)$, where ϕ is the azimuthal angle and $< \cos^2\phi >$ is the weighted average of $\cos^2\phi$ based on the intensity (I) as a function of ϕ, $\frac{\int_0^{\pi/2} I(\phi)\sin\phi\cos^2\phi}{\int_0^{\pi/2} I(\phi)\sin\phi}$. A value of 1 indicates parallel orientation with the direction in question, 0 indicates random orientation, and -0.5 indicates perpendicular orientation.

2.3 Results and Discussion

2.3.1 Reaction Temperature and Mass Loss

DSC of the commercial PAN fibers in air is similar to PAN fibers without a carboxyl-containing copolymer like IA, with two main thermal transitions corresponding to stabilization reactions occurring at 258 and 302 ^{o}C (Fig 2.7). As these temperatures correspond to the maximum of broad peaks, stabilization begins at lower temperatures but proceeds more quickly as the temperature increases. The PAN fibers darkened as

stabilization progresses from light brown to dark brown and finally black (Fig 2.7). In the TGA thermogram, an initial mass loss was observed around 150 ^{o}C, which likely corresponds to the decomposition of comonomer functional groups or an additive, and the first inflection point corresponds to the reaction at 258 ^{o}C (Fig 2.8). As expected, the stabilization reaction rate and mass loss were proportional to stabilization temperature and decreased asymptotically as a majority of the PAN chains cyclize.

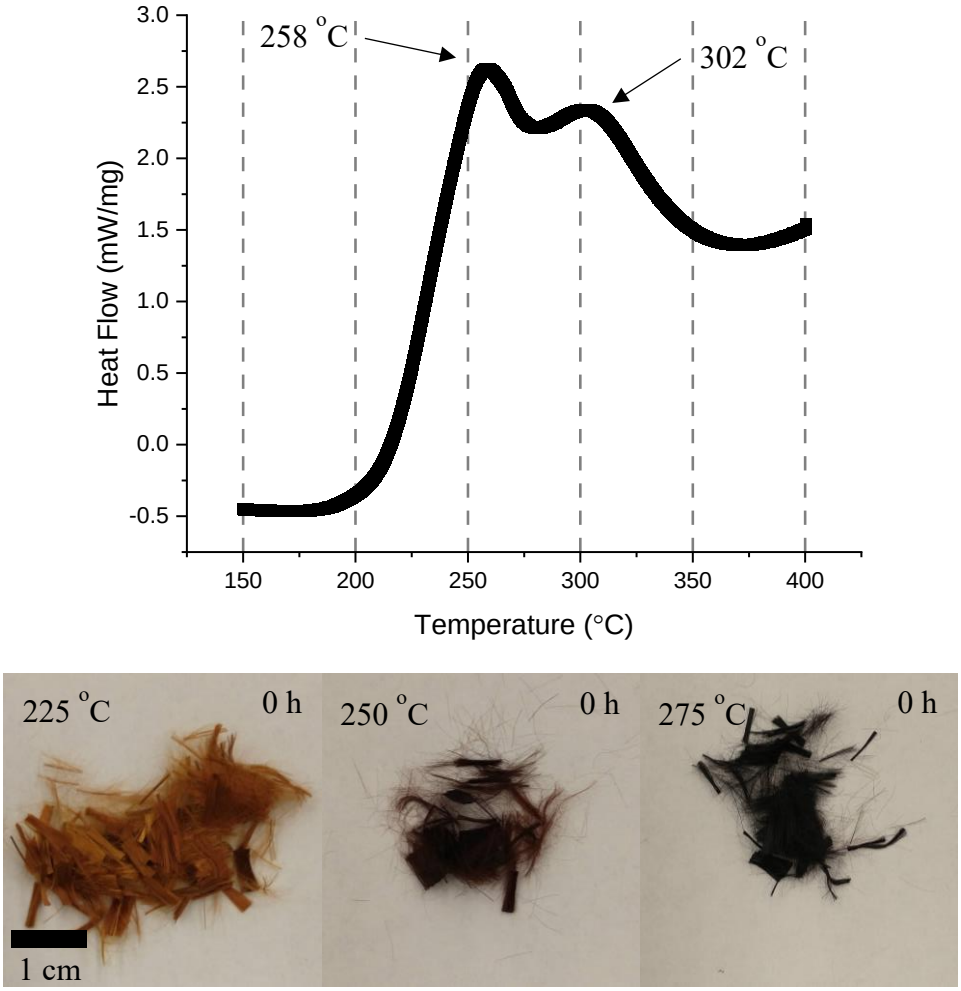

Figure 2.7: DSC of PAN fibers in air and corresponding color changes with stabilization temperature. All fibers stabilized above 275 ^{o}C or for over 1 h appeared black apart from 225 ^{o}C 1 and 5 h, which were dark brown.

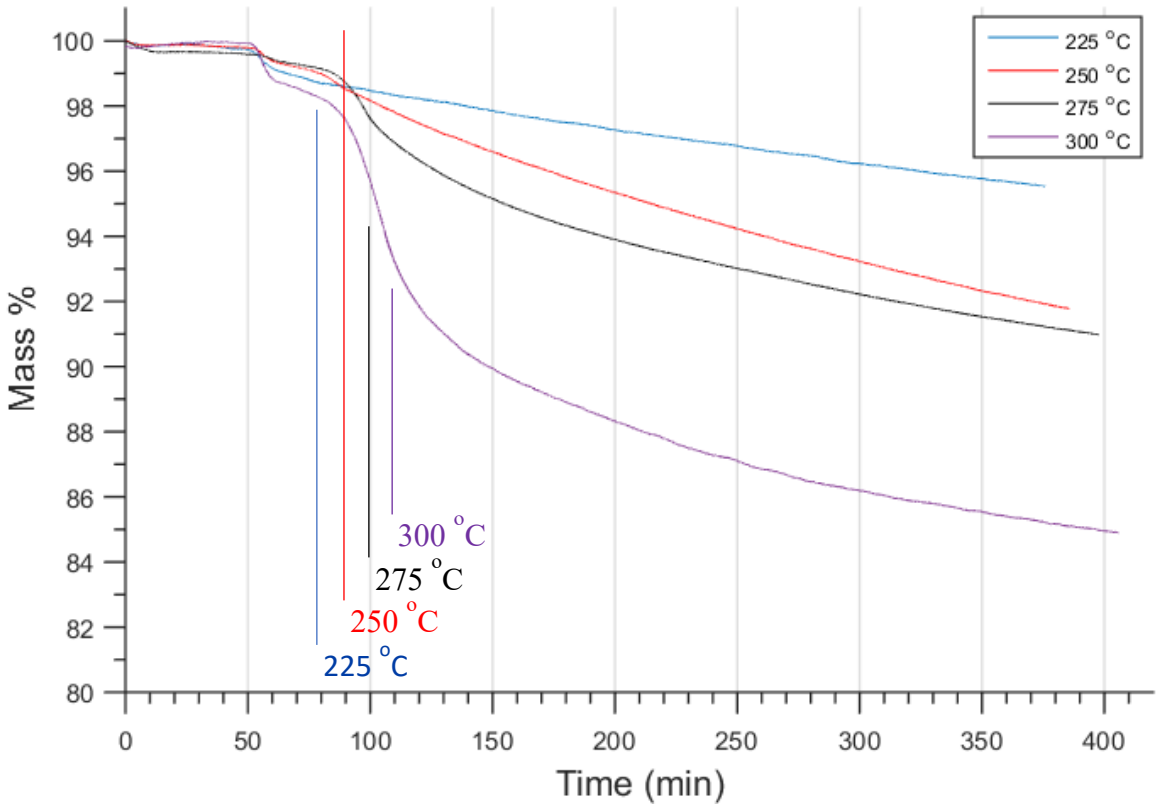

Figure 2.8: TGA of PAN fibers in air with isotherms that begin at the corresponding vertical lines.

2.3.2 Molecular Structure

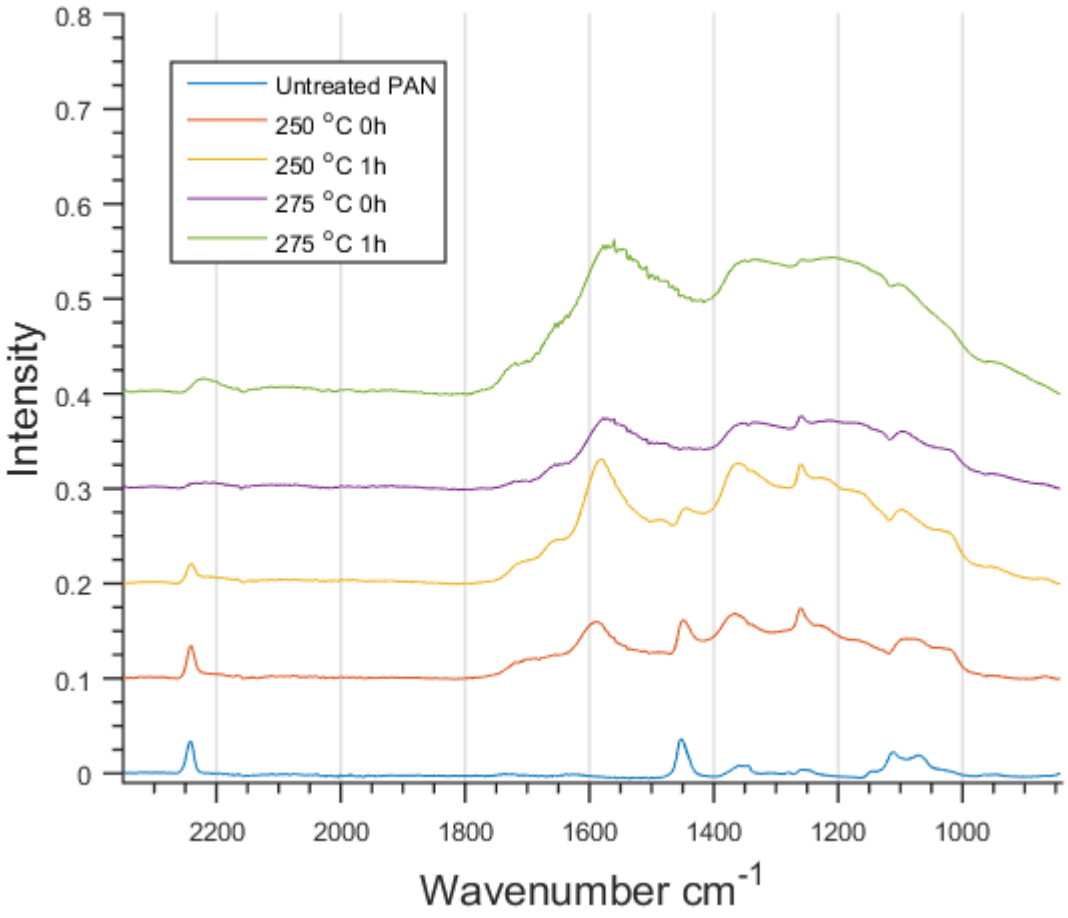

Figure 2.9: FTIR spectra from select time points showing PAN fiber stabilization progress.

Stabilized PAN fibers were difficult to characterize with FTIR due to the presence of a long-period sinusoidal background, so a linear piecewise background subtraction was approximated to obtain comparable spectra (Fig 2.9). The appearance of C=C and C=N peaks ca 1600 cm^{-1} indicate stabilization has begun at 250 ^{o}C, while the nitrile band at 2241 cm^{-1} decreases and mostly dissipates at 275 ^{o}C. The degree of stabilization was calculated using the formula described in section 2.1.2.3 (Table 2.2). This method

suggests stabilization is over halfway complete even at low temperatures, but its reliability is questionable based on the baseline subtraction. It would be optimal to deconvolute the 1600 cm^{-1} peak into individual components to isolate the C=N peak and best indicate the degree of stabilization, but that approach was not appropriate given the baseline correction. Alternately, grinding stabilized fibers into powder and mixing with KBr for transmission FTIR could yield more reliable quantitative results.

Table 2.2: aromatization index of stabilized PAN fibers calculated from FTIR data

Stabilization Conditions	250 °C 0 h	250 °C 1 h	275 °C 0 h	275 °C 1 h
Aromatization Index	0.63	0.86	0.92	0.91

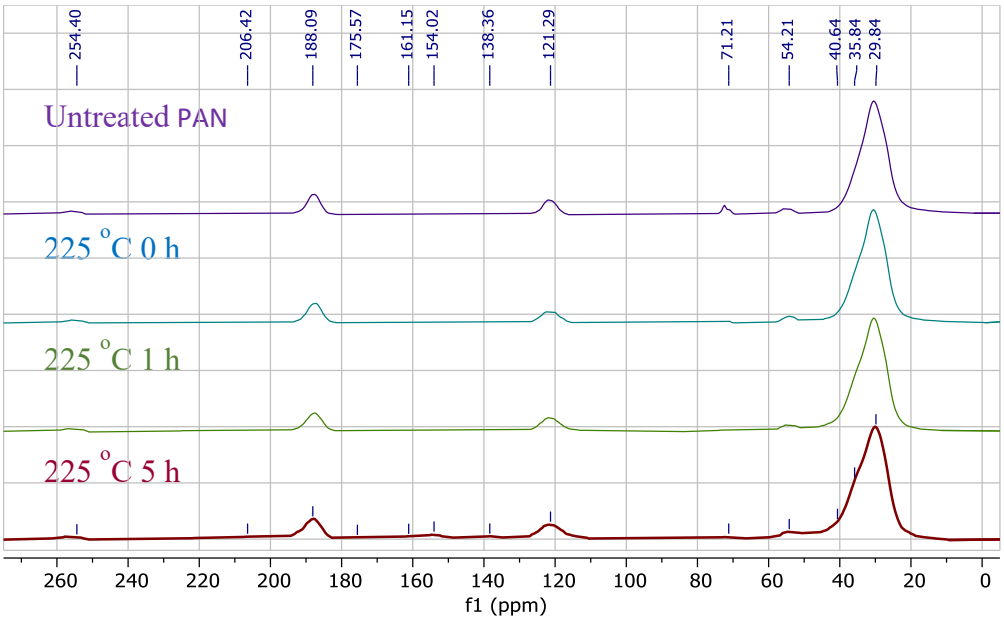

Figure 2.10: ^{13}C SSNMR spectra of PAN fibers stabilized at 225 °C. Many peak labels correspond to where peaks appear at higher stabilization temperatures and times.

^{13}C SSNMR spectra of PAN fibers shows the expected nitrile peak at 121.5 ppm and combined CH and CH_2 peaks at 30.4 ppm. Additional peaks at 187.8, 72.1, and 55.2 ppm are likely from the copolymer or additives, and there is an additional unidentified peak at 255.2 ppm that is present in other PAN copolymer SSNMR spectra (Fig 2.10) [73]. There are no significant structural changes in PAN fibers stabilized at 225 ^{o}C 0 and 1 h and 250 ^{o}C 0 h, and only slight changes at 225 ^{o}C 5h and 250 ^{o}C 1h (Fig 2.10-11).

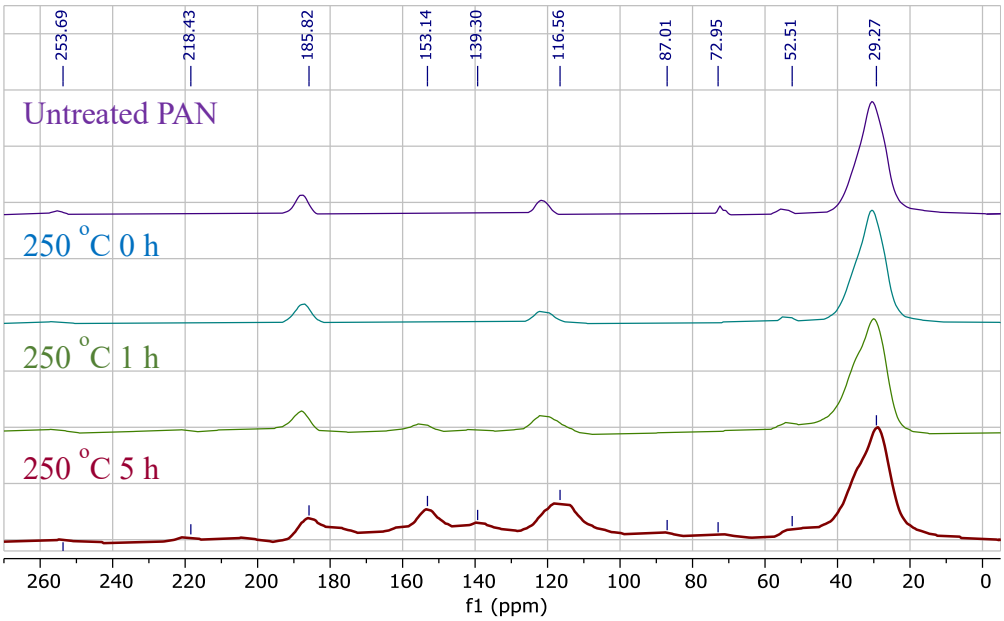

Figure 2.11: ^{13}C SSNMR spectra of PAN fibers stabilized at 250 ^{o}C.

Spectra from 250 ^{o}C 5 h, 275 ^{o}C 0 h, and 300 ^{o}C 0 h depict similar structures based on the peaks present and their relative intensity to the CH/CH_2 peak (Fig 2.11-2.13). These data highlight the importance of the temperature at which the stabilization reactions begin. If PAN fibers are stabilized below this temperature, it will take significant time to achieve cyclization. For example, it is more expensive, both in terms of process and heating time, to stabilize PAN at 250 ^{o}C for 5 h than at 275 ^{o}C for 0 h.

Heating to temperatures above the reaction temperature does little to accelerate the stabilization reaction but results in more mass loss. This observation, along with the steep mass losses observed in TGA data, demonstrates how quickly the stabilization reactions can occur at the appropriate temperature. This can be detrimental, since the heat released in these exothermic reactions can damage the polymer and lead to excessive mass loss or voids which result in weaker carbon fiber.

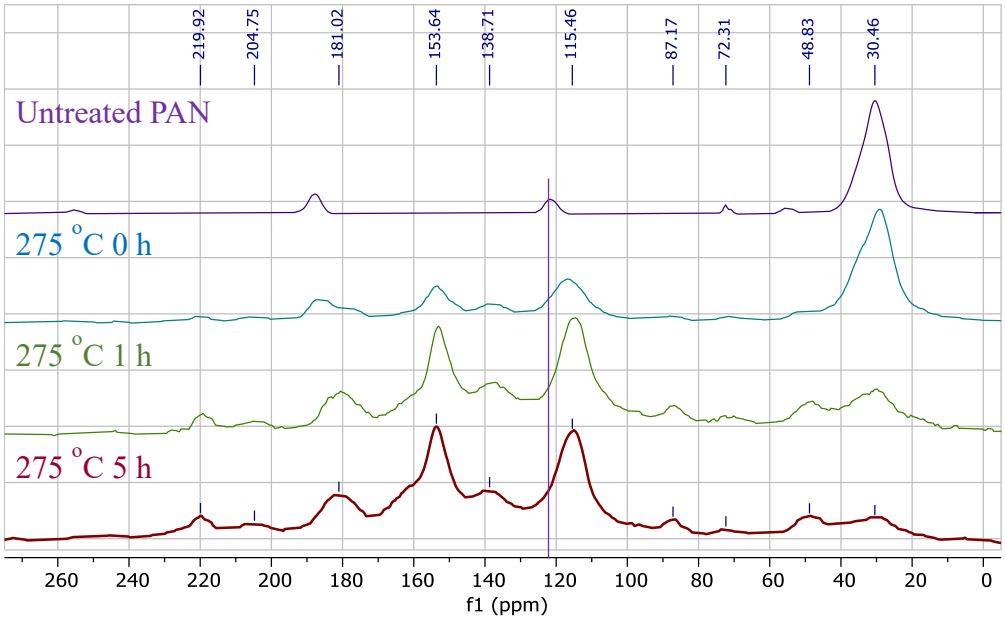

Figure 2.12: ^{13}C SSNMR spectra of PAN fibers stabilized at 275 °C.

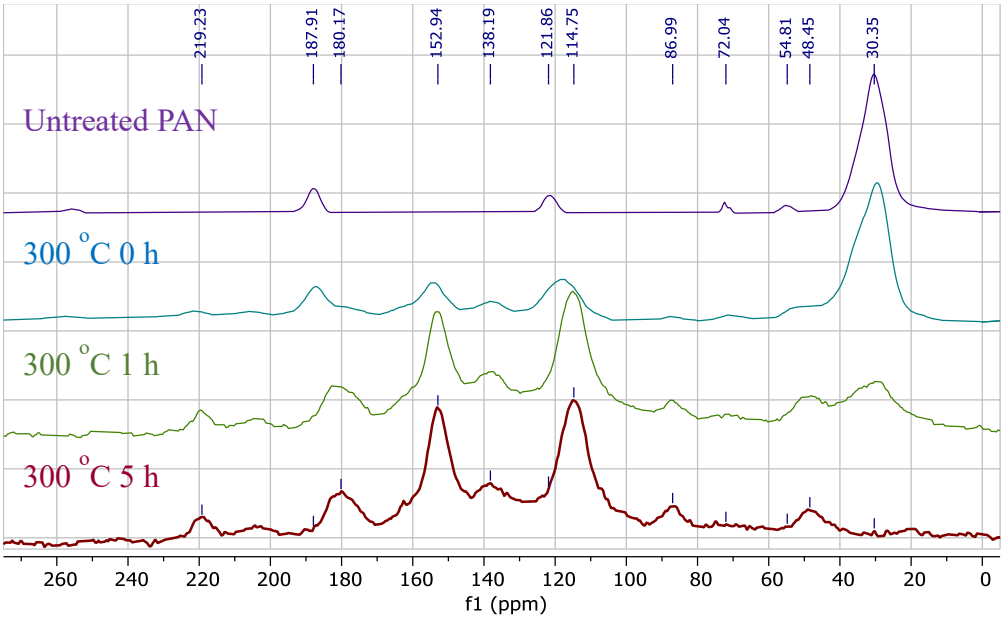

Figure 2.13: ^{13}C SSNMR spectra of PAN fibers stabilized at 300 °C.

Since 250 °C is well past the onset temperature of the first stabilization reaction, more stabilization may be expected to occur at 250 °C 1 h. This apparent lack of stabilization could be due to inaccurate furnace calibration. Tube furnaces use proportional-integral-derivative (PID) software controls to adjust the power supplied to the heating coil based on the temperature recorded by a thermocouple in the furnace. However, since that thermocouple cannot be placed on the sample or even inside the tube, it often reads a temperature higher than the actual sample temperature. This inaccuracy can be circumvented by placing a thermocouple inside the tube to measure the sample temperature, then using a preprogrammed offset in the furnace to adjust the calibration accordingly. However, this calibration was not available for the instrument used for these studies.

FTIR spectra appear to overestimate the degree of stabilization compared to SSNMR spectroscopy. While FTIR spectra at 250 ^{o}C and 275 ^{o}C 1 h have prominent C=C and C=N peaks, those peaks do not appear in NMR until 275 ^{o}C 1 h. This discrepancy could be affected by the difference in absorptivity constants between nitrile and C=N peaks in FTIR spectroscopy [36]. Similarly, peak height in ^{13}C SSNMR spectra is less indicative of the number of carbons present as it varies based on the Nuclear Overhauser Effect between neighboring atoms, especially carbon and hydrogen. Although both methods have their limitations, FTIR spectroscopy is accepted as the better mechanism to use for determining the degree of stabilization, yet there is a risk that FTIR spectroscopy overestimates the degree of stabilization [28,29,33,36,38,39,51,68,73,81,82].

The ideal stabilization temperature is 275 ^{o}C for these PAN fibers. As stabilization progresses at 275 ^{o}C from 0-1 h, the nitrile, CH, and CH_2 peaks decrease, but do not vanish. A variety of peaks corresponding to semi-cyclized, semi-aromatic structures, which include carbonyls and alcohols, arise (Fig 2.14). The most prominent peaks are from cyclized C=N around 153.1 ppm and isolated -C=C< around 114.3 ppm. These data indicates that while most of the PAN cyclizes into aromatic, pyridinic rings, the structure is not uniform. In particular, regions of many consecutive pyridinic rings representing the proposed ladder-like structure are not observed, rather the structure contains oxygen inclusions, breaks in cyclization, and other “impurities” as observed by other researchers [25,40,73].

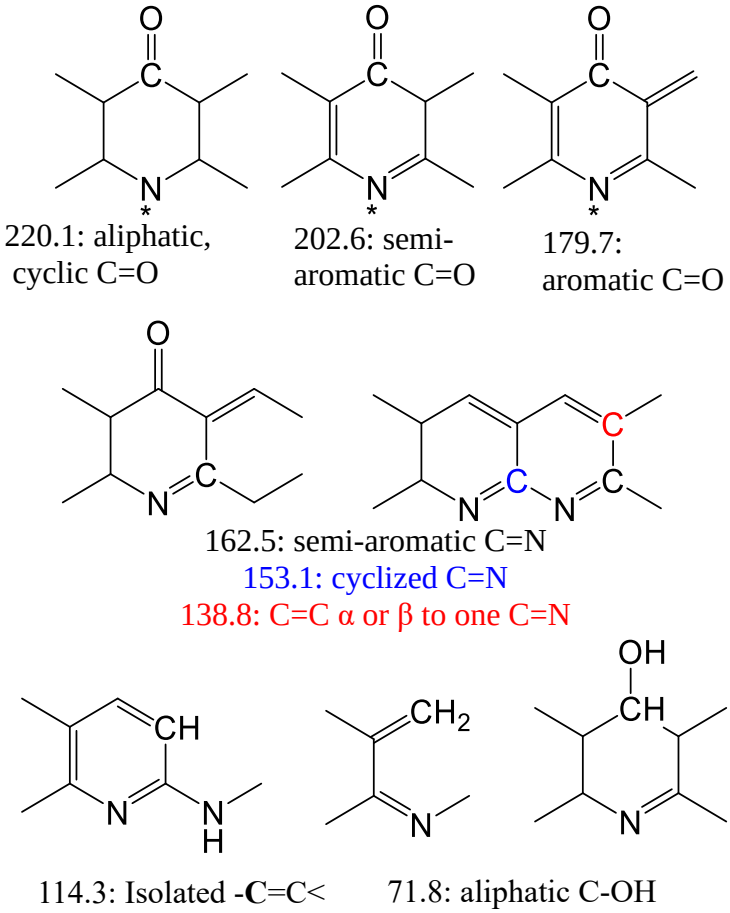

Figure 2.14: Several potential structures matching ^{13}C SSNMR peaks present in stabilized PAN. Nitrogen atoms marked with a * are interchangeable with carbon atoms.

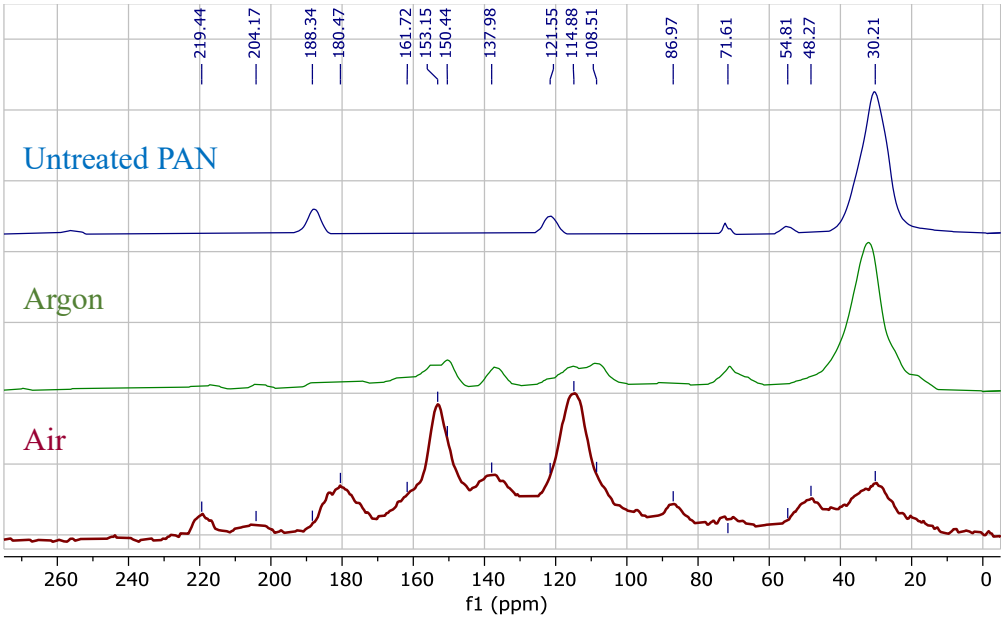

Figure 2.15: ^{13}C SSNMR spectra of PAN fibers stabilized at 275 ^{o}C for 1 h in argon vs air.

Stabilization in argon at 275 ^{o}C for 1 h did not progress as quickly as in air; the carbonyl peaks are less prominent (Fig 2.15) but still present. Thus, some of the oxygen present in the PAN fibers from comonomers is retained in the structure, which can help carbonization to occur. Little difference between carbonized fibers made from PAN fibers stabilized in argon and air was observed (Fig 2.16). The small amount of oxygen present in PAN fibers stabilized in argon from the copolymer could be sufficient to catalyze carbonization, although it is possible the PAN fibers stabilized in air could have larger or more crystalline graphite domains once graphitized. This result is surprising given the structural differences between PAN fibers stabilized at 250 and 275 ^{o}C, but it is likely the stabilization reaction progresses as the fibers are heated up above 500 ^{o}C. After carbonization, peaks corresponding to the cyclized structure (151.1, 118-128 ppm) are even more prominent, indicating larger cyclized domains.

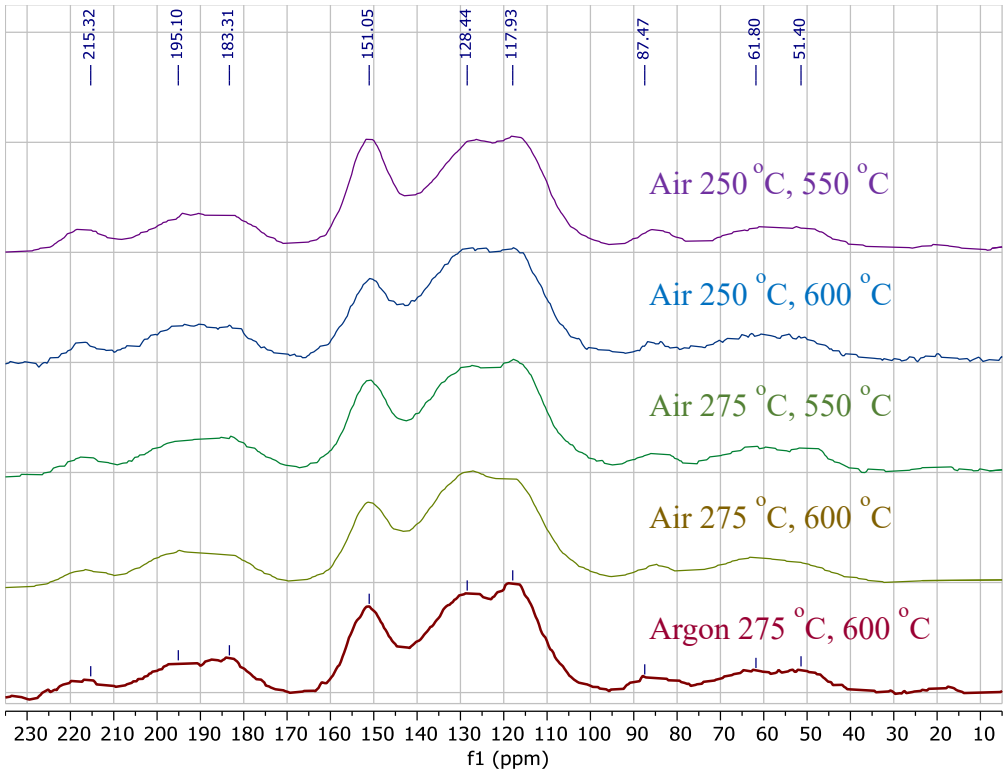

Figure 2.16: ^{13}C SSNMR of PAN fibers stabilized in air or argon for 1 h at the first listed temperature and carbonized in argon for 1 h at the second temperature.

2.3.3 Crystal Structure

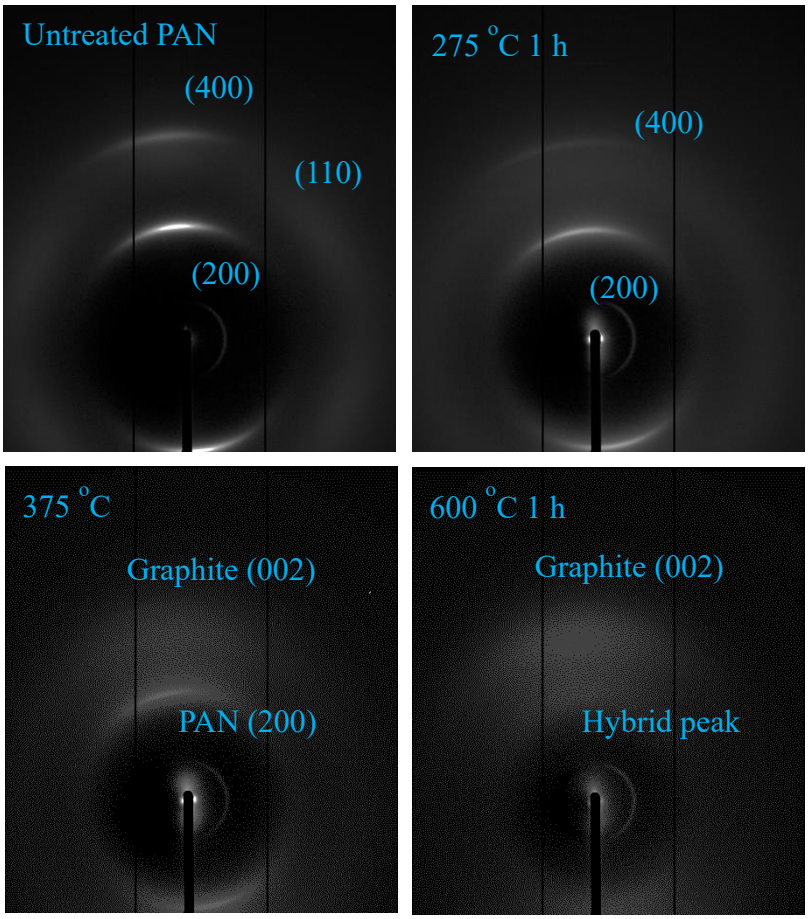

Figure 2.17: 2D WAXS diffraction images from in-situ PAN fiber stabilization and carbonization. The unknown peak, which could be residual PAN, is denoted as a "hybrid peak."

During stabilization and carbonization, the PAN diffraction peaks decrease in intensity and increase in breadth, while a new peak appears around the d-spacing for the graphite (002) diffraction (Fig 2.17) [31,39,47,50,63,64,66,71,73,76,78,80,87,88]. Depending on the PAN fiber composition and process parameters, this transition typically begins at 230-250 ºC and the PAN (200) peak is no longer visible at 250-300 ºC [31,64,71,73,76,80,81]. A broader peak arises in place of the sharp PAN (200) peak but has not been identified and

is less prominent in certain studies, especially after longer stabilization times [76,78,88]. Similar to the SSNMR spectroscopy results in section 2.3.2, stabilization is not complete after long isotherms at low temperatures [39]. The PAN crystals become less oriented as stabilization progresses, evident by a broader arc in 2D WAXS patterns [63,73,78,88]. The two peaks present after stabilization persist through carbonization, and the graphitic peak increases in intensity and decreases in breadth during graphitization [50,87].

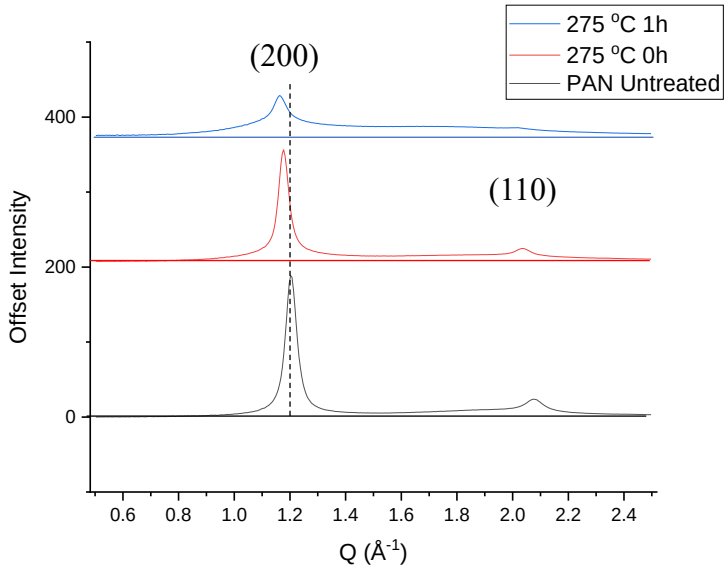

Figure 2.18: 1D diffraction patterns of untreated and stabilized PAN fibers.

Based on the *in-situ* WAXS patterns, the commercial PAN fibers did not stabilize until heated from 375-425 °C (Fig 2.18). This result suggests that although the system was pre-calibrated to compensate for the fibers being cooler than the heating element, the fibers likely did not reach 275 °C during stabilization. Instead, they displayed structures more consistent with PAN fibers stabilized at 250 °C. Based on the NMR results, stabilization at 250 or 275 °C had little effect on the molecular structure of carbonized

fibers. Nonetheless, there is a clear transition from the PAN crystal structure to the stabilized structure (Fig 2.17) [63,73,78,88].

During peak fitting, a 4-peak fit worked best for PAN fibers before stabilization began (Fig 2.19). In this fit, the (200) peak was best fit with two peaks. Often semicrystalline polymer diffraction peaks have crystalline and nanocrystalline components, which explains the necessity for two peaks. The PAN (110) peak contributes slightly to the 1D diffraction plot, but since its maximum diffraction occurs at $\phi \sim 30\text{-}45$ ^{o}C, it is not useful for quantification in these plots. During stabilization, the PAN (200) peak decreases in intensity but remains visible as it convolves with a second, unidentified peak. This second peak, which appears at the same q value as PAN (200), may arise from PAN crystals which have shrank in size due to the stabilization reactions. This peak may also arise from turbostratic stabilized structures which have larger d-spacings than pure graphite crystals. Either option is plausible, so this peak is called a "hybrid." After stabilization, the PAN (200) peak disappears while the hybrid peak remains.

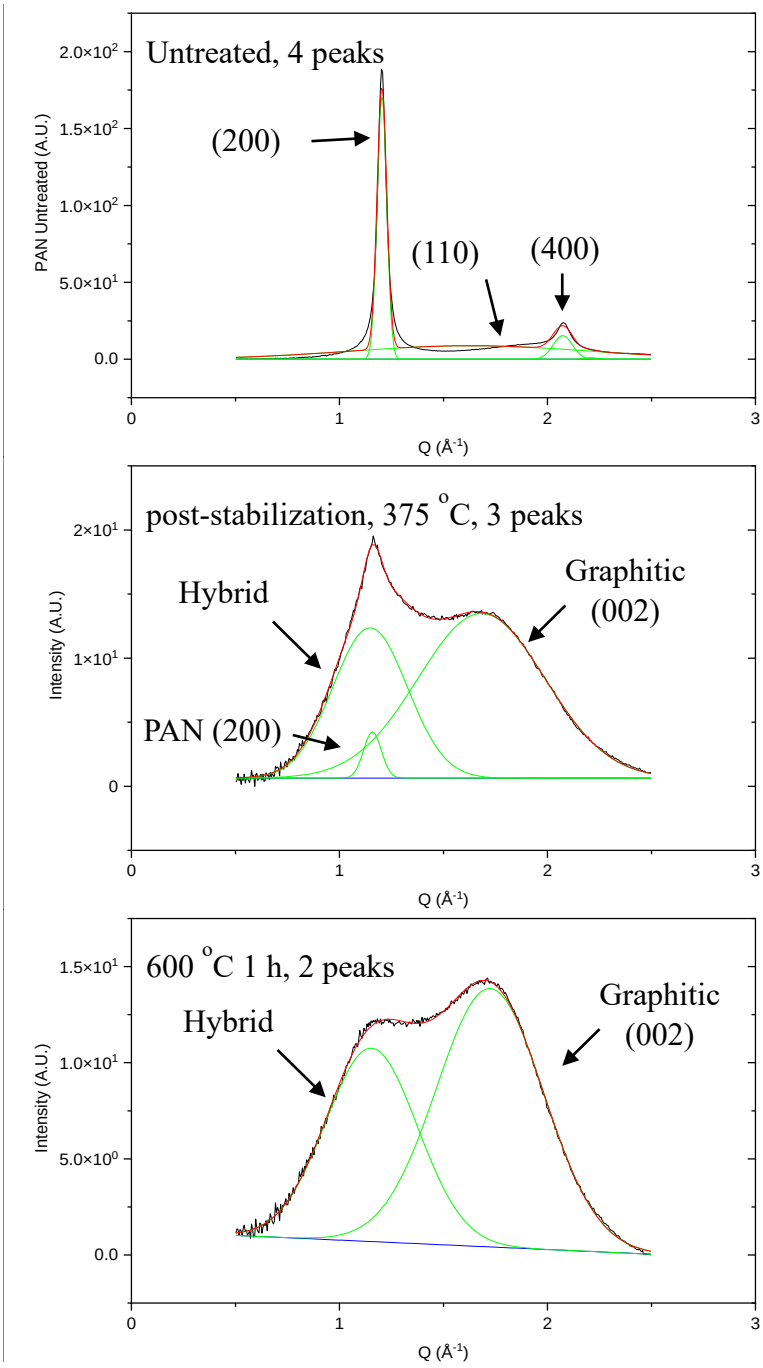

Figure 2.19: Peak fitting for PAN during different points in stabilization and carbonization. A 3-peak fitting was used when PAN (400) became irrelevant, and similarly for a 2-peak fitting and PAN (200).

Measured PAN (200) and graphite (002) d-spacings are 0.53-0.54 and 0.37-0.36 nm, respectively (Fig 2.20). These results are consistent with experimental values reported in literature, though the graphitic d-spacing (distance between crystal planes) is larger than that of pure graphite crystals at 0.34 nm [31,64,66,71,80,87]. Since these graphitic crystals form during stabilization and are not pure graphite, it follows that they are not as densely packed. The stability of these d-spacings across stabilization and low-temperature carbonization suggests an abrupt crystalline phase transition when PAN crystals cyclize. PAN crystals initially increase in size from 27 to 29 nm, then shrink after the initial stabilization temperature is reached. The shrinkage accelerates during heating for carbonization, until the PAN (200) peak becomes negligible after 485 ^{o}C. The PAN (200) intensity follows a similar trend, though the decrease in intensity is linear once stabilization begins. These trends are also consistent with literature, though the PAN crystals reported here are larger than the 7-20 nm crystals reported elsewhere [31,64,66,71,80,87]. Note that the graphitic peak does not appear until 50 minutes into stabilization, based on the change in peak intensity and crystal size. Occasionally Origin's curve fitting algorithm gives certain peaks 0 intensity, which results in the outlier points in the graphs.

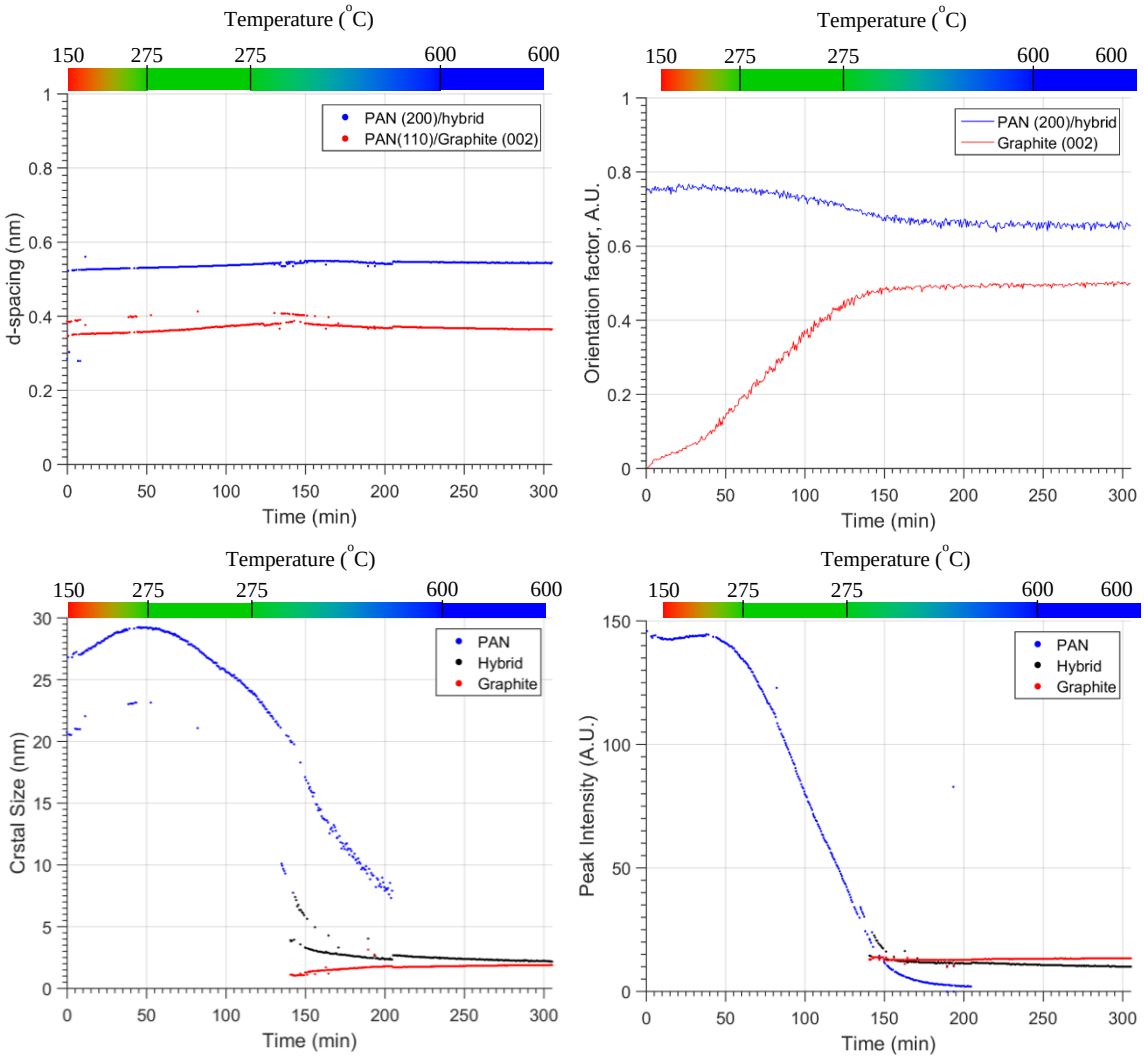

Figure 2.20: PAN crystal spacing, size, and WAXS peak intensity during the *in-situ* study. Gradient color scales represent a 2.5 °C/min heating rate. Air was used from 150-275 °C and argon from 275-600 °C

PAN (200) crystals become less well-oriented along the long axis of the fiber proportional to their decrease in crystal size (fig 2.20), likely due to the molecular rearrangements happening as both crystalline and amorphous regions cyclize. Orientation factor calculations average over the entire radial ϕ range, so the initial orientation values correspond to the PAN (110) relative to the long axis of the fiber. The graphitic crystals

formed during stabilization and cyclization have moderate orientation along the long axis of the fiber, but this orientation increases with the application of tension during stabilization and when the crystals grow in size during graphitization [88]. The hybrid peak interestingly has better alignment than the graphitic one, possibly because it is influenced by residual PAN crystals, or because it represents PAN crystals which have cyclized in an unexpected way, maintaining some of their original crystal structure and orientation.

2.4 Conclusions and Future Work

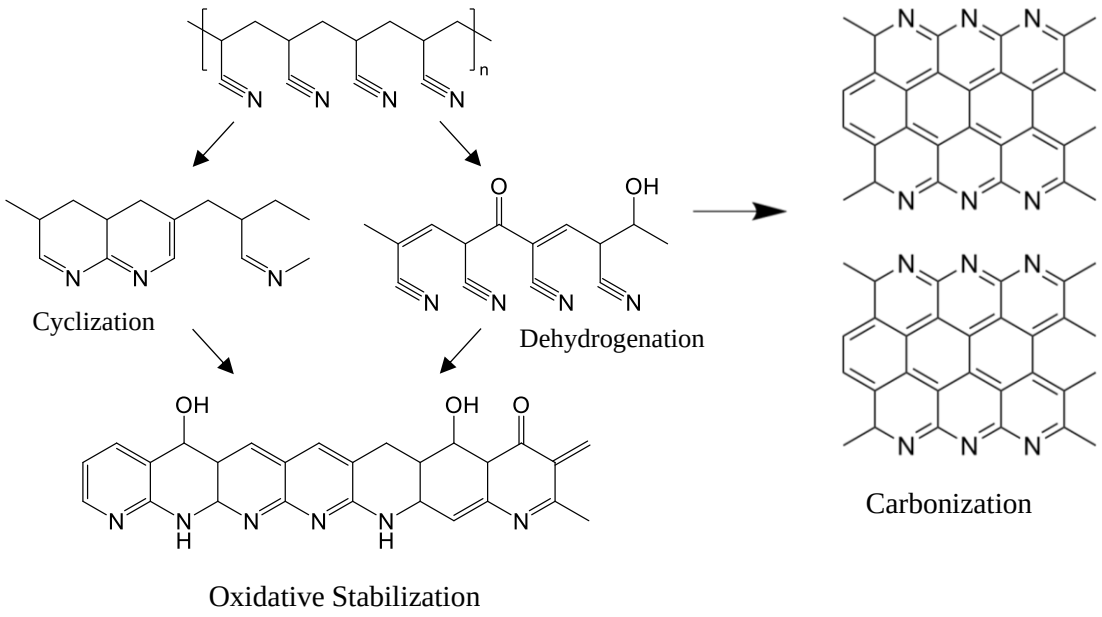

Figure 2.21: Revised depiction of PAN oxidative stabilization.

Researchers over the past 50 years have highlighted that oxidatively stabilized PAN may not be as simple as the accepted ladder structure. (Fig 2.21) Nonetheless, much remains unknown about the stabilization process. While oxygen plays a role and is incorporated into the stabilized structure, the exact mechanism by which this happens has not been studied in detail, partially due to the difficulty of envisioning reaction

mechanisms with diatomic oxygen. FTIR, NMR, and diffraction experiments offer slightly different methods of stabilization. FTIR suggests cyclization and dehydrogenation occur more quickly than NMR does. WAXS results show the PAN crystals deteriorate even before spectroscopic techniques indicate a significant decrease in the nitrile band despite a previous study suggesting smaller PAN crystals cyclize first [80]. We theorized a direct crystalline transition from PAN (200) to graphite (002), but the data show a delayed transition, if any.

Based on experimental NMR data, stabilization temperature and atmosphere do not significantly affect the molecular structure of stabilized PAN copolymers, as they already contain oxygen to facilitate carbonization. This effect could be a result of the carbonization procedure including a gradual ramp to 600 ^{o}C, while most industrial processes will feed room-temperature stabilized fibers into a carbonization furnace of 900-1000 ^{o}C, sometimes with a brief low-temperature zone beforehand. Stabilization continues during this gradual ramp, as shown by *in-situ* WAXS data. Thus, it is likely that PAN stabilized at lower temperatures or in an inert environment will not carbonize well. The graphite crystals which formed during the *in-situ* study are about half the size as those made using the same fibers but annealed in a tube furnace, discussed in chapter 3. This underscores the importance of complementary spectroscopic and crystallographic characterization to evaluate PAN during its processing to carbon fibers. For example, graphite crystal size may differ between two fibers with identical degrees of stabilization.

Although certain elements of PAN oxidative stabilization are well studied, others warrant more investigation. Stabilization should be studied in more depth using WAXS

on *ex*- and *in-situ* stabilized and carbonized fibers to properly account for the lower fiber temperatures when stabilized on a heated microscope stage. Carbonization should be included along with stabilization studies and done using parameters closer to industrial processes. PAN-based carbon fiber is known to have a core-shell structure, but what controls the formation and size of the core-shell and its effects on fiber mechanical properties should be investigated. Molecular dynamics simulation and other molecular modelling techniques could be applied to PAN stabilization and carbonization to help further understand the underlying mechanisms.

Researchers are investigating natural, renewable alternatives to PAN, either as standalone carbon fiber precursors or mixtures with PAN. To date, none of these methods have yielded carbon fibers with a strength and modulus as high as PAN-based carbon fiber. The abundant polysaccharide lignin is being investigated as a precursor, but it is a complex polysaccharide with no polymeric structure, so it is difficult to theorize stabilization mechanisms that apply to the entire lignin molecule. Lignin also has smaller, less oriented crystals than PAN. Given these factors, it is not the best choice for a natural alternative. Instead, researchers should consider natural materials with simple, repeating structures and high crystallinity. Rayon or other cellulosic polysaccharides should be re-investigated for this purpose, especially considering modern techniques to functionalize or modify polysaccharides. Proteins such as spider silk form semicrystalline fibers, although their structures are even more complicated than those of polysaccharides. Given recent advances in genetic engineering, synthetic protein and polysaccharide synthesis, and artificial intelligence-based materials selection researchers should also investigate

designing custom “natural” materials. These materials can be produced in bulk through genetically engineered single-celled organisms, or made synthetically through benign processes.

2.5 References

(1) Zweben, C. In *Mechanical Engineers' Handbook*; Kutz, M., Ed.; Wiley: Hoboken, NJ, 2015; Vol. 1. Ch. 10, pp 1–37.

(2) Huang, X. Fabrication and Properties of Carbon Fibers. *Materials* **2009**, *2* (4), 2369–2403. https://doi.org/10.3390/ma2042369.

(3) Edison, T. Electric Lamp. US Patent No. 223898, January 27, 1880.

(4) Bacon, R. Filamentary Graphite and Method for Producing the Same. 2957756, October 15, 1960.

(5) Soutis, C. Carbon Fiber Reinforced Plastics in Aircraft Construction. *Mater. Sci. Eng. A* **2005**, *412* (1–2), 171–176. https://doi.org/10.1016/j.msea.2005.08.064.

(6) Ford, C. Fibrous Graphite. US Patent No. 3107152, October 15, 1963.

(7) Shindo, A. Process for the Preparation of Carbon Fibers. US Patent No. 3529934, February 20, 1967.

(8) Shindo, A. Producing Method of Carbon or Carbonaceous Material. US Patent No. 3427120, February 11, 1969.

(9) Shindo, A.; Nakanishi, Y.; Sawada, Y. Method for Manufacture of Heat-Resistant Fibers. US Patent No. 3886263, May 27, 1975.

(10) Johnson, W.; Phillips, L.; Watt, W. Production of Carbon Fibres and Compositions Containing Said Fibres. 3412062, November 19, 1968.

(11) Mair, W. N.; Mansfield, E. H. William Watt. 14 April 1912 to 11 August 1985. In *Biographical Memoirs of Fellows of the Royal Society*; The Royal Society, 1987; Vol. 33, pp 642–667.

(12) Schalamon, W.; Bacon, R. Process for Producing Carbon Fibers Having a High Young's Modulus of Elasticity. US Patent No. 3716331, February 13, 1973.

(13) Holcomb, Griffin. Carbon Fiber & Graphene Manufacturing in the US. *IBISWorld Ind. Rep. OD4649* **2019**.

(14) Jain, M. K.; Abhiraman, A. S. Conversion of Acrylonitrile-Based Precursor Fibres to Carbon Fibres: Part 1 A Review of the Physical and Morphological Aspects. *J. Mater. Sci.* **1987**, *22* (1), 278–300. https://doi.org/10.1007/BF01160584.

(15) Gupta, A. K.; Paliwal, D. K.; Bajaj, P. Acrylic Precursors for Carbon Fibers. *Polym. Rev.* **1991**, *31* (1), 1–89. https://doi.org/10.1080/15321799108021557.

(16) Rahaman, M. S. A.; Ismail, A. F.; Mustafa, A. A Review of Heat Treatment on Polyacrylonitrile Fiber. *Polym. Degrad. Stab.* **2007**, *92* (8), 1421–1432. https://doi.org/10.1016/j.polymdegradstab.2007.03.023.

(17) Newcomb, B. A. Processing, Structure, and Properties of Carbon Fibers. *Compos. Part Appl. Sci. Manuf.* **2016**, *91*, 262–282. https://doi.org/10.1016/j.compositesa.2016.10.018.

(18) Merlen, A.; Buijnsters, J.; Pardanaud, C. A Guide to and Review of the Use of Multiwavelength Raman Spectroscopy for Characterizing Defective Aromatic Carbon Solids: From Graphene to Amorphous Carbons. *Coatings* **2017**, *7* (10), 153. https://doi.org/10.3390/coatings7100153.

(19) Dugger, T. W.; Sarkar, S.; Correa-Garhwal, S. M.; Zhernenkov, M.; Zhang, Y.; Kolhatkar, G.; Mohan, R.; Cruz, L.; Lubio, A. D.; Ruediger, A.; Hayashi, C. Y.; Uhrich, K. E.; Kisailus, D. J. Ultrastructures and Mechanics of Annealed *Nephila Clavipes* Major Ampullate Silk. *Biomacromolecules* **2020**, *21* (3), 1186–1194. https://doi.org/10.1021/acs.biomac.9b01615.

(20) Yu, M.; Wang, C.; Zhao, Y.; Zhang, M.; Wang, W. Thermal Properties of Acrylonitrile/Itaconic Acid Polymers in Oxidative and Nonoxidative Atmospheres. *J. Appl. Polym. Sci.* **2009**, n/a-n/a. https://doi.org/10.1002/app.31664.

(21) Tang, M. M.; Bacon, R. Carbonization of Cellulose Fibers-I Low Temperature Pyrolysis. *Carbon* **1964**, *2*, 211–200.

(22) Ross, S. E. Observations Concerning the Carbonization of Viscose Rayon Yarn. *Text. Res. J.* **1968**, *38* (9), 906–913. https://doi.org/10.1177/004051756803800905.

(23) Ezekiel, H. M.; Spain, R. G. Preparation of Graphite Fibers from Polymeric Fibers. *J. Polym. Sci. Part C Polym. Symp.* **2007**, *19* (1), 249–265. https://doi.org/10.1002/polc.5070190120.

(24) Bashir, Z. A Critical Review of the Stabilisation of Polyacrylonitrile. *Carbon* **1991**, *29* (8), 1081–1090. https://doi.org/10.1016/0008-6223(91)90024-D.

(25) Wang, Y.; Xu, L.; Wang, M.; Pang, W.; Ge, X. Structural Identification of Polyacrylonitrile during Thermal Treatment by Selective ^{13}C Labeling and Solid-State ^{13}C NMR Spectroscopy. *Macromolecules* **2014**, *47* (12), 3901–3908. https://doi.org/10.1021/ma500727n.

(26) Mittal, J.; Bahl, O. P.; Mathur, R. B.; Sandle, N. K. IR Studies of PAN Fibres Thermally Stabilized at Elevated Temperatures. *Carbon* **1994**, *32* (6), 1133–1136. https://doi.org/10.1016/0008-6223(94)90222-4.

(27) Sun, T.; Hou, Y.; Wang, H. Mass DSC/TG and IR Ascertained Structure and Color Change of Polyacrylonitrile Fibers in Air/Nitrogen during Thermal Stabilization. *J. Appl. Polym. Sci.* **2010**, *118* (1), 462–468. https://doi.org/10.1002/app.32175.

(28) Ogawa, H.; Saito, K. Oxidation Behavior of Polyacrylonitrile Fibers Evaluated by New Stabilization Index. *Carbon* **1995**, *33* (6), 783–788.

(29) Zhu, Y.; Wilding, M. A.; Mukhopadhyay, S. K. Estimation, Using Infrared Spectroscopy, of the Cyclization of Poly(Acrylonitrile) during the Stabilization Stage of Carbon Fibre Production. *J. Mater. Sci.* **1996**, *31* (14), 3831–3837. https://doi.org/10.1007/BF00352799.

(30) Xue, T. J.; McKinney, M. A.; Wilkie, C. A. The Thermal Degradation of Polyacrylonitrile. *Polym. Degrad. Stab.* **1997**, *58*, 193–202.

(31) Yu, M.; Wang, C.; Bai, Y.; Wang, Y.; Wang, Q.; Liu, H. Combined Effect of Processing Parameters on Thermal Stabilization of PAN Fibers. *Polym. Bull.* **2006**, *57* (4), 525–533. https://doi.org/10.1007/s00289-006-0581-8.

(32) Zhang, W.; Wang, Y.; Sun, C. Characterization on Oxidative Stabilization of Polyacrylonitrile Nanofibers Prepared by Electrospinning. *J. Polym. Res.* **2007**, *14* (6), 467–474. https://doi.org/10.1007/s10965-007-9130-x.

(33) Ouyang, Q.; Cheng, L.; Wang, H.; Li, K. Mechanism and Kinetics of the Stabilization Reactions of Itaconic Acid-Modified Polyacrylonitrile. *Polym. Degrad. Stab.* **2008**, *93* (8), 1415–1421. https://doi.org/10.1016/j.polymdegradstab.2008.05.021.

(34) Wu, X.; Zhang, X.; Lu, C.; Ling, L. Thermo-Chemical Reactions and Structural Evolution of Acrylamide-Modified Polyacrylonitrile. *Chin. J. Polym. Sci.* **2010**, *28* (3), 367–376. https://doi.org/10.1007/s10118-010-9026-9.

(35) Ju, A.; Guang, S.; Xu, H. Effect of Comonomer Structure on the Stabilization and Spinnability of Polyacrylonitrile Copolymers. *Carbon* **2013**, *54*, 323–335. https://doi.org/10.1016/j.carbon.2012.11.044.

(36) Fu, Z.; Gui, Y.; Cao, C.; Liu, B.; Zhou, C.; Zhang, H. Structure Evolution and Mechanism of Polyacrylonitrile and Related Copolymers during the Stabilization. *J. Mater. Sci.* **2014**, *49* (7), 2864–2874. https://doi.org/10.1007/s10853-013-7992-3.

(37) Salim, N. V.; Blight, S.; Creighton, C.; Nunna, S.; Atkiss, S.; Razal, J. M. The Role of Tension and Temperature for Efficient Carbonization of Polyacrylonitrile Fibers: Toward Low Cost Carbon Fibers. *Ind. Eng. Chem. Res.* **2018**, *57* (12), 4268–4276. https://doi.org/10.1021/acs.iecr.7b05336.

(38) Choi, J.; Kim, S.-S.; Chung, Y.-S.; Lee, S. Evolution of Structural Inhomogeneity in Polyacrylonitrile Fibers by Oxidative Stabilization. *Carbon* **2020**, *165*, 225–237. https://doi.org/10.1016/j.carbon.2020.04.027.

(39) Lee, S.; Kim, J.; Ku, B.-C.; Kim, J.; Joh, H.-I. Structural Evolution of Polyacrylonitrile Fibers in Stabilization and Carbonization. *Adv. Chem. Eng. Sci.* **2012**, *02* (02), 275–282. https://doi.org/10.4236/aces.2012.22032.

(40) Xue, Y.; Liu, J.; Liang, J. Correlative Study of Critical Reactions in Polyacrylonitrile Based Carbon Fiber Precursors during Thermal-Oxidative Stabilization. *Polym. Degrad. Stab.* **2013**, *98* (1), 219–229. https://doi.org/10.1016/j.polymdegradstab.2012.10.018.

(41) Grassie, N.; McGuchan, R. Pyrolysis of Polyacrylonitrile and Related Polymers-I: Thermal Analysis of Polyacrylonitrile. *Eur. Polym. J.* **1970**, *6*, 1277–1291.

(42) Usami, T.; Itoh, T.; Ohtani, H.; Tsuge, S. Structural Study of Polyacrylonitrile Fibers during Oxidative Thermal Degradation by Pyrolysis-Gas Chromatography, Solid-State Carbon-13 NMR, and Fourier-Transform Infrared Spectroscopy. *Macromolecules* **1990**, *23* (9), 2460–2465. https://doi.org/10.1021/ma00211a009.

(43) Kakida, H.; Tashiro, K.; Kobayashi, M. Mechanism and Kinetics of Stabilization Reaction of Polyacrylonitrile and Related Copolymers I. Relationship between Isothermal DSC Thermogram and FT/IR Spectral Change of an Acrylonitrile/Methacrylic Acid Copolymer. *Polym. J.* **1996**, *28* (1), 30–34. https://doi.org/10.1295/polymj.28.30.

(44) Zhao, J.; Zhang, J.; Zhou, T.; Liu, X.; Yuan, Q.; Zhang, A. New Understanding on the Reaction Pathways of the Polyacrylonitrile Copolymer Fiber Pre-Oxidation: Online Tracking by Two-Dimensional Correlation FTIR Spectroscopy. *RSC Adv.* **2016**, *6* (6), 4397–4409. https://doi.org/10.1039/C5RA24320C.

(45) Takahagi, T.; Shimada, I.; Fukuhara, M.; Morita, K.; Ishitani, A. XPS Studies on the Chemical Structure of the Stabilized Polyacrylonitrile Fiber in the Carbon Fiber Production Process. *J. Polym. Sci. Part Polym. Chem.* **1986**, *24* (11), 3101–3107. https://doi.org/10.1002/pola.1986.080241134.

(46) Fitzer, E.; Müller, D. J. The Influence of Oxygen on the Chemical Reactions during Stabilization of Pan as Carbon Fiber Precursor. *Carbon* **1975**, *13* (1), 63–69. https://doi.org/10.1016/0008-6223(75)90259-6.

(47) Gupta, A.; Harrison, I. R. New Aspects in the Oxidative Stabilization of PAN-Based Carbon Fibers. *Carbon* **1996**, *34* (11), 1427–1445. https://doi.org/10.1016/S0008-6223(96)00094-2.

(48) Hajir Bahrami, S.; Bajaj, P.; Sen, K. Thermal Behavior of Acrylonitrile Carboxylic Acid Copolymers. *J. Appl. Polym. Sci.* **2003**, *88* (3), 685–698. https://doi.org/10.1002/app.11637.

(49) Devasia, R.; Nair, C. P. R.; Sivadasan, P.; Katherine, B. K.; Ninan, K. N. Cyclization Reaction in Poly(Acrylonitrile/Itaconic Acid) Copolymer: An Isothermal Differential Scanning Calorimetry Kinetic Study. *J. Appl. Polym. Sci.* **2003**, *88* (4), 915–920. https://doi.org/10.1002/app.11706.

(50) Jing, M.; Wang, C.; Wang, Q.; Bai, Y.; Zhu, B. Chemical Structure Evolution and Mechanism during Pre-Carbonization of PAN-Based Stabilized Fiber in the Temperature Range of 350–600°C. *Polym. Degrad. Stab.* **2007**, *92* (9), 1737–1742. https://doi.org/10.1016/j.polymdegradstab.2007.05.020.

(51) Mascia, L.; Paxton, E. G. Physical Changes during Thermal Oxidation of PAN Fibres and Effects of Y-Radiation Pre-Treatment. *Thermochimica Acta.* **1991** *184*, 251-267.

(52) He, J.-H.; Liu, Y.; Xu, L.; Yu, J.-Y.; Sun, G. BioMimic Fabrication of Electrospun Nanofibers with High-Throughput. *Chaos Solitons Fractals* **2008**, *37* (3), 643–651. https://doi.org/10.1016/j.chaos.2007.11.028.

(53) Belyaev, S. S.; Arkhangelsky, I. V.; Makarenko, I. V. Non-Isothermal Kinetic Analysis of Oxidative Stabilization Processes in PAN Fibers. *Thermochim. Acta* **2010**, *507–508*, 9–14. https://doi.org/10.1016/j.tca.2010.04.022.

(54) Thomas, L. C. Use of Multiple Heating Rate DSC and Modulated Temperature DSC to Detect and Analyze Temperature-Time-Dependent Transitions in Materials. *Ameriacan Laboratory.* **2001**.

(55) Bell, F. A.; Lehrle, R. S.; Robb, J. C. Polyacrylonitrile Degradation Kinetics Studied by the Micropyrolysis—g.l.c. Technique. *Polymer* **1971**, *12* (9), 579–599. https://doi.org/10.1016/0032-3861(71)90039-5.

(56) Grassie, N.; McGuchan, R. Pyrolysis of Polyacrylonitrile and Related Polymers—VI. Acrylonitrile Copolymers Containing Carboxylic Acid and Amide Structures. *Eur. Polym. J.* **1972**, *8* (2), 257–269. https://doi.org/10.1016/0014-3057(72)90032-8.

(57) Grassie, N.; McGuchan, R. Pyrolysis of Polyacrylonitrile and Related Polymers—VII. *Eur. Polym. J.* **1972**, *8* (7), 865–878. https://doi.org/10.1016/0014-3057(72)90046-8.

(58) Grassie, N.; McGuchan, R. Pyrolysis of Polyacrylonitrile and Related Polymers—VIII. Copolymers of Acrylonitrile with Vinyl Acetate, Vinyl Formate, Acrolein and

Methyl Vinyl Ketone. *Eur. Polym. J.* **1973**, *9* (2), 113–124. https://doi.org/10.1016/0014-3057(73)90134-1.

(59) Grassie, N.; McGuchan, R. Pyrolysis of Polyacrylonitrile and Related Polymers—IX. *Eur. Polym. J.* **1973**, *9* (6), 507–517. https://doi.org/10.1016/0014-3057(73)90034-7.

(60) Warner, S. B.; Peebles, L. H.; Uhlmann, D. R. Oxidative Stabilization of Acrylic Fibres. *J. Mater. Sci.* **1979**, *14*, 556–564.

(61) Ko, T.-H.; Ting, H.-Y.; Lin, C.-H.; Chen, J.-C. The Microstructure of Stabilized Fibers. *J. Appl. Polym. Sci.* **1988**, *35* (4), 863–874. https://doi.org/10.1002/app.1988.070350402.

(62) Peebles, L. H.; Peyser, P.; Snow, A. W.; Peters, W. C. On the Exotherm of Polyacrylonitrile Pyrolysis of the Homopolymer under Inert Conditions. *Carbon* **1990**, *28* (5), 707–715.

(63) Tsai, J.-S.; Lin, C.-H. Effect of Comonomer Composition on the Properties of Polyacrylonitrile Precursor and Resulting Carbon Fiber. *J. Appl. Polym. Sci.* **1991**, *43* (4), 679–685. https://doi.org/10.1002/app.1991.070430405.

(64) Wang, P.; Liu, J.; Yue, Z.; Li, R. Thermal Oxidative Stabilization of Polyacrylonitrile Precursor Fiber—Progression of Morphological Structure and Mechanical Properties. *Carbon* **1992**, *30* (1), 113–120. https://doi.org/10.1016/0008-6223(92)90114-C.

(65) Cardoso dos Santos, L. G.; Kawano, Y. Degradation of Polyacrylonitrile by X-Ray Radiation. *Polym. Degrad. Stab.* **1994**, *44*, 27–32.

(66) Mukhopadhyay, S. K.; Zhu, Y. Structure-Property Relationships of PAN Precursor Fibers During Thermo-Oxidative Stabilization. *Text. Res. J.* **1995**, *65* (1), 25–31. https://doi.org/10.1177/004051759506500104.

(67) Tsai, J.-S. Tension Effects on the Properties of Oxidized Polyacrylonitrile and Carbon Fibers during Continuous Oxidation. *Polym. Eng. Sci.* **1995**, *35* (16), 1313–1316. https://doi.org/10.1002/pen.760351607.

(68) Gupta, A.; Harrison, I. R. New Aspects in the Oxidative Stabilization of PAN-Based Carbon Fibers: II. *Carbon* **1997**, *35* (6), 809–818. https://doi.org/10.1016/S0008-6223(97)00025-0.

(69) Kakida, H.; Tashiro, K. Mechanism and Kinetics of Stabilization Reaction of Polyacrylonitrile and Related Copolymers II. Relationships between Isothermal DSC Thermograms and FT-IR Spectral Changes of Polyacrylonitrile in Comparison with

the Case of Acrylonitrile/Methacrylic Acid Copolymer. *Polym. J.* **1997**, *29* (4), 353–357. https://doi.org/10.1295/polymj.29.353.

(70) Lee, J. K.; Shim, H. J.; Lim, J. C.; Choi, G. J.; Kim, Y. dae; Min, B. G.; Park, D. Influence of Tension during Oxidative Stabilization on SO2 Adsorption Characteristics of Polyacrylonitrile (PAN) Based Activated Carbon Fibers. *Carbon* **1997**, *35* (6), 837–843. https://doi.org/10.1016/S0008-6223(97)00040-7.

(71) Bang, Y. H.; Lee, S.; Cho, H. H. Effect of Methyl Acrylate Composition on the Microstructure Changes of High Molecular Weight Polyacrylonitrile for Heat Treatment. *J. Appl. Polym. Sci.* **1998**, *68*, 2205–2213.

(72) Surianarayanan, M.; Uchida, T.; Wakakura, M. Evolved Gases by Simultaneous TG–MS Technique and Associated Thermal Hazard in Drying of Polyacrylonitrile. *J. Loss Prev. Process Ind.* **1998**, *11* (2), 99–108. https://doi.org/10.1016/S0950-4230(97)00032-6.

(73) Dalton, S.; Heatley, F.; Budd, P. M. Thermal Stabilization of Polyacrylonitrile Fibres. *Polymer* **1999**, *40* (20), 5531–5543. https://doi.org/10.1016/S0032-3861(98)00778-2.

(74) Paiva, M. C.; Kotasthane, P.; Edie, D. D.; Ogale, A. A. UV Stabilization Route for Melt-Processible PAN-Based Carbon Fibers. *Carbon* **2003**, *41* (7), 1399–1409. https://doi.org/10.1016/S0008-6223(03)00041-1.

(75) Naskar, A. K.; Walker, R. A.; Proulx, S.; Edie, D. D.; Ogale, A. A. UV Assisted Stabilization Routes for Carbon Fiber Precursors Produced from Melt-Processible Polyacrylonitrile Terpolymer. *Carbon* **2005**, *43* (5), 1065–1072. https://doi.org/10.1016/j.carbon.2004.11.047.

(76) Wu, G.; Lu, C.; Ling, L.; Hao, A.; He, F. Influence of Tension on the Oxidative Stabilization Process of Polyacrylonitrile Fibers. *J. Appl. Polym. Sci.* **2005**, *96* (4), 1029–1034. https://doi.org/10.1002/app.21388.

(77) Li, L. L.; Liu, J.; Liang, J. Y. Influence of Cuprous Chloride Treatment on Pre-Oxidized PAN Tow. *Adv. Mater. Res.* **2006**, *11–12*, 453–456. https://doi.org/10.4028/www.scientific.net/AMR.11-12.453.

(78) Chae, H. G.; Minus, M. L.; Rasheed, A.; Kumar, S. Stabilization and Carbonization of Gel Spun Polyacrylonitrile/Single Wall Carbon Nanotube Composite Fibers. *Polymer* **2007**, *48* (13), 3781–3789. https://doi.org/10.1016/j.polymer.2007.04.072.

(79) Yu, M.-J.; Wang, C.-G.; Bai, Y.-J.; Ji, M.-X.; Xu, Y. SEM and OM Study on the Microstructure of Oxidative Stabilized Polyacrylonitrile Fibers. *Polym. Bull.* **2007**, *58* (5–6), 933–940. https://doi.org/10.1007/s00289-007-0737-1.

(80) Yu, M.; Wang, C.; Bai, Y.; Zhu, B.; Ji, M.; Xu, Y. Microstructural Evolution in Polyacrylonitrile Fibers during Oxidative Stabilization: Microstructural Evolution in PAN Fibers. *J. Polym. Sci. Part B Polym. Phys.* **2008**, *46* (7), 759–765. https://doi.org/10.1002/polb.21410.

(81) Liu, J.; Zhou, P.; Zhang, L.; Ma, Z.; Liang, J.; Fong, H. Thermo-Chemical Reactions Occurring during the Oxidative Stabilization of Electrospun Polyacrylonitrile Precursor Nanofibers and the Resulting Structural Conversions. *Carbon* **2009**, *47* (4), 1087–1095. https://doi.org/10.1016/j.carbon.2008.12.033.

(82) Lv, M.; Ge, H.; Chen, J. Study on the Chemical Structure and Skin-Core Structure of Polyacrylonitrile-Based Fibers during Stabilization. *J. Polym. Res.* **2009**, *16* (5), 513–517. https://doi.org/10.1007/s10965-008-9254-7.

(83) Zhou, Z.; Liu, K.; Lai, C.; Zhang, L.; Li, J.; Hou, H.; Reneker, D. H.; Fong, H. Graphitic Carbon Nanofibers Developed from Bundles of Aligned Electrospun Polyacrylonitrile Nanofibers Containing Phosphoric Acid. *Polymer* **2010**, *51* (11), 2360–2367. https://doi.org/10.1016/j.polymer.2010.03.044.

(84) Yuan, H.; Wang, Y.; Yu, H.; Wei, Z.; Ge, B.; Mei, Y. Effect of UV Irradiation on PAN Precursor Fibers and Stabilization Process. *J. Wuhan Univ. Technol.-Mater Sci Ed* **2011**, *26* (3), 449–454. https://doi.org/10.1007/s11595-011-0247-8.

(85) Karacan, İ.; Erdoğan, G. An Investigation on Structure Characterization of Thermally Stabilized Polyacrylonitrile Precursor Fibers Pretreated with Guanidine Carbonate Prior to Carbonization. *Polym. Eng. Sci.* **2012**, *52* (5), 937–952. https://doi.org/10.1002/pen.22160.

(86) Lian, F.; Liu, J.; Ma, Z.; Liang, J. Stretching-Induced Deformation of Polyacrylonitrile Chains Both in Quasicrystals and in Amorphous Regions during the in Situ Thermal Modification of Fibers Prior to Oxidative Stabilization. *Carbon* **2012**, *50* (2), 488–499. https://doi.org/10.1016/j.carbon.2011.09.003.

(87) Qin, X.; Lu, Y.; Xiao, H.; Zhao, W. Effect of Heating and Stretching Polyacrylonitrile Precursor Fibers in Steam on the Properties of Stabilized Fibers and Carbon Fibers. *Polym. Eng. Sci.* **2013**, *53* (4), 827–832. https://doi.org/10.1002/pen.23328.

(88) Morales, M. S.; Ogale, A. A. Wet-Spun, Photoinitiator-Modified Polyacrylonitrile Precursor Fibers: UV-Assisted Stabilization. *J. Appl. Polym. Sci.* **2013**, *130* (4), 2494–2503. https://doi.org/10.1002/app.39442.

(89) Xue, Y.; Liu, J.; Lian, F.; Liang, J. Effect of the Oxygen-Induced Modification of Polyacrylonitrile Fibers during Thermal-Oxidative Stabilization on the Radial Microcrystalline Structure of the Resulting Carbon Fibers. *Polym. Degrad. Stab.* **2013**, *98* (11), 2259–2267. https://doi.org/10.1016/j.polymdegradstab.2013.08.016.

(90) Liu, S.; Han, K.; Chen, L.; Zheng, Y.; Yu, M.; Li, J.; Yang, Z. Influence of External Tension on the Structure and Properties of Melt-Spun PAN Precursor Fibers during Thermal Oxidation: Influence of External Tension on Performances of Pre-Oxidized Melt-Spun Fibers. *Macromol. Mater. Eng.* **2015**, *300* (10), 1001–1009. https://doi.org/10.1002/mame.201500104.

(91) Zhang, Y.; Tajaddod, N.; Song, K.; Minus, M. L. Low Temperature Graphitization of Interphase Polyacrylonitrile (PAN). *Carbon* **2015**, *91*, 479–493. https://doi.org/10.1016/j.carbon.2015.04.088.

(92) Liu, H. C.; Chien, A.-T.; Newcomb, B. A.; Bakhtiary Davijani, A. A.; Kumar, S. Stabilization Kinetics of Gel Spun Polyacrylonitrile/Lignin Blend Fiber. *Carbon* **2016**, *101*, 382–389. https://doi.org/10.1016/j.carbon.2016.01.096.

(93) Sabet, E. N.; Nourpanah, P.; Arbab, S. Quantitative Analysis of Entropic Stress Effect on the Structural Rearrangement during Pre-Stabilization of PAN Precursor Fibers. *Polymer* **2016**, *90*, 138–146. https://doi.org/10.1016/j.polymer.2016.03.001.

(94) Fu, Z.; Liu, B.; Sun, L.; Zhang, H. Study on the Thermal Oxidative Stabilization Reactions and the Formed Structures in Polyacrylonitrile during Thermal Treatment. *Polym. Degrad. Stab.* **2017**, *140*, 104–113. https://doi.org/10.1016/j.polymdegradstab.2017.04.018.

(95) Cho, D. W.; Hong, S. C. Synergistic Effect of Comonomers on the Thermal Oxidative Stabilization of Polyacrylonitrile Copolymers for Carbon Materials. *Polym. Degrad. Stab.* **2019**, *161*, 191–197. https://doi.org/10.1016/j.polymdegradstab.2019.01.027.

(96) Liu, J.; He, L.; Ma, S.; Liang, J.; Zhao, Y.; Fong, H. Effects of Chemical Composition and Post-Spinning Stretching Process on the Morphological, Structural, and Thermo-Chemical Properties of Electrospun Polyacrylonitrile Copolymer Precursor Nanofibers. *Polymer* **2015**, *61*, 20–28. https://doi.org/10.1016/j.polymer.2015.01.063.

(97) Mack, J. J.; Viculis, L. M.; Ali, A.; Luoh, R.; Yang, G.; Hahn, H. T.; Ko, F. K.; Kaner, R. B. Graphite Nanoplatelet Reinforcement of Electrospun Polyacrylonitrile Nanofibers. *Adv. Mater.* **2005**, *17* (1), 77–80. https://doi.org/10.1002/adma.200400133.

(98) Ko, F.; Gogotsi, Y.; Ali, A.; Naguib, N.; Ye, H.; Yang, G. L.; Li, C.; Willis, P. Electrospinning of Continuous Carbon Nanotube-Filled Nanofiber Yarns. *Adv. Mater.* **2003**, *15* (14), 1161–1165. https://doi.org/10.1002/adma.200304955.

(99) Ge, J. J.; Hou, H.; Li, Q.; Graham, M. J.; Greiner, A.; Reneker, D. H.; Harris, F. W.; Cheng, S. Z. D. Assembly of Well-Aligned Multiwalled Carbon Nanotubes in Confined Polyacrylonitrile Environments: Electrospun Composite Nanofiber Sheets. *J. Am. Chem. Soc.* **2004**, *126* (48), 15754–15761. https://doi.org/10.1021/ja048648p.

(100) Hou, H.; Ge, J. J.; Zeng, J.; Li, Q.; Reneker, D. H.; Greiner, A.; Cheng, S. Z. D. Electrospun Polyacrylonitrile Nanofibers Containing a High Concentration of Well-Aligned Multiwall Carbon Nanotubes. *Chem. Mater.* **2005**, *17* (5), 967–973. https://doi.org/10.1021/cm0484955.

(101) Chae, H. G.; Choi, Y. H.; Minus, M. L.; Kumar, S. Carbon Nanotube Reinforced Small Diameter Polyacrylonitrile Based Carbon Fiber. *Compos. Sci. Technol.* **2009**, *69* (3–4), 406–413. https://doi.org/10.1016/j.compscitech.2008.11.008.

(102) Şahin, K.; Fasanella, N. A.; Chasiotis, I.; Lyons, K. M.; Newcomb, B. A.; Kamath, M. G.; Chae, H. G.; Kumar, S. High Strength Micron Size Carbon Fibers from Polyacrylonitrile–Carbon Nanotube Precursors. *Carbon* **2014**, *77*, 442–453. https://doi.org/10.1016/j.carbon.2014.05.049.

(103) Kumar, S. *Polyacrylonitrile/Carbon Nanotube Composite: Precursor for Next Generation Carbon Fiber*; FA9550-07-1–0233; Georgia Institute of Technology: Air Force office of Scientific Research, 2010.

(104) Park, Su-Jin. A Review of the Preparation and Properties of Carbon Nanotubes-Reinforced Polymer Compositess. *Carbon Lett.* **2011**, *12* (2), 57–69. https://doi.org/10.5714/CL.2011.12.2.057.

(105) Liu, Y.; Kumar, S. Polymer/Carbon Nanotube Nano Composite Fibers–A Review. *ACS Appl. Mater. Interfaces* **2014**, *6* (9), 6069–6087. https://doi.org/10.1021/am405136s.

(106) Hiremath, N.; Mays, J.; Bhat, G. Recent Developments in Carbon Fibers and Carbon Nanotube-Based Fibers: A Review. *Polym. Rev.* **2017**, *57* (2), 339–368. https://doi.org/10.1080/15583724.2016.1169546.

(107) Dietrich, J.; Hirt, P.; Herlinger, H. Electron-Beam-Induced Cyclisation to Obtain C-Fibre Precursors from Polyacrylonitrile Homopolymers. *Eur. Polym. J.* **1996**, *32* (5), 617–623. https://doi.org/10.1016/0014-3057(95)00185-9.

(108) Zhao, W.; Yamamoto, Y.; Tagawa, S. Regulation of the Thermal Reactions of Polyacrylonitrile by γ-Irradiation. *Chem. Mater.* **1999**, *11* (4), 1030–1034. https://doi.org/10.1021/cm9806836.

(109) Murthy, M. R.; Radhakrishna, S. Radiation Damage in Polyacrylonitrile. *Pramana* **1983**, *20* (1), 85–90. https://doi.org/10.1007/BF02846184.

(110) Shin, H. K.; Park, M.; Kim, H.-Y.; Park, S.-J. An Overview of New Oxidation Methods for Polyacrylonitrile-Based Carbon Fibers. *Carbon Lett.* **2015**, *16* (1), 11–18. https://doi.org/10.5714/CL.2015.16.1.011.

(111) Hexemer, A.; Bras, W.; Glossinger, J.; Schaible, E.; Gann, E.; Kirian, R.; MacDowell, A.; Church, M.; Rude, B.; Padmore, H. A SAXS/WAXS/GISAXS Beamline with Multilayer Monochromator. *J. Phys. Conf. Ser.* **2010**, *247*, 012007. https://doi.org/10.1088/1742-6596/247/1/012007.

Chapter 3: Spider Silk: Protein Folding, Biomimetic Silk Spinning, and Silk as a Natural Carbon Fiber Precursor

3.1 Introduction

3.1.1 Personal Background

Spider silk is an amazing material that has captivated humanity for centuries, evident by its expression in art [1], popular culture [2], children's literature [3], science, and engineering. While spiders are often viewed as alien and terrifying, their silken webs are objects of beauty and strength. These physical properties stem from silk's unique protein structure. Spiders are arthropods, like insects and crustaceans, invertebrates classified by their segmented body, jointed appendages, and exoskeleton. They fall into the class Arachnida along with scorpions and mites, distinguished from insects by having 8 walking legs and an additional appendage pair. Spiders belong to the >380 million-year-old order Araneae, which is characterized by the ability to produce silk. Since the earliest spider ancestor, spiders have evolved into what we encounter today: large hunters like tarantulas of infraorder Mygalomorphae, and the more diverse families of infraorder Araneomorphae found in our homes and gardens [1]. Different species are fascinating in their own right, such as the elaborate mating rituals of peacock spiders (*Maratus)*, the medical and pesticidal uses of Australian funnel web spider (Atracidae) venom [4], the waterproof egg sacs of the fishing spider (*Dolomedes triton*) [5], or the strength and toughness of black widow (*Latrodectus hesperus*) and golden orb-weaver (*Trichonephila clavipes*) silks (Fig 3.1).

3.1.2 Scientific Background

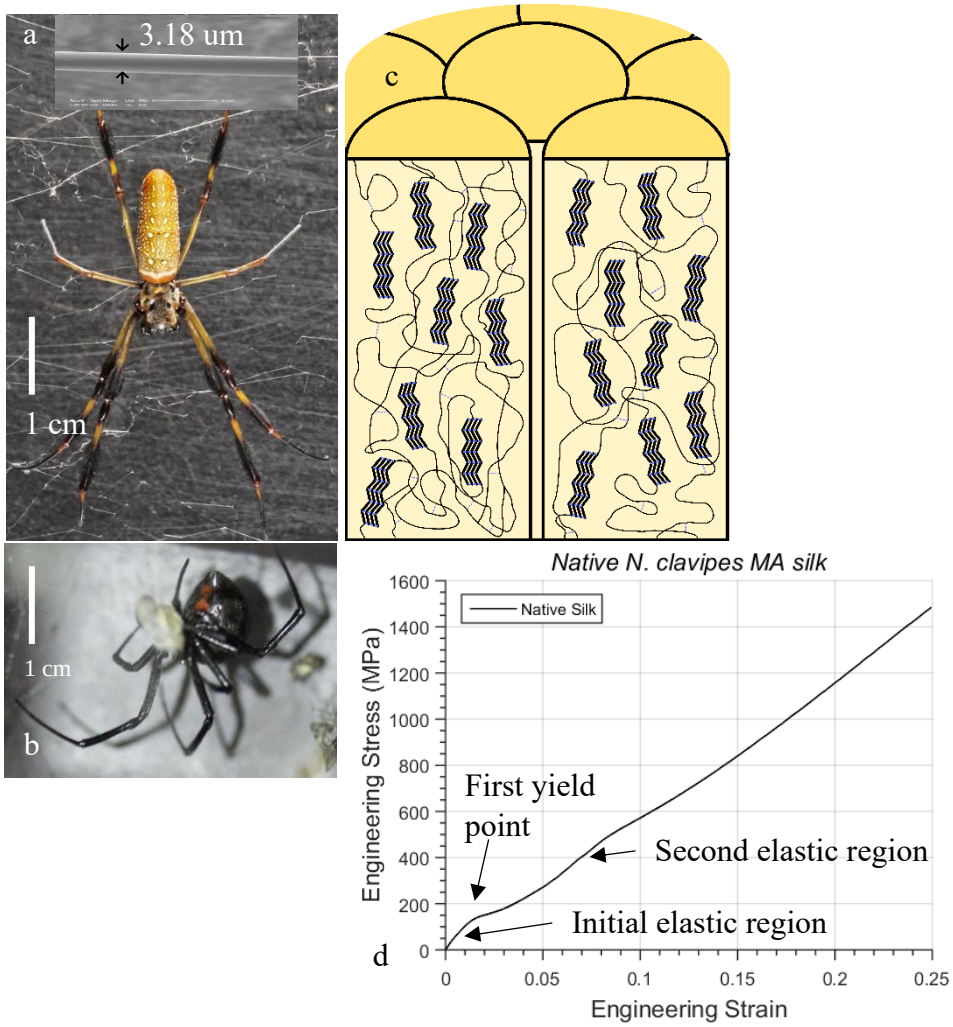

Figure 1: *Trichonephila clavipes* (golden orb weaver, a), *Latrodectus hesperus* (black widow, b) spin Major Ampullate (MA) silk with a unique semicrystalline protein structure of polyalanine β-sheets and amorphous spacer regions (c). This protein structure results in a unique stress-strain curve under tension (d) [6].

Spiders make many types of silk, each with specialized functions, including tubuliform (also known as cylindrical) silk for covering egg sacs, flagelliform silk and silk "glue" from the aggregate glands for capturing prey in the web, aciniform silk for wrapping prey, minor ampullate silk for scaffolding, and major ampullate (MA) or

draglines and web construction [7–10]. MA silk is the most widely studied as researchers hope to harness its strength and toughness for structural engineering applications like light-weight vehicles and body armor. MA silk has a higher strength per-weight than steel (~1 GPa/g vs ~60 MPa/g), is stronger than any synthetic or natural polymer fiber (with the possible exception of hagfish slime), but is not as stiff (~15 GPa) as Kevlar (~100 GPa) or carbon fiber (~225 GPa)) [11,12].

Each MA silk fiber is composed of protein fibrils aligned along the long axis of the fiber, similar to muscle fiber [7,8,10,12]. The protein fibrils mostly contain MA spidroins (a contraction of "spider fibroins") [13–16]. The spidroin fibrils are bonded to their neighbors through hydrogen bonding and disulfide bridges to prevent slip when the fibers are loaded in tension [17–19]. The main secondary structures within MA silk are polyalanine β-sheet nanocrystals and amorphous regions, all held together through hydrogen bonding (Fig 3.1c) [7,11,20–24]. MA silk has a unique deformation behavior when pulled in tension (Fig 3.1d) [18,19]. After the initial elastic region, the first yield point corresponds to hydrogen bonds breaking within the amorphous regions. This is followed by plastic deformation as the spidroins straighten and a second elastic region once the β-sheets are engaged. Ultimate failure occurs when the β-sheets and the peptide backbones break. Because of the large amount of hydrogen bonding, MA silk benefits from a "stick-slip" mechanism where hydrogen bonds break and reform between different parts of the amorphous regions and within the β-sheets as the spidroins deform [18,19]. MA silk also undergoes a phenomenon called supercontraction when saturated with water, where it absorbs water and contracts. This phenomenon has been theorized to stiffen webs to aid

in prey capture and can regenerate the structure of MA silks deformed beyond their first two yield points [25–33].

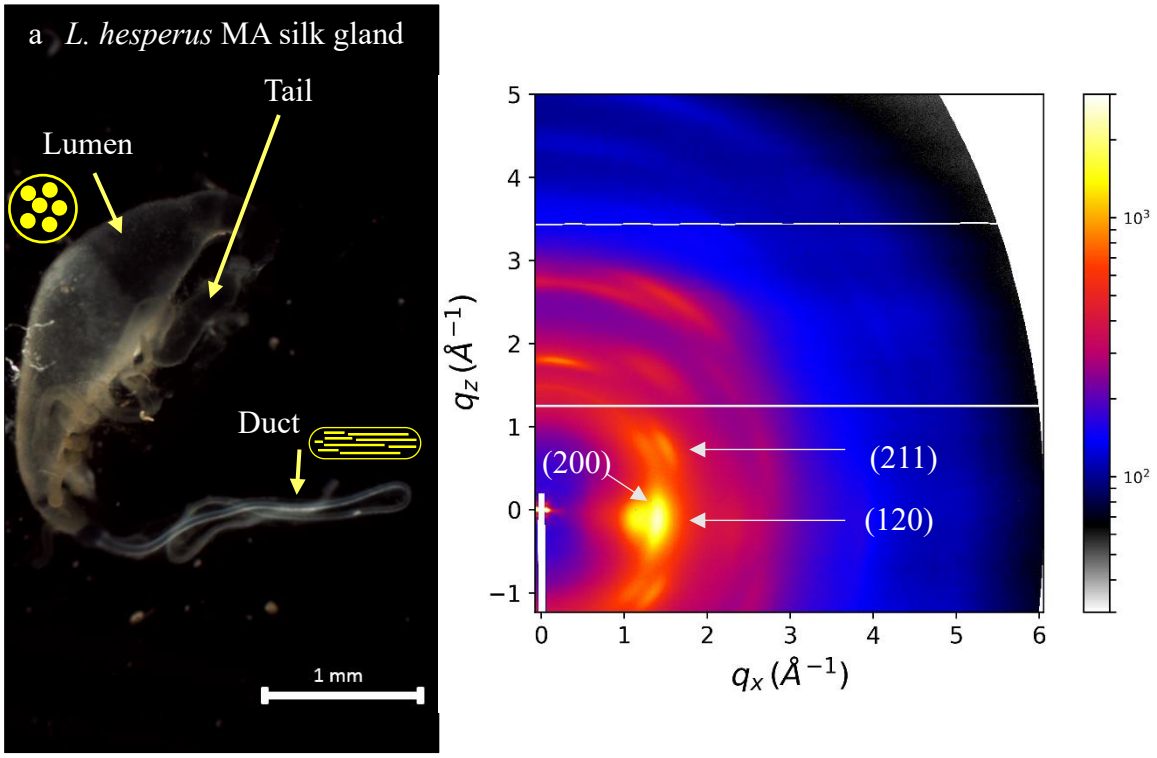

Figure 3.2: MA spidroins are secreted in the MA gland tail (a), stored as micelles in a 50% aqueous solution in the gland lumen, and are extruded into fibers and dehydrated in the gland duct. When interrogated with an X-ray beam, the crystals in MA silk produce a diffraction pattern based on their orientation and d-spacing (reported here as 'q' which equals 2π/d, b). Diffractions from prominent planes are indicated with arrows.

Most MA silk research centers around understanding how spidroins fold during silk spinning, processing or modifying MA silk for specific applications, characterizing MA silk properties across many species and conditions, and attempts to create synthetic MA spidroins and MA silk fibers. While silkworms are docile, easy to care for, and easily farmed for their silks, spiders are territorial, aggressive, and it is labor intensive to care for them and collect silk on a large scale. These limitations led researchers to engineer

bacteria, yeast, and even goats to express truncated versions of MA spidroins that can be isolated, purified, and extruded into fibers [34–36]. However, these synthetic silks lack the mechanical properties of their natural progenitors, likely because the synthetic spidroins lack a key structural element, or the synthetic spidroins do not fold properly during a synthetic spinning process.

This project focused on understanding how spidroins fold during silk spinning and post-spinning processing. Previous studies on the MA gland suggest that the MA spidroins are stored as spheres in a 50% aqueous dope, then elongate to form liquid crystalline fibrils as they are extruded through the spinning duct (Fig 3.2) [25,37–45]. The crystallinity of MA silk fibers has been shown in many works using Wide-Angle X-Ray Scattering (WAXS, Fig 3.2) [46–49]. During spinning, the spider exerts a shear force on the dope as it is pulled through the duct [7,38,39,50]. The dope is also dehydrated, decreases in pH, and shows a decrease in sodium concentration and an increase in potassium and phosphorus concentration from the proximal to distal end of the duct [7,38,51–55]. Xu et. al. showed that a decrease in pH, coupled with the centrifugal force of spinning in an NMR spectrometer forms needle-like structures out of MA spidroins [54]. However, shear, dehydration, and salt exchange have not been thoroughly investigated. In understanding how these factors affect MA spidroin folding, we can improve synthetic silk spinning and develop appropriate manufacturing processes for structural silk products. Understanding the liquid crystallinity, which results in ordered, relatively defect-free fibers, could be applied to improve synthetic polymer fiber manufacture.

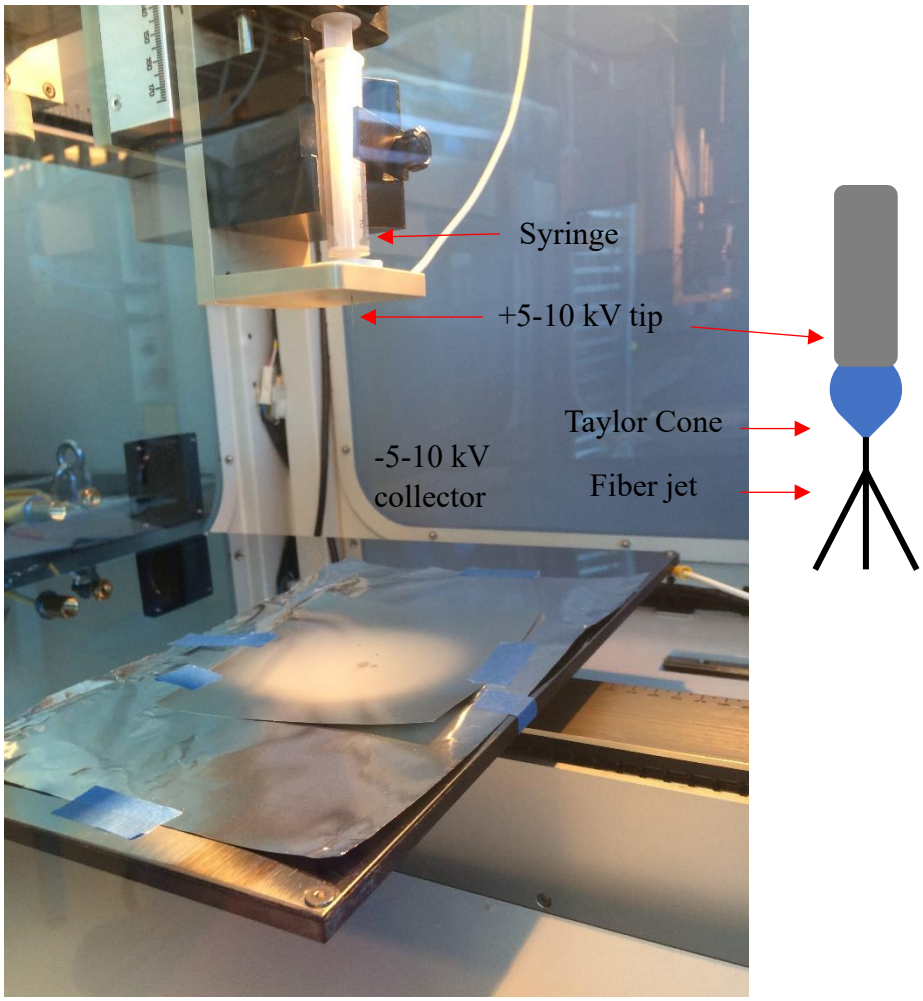

Figure 3.3: Electrospinner setup for MA silk spinning and Taylor cone schematic.

Electrospinning has been used to spin synthetic or regenerated (natural silk-derived) silk fibers and to study shear effects [56–59]. In the electrospinning process, a polymer solution is extruded through a syringe with a metal tip set to a certain voltage, usually 1-30 kV, onto a metal collector with an opposite charge in the same kV range (Fig 3.3). The electric field "pulls" certain polymers, generally ones with polar side chains, as the polymer solution is extruded. The solution's surface tension counteracts this pull up to a point where it is not strong enough, creating a cone-like shape called the

Taylor cone (Fig 3.3) [56–59]. When the electrostatic force exceeds the solution's surface tension, the polymer is pulled into a fiber "jet" which whips rapidly about, shedding most of the remaining solvent. This fiber deposits on the collector, which is typically a metal plate or rotating cylinder to help align the fibers and often covered with aluminum foil so fiber mats can be easily removed. Fiber diameters of 10 nm – 5 μm can be achieved, and the extrusion rate, polymer concentration, solvent, voltages, and rotating collector speed can be modified to apply different shear forces to the polymer and control fiber morphology. In this research, electrospinning was used to probe the effects of shear, salt concentration, humidity, and spidroin concentration on electrospun MA silk fibers.

As described in chapter 2, heat-treating polymer fibers graphitizes them, increasing their stiffness and strength. A similar process to the stabilization and carbonization of PAN was investigated to determine if MA silk would be sufficiently stiff and strong for structural engineering applications compared with PAN-based carbon fibers, and to determine the mechanisms by which MA silk graphitizes.

3.2 Methods

3.2.1 Synthetic Materials

All chemicals were purchased from Millipore-Sigma unless otherwise noted. Chopped PAN fibers were purchased from Smooth On Inc (Macungie, PA, USA) and known to include a small amount of a carbonyl-containing comonomer. Poly(vinyl alcohol) fibers were donated by Kuraray Co. (Tokyo, Japan) Commercial carbon fiber was donated by Hexcel Co. (Stamford, CT, USA) *Bombyx mori* silk fibers were donated

by Prof. Tetsuo Asakura (Tokyo University of Agriculture and Technology, Tokyo, Japan).

3.2.2 Spiders, Dissections, and Silk Collection

Female *L. hesperus* were collected from Riverside, California, housed in Tupperware containers, and fed one live cricket every 2 weeks. Female *T. clavipes* were collected in northern Florida and shipped overnight to UCR, housed in 10" x 10" x 16" glass or plastic terrariums, and fed cricket abdomens and misted with water every 2-3 days. All spiders used for research were mature adults. For silk collection (silking), spiders were anesthetized using CO_2 or N_2 for 5 minutes, then their legs were taped down, and their abdomens secured so they remain stationary during silking [38]. Single or double MA silk fibers were isolated with forceps. Silking was performed at a constant rate of 2 cm/s using either a motor to collect fiber bundles, or by hand to collect single fibers [60,61]. Each spider was silked for up to an hour, then gently untapped and returned to her terrarium. MA silk fibers were stored in a dark, dry drawer where they are stable for years [62].

For dissections, spiders were anesthetized in a conventional freezer for 5-7 minutes. Their cephalothorax was severed immediately upon removal with forceps. The abdomen skin and fat were peeled away using forceps, and a 1x saline sodium citrate dissection buffer, consisting of 0.15 M NaCl and 0.015 M sodium citrate, was typically used to keep the MA glands hydrated and wash away debris. This buffer is used to balance pH, prevent microbial contamination, and because it contains elements similar to those in arthropod hemolymph (fluid present throughout their body). If desired, the skin

of the MA gland was also removed using forceps. Dissected glands were used in experiments immediately following dissection.

3.2.3 Dope Drying Procedures

Dissected *L. hesperus* MA glands were dried at different % relative humidity (RH) after dissection and washing with different buffers to probe how these parameters affected spidroin folding and β-sheet nanocrystal formation. Humidity in plastic desiccators was measured using a SensorPush ® Bluetooth humidity sensor and adjusted from 10-70% using $CaSO_4$ desiccant to dry or by pumping humid air in using a Reptifogger (Zoo Med Laboratories, Inc., San Luis Obispo, CA). Dissection solutions were modified by replacing NaCl with different salts at the same concentration (0.15 M) to mimic the different ion concentrations found in the MA gland duct: KCl, NaH_2PO4, and KH_2PO_4, at a constant 30% RH [51–53,55]. Glands were dried on Kapton film that was taped to a 1/2" inner diameter metal washer. For *in-situ* studies, 1x SSC buffer or ultrapure water was pipetted onto the gland, then another piece of Kapton film was taped on top of the washer, sealing the gland in.

3.2.4 Electrospinning

Dissected *T. clavipes* MA silk and MA glands (dried and fresh) were dissolved in hexafluoroisopropanol (HFIP) overnight, and for certain experiments the salts mentioned in section 3.2.3 at 0.5 M concentrations were added. Although fresh glands were weighed before mixing, up to half of that mass could be water, so calculating solution concentrations from fresh glands was difficult; they ranged from 0.5 – 5 wt%. Silk fibers were electrospun (NanoNC ES-robot, Seoul, Republic of Korea) onto aluminum foil

taped to a flat plate collector with a 15 cm distance between the collector and syringe tip, flow rates between 0.5 and 1 mL/min to achieve a steady jet, and voltages of either 5/-5 kV or 10/-5 kV (tip/collector). Electrospinner humidity was controlled following a similar procedure to section 3.2.3, except for high humidity where the reptifogger ran continuously during electrospinning. Fibers were dried at least overnight before further characterization.

3.2.5 Fiber Annealing and Thermal Characterization

PAN, PVA, *B. mori* silk, and *T. clavipes* MA silk fiber bundles and Poly-L-alanine powder were oxidized in a tube furnace (Lindberg Blue M, Thermo Fisher Scientific, USA) with a 100 ccm air flow rate with a 2.5 °C/min ramp and a 275 °C hold for 1 h. Some oxidized fibers were set aside for characterization. Room temperature oxidized fibers were further heated at 2.5 °C/min and held at 400 °C, 500 °C, and 600 °C for 1 h in 100 ccm of a reducing 5% H_2/N_2 atmosphere, chosen to potentially catalyze carbonization within the fibers. When annealed under tension, ~75% of the MA silk fibers broke, so they were given 30-50% of their length in slack when oxidized and annealed. To be consistent, all other fibers were annealed freestanding.

Single MA silk fibers were secured to pieces of aluminum foil with high temperature-stable Pyro-Putty® (Aremco, Valley Cottage, NY) adhesive, then oxidized and annealed following the same process described above. Fiber bundle masses before and after oxidation and annealing were measured using a Mettler-Toledo XS 104 balance. Since spiders produce silk fibers slowly and can only be silked for an hour without potentially harmful stress to the individual, the MA silk mass change was measured on

0.5-1 mg bundles of MA silk, while PAN fiber bundle masses were 10-100 mg. TGA was performed on a Mettler-Toledo TGA/DSC 3+ (Greifensee, Switzerland) following the same oxidation and annealing procedures but using 125 ccm of 4% H_2/Argon to reduce the possibility of damaging the platinum elements in the instrument.

3.2.6 Spectroscopy

FTIR was performed using an Agilent Cary 630 (Santa Clara, CA) with a diamond ATR crystal and a DLA-TGS detector or by transmittance through electrospun nanofibers using an attached microscope with an MCT detector. Raman spectra of annealed fibers were acquired on a Horiba LabRAM (Irvine, CA) system using a 532 nm excitation laser focused through a 100x objective. Laser power and exposure time were varied to ensure the fibers did not burn. A linearly interpolated baseline correction with points at 900, 1800, 2400, and 3200 cm^{-1} was performed on Raman spectra, while a linear baseline was performed on FTIR spectra. Raman spectra from 900-1800 cm^{-1} were deconvoluted as 2-3 pseudo-voigt (70% Lorentzian, 30% Gaussian) peaks representing ordered graphitic (G) and disordered (D) bands using OriginPro 2018. Raman mapping was performed on a Horiba LabRAM system using a 473 nm laser focused through a 100x objective with a 300 nm spatial resolution. Linear background subtraction and peak fitting was performed using Origin with a Lorentzian function.

3.2.7 Microscopy

SEM and EDS were performed on an FEI XL-30 or a Tescan Mira-3 (Brno, Czech Republic) after samples were sputter-coated (Cressington 108 Auto, Watford, UK) for 15 seconds using a 20 mA current to create a thin layer of platinum (Pt) and palladium (Pd) for improved conductivity. Fiber diameters were measured using ImageJ from at least 3 locations per fiber. Since PAN fiber cross-sections are not circular, their average cross-sectional area was calculated from polished cross-sections of 100 fibers embedded in resin (Fiber Glast Development Corp., USA).

3.2.8 Tensile Testing

Tensile testing was performed on untreated, oxidized, and annealed single MA silk fibers using a Nano Bionix tensile tester (KLA Tencor, USA) and untreated, oxidized, and annealed single PAN fibers using an Electroforce 3200 (TA Instruments, USA) with a 2 mm gauge length. Untreated, oxidized, and annealed PAN fibers as well as untreated MA silk fibers were glued to cardstock mounts with cyanoacrylate superglue, while oxidized and annealed MA silk fibers remained mounted on the aluminum foil on which they were annealed. These mounts were placed in tensile grips and their edges either cut with scissors or burnt through using a pyrography pen, leaving only the fiber spanning the gauge length. Fibers were extended at a constant quasi-static strain rate of 10^{-2} s^{-1} at ambient conditions until failure. Stress and strain were calculated from the force and extension data. Testworks 4.0 software (MTS Corp., USA) was used to calculate the Young's modulus from the initial slope of the elastic region of the stress-strain curves.

3.2.9 Wide-Angle X-Ray Scattering (WAXS)

Crystallinity of polymer and silk fibers and MA glands was investigated using synchrotron X-ray radiation at LBNL and Brookhaven National Laboratory (BNL). The high X-ray flux in synchrotrons is necessary to interrogate silk crystallinity, as the crystals are small and disperse. Single glands and bundles of 1,000-10,000 fibers (untreated, oxidized, and annealed) were tested. LBNL parameters: 10 KeV X-rays, 0.124 nm wavelength, beam spot size ~300 x 700 μm, Pilatus 2M detector, 0.172 mm square pixels in a 1475 x 1679 array [63]. BNL parameters: 16-20.1 keV, beam spot size ~2 × 25 μm in vacuum, rotatable PILATUS3 300KW detector, 0.172 mm square pixels in a 1475 × 195 array [64]. 5-60s exposures were taken after confirming that exposure duration did not damage the samples, and 3-5 spots were taken per sample. For *in-situ* testing, 2-5 second exposures were taken to further minimize the damage from extended beam exposure. Images of the diffraction patterns were generated using Datasqueeze or through custom software at BNL which stitched diffraction patterns from each detector together. 2D plots of intensity vs Q ($Å^{-1}$) were created by radially averaging the diffraction patterns over a certain ϕ from 0-360. Background diffraction patterns were collected from air or substrates (e.g. Kapton) and subtracted from all data. A double exponential background subtraction was performed using Origin.

3.3 Results and Discussion

3.3.1 Gland Drying and β-Sheet Crystallization

WAXS scans of freshly dissected silk dope from the MA gland showed no crystallinity, apart from a broad water peak. As the glands dried, the spidroins self-assembled to form crystals with d-spacings slightly higher than those found from polyalanine β-sheets in native silk (Fig 3.4, Table 3.1). These data suggest the crystals are not as tightly packed, which could be due to residual water. Another theory is that the forces exerted on the silk dope during spinning (absent during free-standing drying) pack the β-sheets, exceeding a potential activation energy barrier required to pack the crystals into a stable energetic state. Attempts to extrude diluted dope through syringes failed; some material was extruded for study but produced inconsistent diffraction patterns regardless of concentration and syringe gauge. Changing the humidity, salts present, or drying technique had no significant effect on the β-sheet crystallinity (Fig 3.5). It is possible the salts were not able to diffuse into the dope, their concentrations were too low to affect spidroin self-assembly, or the change in salt ion concentration along the MA gland duct is a byproduct of proton pumps using different salts to lower the dope pH [51,55].

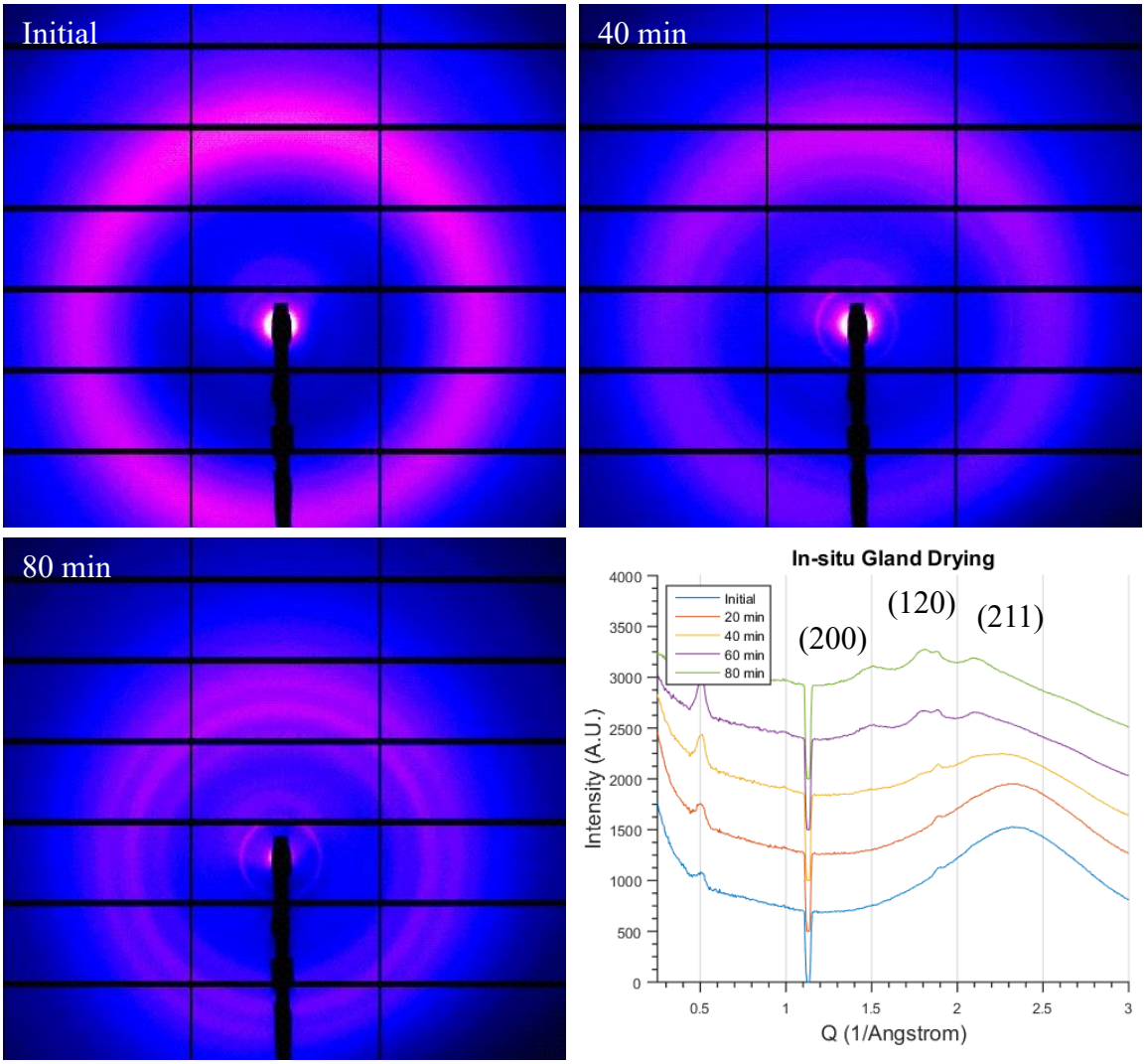

Fig 3.4: As the MA gland dries, scattering from water at ~2.35 $Å^{-1}$ decreases and the polyalanine β-sheets self-assemble, scattering X-rays in rings showing no preferred orientation but at similar d-spacings to those of native silk [46–49]. All unlabeled peaks are from the washer-Kapton setup which enclosed the gland.

Attempts to dilute the dope in aqueous solutions with different salt contents or use a dialysis bag to modify the dope solution contents were unsuccessful. Other studies have used 8M urea solutions to solubilize silkworm and MA silk dope [34]. While this is a departure from the natural system, it is less aggressive than using acid or HFIP to

dissolve the dope. Microfocused WAXS scans at BNL at different points along the MA gland duct were unsuccessful because the signal was too low.

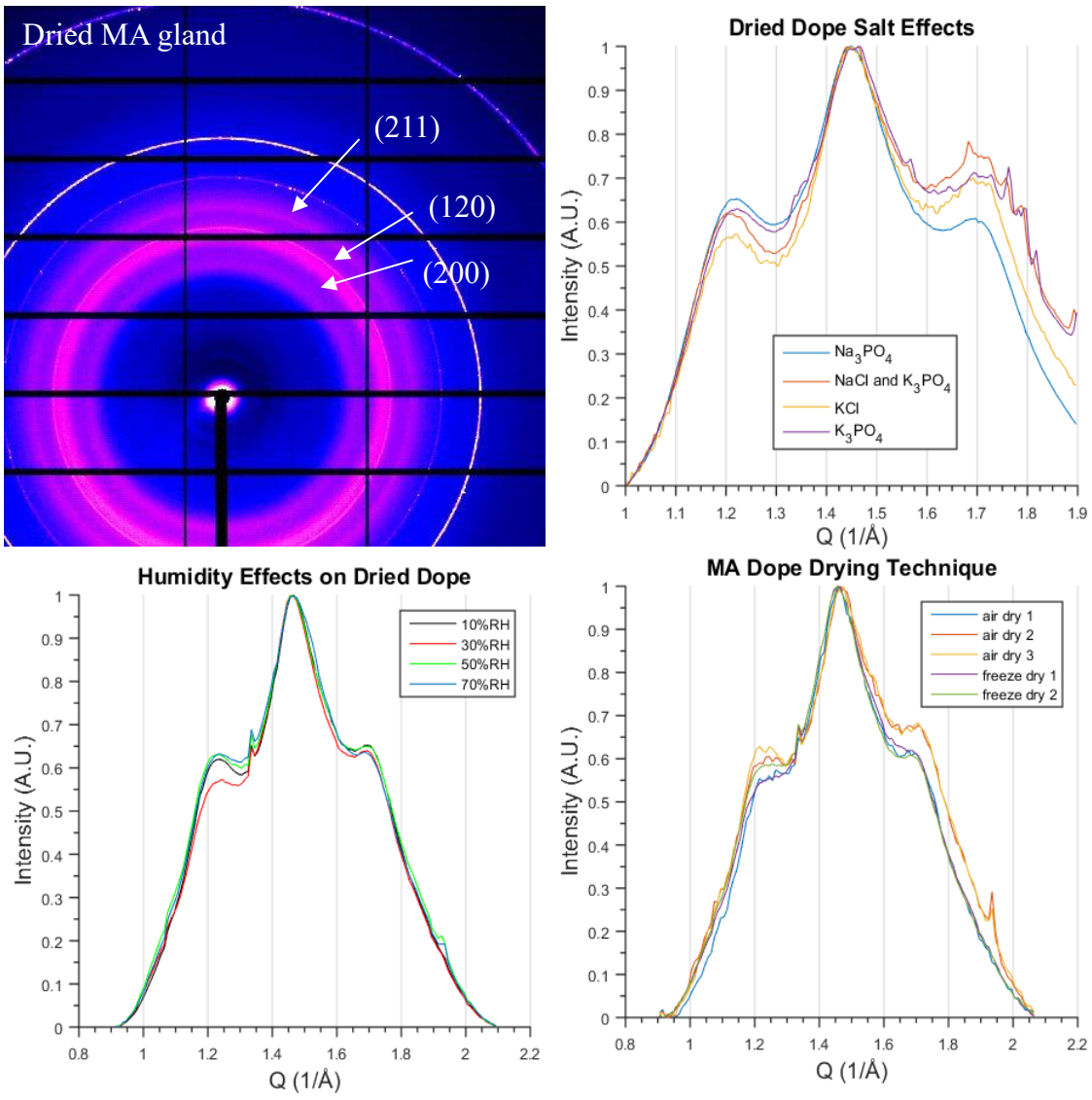

Fig 3.5: Example diffraction pattern from an MA gland dried in a solution containing NaCl showing diffraction from the polyalanine crystals and residual salt crystals (sharp rings). There is no significant difference between radially averaged slices of dried dopes with different dissection buffers, relative humidity, or drying technique.

Table 3.1: WAXS diffraction peaks of differently processed MA silk

Material	Diffraction peaks and corresponding crystal planes ($Å^{-1}$)			
T. clavipes MA silk	1.19 (200)	1.41 (120)	1.68 (211)	1.80 (002)
Dried *L. hesperus* MA dope	1.20-1.22 (200)	1.44-1.46 (120)	1.67-1.72 (211)	
Electrospun *T. clavipes* MA dope	0.88 (unknown)	1.48 (120)		

3.3.2 Electrospun MA Silk

T. clavipes MA dope was dissolved in HFIP and electrospun into a nanofiber mesh. The MA spidroins dissolved completely, although remnants of the gland skin did not. Initial dope/HFIP solutions were made directly after dissection, and their concentrations were estimated using the wet weight of the MA gland and the assumption of 50% water. Some solutions did not form fibers, likely because they were too dilute. Later solutions were made with dried glands after determining that drying the gland did not significantly affect the spidroins or electrospun fibers. Electrospinning went smoothly, with some interruptions in flow, possibly due to gland skin debris. HFIP is less viscous than many solvents used in electrospinning, so it was difficult to adjust the flow rate to completely avoid drops of solution falling onto the collector. Occasionally, up to three separate jets were observed emanating from the Taylor cone.

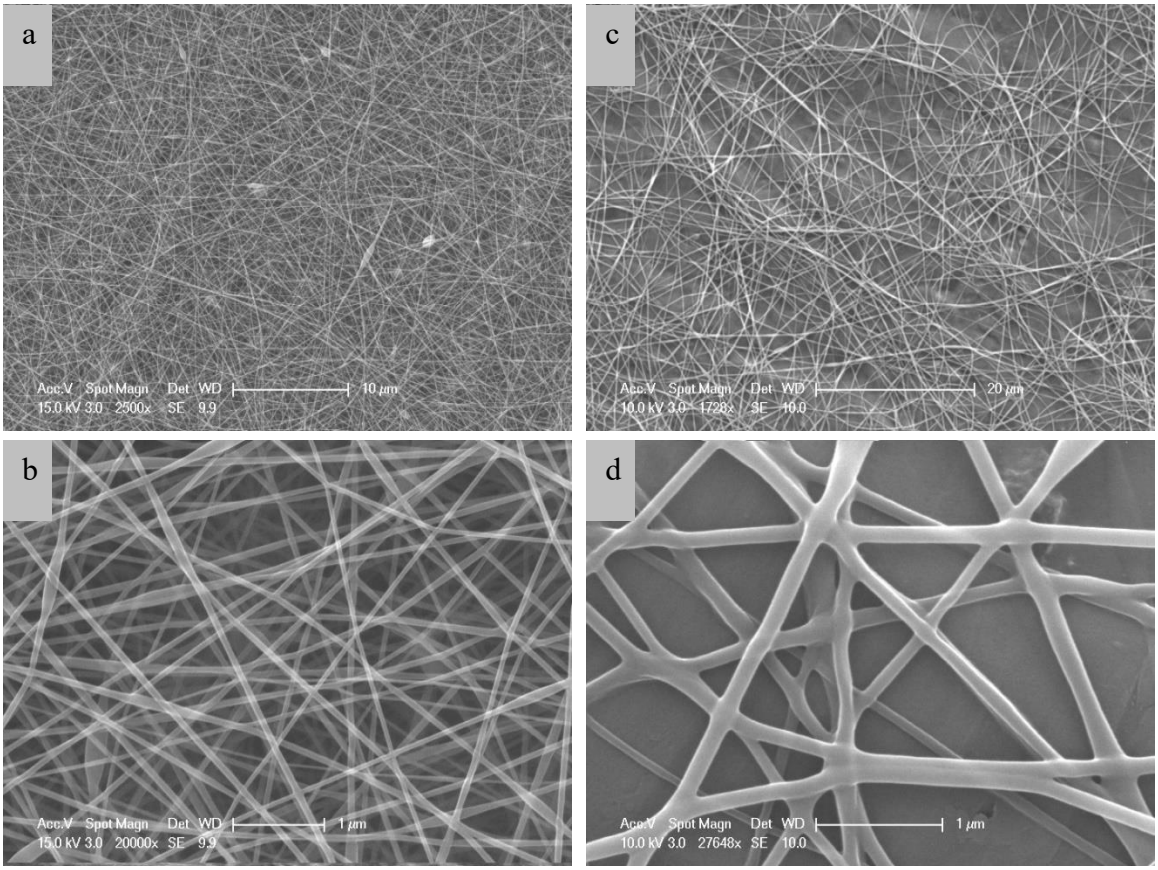

Figure 3.6: Regenerated electrospun *T. clavipes* MA silk (a, b) and electrospun silk from dissolved *T. clavipes* MA glands (c, d)

Most electrospun fiber mats had a small amount of debris or beads present along the nanofibers (Fig 3.6). The nanofibers were smooth and uniform and would weld together occasionally as residual HFIP remained after the fibers were deposited (Fig 3.6d). As expected, more concentrated solutions generally yielded thicker fibers (Table 3.2). It was difficult to spin fibers at voltages different from +/- 5 kV, thus insufficient data were available to test the effect of voltage on fiber structure.

Table 3.2: Electrospun silk conditions and fiber diameters

Spidroin source	Concentration (wt %)	Flow Rate (mL/h)	Voltage (kV)	Avg. Diameter (nm)	Standard Deviation (nm)
Gland	~0.90	1.0	(+5,-5)	302	120
Gland	~0.72	0.5	(+5,-5)	54	15
Gland	~0.29	0.5	(+5,-5)	138	36
Gland	~0.54	0.5	(+5,-5)	280	95
Silk	0.74	0.5	(+5,-5)	280	95
Silk	0.74	1.0	(+5,-5)	225	55
Silk	0.50	0.5	(+5,-5)	211	45
Silk	0.50	0.7	(+5,-5)	61	18
Silk	0.25	1.0	(+10,-5)	72	18

Electrospun MA silk fibers from regenerated silk and dissolved dope had similar molecular structures to native silk, although there were small differences in their FTIR spectra (Fig 3.7a) [23]. Native and regenerated silks had the most similar spectra, possibly because the mass ratio between each spidroin, sugars, and lipids used to coat the silk fibers differs between native silk and the glands. Although spectroscopic peak absorbance is generally proportional to the amount of absorbing material (e.g. C=O bonds), the differences in intensity between the Amide I and II bands may result from detector saturation from the Amide I band, a different degree of hydrogen bonding in the Amide II N-H bond, or differences in molecular structure. Amino acid analysis showed native silk had 1.3 mol % asparagine/aspartate and 0.5 mol % lysine, while electrospun dope had 1.9 and 1.3 mol %, respectively. This slight difference could account for part of the different amide band intensities between native silk and electrospun dope; amino acid analysis was not performed on regenerated silk.

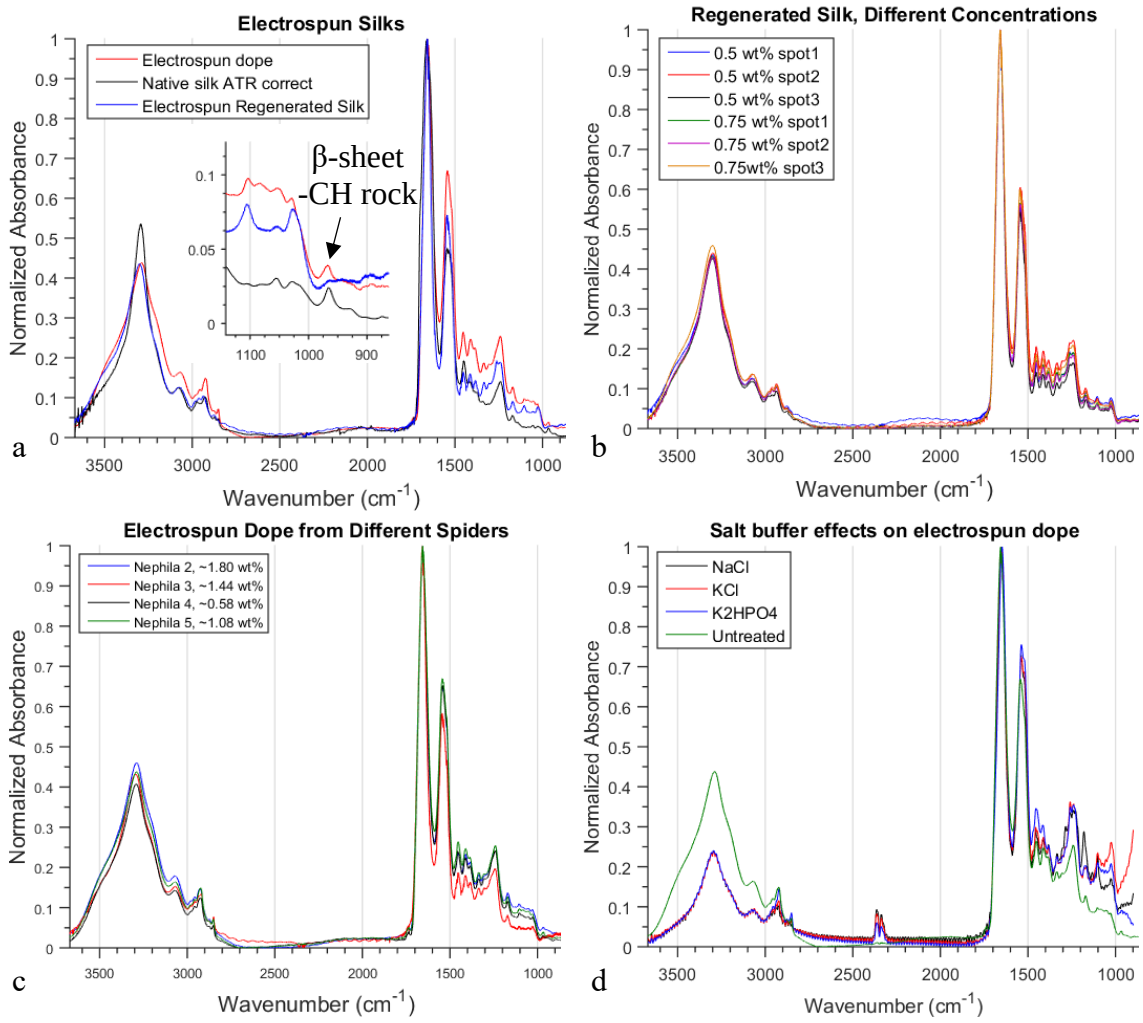

Figure 3.7: FTIR spectra comparing electrospun MA silk with different sources (a), concentrations (b), spiders (c), and salt ion concentrations (d).

The different intensities and peak breadths in the -OH stretch region could be due to the imperfect ATR correction used to convert data collected using an ATR crystal for comparison with data collected in transmittance or minor structural differences. The 977 cm^{-1} band is attributed to -CH rocking from polyalanine β-sheets in MA silk, and is absent in regenerated silk [32]. Although this is a key finding, the mechanism is uncertain. It is possible something in the dope—salt ions or other organic species for example—aid

in the polyalanine crystal alignment. Spectra were similar across silks and MA dope from multiple individuals (Fig 3.7b-c). Changing the salt concentration and humidity (data unavailable) did not significantly affect the crystallinity or molecular structures of electrospun MA dope (Fig 3.7d and 3.8).

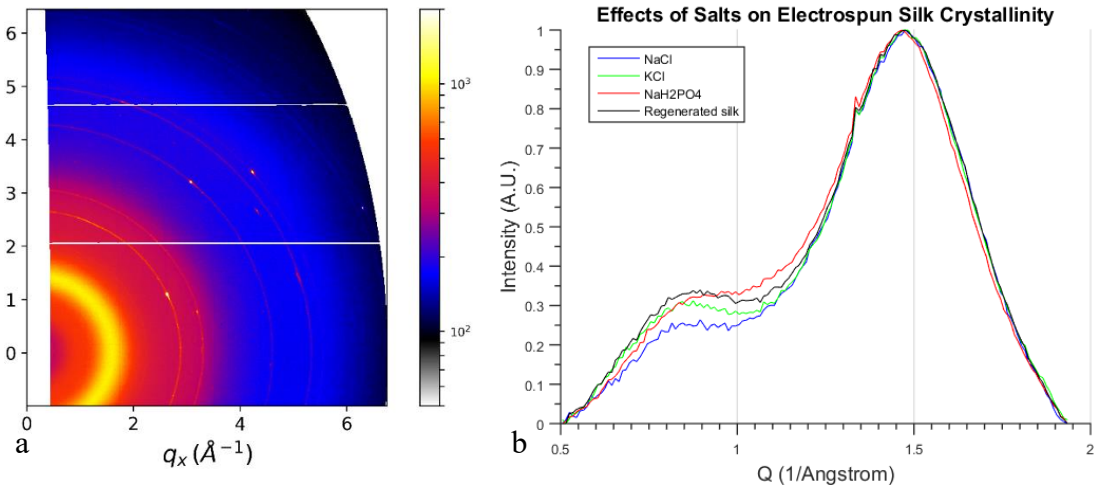

Figure 3.8: WAXS diffraction pattern from electrospun regenerated silk (a), and radially averaged WAXS diffraction patterns (b). Sharp rings and spikes in (a) are from aluminum foil.

To get sufficient signal from WAXS measurements, electrospun fibers were rolled up into a ~1cm diameter ball. This method also collected bits of the aluminum foil on which the fibers were electrospun, which appear in the diffraction pattern (Fig 3.8). Electrospun silk has a prominent diffraction peak at 1.48 $Å^{-1}$, which could correspond to the polyalanine (120) plane, but the other major MA silk diffraction peaks were not present [48,49]. Given that the electrospun silk samples were balls of randomly oriented fibers while the MA silk samples were unidirectional fibers, it is possible the (200), (120), and (211) peaks are broad and overlapping enough to appear as one broad peak.

This peak is broader than the main MA silk peaks, so the polyalanine crystals in electrospun silk are smaller than those in native silk, but given the peak overlap, the crystal size cannot be reliably estimated. Given the unknown peak at 0.88 $Å^{-1}$, it is also possible the crystals in electrospun silk arise from a different molecular structure than the polyalanine β-sheets in MA silk.

3.3.3 Annealed silks and Polymer Fibers

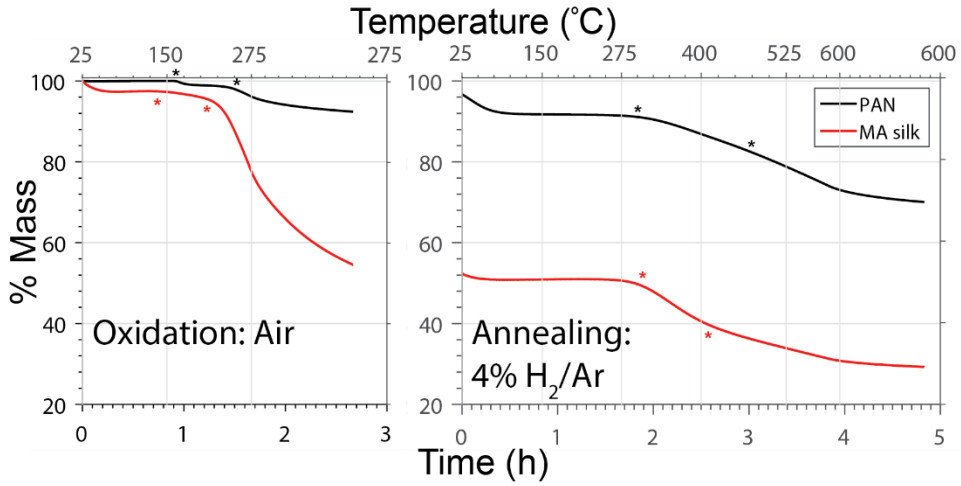

Figure 3.9: TGA of PAN and MA silk during the oxidation (air) and annealing (4% H_2/Ar) steps. Stars indicate inflection points at 162, 242, 316, and 482 ºC in PAN and 145, 230, 298, and 411 ºC in MA silk. Initial drops below 100 ºC are likely the evaporation of adsorbed water vapor or other volatiles.

Table 3.3: mass loss and fiber diameters of annealed MA silk and PAN

	Property	Untreated	Oxidized	400 ºC Annealed	500 ºC Annealed	600 ºC Annealed
MA silk	Avg fiber diameter (µm)	3.65 ± 0.33	3.04 ± 0.39	2.69 ± 0.44	2.56 ± 0.32	2.89 ± 0.59
	Mass loss	N/A	44%	56%	62%	69%
PAN	Avg fiber diameter (µm)	10.97 ± 1.08	11.60 ± 1.59	10.88 ± 1.07	10.00 ± 1.34	8.76 ± 1.58
	Mass loss	N/A	1%	14%	20%	30%

As expected, each polymer and polypeptide fiber lost mass during oxidation and annealing as oxygen-containing functional groups combusted and the polymer backbones cyclized (Table 3.3). *T. clavipes* MA silk quickly lost mass during oxidation beginning at 230 ºC, while PAN cyclized and began losing mass at 242 ºC (Fig 3.9). Minor mass losses at 162 and 145 ºC were likely the combustion of volatile side chains in MA silk and copolymers in PAN [65,66]. In MA silk, the abundance of nitrogen and the versatility of the peptide carbonyl to cyclize with neighboring peptides likely initiates cyclization at a lower temperature and provides stability to silk fibers during oxidation and annealing. Consequently, MA silk fibers maintained their shape and surface morphology after oxidation and annealing despite significant mass loss (Fig 3.10). *B. mori* silk fibers behave similarly to MA silk, but PVA fibers shrivel, shrink, and fuse together. The abundant alcohol groups could facilitate cyclization, but upon combustion, the fibers lose almost 40% of their mass, causing shrinkage which renders them unusable for structural applications and carbon fiber production. Fiber diameter variation falls within an acceptable range for natural materials and is higher for 600 ºC annealed fibers. Diameter variation will affect calculated stress values, yet no direct correlation was observed in this study. PAN fibers showed a shriveled surface morphology (Fig 3.10) after annealing and lost less mass, as their nitrile groups are incorporated into the cyclized structure rather than being released during oxidation like many side chains in oxygen-rich proteins [65].

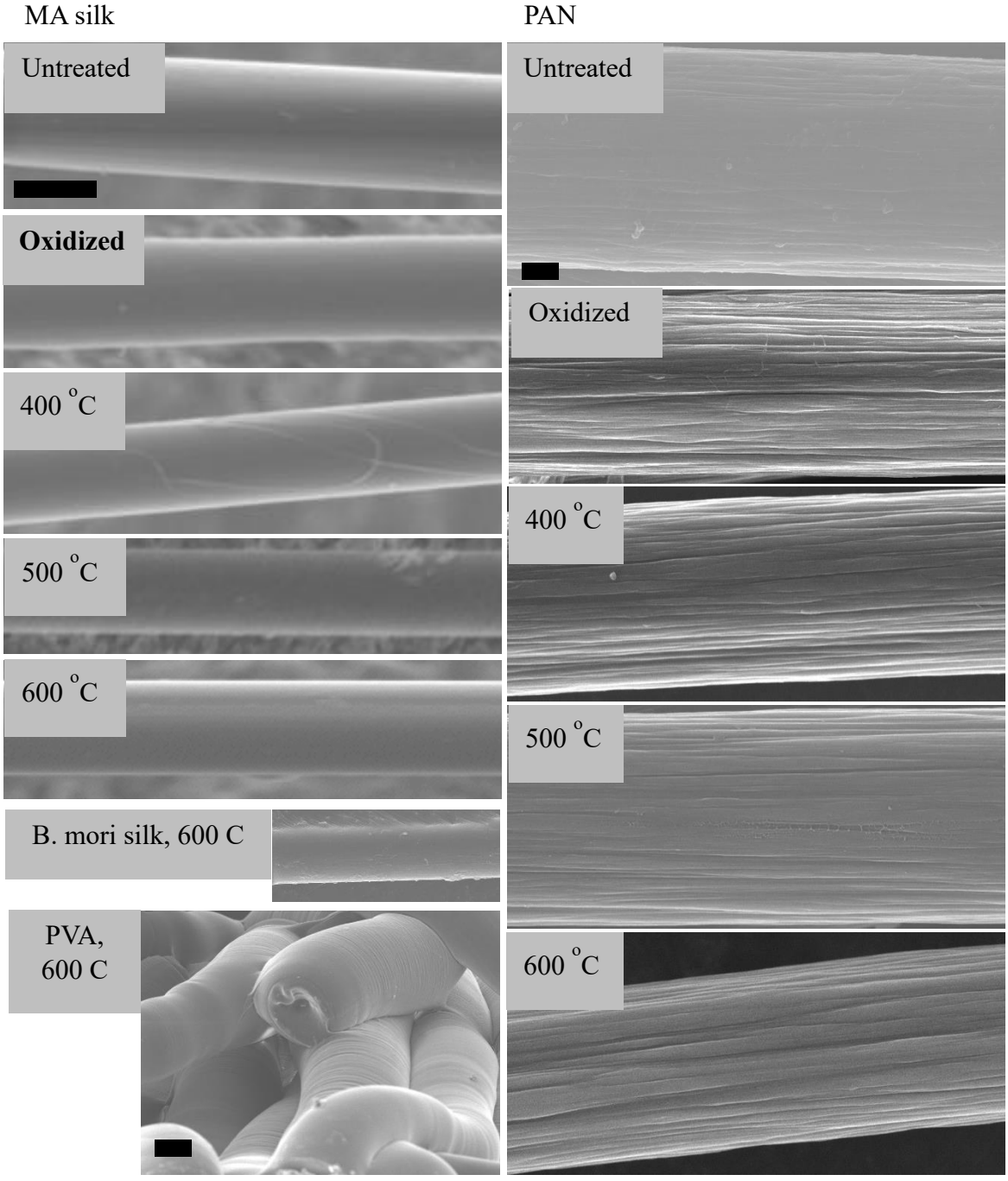

Figure 3.10: SEM of *T. clavipes* MA silk and PAN in untreated, oxidized, and annealed conditions, and annealed *B. mori* silk and PVA. Silk retains a smooth surface finish, while the PAN surface becomes rougher and more fibrillar. PVA fibers shrink considerably and fuse together. Scale bars for the silks and PAN are 2 μm and 25 μm for the PVA.

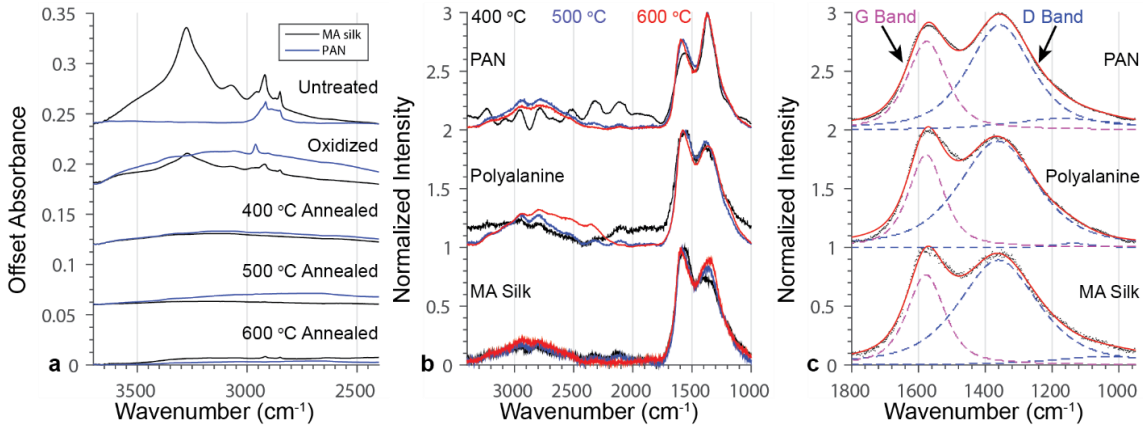

Figure 3.11: FTIR (a) and Raman (b) spectra of annealed MA silk, PAN, and polyalanine with deconvoluted and fitted spectra of 600 ºC annealed materials (c).

MA silk loses its ability to hydrogen bond as oxygen is burnt off and nitrogen is cyclized, shown by a decreasing OH/NH stretch peak ca 3200 cm-1 with annealing temperature (Fig 3.11a). The sharp amide band from untreated MA silk at 1670 cm^{-1} would appear as a shoulder in the G band if present in annealed fibers (Fig 3.12). Since it is absent in both Raman and FTIR spectra, as are the other sharp peaks in the fingerprint region, and the FTIR spectra of oxidized MA silk looks similar to that of oxidized PAN, the peptide backbone is cyclized similarly to oxidized PAN [67].

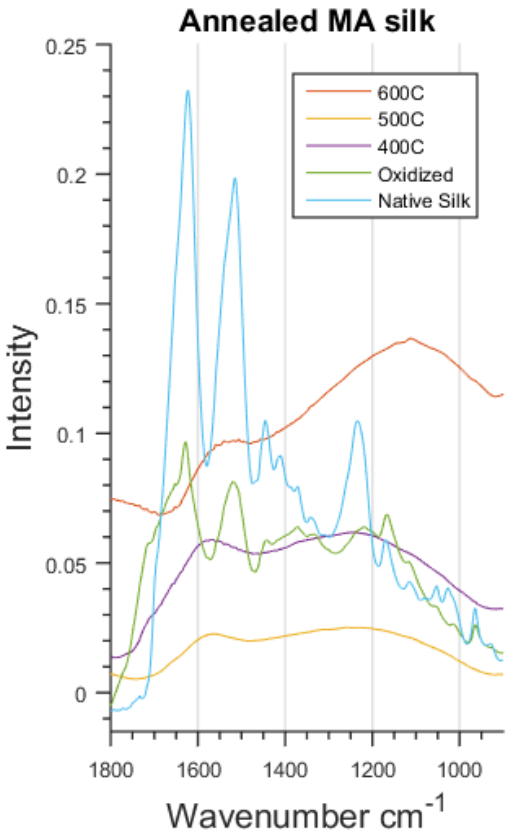

Figure 3.12: Strong amide bands from untreated silk decrease in intensity upon oxidation and are not present after annealing.

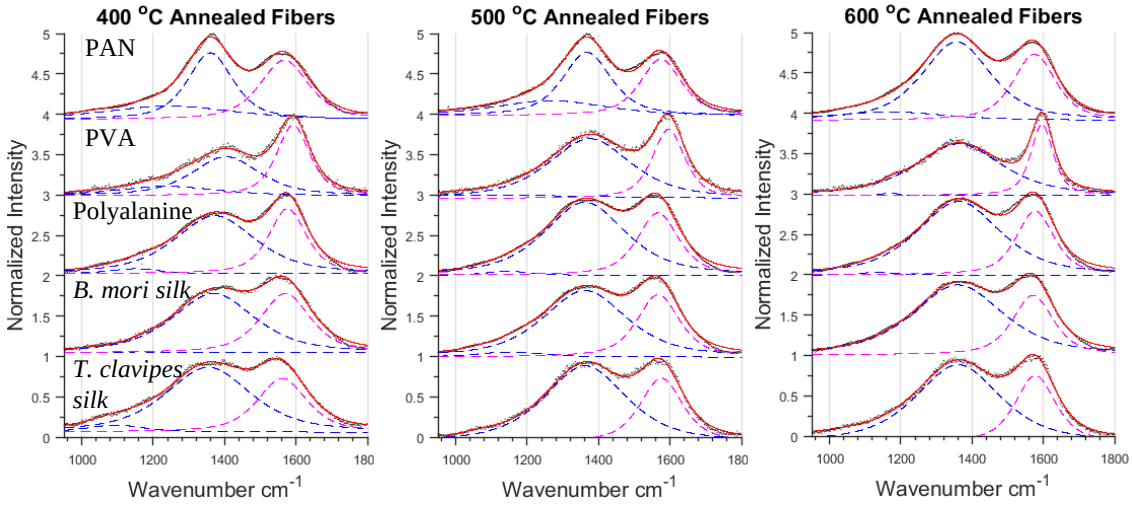

Figure 3.13: Fitted Raman spectra of different materials and annealing temperatures

Raman spectroscopy can measure graphite content by comparing the intensity (I) of the disordered (D) and graphitic (G) bands [69–71]. MA silk, *B. mori* silk, PAN, and polyalanine powder graphitized to a similar extent upon annealing based on I_D/I_G, while PVA graphitized more quickly (Fig 3.11 and 3.13, Table 3.4). The singular G band comes from vibrations of the ordered graphite lattice; multiple vibrations from disordered regions, such as edges, voids, heteroatoms, or topological defects, make up the D band. Similar to previous works on pyrolyzed materials, the annealed fibers have multiple D bands, but the amount of impurities and D bands decrease as annealing temperature increases while the graphite crystals grow in size and number [69]. Natural polymers like silks have a less homogenous structure and are more likely to have many D bands. The high I_D/I_G ratios, breadth of D and G bands, and multiple, broad 2D bands suggest the annealed fibers are mostly amorphous carbon with nitrogen-containing turbostratic graphite nanocrystals, since the fibers were not annealed at temperatures high enough to combust nitrogen (Fig 3.11) [65,69,72].

Table 3.4: I_D/I_G ratios

	MA silk	Polyalanine	PAN	*B. mori silk*
400 ºC	1.21	0.90	1.31	1.00
500 ºC	1.19	1.17	1.33	1.08
600 ºC	1.18	1.15	1.25	1.18

Raman spectra from oxidized fibers were overwhelmed with fluorescence and not reported. Curve fitting can be a deceptive process, as least-squares fitting algorithms can usually converge a proposed fit, but often using unrealistic values. For consistency, 3-peak fits on all Raman spectra were used unless Origin's algorithm determined the third

peak was null. While it is possible additional D bands are present and fits with less than 3 peaks did converge, these additional peaks did not significantly affect the I_D/I_G values.

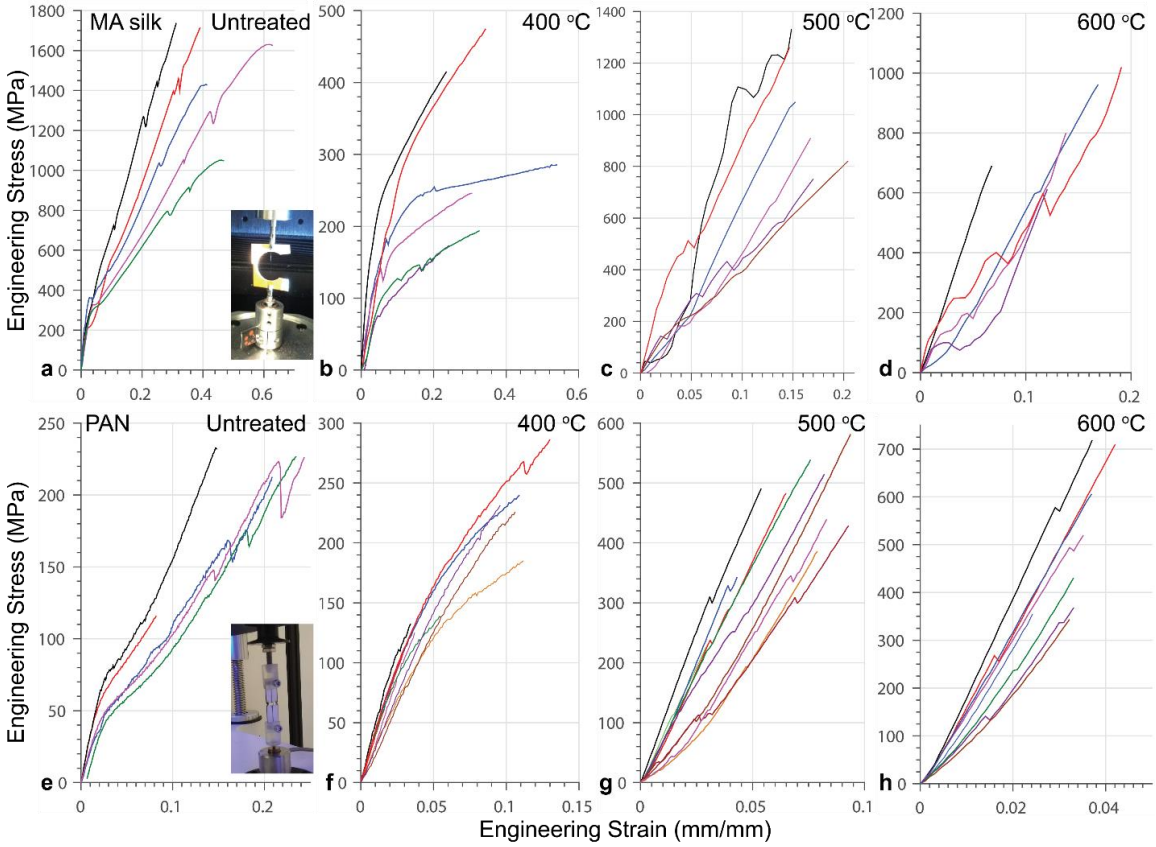

Figure 3.14: Stress-strain plots of untreated and annealed fibers. Each color in a plot represents a unique sample. Insets show mounting setup of untreated MA silk (a) and all PAN fibers (f). Spikes in the stress-strain plots correspond to slippage in the grips.

After annealing, MA silk fibers have a lower Young's modulus, ultimate tensile strength, and toughness (Fig 3.14 a-d, Table 3.5). The Young's modulus of oxidized MA silk fibers was 3-20 times lower than untreated MA silk with a large variation in stress-strain curves (Fig 3.15). MA silk annealed at 400 ºC had more consistent, slightly elastomeric stress-strain curves but three times less ultimate tensile strength than untreated MA silk (Fig 3.14). MA silk fibers annealed at 600 ºC had a Young's modulus

equal to that of untreated silk, but half the ultimate strength and 10% the toughness. This behavior highlights the significant contribution of hydrogen bonding between structural motifs in MA silk, especially the stick-slip mechanism in the polyalanine nanocrystals, to MA silk's strength and toughness [18,19]. After oxidation, few cyclized regions are observed so the fibers have little resistance to tensile loading without hydrogen bonding to add mechanical support. The fiber Young's modulus and strength increases with annealing temperature as cyclized regions grow in size and number, fusing adjacent spidroins similar to the fusion of cyclized PAN chains.

Table 3.5: Annealed MA silk and PAN mechanical properties

	Young's Modulus (GPa)		Ultimate Tensile Strength (MPa)		Bulk Toughness (J/cm^3)	
Annealing Temperature	MA silk	PAN	MA silk	PAN	MA silk	PAN
None	11.2 ± 2.1	2.50 ± 0.74	1,430 ± 270	202 ± 49	501 ± 200	21.0 ± 9.5
400 ºC	3.62 ± 1.6	3.68 ± 0.69	280 ± 120	186 ± 63	62.7 ± 41	9.92 ± 7.5
500 ºC	8.03 ± 3.3	7.61 ± 1.5	908 ± 290	444 ± 100	74.4 ± 20.	15.3 ± 6.3
600 ºC	10.0 ± 3.1	15.9 ± 2.6	815 ± 170	503 ± 160	52.2 ± 30.	8.53 ± 3.9

Annealed PAN also transitioned from ductile to brittle failure. Its Young's modulus and ultimate strength increased above the values of untreated PAN when annealed above 500 ºC, more quickly than in MA silk (Fig 3.14 e-h). Although PAN chains do align in crystalline regions, neighboring chains are not bound together and slip past each other during tensile loading [73]. Neighboring PAN chains start fusing together

during carbonization and more so during graphitization, limiting chain slip and stiffening the fibers. Comparing fibers annealed at 600 ºC, PAN has a higher Young's modulus, but MA silk is stronger and tougher. In addition to structural differences between the fibers, the PAN fibers have larger diameters and thus have more defects serving as crack initiators. It is known that carbon fiber strength and modulus increase with decreasing fiber diameter [74]. Further studies must be conducted using fibers of similar diameters to better compare their mechanical properties.

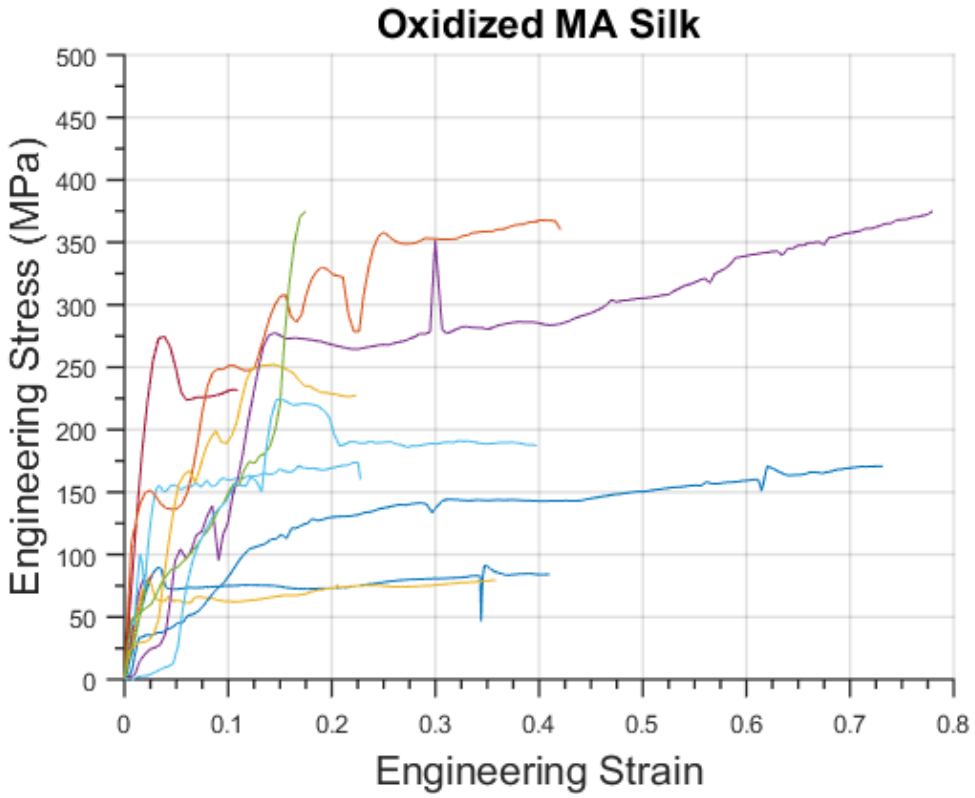

Figure 3.15: Stress-strain plots of 13 oxidized fibers tested showing a wide range of behaviors from elastomeric to brittle. This spread made the error in calculated stiffness and strength too high to report with confidence.

Although single fiber mechanical testing can show truer mechanical properties, without any contributions from fiber weaving or slip between fibers, it has inherent difficulties that can lead to sources of error. Fibers must be individually mounted for tensile testing by hand, which can result in fibers being slightly misaligned and not parallel to the loading direction. Each load-deflection curve was individually analyzed and determined where initial loading began, defined as the point where the slope was constant and within 90% of the calculated Young's Modulus. All these factors, in addition to biological variation and processing defects, can explain the spread in the stress-strain plots.

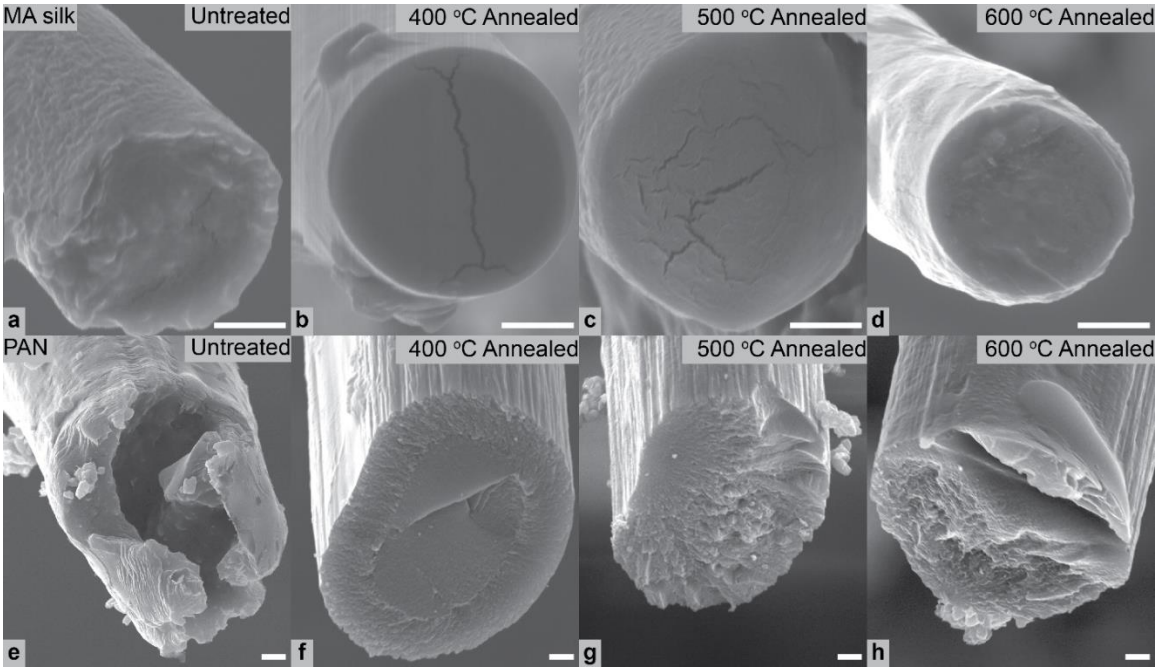

Figure 3.16: Untreated MA silk (a) and PAN (e) fibers have ductile fracture surfaces, 400 ºC fibers show a combination of ductile and brittle fracture, and fibers annealed at 500 and 600 ºC show brittle fractures (b-d, f-h). Scale bars are 1 μm.

The ductile-to-brittle transition with increasing annealing temperatures seen in stress-strain curves is also evident in MA silk and PAN fracture surfaces (Fig 3.16).

Some oxidized and 400 ºC annealed fibers necked, while others had an outer shell fracture first and relax before the fiber broke (Fig 3.17). This 100-200 nm shell can be seen in annealed fibers through deflected cracks, differing contrast in the electron micrographs, and sword-in-sheath fracture patterns (Figs 3.16b, 3.16c, and 3.17) [75,76]. The core-shell phenomenon discussed in chapter 2 is evident in oxidized and 400 ºC annealed PAN, but PAN fibers annealed at higher temperatures often fractured by shear, making it difficult to observe (Fig 3.16 and 3.18). Mirror mist hackle and shear fracture surfaces (Fig 3.16 g, h) suggest that annealed PAN is more brittle than annealed MA silk [75,76].

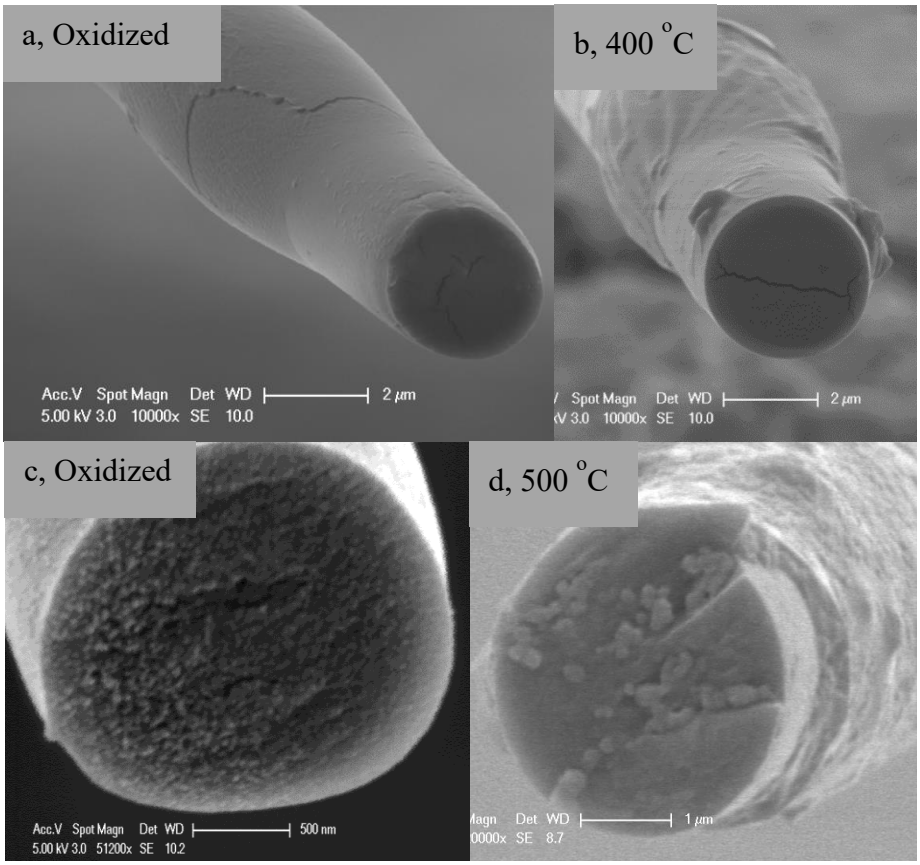

Figure 3.17: Additional MA silk fracture surfaces showing necking (a, b), possible nanofibrils where the spidroins have cyclized individually but not fused together (c), and core-shell structures (d), identified by contrast differences, crack deflection, or sword-in-sheath fracture.

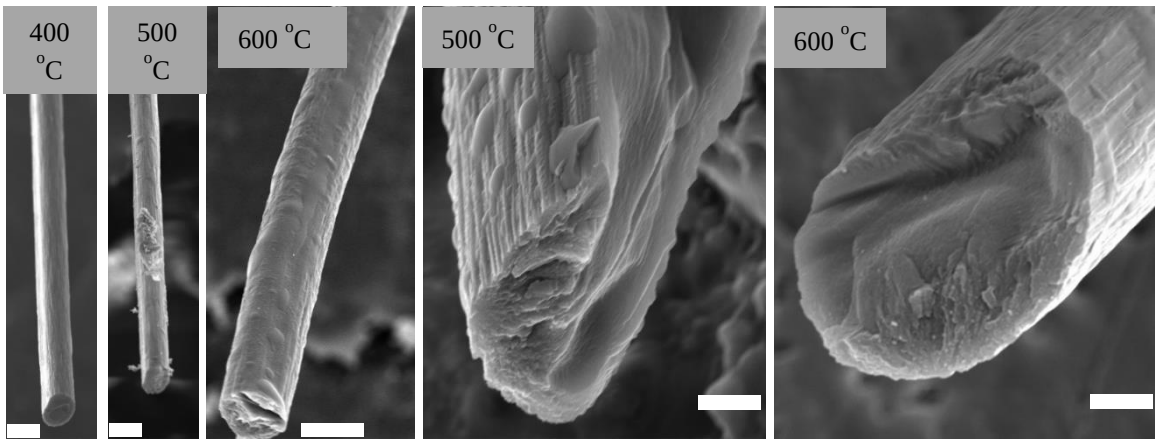

Figure 3.18: Fractured PAN fibers show no necking (left three micrographs, scale bars 10 μm). Some 500 and 600 °C fibers failed via shear across the entire fiber cross section (right two micrographs, scale bars 2 μm).

Some researchers theorized that MA silk has a core-shell structure largely comprised of two proteins, MA spidroins (MaSp) 1 and 2 [77,78]. This structure could translate to annealed fibers, since MaSp 1 is theorized to be stiffer with more polyalanine nanocrystals while MaSp 2 has more helical secondary structures [24,79–81]. The fiber core contains both MaSp 1 and 2, but the 300-400 nm fiber shell may only contain MaSp 1. Since MaSp 1 has more polyalanine nanocrystals to serve as templates for graphite formation, the shell should graphitize more [82]. This hypothesis could explain the crack deflection seen at the core-shell interface, since the shell would be stiffer. Raman maps of annealed MA silk fibers and PAN show the 100-300 nm fiber shell is more graphitic, with I_D/I_G ratios of ~1.2 and 0.8 for PAN core and shell, respectively, and ~0.8 and 0.2 for silk core and shell, respectively. Thus, the core-shell structure could form during oxidation is it does in carbon fiber and be influenced by spidroin distribution (Fig 3.19). However, there was low Raman signal and overlapping peaks caused by the resin in

which fibers were embedded, so further studies are required to see if the 0.2 I_D/I_G ratio for annealed silks is real. Initial data from Raman maps of PAN and annealed MA silk suggest significantly more graphite in the silk fiber shell for all annealing temperatures; however, further investigations are necessary to confirm this.

I_D/I_G is inversely proportional to graphite crystal size and can estimate one-dimensional crystal size (L_α) using the Tuinstra-Koenig relationship $\frac{I_D}{I_G} = \frac{C_\lambda}{L_a}$, where and C_λ is calculated based on the laser wavelength [70,72,83,84]. Using this relationship, estimated graphite crystal sizes range from 3.7-5.5 nm for bulk fibers and 2.5 to ~10 nm for fiber cross-sections. The Tuinstra-Koenig approximation becomes less reliable for crystals below 2 nm, where the proportionality between Lα and I_D/I_G changes [85,86]. Consequently, the correlation between I_D/I_G values and crystal size becomes discontinuous, and alternate methods of measuring crystal size are required.

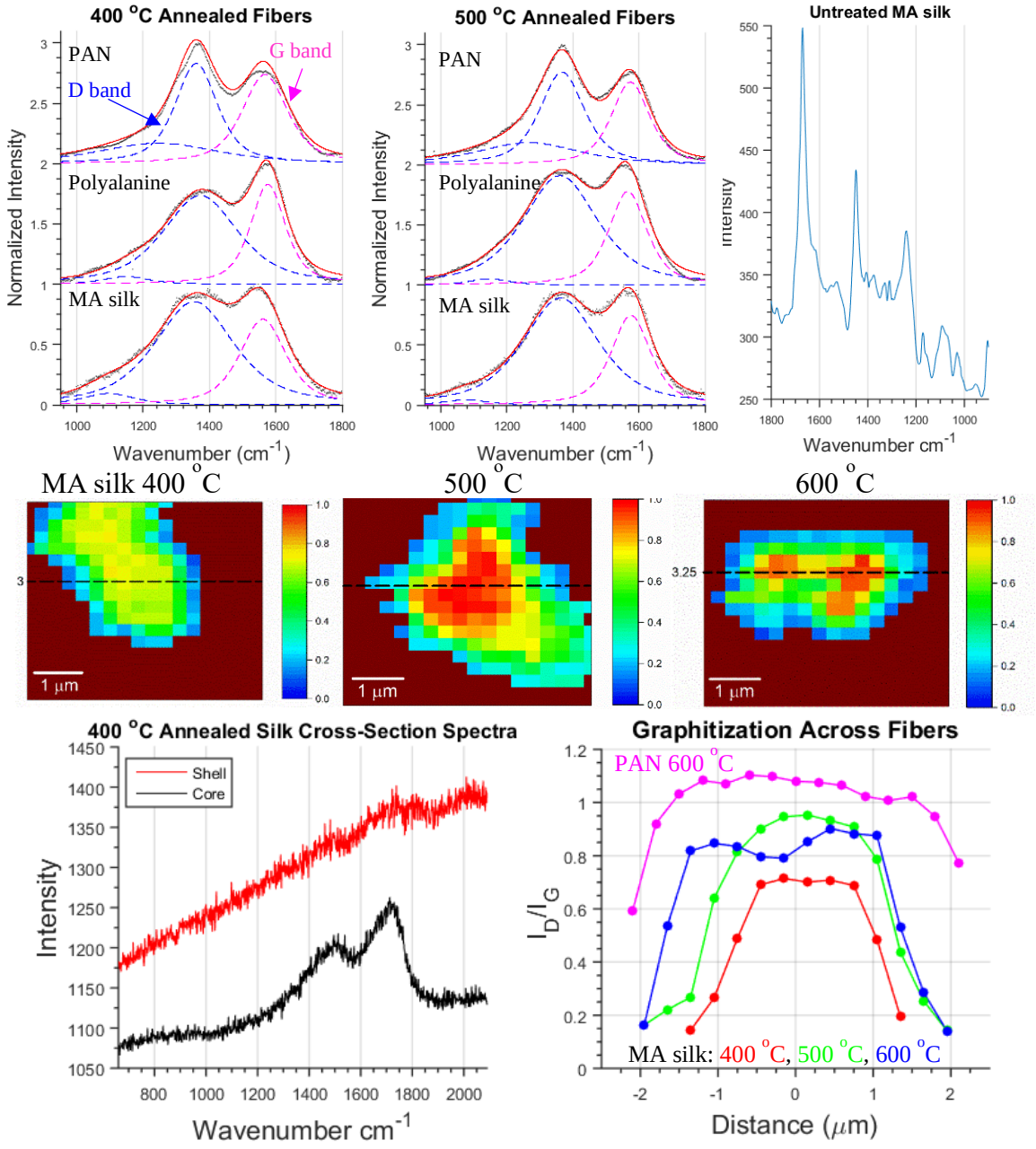

Figure 3.19: Deconvolution of Raman spectra from 400 ºC and 500 ºC MA silk shows no significant difference in graphitization and the absence of the amide band seen in untreated fibers. Raman maps show a core-shell distribution if I_D/I_G ratios tending towards a more graphitic shell, but data from the shell have a low signal to noise ratio.

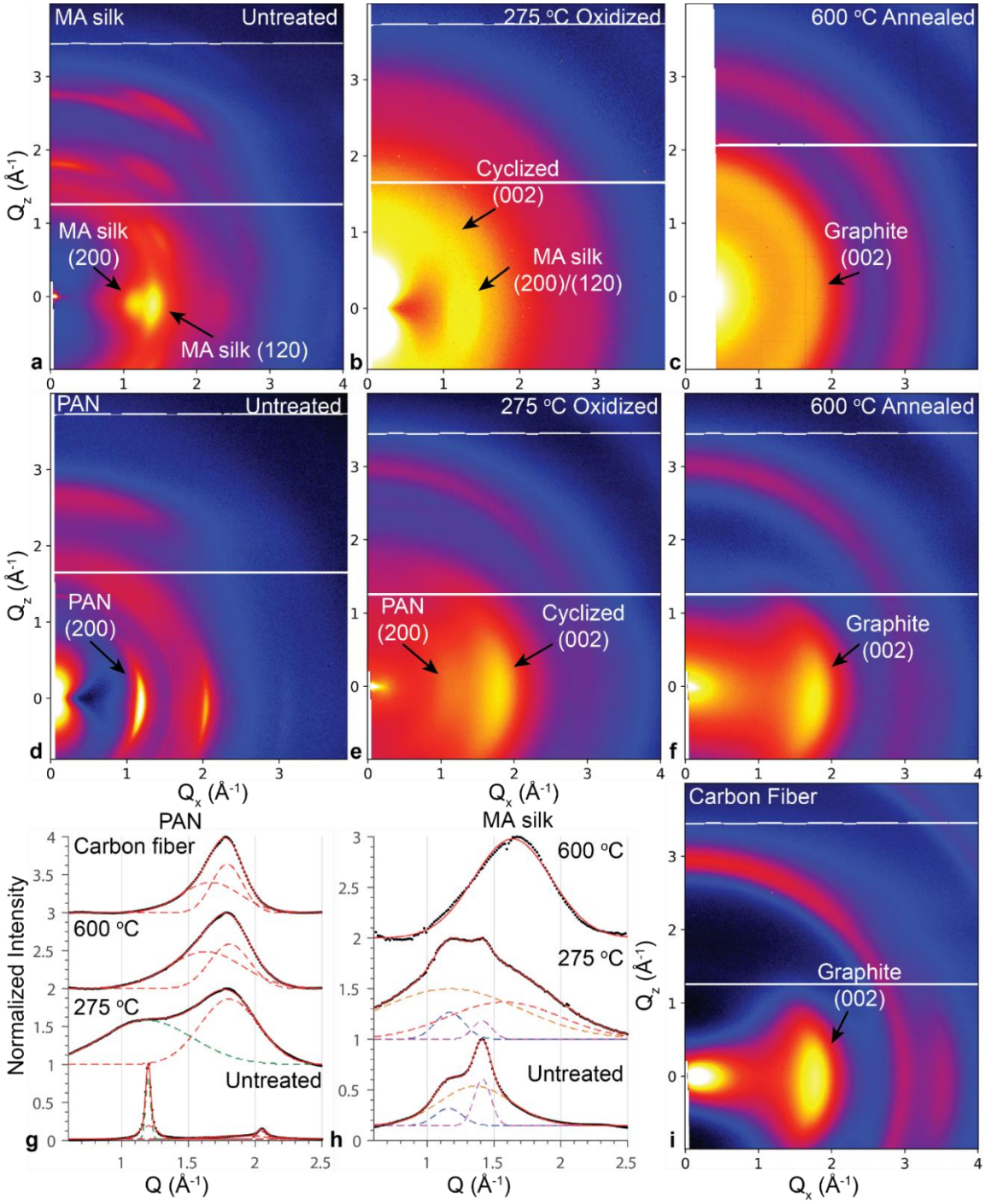

Figure 3.20: WAXS patterns of annealed silks, PAN, and commercial carbon fiber. Radially averaged plots from ϕ = -10 to 10 highlight the PAN (200), MA silk (200) and (120), and graphite (002) diffraction peaks.

X-ray diffraction is a more widely used method for determining crystal size and has been used to correlate I_D/I_G to graphite crystal size [70,71,86]. WAXS with an area detector has the additional benefit of revealing crystal alignment within fibers. WAXS of untreated PAN, MA silk, and *B. mori* silk fibers showed sharp arcs, indicating preferential crystalline alignment along the length of the fiber (Fig 3.20a, 3.20d, 3.21a, 3.22a, and 3.22d), due largely to the extrusion drawing process [7,88]. Crystals in PAN are larger but have a lower number density than in MA silk, which is one contributing factor to silk's superior strength [48,89]. Oxidized PAN and MA silk both showed remnants of the untreated peaks, suggesting that some native crystals remain aligned but uncyclized, or that cyclization begins on the crystal faces and is a slow process [47]. A peak close to the graphite (002) diffraction appears in oxidized PAN and MA silk, likely arising from the (002) planes of cyclized crystals (Fig 20 g, h). The cyclized crystals which formed in MA silk were unaligned, producing uniform scattering across the detector visible as a ring (Figs 20 b and 22 b). Conversely, the PAN (200) reflection shrank as the graphite (002) increased, both maintaining similar alignment (Fig 20 e). Vertical scattering at 0.1-0.5 Å-1 is from the beamstop (Fig 20 b, d).

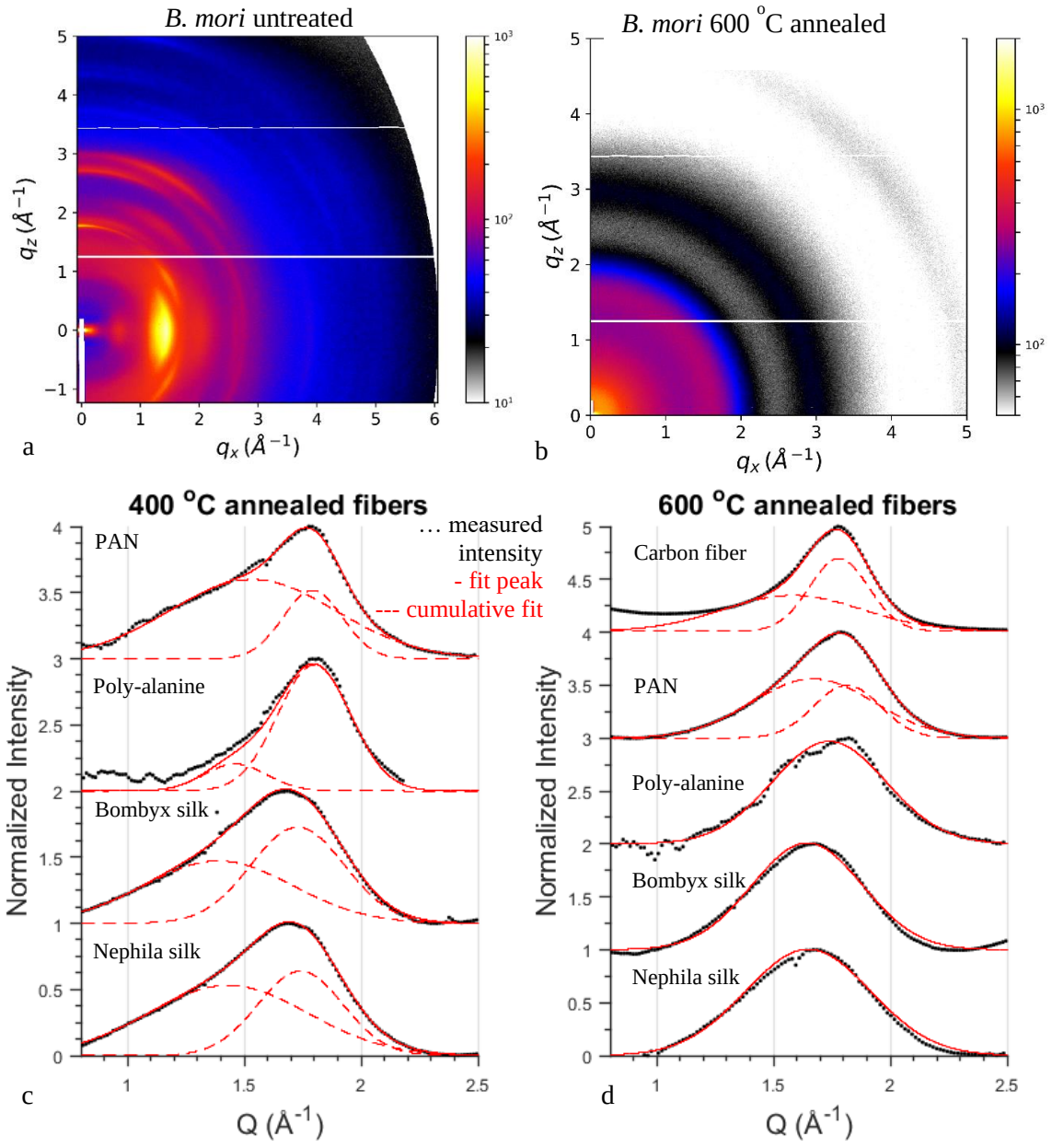

Figure 3.21: *B. mori* and polyalanine have similar diffraction patterns and crystal sizes to annealed MA silk.

There are two main theories for the crystal structure of PAN; both agree that the polymer chains aggregate parallel to each other and the long axis of the fiber, but there is disagreement over the chains folding as a planar zigzag or spiral with the nitrile groups

pointing outward along the (200) plane (Fig 3.22) [73,89–92]. Since cyclization converts nitrile groups to aromatic rings, which then stack to form graphite, a direct translation from PAN (200) to graphite (002) is possible. The exact reaction pathways during PAN oxidation have yet to be confirmed experimentally, but this evidence suggests the cyclization occurs along the c-axis of PAN crystals, forming cyclized regions roughly parallel to the fiber axis (Fig 3.22 e). Further in-situ studies should be performed to confirm this process.

Table 3.6 Crystal parameters of annealed silk, PAN, and carbon fiber

Sample	MA silk 600 °C	Bombyx silk 600 °C	Polyalanine 600 °C	PAN 600 °C	Carbon fiber
q ($Å^{-1}$)	1.65	1.64	1.74	1.82	1.78
Crystal size (nm)	1.80	2.04	1.97	3.38	3.78
Orientation factor	0.041	0.006	N/A	0.460	0.725

As annealing temperature increased, the cyclized structures became larger and more densely packed, indicated by sharper diffraction peaks (Figs 20 c, f, 21 b-d, 22 c, f). Annealed PAN and carbon fiber had slightly larger graphite crystals than annealed MA silk, polyalanine, and *B. mori* silk (Table 3.6), as estimated using the graphite (002) peak through the Scherrer approximation, $L_a = \frac{K\lambda}{w \cos\theta}$. λ is the X-ray wavelength, K is a constant of 0.9 based on the type of unit cell, θ is the diffracted peak position, and w is the peak full-width at half-maximum [87]. The graphite (002) q value in every material tested is notably less than that of pure graphite, 1.872 Å-1, which is characteristic of turbostratic graphite and likely a result of the low annealing temperatures and nitrogen

inclusions [93]. Annealed PAN and the carbon fiber control had the most densely packed graphite, and their (002) diffraction deconvoluted to two peaks instead of the one peak present in MA silk. The additional peak is the hybrid peak discussed in chapter 2.

Graphite in annealed PAN and the carbon fiber control shows a preferential alignment along the length of the fiber, unlike MA silk (Figs 3.20 f and 3.23). As the graphite in MA silk is randomly oriented, it scatters X-rays in a ring instead of a sharp arc [94]. This effect is quantified using Herman's orientation function, $f_c = \frac{3}{2}(< \cos^2 \phi > -1)$, where ϕ is the azimuthal angle and $< \cos^2 \phi >$ is the weighted average of $\cos^2 \phi$ based on the intensity (I) as a function of ϕ, $\frac{\int_0^{\pi/2} I(\phi) \sin \phi \cos^2 \phi}{\int_0^{\pi/2} I(\phi) \sin \phi}$ [94,95]. Annealed MA silk showed no preferred graphite orientation (Table 3.6, Fig 3.23), while the degree of alignment increased in PAN proportional to the annealing temperature, with the carbon fiber control as the highest. Horizontal scattering at 0.1-0.5 Å-1 in annealed PAN and carbon fiber is due to the graphite alignment (Fig 3.20 f, i), but the intensity of the circular scattering in annealed MA silk is so high that this feature cannot be observed if present. Previous studies have shown carbon fibers produce both types of scattering in the 0.1-0.5 Å-1 range [96,97].

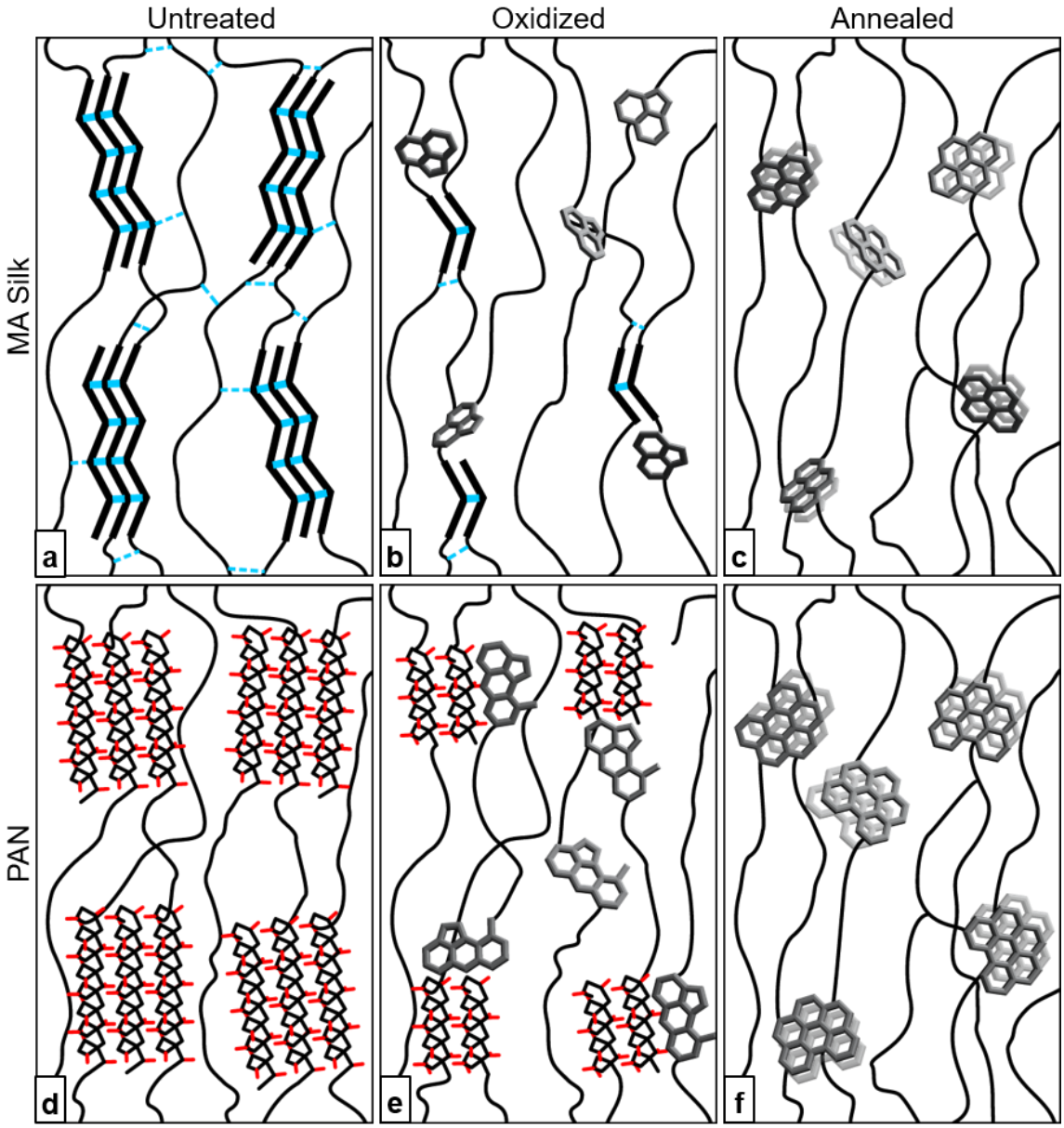

Figure 3.22: Schematic depicting graphite formation in annealed MA silk (a-c) and PAN (d-f). Polyalanine β-sheet nanocrystals and amorphous regions of MA silk are aligned through hydrogen bonding (a, dashed blue lines). PAN crystals contain neighboring chains aligned closely with the long axis with the fiber in either a planar zigzag or helical conformation (d). During oxidation, few, smaller polyalanine or PAN crystals remain while small, cyclized domains form (b, e). These are aligned in PAN but not in MA silk due to significantly reduced hydrogen bonding. After annealing at 600 ºC, graphite nanocrystals form, maintaining the alignment seen after oxidation (c, f).

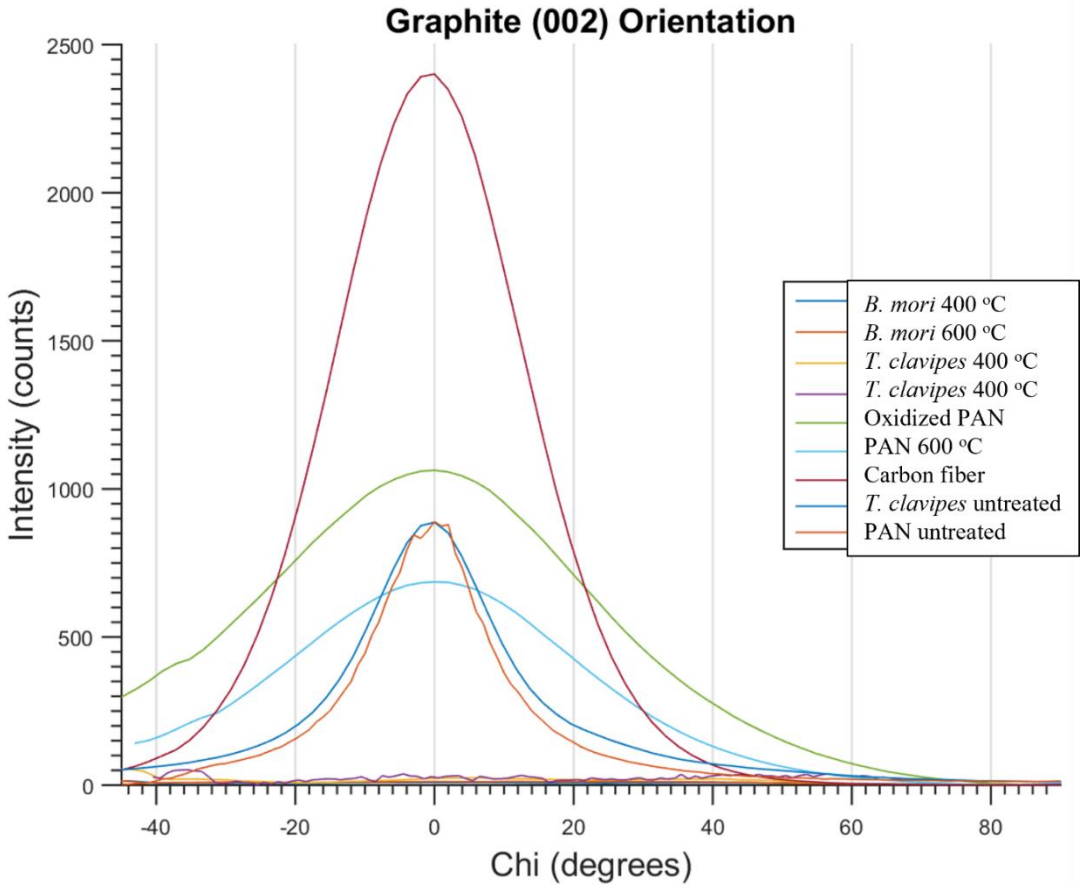

Figure 3.23: 600 °C annealed fibers, Oxidized PAN, and Carbon fiber plots represent graphite (002). PAN represents the (200). MA silk represents the (020) with some overlap from the (120). Scattering from the beamstop interfered with the orientation calculation from Oxidized silk, so are not reported here.

P.F. Herman originally defined his orientation parameter as $1 - \frac{3}{2} * \frac{\int_0^{\pi/2} I(\phi) \sin^3(\phi)}{\int_0^{\pi/2} I(\phi) \sin(\phi)}$, where ϕ is the angle between the plane in question and the fiber cross section. The modern representation replaces the integral with the shorthand $\langle \cos^2(\phi) \rangle$. If $\sin^3(\phi)$ is replaced with $\sin(\phi)*\cos^2(\phi)$ and the orientation function is multiplied by -1, ϕ becomes the angle between the plane in question and the vertical axis of the fiber, which is more useful when discussing the effect orientation has on other fiber properties. The

integration limits of 0 to $\pi/2$ are necessary due to the two perpendicular mirror planes present in diffraction patterns on radial detectors. Every real peak will be mirrored by 180^{o}. If the integral is evaluated over the entire detector (0 to 2π), the result will be 0 since the sin function will be positive from 0 to π and negative from π to 2π, which corresponds with the symmetry of $I(\phi)$. Integrating from 0 to π will yield twice the result as from 0 to $\pi/2$ due to the second mirror plane, which arises from the symmetric nature of the distribution functions. Since the orientation function contains the quotient of two integrals, the factor of two obtained by integrating from 0 to π will cancel.

Practically, the real data will have noise that interferes with the symmetry. This effect is insignificant given a good signal-to-noise ratio, and $I(\phi)$ can be modeled with various distribution functions, such as Gaussian, Pearson, or Lorentzian [94]. In Herman's time, these integrals were evaluated graphically. Now, they can be evaluated discretely or approximated as a Taylor series, with $I(\phi)$ as $\exp(-x^2)$. Certain publications have further approximated $\langle\cos^2(\phi)\rangle$ as a function of the full width at half maximum (FWHM) of the distribution function used to model $I(\phi)$, however these approximations do not hold true for all values of the FWHM [14,48,98,99]. Values reported from the FWHM approximations are significantly higher than those discretely evaluated from the integral form of $\langle\cos^2(\phi)\rangle$ [6,95]. Particularly in the cases of older data evaluated graphically, this value is influenced by background subtraction, as the FWHM does not directly relate to the intensity in $I(\phi)$. Data with higher background scattering and thus a higher baseline will produce a lower Herman's parameter.

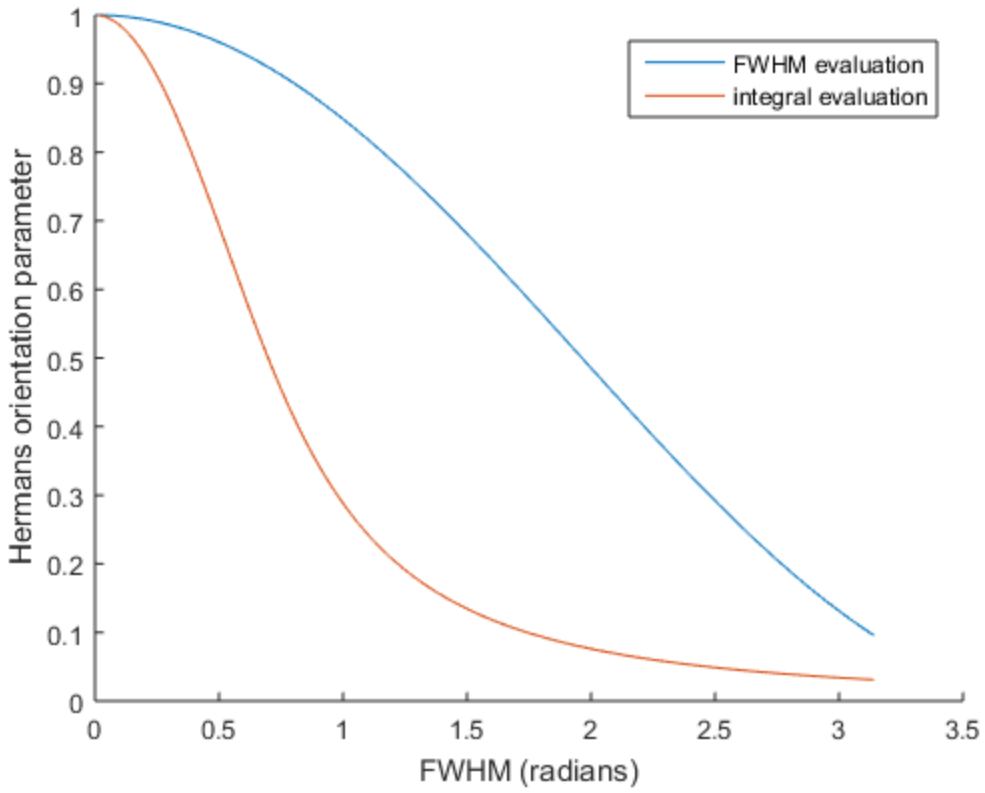

Figure 3.24: Calculation of Herman's orientation factor using his original equation or the FWHM method used in some spider silk literature

However, these data do not fully explain the observed discrepancy. Fig 3.24 compares these two methods analytically over an excessive range of FWHM (0 to π). In real data, the FWHM cannot be greater than π/2, given the symmetry constraints. In the FWHM evaluation, I(ϕ) is modeled as a simple Gaussian distribution of I(ϕ) = exp(-x^2/w^2), where w is the FWHM. $\langle\cos^2\phi\rangle$ is evaluated discretely (integral evaluation) or using the FWHM approximation, $\langle\cos^2(\phi)\rangle$ = cos(0.4*FWHM). The FWHM evaluation produces a significantly higher H_f, especially in the relevant range of 0 to π/2. The FWHM approximation can be altered by changing the factor of 0.4, but then the period of

$<\cos^2(\phi)>$ becomes less than π, which makes the function become illogical, as it would mean a broad peak can also correspond to high orientation, which is known to be false.

In the case that the orientation does not fit a distribution, the integral must be evaluated discretely using the collected data. Here, a background subtraction is often detrimental, as it gives the noise more weight when evaluating the integral and can lead to erroneous orientation factors. Given the linear nature of the intensity vs chi plot for the annealed silks, it was determined that Herman's parameter was 0. This fits with an integral evaluation of the data given a baseline correction where the lowest point of noise = 0.

3.4 Conclusions and Future Work

Uncovering the mechanism by which spiders fold MA spidroins into strong, tough silk fibers is a challenge. While polyalanine β-sheets do self-assemble into nanocrystals when MA dope dries in air or is electrospun, the subtle changes made to salt ion concentration, drying rate via % relative humidity, and shear did not significantly affect the molecular or crystal structure of the MA spidroins. Perhaps these factors are just byproducts of the real agents of change, like pH, or perhaps we didn't vary them drastically enough (e.g. shear). WAXS scattering is a useful tool to study silk crystallinity and, coupled with cryo-TEM, could give a better understanding of how the spidroin structure changes during silk spinning.

Although the polyalanine β-sheet nanocrystals in MA silk may be good templates for graphite formation, that alone is not sufficient to produce carbon fibers better than

PAN. A major contributing factor is the loss of crystal alignment upon oxidation and annealing. Hydrogen bonding plays a crucial role in maintaining spidroin and polyalanine alignment, which is disrupted with the loss of -OH groups and cyclization of the peptide nitrogen [18,19,48]. This bonding disrupts the secondary-quaternary structure of the spidroins and removes MA silk's primary load-bearing mechanism. Non-oriented polyalanine nanocrystals, even if they are cyclized to small graphitic domains, are unlikely to offer an appreciable resistance to tensile fracture.

For polymers, natural or otherwise, to produce carbon fiber of a similar quality as PAN, they cannot rely on hydrogen bonding for structural stability or contain a high mass fraction of oxygen, lest they shrink to an unusable extent. A direct pathway, without significant molecular rearrangement or combustion, to form graphite from existing crystals in the polymer is useful in maintaining alignment, as observed with PAN. Given sufficiently high temperatures, the graphite crystals in PAN can grow by accumulating amorphous parts of the polymer, while maintaining sufficient amorphous carbon to keep the fibers intact. One common strategy to create graphitic fibers is to include cyclic or aromatic structures into a precursor fiber, but this often leaves no mechanism for the fusion of separate polymer chains, likely limiting the overall extent of graphitization [100]. Polyalanine-like domains could be incorporated into block copolymers for biomimetic graphite precursors. However, careful attention must be paid to the graphitization mechanisms of the other blocks with intentional design to maximize the bonding between neighboring polymer chains and the eventual formation of graphite aligned along the fiber.

3.5 References

(1) Foelix, R. *Biology of Spiders*, 3rd ed.; Oxford University Press: New York, 2011.

(2) Lee, S. *Amazing Fantasy*; Marvel Comics, 1962; Vol. 15.

(3) White, E. B. *Charlotte's Web*; Harper & Brothers: New York, 1952.

(4) Tedford, H. W.; Sollod, B. L.; Maggio, F.; King, G. F. Australian Funnel-Web Spiders: Master Insecticide Chemists. *Toxicon* **2004**, *43* (5), 601–618. https://doi.org/10.1016/j.toxicon.2004.02.010.

(5) Correa-Garhwal, S. M.; Chaw, R. C.; Dugger, T.; Clarke, T. H.; Chea, K. H.; Kisailus, D.; Hayashi, C. Y. Semi-aquatic Spider Silks: Transcripts, Proteins, and Silk Fibres of the Fishing Spider, *Dolomedes Triton* (Pisauridae). *Insect Mol. Biol.* **2019**, *28* (1), 35–51. https://doi.org/10.1111/imb.12527.

(6) Dugger, T. W.; Sarkar, S.; Correa-Garhwal, S. M.; Zhernenkov, M.; Zhang, Y.; Kolhatkar, G.; Mohan, R.; Cruz, L.; Lubio, A. D.; Ruediger, A.; Hayashi, C. Y.; Uhrich, K. E.; Kisailus, D. J. Ultrastructures and Mechanics of Annealed *Nephila Clavipes* Major Ampullate Silk. *Biomacromolecules* **2020**, *21* (3), 1186–1194. https://doi.org/10.1021/acs.biomac.9b01615.

(7) Vollrath, F.; Knight, D. P. Liquid Crystalline Spinning of Spider Silk. *Nature* **2001**, *410* (6828), 541–548. https://doi.org/10.1038/35069000.

(8) Lewis, R. V. Spider Silk: Ancient Ideas for New Biomaterials. *Chem. Rev.* **2006**, *106* (9), 3762–3774. https://doi.org/10.1021/cr010194g.

(9) Babb, P. L.; Lahens, N. F.; Correa-Garhwal, S. M.; Nicholson, D. N.; Kim, E. J.; Hogenesch, J. B.; Kuntner, M.; Higgins, L.; Hayashi, C. Y.; Agnarsson, I.; Voight, B. F. The Nephila Clavipes Genome Highlights the Diversity of Spider Silk Genes and Their Complex Expression. *Nat. Genet.* **2017**, *49* (6), 895–903.

(10) Vollrath, F.; Porter, D. Spider Silk as Archetypal Protein Elastomer. *Soft Matter* **2006**, *2* (5), 377. https://doi.org/10.1039/b600098n.

(11) Gosline, J. M.; Guerette, P. A.; Ortlepp, C. S.; Savage, K. N. The Mechanical Design of Spider Silks: From Fibroin Sequence to Mechanical Function. *J. Exp. Biol.* **1999**, *202* (23), 3295–3303.

(12) Brown, C. P.; Whaite, A. D.; MacLeod, J. M.; Macdonald, J.; Rosei, F. With Great Structure Comes Great Functionality: Understanding and Emulating Spider Silk. *J. Mater. Res.* **2015**, *30* (1), 108–120. https://doi.org/10.1557/jmr.2014.365.

(13) Hijirida, D. H.; Do, K. G.; Michal, C.; Wong, S.; Zax, D.; Jelinski, L. W. 13C NMR of Nephila Clavipes Major Ampullate Silk Gland. *Biophys. J.* **1996**, *71* (6), 3442–3447. https://doi.org/10.1016/S0006-3495(96)79539-5.

(14) Xu, G.; Gong, L.; Yang, Z.; Liu, X. Y. What Makes Spider Silk Fibers Stronger: From Molecular-Crystallite Network to Hierarchical Structure. **2014**, 6.

(15) Chaw, R. C.; Correa-Garhwal, S. M.; Clarke, T. H.; Ayoub, N. A.; Hayashi, C. Y. Proteomic Evidence for Components of Spider Silk Synthesis from Black Widow Silk Glands and Fibers. *J. Proteome Res.* **2015**, *14* (10), 4223–4231. https://doi.org/10.1021/acs.jproteome.5b00353.

(16) Lombardi, S., J.; Kaplan, D. L. The Amino Acid Composition of Major Ampullate Gland Silk (Dragline) of Nephila Clavipes (Araneae, Tetragnathidae). *J. Arachnol.* **1990**, *18*, 297–306.

(17) Sponner, A.; Schlott, B.; Vollrath, F.; Unger, E.; Grosse, F.; Weisshart, K. Characterization of the Protein Components of *Nephila Clavipes* Dragline Silk †. *Biochemistry* **2005**, *44* (12), 4727–4736. https://doi.org/10.1021/bi047671k.

(18) Keten, S.; Buehler, M. J. Nanostructure and Molecular Mechanics of Spider Dragline Silk Protein Assemblies. *J. R. Soc. Interface* **2010**, *7* (53), 1709–1721. https://doi.org/10.1098/rsif.2010.0149.

(19) Keten, S.; Xu, Z.; Ihle, B.; Buehler, M. J. Nanoconfinement Controls Stiffness, Strength and Mechanical Toughness of β-Sheet Crystals in Silk. *Nat. Mater.* **2010**, *9* (4), 359–367. https://doi.org/10.1038/nmat2704.

(20) Simmons, A. H.; Michal, C. A.; Jelinski, L. W. Molecular Orientation and Two-Component Nature of the Crystalline Fraction of Spider Dragline Silk. *Science* **1996**, *271* (5245), 84–87. https://doi.org/10.2307/2890379.

(21) Creager, M. S.; Jenkins, J. E.; Thagard-Yeaman, L. A.; Brooks, A. E.; Jones, J. A.; Lewis, R. V.; Holland, G. P.; Yarger, J. L. Solid-State NMR Comparison of Various Spiders' Dragline Silk Fiber. *Biomacromolecules* **2010**, *11* (8), 2039–2043. https://doi.org/10.1021/bm100399x.

(22) Dong, Z.; Lewis, R. V.; Middaugh, C. R. Molecular Mechanism of Spider Silk Elasticity. *Arch. Biochem. Biophys.* **1991**, *284* (1), 53–57. https://doi.org/10.1016/0003-9861(91)90262-H.

(23) Lefèvre, T.; Paquet-Mercier, F.; Rioux-Dubé, J.-F.; Pézolet, M. Structure of Silk by Raman Spectromicroscopy: From the Spinning Glands to the Fibers. *Biopolymers* **2012**, *97* (6), 322–336. https://doi.org/10.1002/bip.21712.

(24) Hayashi, C. Y.; Shipley, N. H.; Lewis, R. V. Hypotheses That Correlate the Sequence, Structure, and Mechanical Properties of Spider Silk Proteins. *Int. J. Biol. Macromol.* **1999**, *24* (2–3), 271–275. https://doi.org/10.1016/S0141-8130(98)00089-0.

(25) Shao, Z.; Young, R. J.; Vollrath, F. The Effect of Solvents on Spider Silk Studied by Mechanical Testing and Single-Fibre Raman Spectroscopy. *Int. J. Biol. Macromol.* **1999**, *24* (2), 295–300.

(26) Guinea, G. V.; Elices, M.; Pérez-Rigueiro, J.; Plaza, G. Self-Tightening of Spider Silk Fibers Induced by Moisture. *Polymer* **2003**, *44* (19), 5785–5788. https://doi.org/10.1016/S0032-3861(03)00625-6.

(27) Elices, M.; Pérez-Rigueiro, J.; Plaza, G.; Guinea, G. V. Recovery in Spider Silk Fibers: Recovery in Spider Silk Fibers. *J. Appl. Polym. Sci.* **2004**, *92* (6), 3537–3541. https://doi.org/10.1002/app.20383.

(28) Guinea, G. V.; Elices, M.; Pérez-Rigueiro, J.; Plaza, G. R. Stretching of Supercontracted Fibers: A Link between Spinning and the Variability of Spider Silk. *J. Exp. Biol.* **2005**, *208* (1), 25–30. https://doi.org/10.1242/jeb.01344.

(29) Plaza, G. R.; Guinea, G. V.; Pérez-Rigueiro, J.; Elices, M. Thermo-Hygro-Mechanical Behavior of Spider Dragline Silk: Glassy and Rubbery States. *J. Polym. Sci. Part B Polym. Phys.* **2006**, *44* (6), 994–999. https://doi.org/10.1002/polb.20751.

(30) Vehoff, T.; Glišović, A.; Schollmeyer, H.; Zippelius, A.; Salditt, T. Mechanical Properties of Spider Dragline Silk: Humidity, Hysteresis, and Relaxation. *Biophys. J.* **2007**, *93* (12), 4425–4432. https://doi.org/10.1529/biophysj.106.099309.

(31) Blackledge, T. A.; Boutry, C.; Wong, S.-C.; Baji, A.; Dhinojwala, A.; Sahni, V.; Agnarsson, I. How Super Is Supercontraction? Persistent versus Cyclic Responses to Humidity in Spider Dragline Silk. *J. Exp. Biol.* **2009**, *212* (13), 1981–1989. https://doi.org/10.1242/jeb.028944.

(32) Ene, R.; Papadopoulos, P.; Kremer, F. Supercontraction in Nephila Spider Dragline Silk – Relaxation into Equilibrium State. *Polymer* **2011**, *52* (26), 6056–6060. https://doi.org/10.1016/j.polymer.2011.10.056.

(33) Boutry, C.; Blackledge, T. A. Wet Webs Work Better: Humidity, Supercontraction and the Performance of Spider Orb Webs. *J. Exp. Biol.* **2013**, *216* (19), 3606–3610. https://doi.org/10.1242/jeb.084236.

(34) Jones, J. A.; Harris, T. I.; Tucker, C. L.; Berg, K. R.; Christy, S. Y.; Day, B. A.; Gaztambide, D. A.; Needham, N. J. C.; Ruben, A. L.; Oliveira, P. F.; Decker, R. E.; Lewis, R. V. More Than Just Fibers: An Aqueous Method for the Production of

Innovative Recombinant Spider Silk Protein Materials. *Biomacromolecules* **2015**, *16* (4), 1418–1425. https://doi.org/10.1021/acs.biomac.5b00226.

(35) Jones, J.; Harris, T.; Oliveira, P.; Bell, B.; Alhabib, A.; Lewis, R. Importance of Heat and Pressure for Solubilization of Recombinant Spider Silk Proteins in Aqueous Solution. *Int. J. Mol. Sci.* **2016**, *17* (11), 1955. https://doi.org/10.3390/ijms17111955.

(36) Andersson, M.; Jia, Q.; Abella, A.; Lee, X.-Y.; Landreh, M.; Purhonen, P.; Hebert, H.; Tenje, M.; Robinson, C. V.; Meng, Q.; Plaza, G. R.; Johansson, J.; Rising, A. Biomimetic Spinning of Artificial Spider Silk from a Chimeric Minispidroin. *Nat. Chem. Biol.* **2017**, *13* (3), 262–264. https://doi.org/10.1038/nchembio.2269.

(37) Willcox, P. J.; Gido, S. P.; Muller, W.; Kaplan, D. L. Evidence of a Cholesteric Liquid Crystalline Phase in Natural Silk Spinning Processes. *Macromolecules* **1996**, *29* (15), 5106–5110. https://doi.org/10.1021/ma960588n.

(38) Vollrath, F.; Knight, D. P. Structure and Function of the Silk Production Pathway in the Spider Nephila Edulis. *Int. J. Biol. Macromol.* **1999**, *24* (2–3), 243–249. https://doi.org/10.1016/S0141-8130(98)00095-6.

(39) Knight, D. P.; Vollrath, F. Liquid Crystals and ¯ow Elongation in a Spider's Silk Production Line. **1999**, 6.

(40) Casem, M. L.; Tran, L. P. P.; Moore, A. M. F. Ultrastructure of the Major Ampullate Gland of the Black Widow Spider, Latrodectus Hesperus. *Tissue Cell* **2002**, *34* (6), 427–436. https://doi.org/10.1016/S0040816602000836.

(41) Kenney, J. M.; Knight, D.; Wise, M. J.; Vollrath, F. Amyloidogenic Nature of Spider Silk: Amyloidogenic Nature of Spider Silk. *Eur. J. Biochem.* **2002**, *269* (16), 4159–4163. https://doi.org/10.1046/j.1432-1033.2002.03112.x.

(42) Moon, M.; Tillinghast, E. K. Fine Structure of the Glandular Epithelium during Secretory Silk Production in the Black Widow Spider *Latrodectus Mactans*. *Korean J. Biol. Sci.* **2002**, *6* (4), 327–333. https://doi.org/10.1080/12265071.2002.9647672.

(43) Jin, H.-J.; Kaplan, D. L. Mechanism of Silk Processing in Insects and Spiders. *Nature* **2003**, *424* (6952), 1057–1061. https://doi.org/10.1038/nature01809.

(44) Moon, M.; Townley, M. A.; Tillinghast, E. K. Fine Structural Analysis of Secretory Silk Production in the Black Widow Spider, *Latrodectus Mactans*. *Korean J. Biol. Sci.* **1998**, *2* (1), 145–152. https://doi.org/10.1080/12265071.1998.9647401.

(45) Knight, D.; Vollrath, F. Hexagonal Columnar Liquid Crystal in the Cells Secreting Spider Silk. *Tissue Cell* **1999**, *31* (6), 617–620. https://doi.org/10.1054/tice.1999.0076.

(46) Trancik, J. E.; Czernuszka, J. T.; Bell, F. I.; Viney, C. Nanostructural Features of a Spider Dragline Silk as Revealed by Electron and X-Ray Diffraction Studies. *Polymer* **2006**, *47* (15), 5633–5642. https://doi.org/10.1016/j.polymer.2005.01.110.

(47) Glišović, A.; Salditt, T. Temperature Dependent Structure of Spider Silk by X-Ray Diffraction. *Appl. Phys. A* **2007**, *87* (1), 63–69. https://doi.org/10.1007/s00339-006-3849-9.

(48) Sampath, S.; Isdebski, T.; Jenkins, J. E.; Ayon, J. V.; Henning, R. W.; Orgel, J. P. R. O.; Antipoa, O.; Yarger, J. L. X-Ray Diffraction Study of Nanocrystalline and Amorphous Structure within Major and Minor Ampullate Dragline Spider Silks. *Soft Matter* **2012**, *8* (25), 6713. https://doi.org/10.1039/c2sm25373a.

(49) Sampath, S.; Yarger, Jeffery. L. Structural Hysteresis in Dragline Spider Silks Induced by Supercontraction: An X-Ray Fiber Micro-Diffraction Study. *RSC Adv* **2015**, *5* (2), 1462–1473. https://doi.org/10.1039/C4RA13936D.

(50) Knight, D. P.; Knight, M. M.; Vollrath, F. Beta Transition and Stress-Induced Phase Separation in the Spinning of Spider Dragline Silk. *Int. J. Biol. Macromol.* **2000**, *27* (3), 205–210. https://doi.org/10.1016/S0141-8130(00)00124-0.

(51) Knight, D.; Vollrath, F. Changes in Element Composition along the Spinning Duct in a Nephila Spider. *Naturwissenschaften* **2001**, *88* (4), 179–182. https://doi.org/10.1007/s001140100220.

(52) Dicko, C.; Kenney, J. M.; Knight, D.; Vollrath, F. Transition to a β-Sheet-Rich Structure in Spidroin in Vitro: The Effects of PH and Cations †. *Biochemistry* **2004**, *43* (44), 14080–14087. https://doi.org/10.1021/bi0483413.

(53) Wang, X.; Zhao, P.; Li, Y.; Yi, Q.; Ma, S.; Xie, K.; Chen, H.; Xia, Q. Modifying the Mechanical Properties of Silk Fiber by Genetically Disrupting the Ionic Environment for Silk Formation. *Biomacromolecules* **2015**, *16* (10), 3119–3125. https://doi.org/10.1021/acs.biomac.5b00724.

(54) Xu, D.; Guo, C.; Holland, G. P. Probing the Impact of Acidification on Spider Silk Assembly Kinetics. *Biomacromolecules* **2015**, *16* (7), 2072–2079. https://doi.org/10.1021/acs.biomac.5b00487.

(55) Vollrath, F.; Knight, D. P.; Hu, X. W. Silk Production in a Spider Involves Acid Bath Treatment. *Proc. R. Soc. Lond. B Biol. Sci.* **1998**, *265* (1398), 817–820. https://doi.org/10.1098/rspb.1998.0365.

(56) Jin, H.-J.; Fridrikh, S. V.; Rutledge, G. C.; Kaplan, D. L. Electrospinning *Bombyx Mori* Silk with Poly(Ethylene Oxide). *Biomacromolecules* **2002**, *3* (6), 1233–1239. https://doi.org/10.1021/bm025581u.

(57) Stephens, J. S.; Fahnestock, S. R.; Farmer, R. S.; Kiick, K. L.; Chase, D. B.; Rabolt, J. F. Effects of Electrospinning and Solution Casting Protocols on the Secondary Structure of a Genetically Engineered Dragline Spider Silk Analogue Investigated via Fourier Transform Raman Spectroscopy. *Biomacromolecules* **2005**, *6* (3), 1405–1413. https://doi.org/10.1021/bm049296h.

(58) Zhou, S.; Peng, H.; Yu, X.; Zheng, X.; Cui, W.; Zhang, Z.; Li, X.; Wang, J.; Weng, J.; Jia, W.; Li, F. Preparation and Characterization of a Novel Electrospun Spider Silk Fibroin/Poly(D , L -Lactide) Composite Fiber. *J. Phys. Chem. B* **2008**, *112* (36), 11209–11216. https://doi.org/10.1021/jp800913k.

(59) Zhang, F.; Zuo, B.; Fan, Z.; Xie, Z.; Lu, Q.; Zhang, X.; Kaplan, D. L. Mechanisms and Control of Silk-Based Electrospinning. *Biomacromolecules* **2012**, *13* (3), 798–804. https://doi.org/10.1021/bm201719s.

(60) Blackledge, T. A.; Cardullo, R. A.; Hayashi, C. Y. Polarized Light Microscopy, Variability in Spider Silk Diameters, and the Mechanical Characterization of Spider Silk: Polarized Light Microscopy of Spider Silk. *Invertebr. Biol.* **2005**, *124* (2), 165–173. https://doi.org/10.1111/j.1744-7410.2005.00016.x.

(61) Ortlepp, C. S.; Gosline, J. M. Consequences of Forced Silking. *Biomacromolecules* **2004**, *5* (3), 727–731. https://doi.org/10.1021/bm034269x.

(62) Agnarsson, I.; Boutry, C.; Blackledge, T. A. Spider Silk Aging: Initial Improvement in a High Performance Material Followed by Slow Degradation. *J. Exp. Zool. Part Ecol. Genet. Physiol.* **2008**, *309A* (8), 494–504. https://doi.org/10.1002/jez.480.

(63) Hexemer, A.; Bras, W.; Glossinger, J.; Schaible, E.; Gann, E.; Kirian, R.; MacDowell, A.; Church, M.; Rude, B.; Padmore, H. A SAXS/WAXS/GISAXS Beamline with Multilayer Monochromator. *J. Phys. Conf. Ser.* **2010**, *247*, 012007. https://doi.org/10.1088/1742-6596/247/1/012007.

(64) Zhernenkov, Mikhail. Soft Matter Interfaces Beamline at NSLS-II: Geometrical Ray-Tracing vs. Wavefront Propagation Simulations. In *Advances in Computational Methods for X-Ray Optics III*; Sanchez del Rio, M., Chubar, O., Eds.; 2014; Vol. 9209.

(65) Rahaman, M. S. A.; Ismail, A. F.; Mustafa, A. A Review of Heat Treatment on Polyacrylonitrile Fiber. *Polym. Degrad. Stab.* **2007**, *92* (8), 1421–1432. https://doi.org/10.1016/j.polymdegradstab.2007.03.023.

(66) Park, S.-J.; Heo, G.-Y. Precursors and Manufacturing of Carbon Fibers. In *Carbon Fibers*; Springer Netherlands: Dordrecht, 2015; Vol. 210, pp 31–66. https://doi.org/10.1007/978-94-017-9478-7_2.

(67) Zhao, J.; Zhang, J.; Zhou, T.; Liu, X.; Yuan, Q.; Zhang, A. New Understanding on the Reaction Pathways of the Polyacrylonitrile Copolymer Fiber Pre-Oxidation: Online Tracking by Two-Dimensional Correlation FTIR Spectroscopy. *RSC Adv.* **2016**, *6* (6), 4397–4409. https://doi.org/10.1039/C5RA24320C.

(68) Cipriani, E.; Zanetti, M.; Bracco, P.; Brunella, V.; Luda, M. P.; Costa, L. Crosslinking and Carbonization Processes in PAN Films and Nanofibers. *Polym. Degrad. Stab.* **2016**, *123*, 178–188.

(69) Merlen, A.; Buijnsters, J.; Pardanaud, C. A Guide to and Review of the Use of Multiwavelength Raman Spectroscopy for Characterizing Defective Aromatic Carbon Solids: From Graphene to Amorphous Carbons. *Coatings* **2017**, *7* (10), 153. https://doi.org/10.3390/coatings7100153.

(70) Tuinstra, F.; Koenig, J. L. Raman Spectrum of Graphite. *J. Chem. Phys.* **1970**, *53* (3), 1126–1130. https://doi.org/10.1063/1.1674108.

(71) Knight, D. S.; White, W. B. Characterization of Diamond Films by Raman Spectroscopy. *J. Mater. Res.* **1989**, *4* (2), 385–393. https://doi.org/10.1557/JMR.1989.0385.

(72) Ferrari, A. C. Raman Spectroscopy of Graphene and Graphite: Disorder, Electron–Phonon Coupling, Doping and Nonadiabatic Effects. *Solid State Commun.* **2007**, *143* (1–2), 47–57.

(73) Fitzer, E. Pan-Based Carbon Fibers—Present State and Trend of the Technology from the Viewpoint of Possibilities and Limits to Influence and to Control the Fiber Properties by the Process Parameters. *Carbon* **1989**, *27* (5), 621–645.

(74) Jones, B.; Duncan, R. The Effect of Fibre Diameter on the Mechanical Properties of Graphite Fibres Manufactured from Polyacrylonitrile and Rayon. *J. Mater. Sci.* **1971**, *6*, 289–293.

(75) Faber, K. T.; Evans, A. G. Crack Deflection Processes—I. Theory. *Acta Metall.* **1983**, *31* (4), 565–576.

(76) Faber, K. T.; Evans, A. G. Crack Deflection Processes—II. Experiment. *Acta Metall.* **1983**, *31* (4), 577–584.

(77) Vollrath, F.; Holtet, T.; Thogersen, H. C.; Frische, S. Structural Organization of Spider Silk. In *Proceedings: Biological Sciences*; The Royal Society, 1996; Vol. 263, pp 147–151.

(78) Sponner, A.; Vater, W.; Monajembashi, S.; Unger, E.; Grosse, F.; Weisshart, K. Composition and Hierarchical Organisation of a Spider Silk. *PLoS ONE* **2007**, *2* (10), e998. https://doi.org/10.1371/journal.pone.0000998.

(79) Rising, A.; Nimmervoll, H.; Grip, S.; Fernandez-Arias, A.; Storckenfeldt, E.; Knight, D. P.; Vollrath, F.; Engström, W. Spider Silk Proteins – Mechanical Property and Gene Sequence. *Zoolog. Sci.* **2005**, *22* (3), 273–281. https://doi.org/10.2108/zsj.22.273.

(80) Brooks, A. Distinct Contributions of Model MaSp1 and MaSp2 like Peptides to the Mechanical Properties of Synthetic Major Ampullate Silk Fibers as Revealed in Silico. *Nanotechnol. Sci. Appl.* **2008**, *Volume 1*, 9–16. https://doi.org/10.2147/NSA.S3961.

(81) Tokareva, O.; Michalczechen-Lacerda, V. A.; Rech, E. L.; Kaplan, D. L. Recombinant DNA Production of Spider Silk Proteins: Recombinant Spider Silks. *Microb. Biotechnol.* **2013**, *6* (6), 651–663. https://doi.org/10.1111/1751-7915.12081.

(82) Cho, S. Y.; Yun, Y. S.; Lee, S.; Jang, D.; Park, K.-Y.; Kim, J. K.; Kim, B. H.; Kang, K.; Kaplan, D. L.; Jin, H.-J. Carbonization of a Stable β-Sheet-Rich Silk Protein into a Pseudographitic Pyroprotein. *Nat. Commun.* **2015**, *6* (1). https://doi.org/10.1038/ncomms8145.

(83) Matthews, M. J.; Pimenta, M. A.; Dresselhaus, G.; Dresselhaus, M. S.; Endo, M. Origin of Dispersive Effects of the Raman ***D*** Band in Carbon Materials. *Phys. Rev. B* **1999**, *59* (10), R6585–R6588. https://doi.org/10.1103/PhysRevB.59.R6585.

(84) Chu, P. K.; Li, L. Characterization of Amorphous and Nanocrystalline Carbon Films. *Mater. Chem. Phys.* **2006**, *96* (2–3), 253–277.

(85) Ferrari, A. C.; Robertson, J. Interpretation of Raman Spectra of Disordered and Amorphous Carbon. *Phys. Rev. B* **2000**, *61* (20), 14095–14107.

(86) Zickler, G. A.; Smarsly, B.; Gierlinger, N.; Peterlik, H.; Paris, O. A Reconsideration of the Relationship between the Crystallite Size La of Carbons Determined by X-Ray Diffraction and Raman Spectroscopy. *Carbon* **2006**, *44* (15), 3239–3246. https://doi.org/10.1016/j.carbon.2006.06.029.

(87) Langford, J. I.; Wilson, A. J. C. Scherrer after Sixty Years: A Survey and Some New Results in the Determination of Crystallite Size. *J. Appl. Crystallogr.* 12.

(88) Tsai, J.-S. Effect of Drawing Ratio during Spinning and Oxidation on the Properties of Polyacrylonitrile Precursor and Resulting Carbon Fibre. *J. Mater. Sci. Lett.* **1992**, *11* (3), 140–142. https://doi.org/10.1007/BF00724670.

(89) Colvin, B. G.; Storr, P. The Crystal Structure of Polyacrylonitrile. *Eur. Polym. J.* **1974**, *10* (4), 337–340.

(90) Stéfani, R.; Chevreton, M.; Garnier, M.; Eyraud, C. Les Structures Cristallines Du Polyacrylonitrile. In *Comptes rendus Hebdomadaires des Séances de l'Académie des Sciences*; Académie des Sciences, 1960; Vol. 251, pp 2174–2176.

(91) Bohn, C. R.; Schaefgen, J. R.; Statton, W. O. Laterally Ordered Polymers: Polyacrylonitrile and Poly(Vinyl Trifluoroacetate). *J. Polym. Sci.* **1961**, *55* (162), 531–549.

(92) Karbownik, I.; Fiedot, M.; Rac, O.; Suchorska-Woźniak, P.; Rybicki, T.; Teterycz, H. Effect of Doping Polyacrylonitrile Fibers on Their Structural and Mechanical Properties. *Polymer* **2015**, *75*, 97–108. https://doi.org/10.1016/j.polymer.2015.08.015.

(93) Li, Z. Q.; Lu, C. J.; Xia, Z. P.; Zhou, Y.; Luo, Z. X-Ray Diffraction Patterns of Graphite and Turbostratic Carbon. *Carbon* **2007**, *45* (8), 1686–1695. https://doi.org/10.1016/j.carbon.2007.03.038.

(94) Alexander, L. *X-Ray Diffractio Methods in Polymer Science*; John Wiley & Sons, Inc.: New York, 1969.

(95) Hermans, P. H. *Contribution to the Physics of Cellulose Fibers*; Elsevier Publishing Company, INC: Amsterdam, 1946.

(96) Tang, M.; Rice, G. G.; Fellers, J. F.; Lin, J. S. X-ray Scattering Studies of Graphite Fibers. *J. Appl. Phys.* **1986**, *60* (2), 803–810. https://doi.org/10.1063/1.337378.

(97) Gupta, A.; Harrison, I. R.; Lahijani, J. Small-Angle X-Ray Scattering in Carbon Fibers. *J. Appl. Crystallogr.* **1994**, *27* (4), 627–636. https://doi.org/10.1107/S002188989400227X.

(98) Grubb, D. T.; Jelinski, L. W. Fiber Morphology of Spider Silk: The Effects of Tensile Deformation. *Macromolecules* **1997**, *30* (10), 2860–2867. https://doi.org/10.1021/ma961293c.

(99) Li, X.; Meng, L.; Lin, Y.; Chen, X.; Zhang, Q.; Zhang, R.; Wu, L.; Zhang, W.; Li, L. Preparation of Highly Oriented Polyethylene Precursor Film with Fibril and Its Influence on Microporous Membrane Formation. *Macromol. Chem. Phys.* **2016**, *217* (8), 974–986. https://doi.org/10.1002/macp.201500471.

(100) Souto, F.; Calado, V.; Pereira, N. Lignin-Based Carbon Fiber: A Current Overview. *Mater. Res. Express* **2018**, *5* (7), 072001. https://doi.org/10.1088/2053-1591/aaba00.

Chapter 4: Salicylic Acid-based Poly(Anhydride Esters) (SAPAEs) with Controllable Degradation Rates

4.1 Introduction

Salicylic Acid (SA) is naturally occurring in willow tree bark and many other plants. It is the main metabolic product of aspirin [1], a non-steroidal anti-inflammatory drug and painkiller [2], and also used in skin care products [3]. Its alcohol and carboxyl functional groups are readily conjugatable, allowing it to be modified or incorporated into macromolecules, like SAPAEs [4,5]. These polymers combine SA with biocompatible "linker" molecules (Scheme 4.1) via ester bonds to form a "diacid." Adipic acid was primarily used as a linker for adipic SAPAE (SAA), but other linkers were substituted depending on the application [4]. Condensation polymerization couples these diacids by anhydride linkages to form poly(anhydride-esters), which are biodegradable as water hydrolyzes the anhydride and ester bonds (Scheme 4.1).

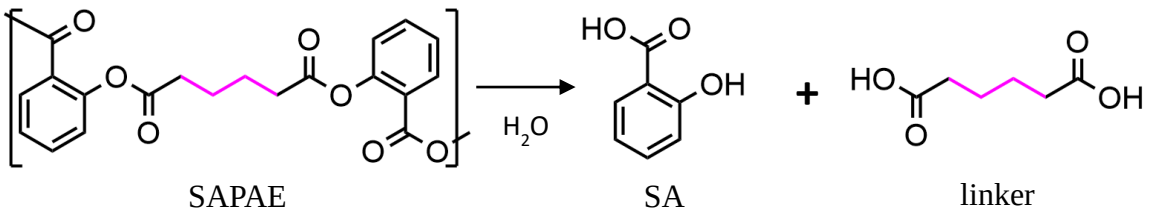

Scheme 4.1: SAPAE hydrolytically degrades into biocompatible salicylic acid (SA) and linker molecules through anhydride and ester bond hydrolysis, respectively. In this case, the adipic acid linker is released from adipic SAPAE (SAA). The pink linker segment can be modified to change the polymer properties, in particular degradation rate.

SAPAEs are useful for biomedical applications since the bioactive SA is incorporated at a high loading and gradually released over a controllable time frame. This delivers anti-inflammatory SA to a wound, surgical site, or other inflamed or infected area over time necessary to promote healing [6,7]. *In vivo* studies have shown that SAPAEs can successfully coat stents, function as dental implants in treating periodontal disease, prevent bacterial and biofilm buildup, and promote bone regeneration [6–10]. In this chapter, a new application of SAPAE is explored for coating Magnesium (Mg) implants for bone regeneration. Mg has similar mechanical properties to bone and degrades over time, eliminating the need for a second surgery to remove the implant [11]. However, it often degrades too quickly, so researchers are investigating polymer coatings to slow this degradation [11,12]. An SAPAE coating has the added benefit of releasing anti-inflammatory SA at the implant site to mitigate inflammation from the surgery. SAPAE can also be processed into microspheres to encapsulate other bioactives such as insulin to further promote bone regeneration.

SAPAE degradation rate depends on the polymer's M_w and structure. More hydrophilic linkers accelerate degradation, while more hydrophobic, aromatic, and branched linkers slow degradation [4,13–17]. Alternately, copolymerizing differing monomers expands the range of SAPAEs degradation behavior. In this chapter, the parameters affecting the polymerization process to better control molecular weight are investigated and a process to form microspheres and encapsulate bioactives is evaluated. Previous studies on insulin encapsulation focused on only one SAPAE polymer [18,19]; the previous work was expanded to evaluate microspheres created from various SAPAEs and

used to encapsulate the well-studied protein Bovine Serum Albumin (BSA). In another project, thin SAPAE films were spin-coated onto Mg substrates to study their effectiveness as a protective coating for bone implants.

4.2 SAPAE Synthesis

4.2.1 Materials and Characterization Methods

The following chemicals were used for SAPAE synthesis and characterization: salicylic acid (>99%, Millipore-Sigma), adipoyl chloride (>98%, TCI), tetrahydrofuran (>99.9%, Millipore-Sigma), pyridine (>99.8%, Millipore-Sigma), deionized water, hydrochloric acid (37-38% in water, Fisher), acetone (>99.5%, Fisher), acetic anhydride (>99%, Fisher), dichloromethane (DCM, >99.8%, Millipore-Sigma), deuterated chloroform (99.8%, Cambridge Isotope Labs), deuterated dimethylsulfoxide (99.5% deuterated, Millipore-Sigma), diethyl ether (>99%, Fisher), methyl ethyl ketone (MEK 99%, Fisher). The chemicals listed above are used for all future sections in this chapter unless otherwise noted.

SAPAE and its precursors were characterized using NMR (Bruker Avance 300), GPC (Tosoh EcoSec, Tokyo, Japan, TSKgel GMH_{HR}-N polymer bead sample column, TSKgel SuperH-RC reference column, 0.6 mL/min elution rate), TGA (Netzsch TGA 209 F1 Libra), and thin layer chromatography (TLC, Silica gel 60 F_{254}, Merck). Concentrations of 5-20 mg/mL were used for NMR and GPC, the NMR shift was adjusted to the solvent reference peak, polystyrene standards with a M_w range of 266-427,000 kDa to were used to create a GPC calibration curve, and Tosoh's ECOSec

software was used to identify peak positions and determine M_w and PDI. Sample masses for TGA were around 15 mg.

4.2.2 Diacid Synthesis

Diacid purity and water content had a significant effect on the SAPAE synthesis. Diacids were synthesized using previously published procedures [4] by Erica Burnham and Dr. Shuang Song (Scheme 4.2). Their purity was assessed with ^{1}H NMR spectroscopy and TLC. Water was the most abundant impurity as well as a small amount of SA. The presence of water is unavoidable, as the diacid is washed with acidic water to remove solvents and unreacted adipic acid or adipoyl chloride.

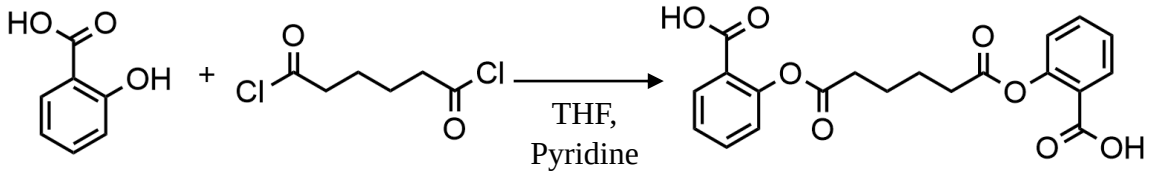

SA Adipoyl Chloride Adipic Diacid

Scheme 4.2: Adipic diacid synthesis

SA can be removed using acetone through a "recrystallization" process, as it is more soluble in acetone than the diacid, so the best way to remove excess SA is to suspend the diacid in acetone at 50 g/L, stir for 10 minutes, filter to collect the purified diacid, and then repeat the process if needed. It is possible to dissolve the diacid in acetone at concentrations under 10 g/L, then precipitate in hexanes > 5x the volume of acetone but this process is less desirable because of the large amount of solvent used. Recrystallization also removes much of the excess water present in the diacid. Additional measures were taken to decrease the amount of water present, such as using anhydrous

solvents, baking glassware at 110 ^{o}C, and drying glassware in a vacuum desiccator before use. Diacids were stored in sealed containers in a desiccator.

4.2.3 Monomer isolation

The first step in polymerizing SAPAE is to acetylate the diacid (scheme 4.3), through an "anhydride exchange [4]." This reaction is achieved by dissolving the diacid in excess acetic anhydride (concentrations < 6 mL/g) and heating to reflux temperatures > 80 ^{o}C while stirring at > 500 rpm. The diacid generally dissolved within 15 minutes after the oil bath reached 80 ^{o}C. It dissolved more quickly at higher temperatures and lower concentrations. Once the majority of the diacid dissolved, it was left to stir for 15 minutes to ensure it completely dissolved, and was then removed from the oil bath to cool for 30 minutes.

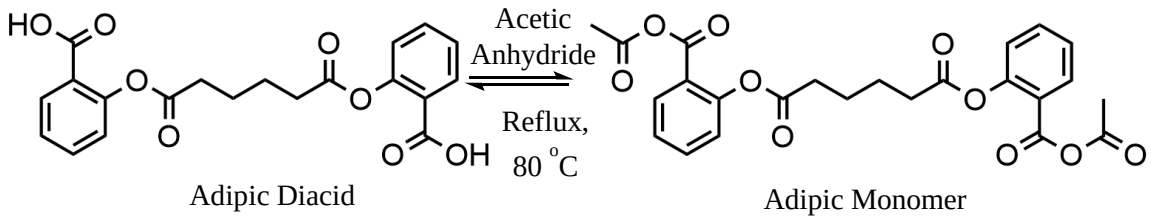

Scheme 4.3: Anhydride exchange process to synthesize the adipic monomer. After the monomer was acetylated, excess acetic anhydride was removed by vacuum distillation at 50-70 ^{o}C.

The second step is removing excess acetic anhydride via vacuum distillation, stirring at > 500 rpm, to isolate the SAPAE monomer. This process was done to collect as much acetic anhydride by distillation before polymerization and can use the same glassware as the anhydride exchange to minimize exposure to airborne water vapor. Both the polymerization and distillation setups used a Schlenk line and cold trap to prevent

acetic acid or acetic anhydride vapor from getting to the vacuum pump, but it is best to capture as much acid as possible through distillation to reduce the risk of corroding the vacuum pump. The monomer/acetic anhydride solution was cooled to 30-50 ^{o}C before distillation. If the solution was warmer than 50 ^{o}C, it bubbled vigorously after the vacuum pump was turned on. This process left monomer stuck to the sides of the round-bottomed flask or drawn into the Schlenk line, decreasing the polymer yield. Vacuum distillation was performed for at least 30 minutes at 50 ^{o}C under constant stirring > 500 rpm, leaving the gray, paste-like monomer for materials synthesized at scales < 5 g. After distillation for a certain time, enough acetic anhydride was removed from the system for the monomers to form stable oligomers and polymerize.

4.2.4 Polymerization

Melt condensation polymerization was performed at 160-180 ^{o}C (Scheme 4.4) and conditions varied depending on the desired polymer M_w [4]. Polymerization can be done using an overhead stirrer or in the same glassware as vacuum distillation, though there is a viscosity limit at which point a magnetic stir bar can no longer stir the molten polymer [20]. The main process parameters were temperature, vacuum conditions, time, and ambient humidity. The optimal process parameters vary depending on the diacid purity. Vacuum was measured with a simple vacuum gauge in -in Hg, and it **must** be < 29 -in Hg (25 torr). Other protocols suggest 2 Torr, and although vacuum pumps are rated to < 1 Torr, only a vacuum of 10 Torr was practically achieved regardless of the glassware setup. If the vacuum pump is not working sufficiently, several solutions are offered: replace the pump oil (should be done monthly), tighten the fittings for the overhead

stirrer using pliers, grease the fittings and stir shaft, or adjust the height of the stir shaft so there the reaction flask remains stationary during stirring. Temperature and time are set parameters for each polymerization for specific quantities of monomers.

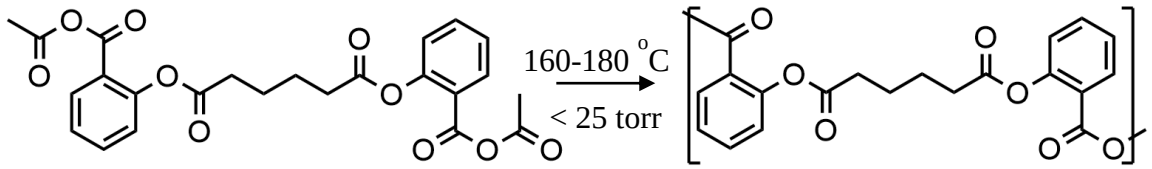

Adipic Monomer SAA

Scheme 4.4: SAA melt polymerization

The presence of water hydrolyzes the monomer or polymer chain ends, rendering them unreactive (Scheme 4.3); thus, less water means a higher maximum M_w. Water can interfere with the anhydride exchange and distillation steps as well, but since acetylation occurs in equilibrium with an excess of acetic anhydride, the equilibrium is driven towards forming more monomer than diacid. However, acetic anhydride is not in significant excess after vacuum distillation, so if any monomer or polymer is hydrolyzed, it is less likely to be re-acetylated. The polymerization temperature is hot enough to boil acetic acid, water, and acetic anhydride from the reaction mixture. Through multiple polymerizations, the effects of different parameters have been cataloged on the M_w and polymer purity. The optimal parameters depend on the diacid purity, vacuum, and desired M_w and are discussed later.

4.2.5 Purification

After polymerization was complete, the resulting solid was cooled to room temperature, then dissolved, stirring at > 500 rpm, in anhydrous DCM at 0.5 g/mL. This

process can take up to 30 minutes. Once dissolved, the solution was poured over excess diethyl ether in a beaker (40x the DCM volume, stirring at > 500 rpm) to precipitate the polymer. High M_w polymer was tan in color and either settled to the bottom of the ether or aggregated but remained floating. Low M_w polymer and other impurities were either soluble or precipitated as a white solid floating in the ether. The excess ether and as much of the white solids as possible were decanted, leaving the high M_w polymer in the beaker. The polymer was transferred to a vacuum desiccator to dry overnight at < -29 in Hg. The majority of the ether and DCM evaporated quickly, and often the polymer expanded into a foam. The resulting product was white to light tan and stored in sealed containers, covered with parafilm, and double-bagged with desiccant in a -20-30 ^oC freezer. Additional notes on SAPAE synthesis are found in Appendix A.

4.2.6 Characterization During Polymer Synthesis

4.2.6.1 Diacid

NMR spectroscopy was performed on each diacid batch to assess purity and water content. Water content was calculated from the integral ratio of one aromatic diacid peak to the water peak, corrected for the amount of water in a negative control of the solvent alone as follows:

$$\left(\frac{I_w,diacid\ sample}{I_s,diacid\ sample} - \frac{I_w,solvent\ alone}{I_s,solvent\ alone}\right) * I_s, diacid\ sample$$

I_w and I_s are the integration of the water and solvent peaks, respectively. TGA was performed on glycolic (used for faster degrading polymer) and adipic diacids in air with a 2.5 ^oC/min ramp and inert atmosphere in an attempt to determine heating temperatures to

remove water (Fig 4.1). The glycolic diacid lost mass around 80 °C, which could be solvent evaporation but is below the boiling point of water. Both diacids began to degrade at 145 °C. Thus, while the glycolic diacid (structure shown in Fig 1) can be heated to remove solvent, the adipic diacid (structure shown in Fig 1) cannot.

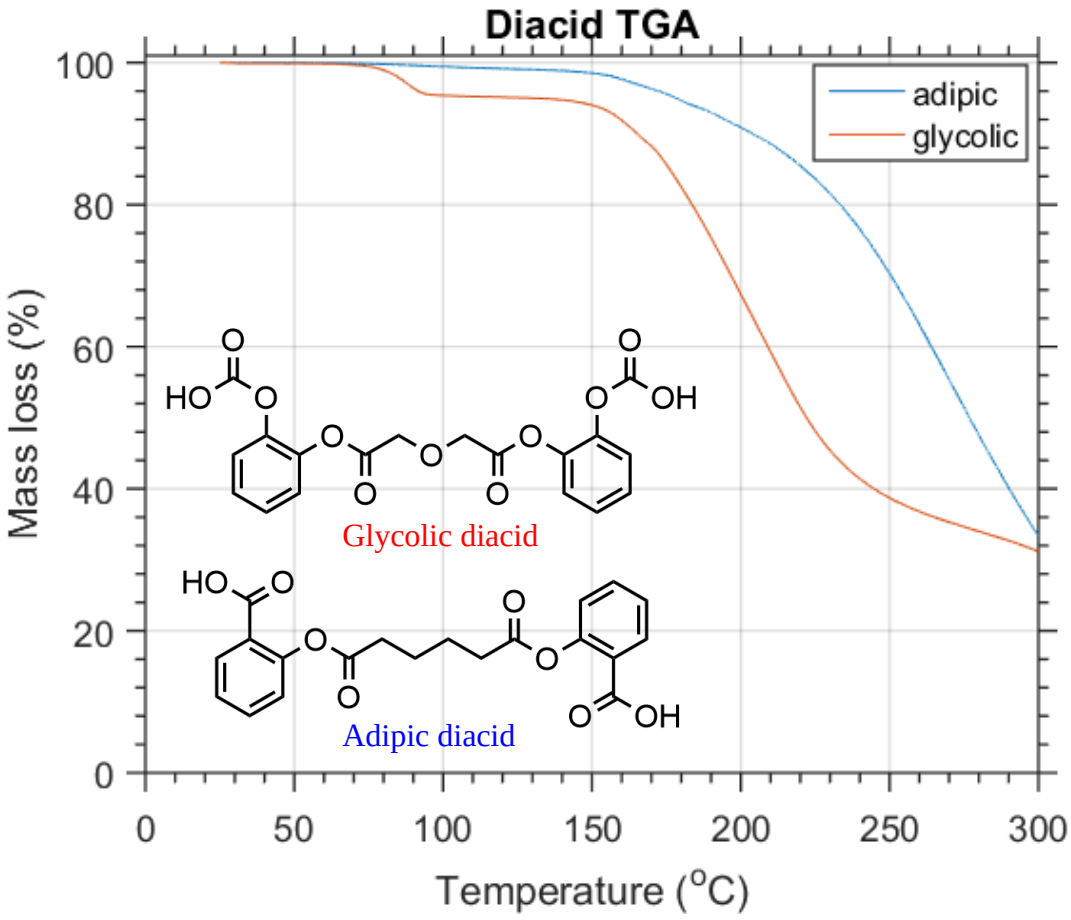

Figure 4.1: TGA of adipic and glycolic diacids. Both begin to degrade at 145 °C, while the glycolic has an additional mass loss around 80 °C that could be the release of bound volatiles.

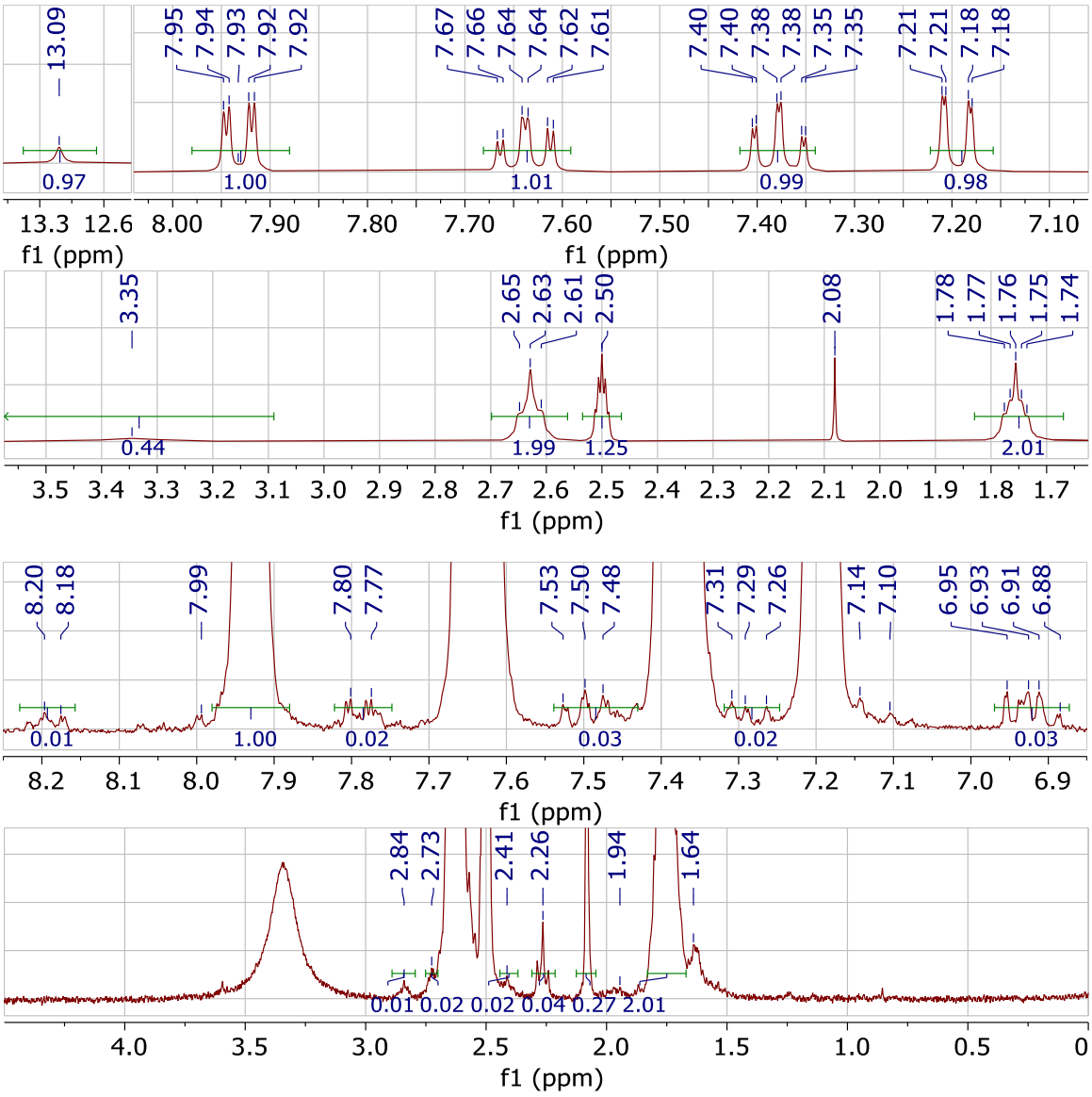

Figure 4.2: ^{1}H-NMR spectra in DMSO-d_6 of adipic diacid EBTD 2-13-21 showing major peaks (top two panels) and common impurities (bottom two panels).

Using the diacid batch (prepared by Erica Burnham, EBTD 2-13-21) as an example, the adipic diacid has the following ^{1}H NMR peaks in DMSO-d_6: δ = 13.09 (b, 2H), δ = 7.93 (dd, 2H), δ =7.64 (td 2H), δ =7.38 (td 2H), δ = 7.20 (dd 2H), δ = 2.63 (t 4H), δ = 1.76 (tt 4H) (Figure 4.2). Water (δ = 3.35) and acetone (δ = 2.08) are the most

abundant impurities. Although no SA was visible using TLC, there are residual SA peaks at δ = 7.8, 7.5 (both 1H), and 6.9 (2H). There are similarly small aromatic impurity peaks at δ = 8.2, 7.48, 7.3, and possibly 7.2. This impurity could also have peaks overlapping with SA. The 8.2 peak is close to the theoretical 8.1 and 8.15 peaks from the SAA monomer and polymer, respectively, but it its unlikely an anhydride bond formed during diacid synthesis. The impurities at δ = 1.64 and 2.25 match the shifts of cyclohexanone ($C_6H_{10}O$), which is a feasible side product of the diacid synthesis. The 2.25 peak could also be residual adipic acid, although the shift is 0.05 ppm too high. Additional impurities at δ = 1.94, 2.41, 2.73, 2.84 have shifts similar to acetic acid, MEK, and dimethylformamide (DMF), respectively (2.73 and 2.84 are DMF) but the solvents MEK and DMF were not used in either the reaction or work-up.

4.2.6.2 Monomer

To troubleshoot and better understand the polymerization process, the monomer was sampled during the anhydride exchange and after vacuum distillation. All diacids used had similar impurities and amounts as the test sample (EBTD 2-13-21). After the diacid dissolved in acetic anhydride during the anhydride exchange at 80 °C, 100 μL of that solution was added to 400 μL of DMSO-d_6. The characteristic SAA monomer ^{1}H peaks are as follows: δ = 8.07 (d, 2H), δ = 7.79 (t, 2H), δ = 7.45 (t, 2H), δ = 7.28 (d, 2H), δ = 2.73 (t 4H), δ = 2.36 (s, 6H) (Figure 4.3). Impurities matching the diacid, MEK (2.43), ethyl acetate (1.99), and acetic acid (1.92) are present. Diacid impurities may be expected, as water in the DMSO-d_6 will hydrolyze the anhydride bonds in the monomer, reverting it back to the diacid. As the anhydride exchange progressed from 1 to 2 hours,

the diacid impurity peaks became more defined but there was otherwise no change. This supports additional experimental evidence that the duration of the anhydride exchange does not significantly affect the monomer purity or % conversion.

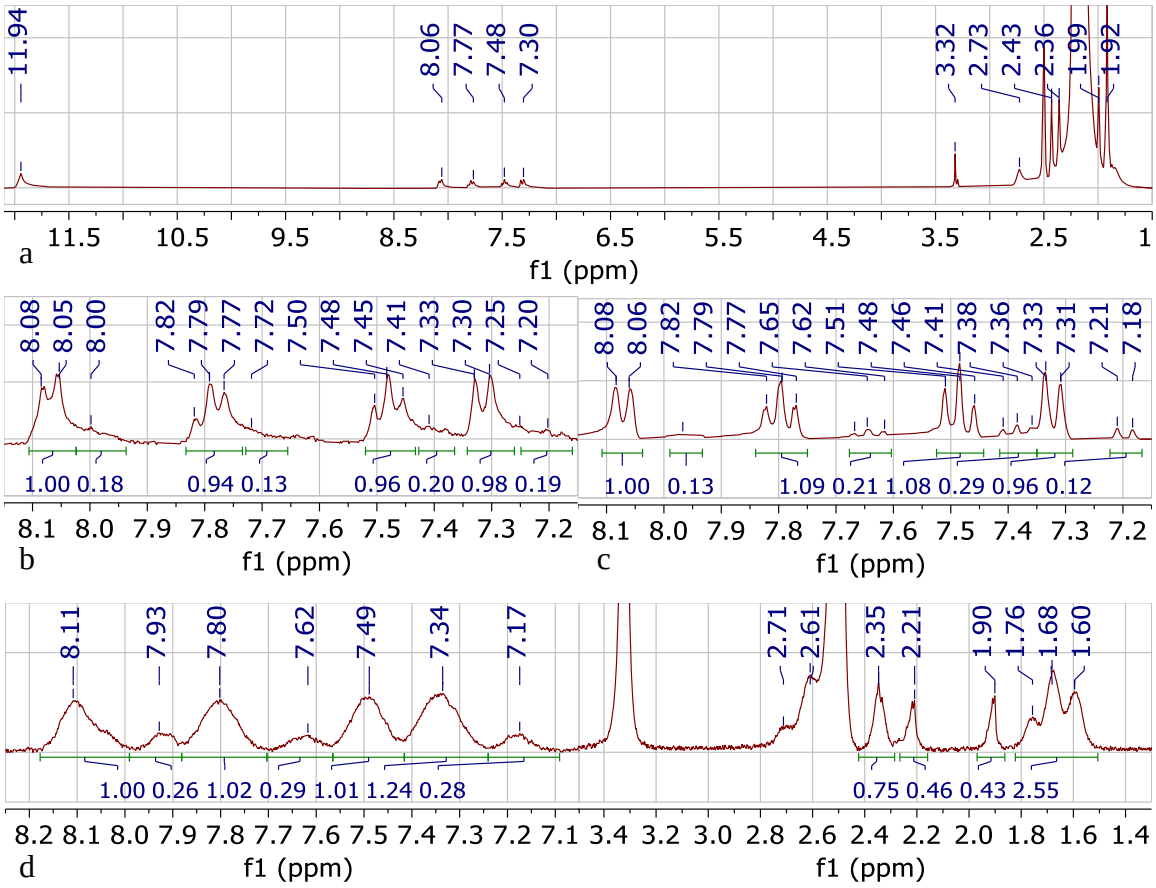

Figure 4.3: ^{1}H-NMR spectra in DMSO-d_6 of SAA monomer during anhydride exchange of SAA diacid EB 01-2020 at 80 ^{o}C for 1 (a, b) and 2 (c) hours, and after vacuum distillation of excess acetic anhydride at 50 ^{o}C for 30 min using SAA diacid EBTD 2-13-21 (d).

Once the monomer was isolated, it had poor solubility in non-acidic solvents, but was sampled for ^{1}H NMR in DMSO-d_6. The SAA monomer peaks have slightly different shifts and integrations, some closer to those reported in literature (Fig 4.4). Two sets of peaks appear in the aromatic region: SAA monomer peaks at $\delta = 8.11$ (b, 2H), $\delta = 7.80$

(b, 2H), δ = 7.49 (b, 2H), and δ = 7.34 (b, 2H) and peaks matching the SAA diacid (δ = 7.9, 7.62, ~7.34, 7.17) at a 1:4 integration ratio with the SAA monomer peaks. While water from the NMR solvent will revert some monomer into diacid, it should not do so to the extent seen in Figure 4.3. This spectrum suggests the water present during the anhydride exchange remains in the mixture or reaction glassware setup and reverts the monomer to diacid. A small monomer peak is observed at δ = 2.73, and a possibly larger diacid peak at δ = 2.61, but it is difficult to tell given the dominant DMSO peak. The peak at δ = 2.21 corresponds to adipic acid, and the peak at 1.90 could be acetic acid. The peaks at δ = 1.76, 1.68, and 1.60 are around the position of monomer, polymer, and diacid peaks. Further studies are necessary to determine the monomer consistency and how different vacuum distillation parameters affect it.

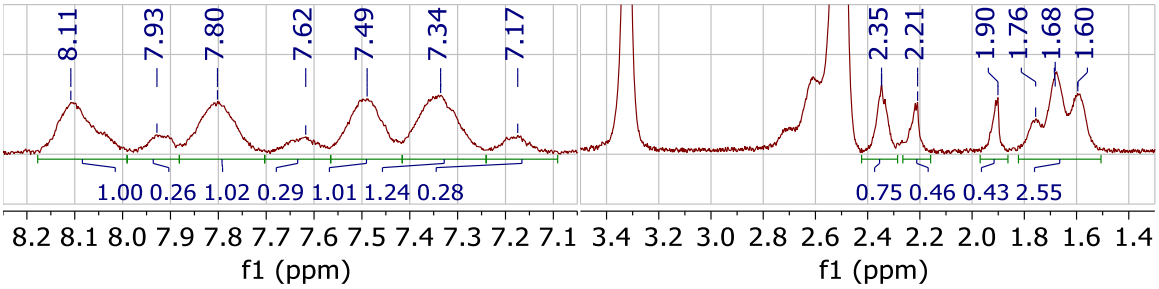

Figure 4.4: ^{1}H-NMR spectra in DMSO-d_6 of SAA monomer made from diacid EBTD 2-13-21 after vacuum distilling excess acetic anhydride.

4.2.6.2 Polymer

Melt condensation polymerization produces acetic anhydride as a byproduct, which should be removed during vacuum polymerization along with water given the high temperature and low vacuum. As the polymerization progressed, the molten polymer color became a darker brown. At some point, the molten polymer began to settle to the

bottom of the round-bottomed flask, which we term vitrification since it indicates a viscosity increase. This process was affected by the position of the stirring blade in the flask; the lower the blade, the more polymer it spread around the flask walls, and the longer vitrification took. After Feb. 2021, vitrification was used as an indication that polymerization was complete. Occasionally, bubbles were noticed in the polymer as it was spread by the stir blade. These could be acetic anhydride and/or water evaporating, indicating the reaction is still ongoing, or gas trapped during the agitation of stirring. SAA polymerization was inconsistent, yielding polymers with a wide range of M_w over different polymerization conditions.

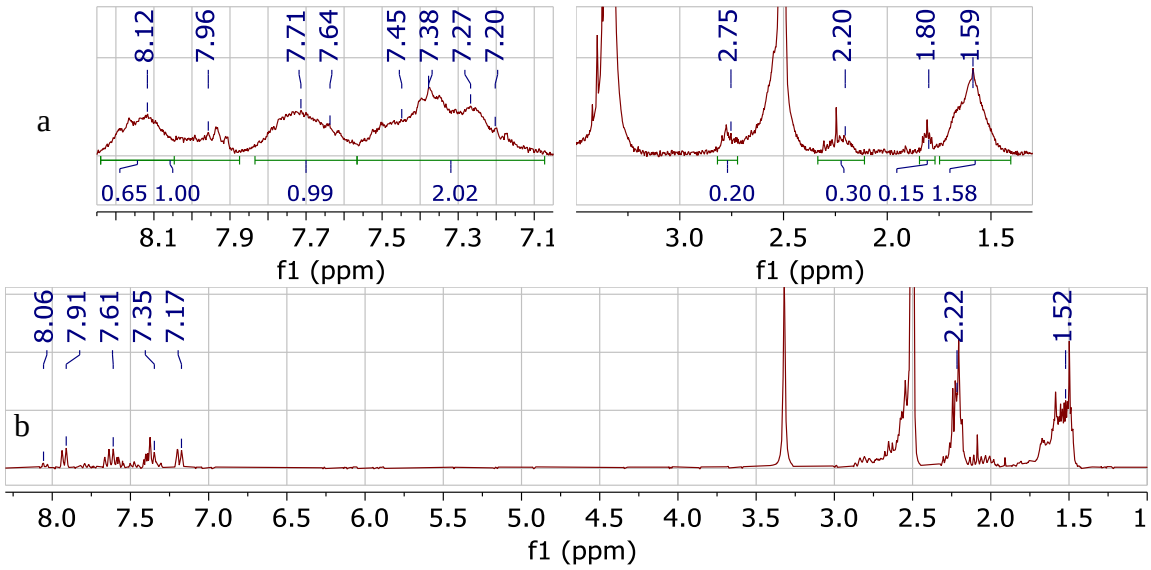

Figure 4.5: ^{1}H-NMR spectra in DMSO-d_6 of SAA polymer made from diacid EB1 (a) and residue from the stir shaft and Teflon inserts (b).

SAPAE polymer typically had a PDI > 2 and consequently broad peaks with ^{1}H NMR spectral shifts in DMSO-d_6 as follows: δ = 8.12 (b, 2H), δ = 7.71 (b, 2H), δ = (7.38, b 4H), 1.59 (b, 4H), and a peak at δ ~ 2.6 that is overshadowed by the DMSO solvent

peak (Fig 4.5). Aromatic impurity peaks are present at δ = 7.96, 7.64, and 7.20-27. They are broad and thus could be a combination of diacid, monomer, cyclized polymer, or an unknown impurity. The impurity at δ = 2.21 is from adipic acid. The impurity peaks at δ = 2.75 and 1.80 ppm could be persistent impurities such as cyclohexanone from the diacid or new molecules that formed during the polymerization.

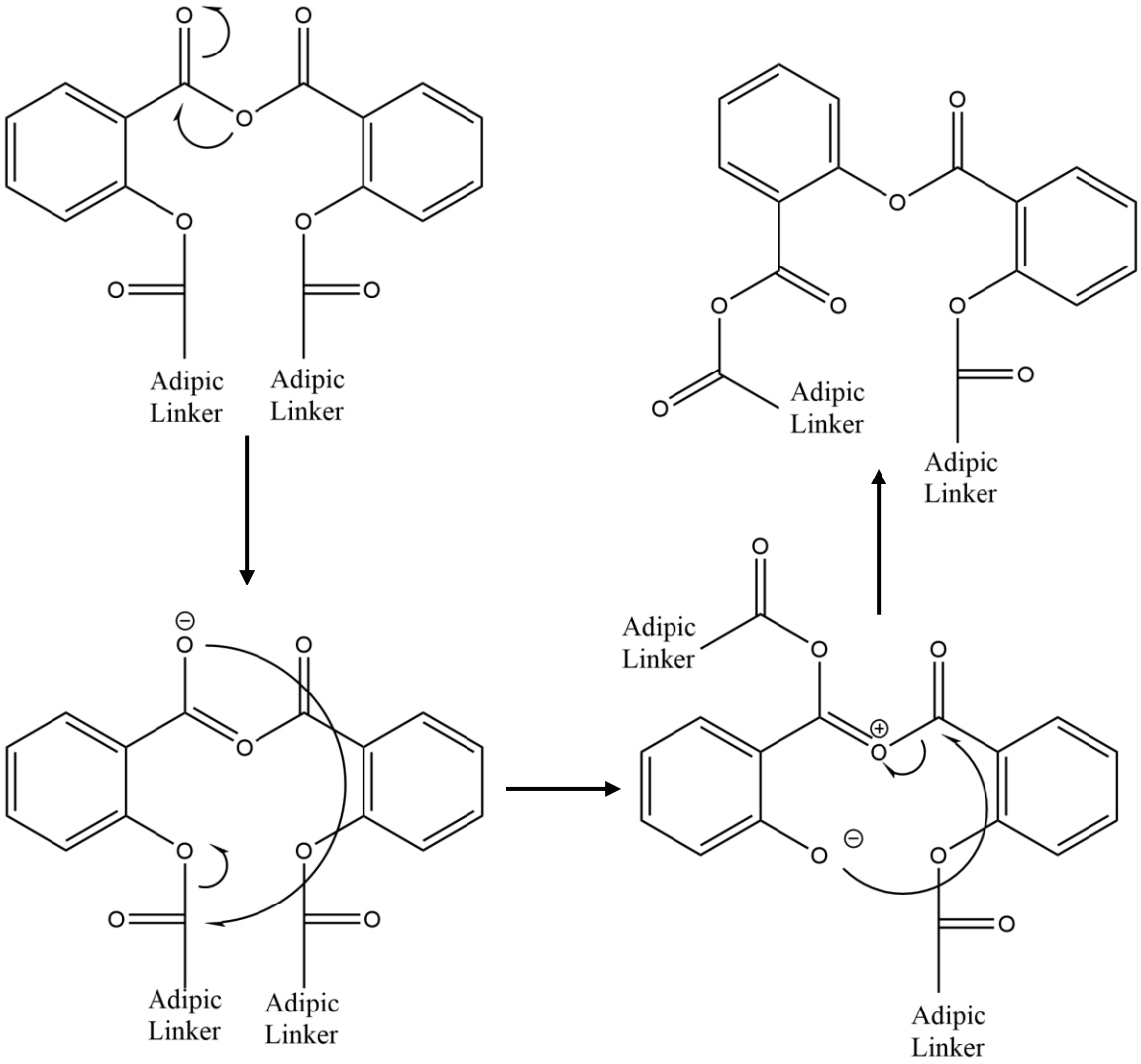

Scheme 4.5: Anhydride-ester rearrangement in SAA

Residue was often found on the stirring shaft and Teflon inserts. The NMR of this residue is expectedly messy, but the peaks are concentrated around the peaks for adipic acid at $\delta = 2.20$ and 1.5 (Fig 4.5). These data, along with the residual adipic acid in the polymer, suggests the adipic linker is being cleaved from the polymer and upon heating, condenses quickly on the stir shaft and Teflon inserts. Previous studies have shown the polymer can undergo rearrangement during melt polymerization, especially as the temperature and duration increase (Scheme 4.5) [21]. This rearrangement shifts to the more stable ester bond from the anhydride bond. Since water hydrolyzes this anhydride bond, it could then cleave the linker from the polymer. This could be the main mechanism by which the adipic linker is removed from the SAA, leading to the inconsistent polymer structure and aromatic:aliphatic integration ratios (Table 4.1).

Comparing SAA ^{1}H NMR in DMSO-d_6 and $CDCl_3$, there is a slight peak shift, but all the polymer and aromatic impurity peaks remain present (Fig 4.6). The most downfield aromatic polymer and impurity peaks in $CDCl_3$ are distinct, showing two impurities. This peak appears at a similar shift as the diacid, so it is possible some of it comes from aromatic rings with -COOH groups on polymer chain ends. However, there is no -COOH peak present and in order for the integration ratio between the two most downfield aromatic peaks to be 2:1, the average polymer chain would contain only 3 repeat units. This would give it a M_w of ~1 kDa, much lower than the M_w measured using GPC (10.3 for the SAA in Fig 4.6), suggesting these peaks are not from -COOH end groups. In addition, the aliphatic peaks have prominent upfield tails but the aromatic:aliphatic integration is 1:2. Thus, the aliphatic impurities seen in DMSO-d_6

could be from oligomers instead of other molecules, and it is possible the linker is not removed from the system, but could still be cleaved from the polymer.

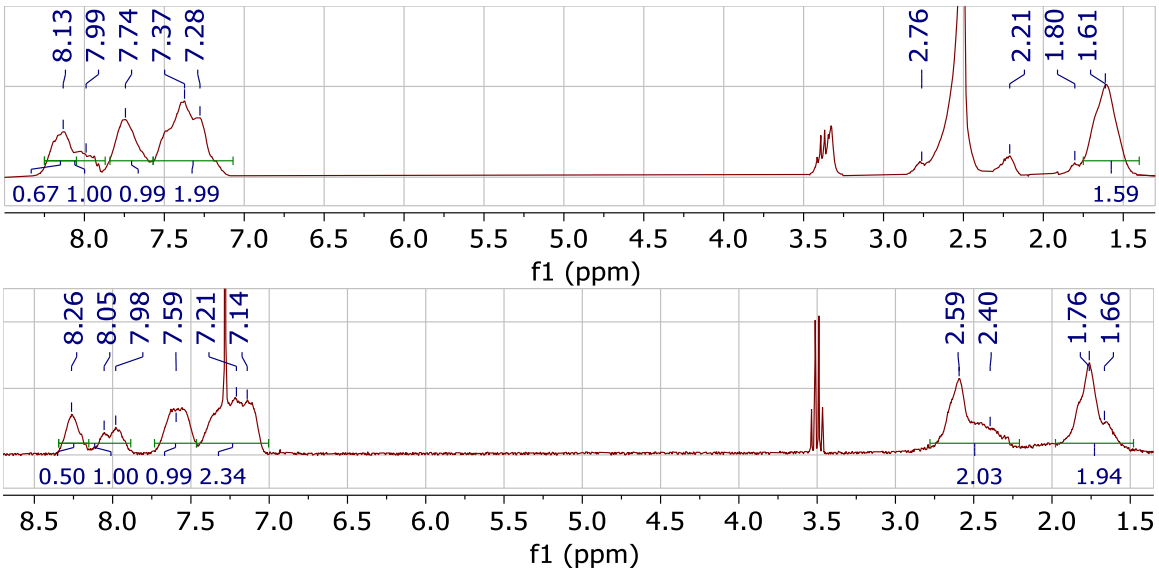

Figure 4.6: ^{1}H-NMR in DMSO-d_6 (a) and $CDCl_3$ (b) of SAA polymerized using diacid EBTD 2-13-21

During polymerizations, vacuum of 29-29.5 -in Hg was consistently achieved with an ambient humidity of 10-30 %RH. Diacid water content varied per batch, though more recent batches had 5-10 times less water than batches used before February 2021. Table 4.1 details the relevant parameters from polymerizations over the past 9 months. All ^{1}H NMR spectra are in DMSO-d_6. All integrals are normalized to the integral of 7.87-8.25 ppm for the polymer and 7.88-7.98 ppm for the diacid. The diacid water integral is from 3.09-3.59 ppm, the polymer aliphatic is from 1.40-1.75 ppm, and the polymer aromatic impurity is from 7.87-8.05.

Table 4.1: SAA polymerization conditions and properties

Polymeri-zation date	Diacid water integral	Vacuum distillation conditions	Polymeriza-tion conditions	Mw (kDa)	PDI	Alipha-tic integral	Aromatic impurity integral
1/14/2020	1.2	70 °C, 2h	180 °C, 18h	8.6	6.3	0.79	0.27
5/18/2020	3.5	70 °C, 2h	180 °C, 16h	2.4	6.3	1.40	0.42
5/28/2020	3.5	70 °C, 2h	180 °C, 14h	7.4	3.1	1.65	0.34
6/1/2020	3.5	70 °C, 2h	180 °C, 17h	6.4	4.1	1.36	0.34
9/9/2020	4.7	70 °C, 1h	180 °C, 7h	18.9	4.7	1.58	0.65
9/10/2020	4.7	70 °C, 1h	180 °C, 7h	16.5	1.56	2.04	0.24
9/11/2020	4.7	50 °C 30m, 70 °C 30m	180 °C, 8h	19.5	5.6	1.52	0.34
9/12/2020	4.7	50 °C 30m, 70 °C 30m	180 °C, 7h	17.1	5.6	1.51	0.37
12/10/2020	0.63	*repolymer-ization	180 °C, 6h	6.0	5.1	1.15	0.32
2/1/2021	0.63	50 °C 30m, 70 °C 30m	180 °C, 6h	7.7	5.9	1.08	0.31
2/9/2021	0.63	50 °C 30m, 90 °C (hot plate error) 30m	180 °C, 4h	10.4	3	1.82	0.38
2/21/2021	0.16	50 °C 30m, 70 °C 30m	180 °C, 6h	8.8	5.6	0.77	0.26
2/25/2021	0.16	50 °C 1h, 70 °C 15m	180 °C, 7h	6.5	5.4	1.42	0.34
2/28/2021	0.16	50 °C 30m, 70 °C 10m	180 °C, 4h	7.5	5.1	1.36	0.33
3/4/2021	0.16	50 °C 30m, 70 °C 30m	180 °C, 3h	9.8	5.6	1.55	0.33
3/7/2021	0.16	50 °C 30m, 70 °C 30m	180 °C, 2h	7.4	5.4	1.43	0.34
3/16/2021	0.16	50 °C 30m, 70 °C 30m	180 °C, 1.25h	10.3	5.1	1.60	0.34
3/21/2021	0.16	50 °C 30m, 70 °C 30m	180 °C, 0h	6.6	2.4	1.9	0.34
3/31/2021	0.16	50 °C 30m, 70 °C 15m	125 °C, 0h	6.4	2.3	1.96	0.24
4/1/2021	0.16	50 °C, 30m	100 °C, 0h	0.5-3.2	1.4	1.98	0.37

The plethora of polymerizations completed show the relationship between the diacid purity, polymerization time, and resulting SAPAE chemical formulas. In 9/2020, 15-20 kDa polymer was synthesized using a diacid with a large amount of water by polymerizing for 7-8 hours at 180 ^{o}C, although the aromatic:aliphatic integration ratio was usually < 1:2. There was little to no difference between the procedures, yet the integration ratios, M_w, and PDI did vary, especially for the best batch on 9/10. In 12/2020, several older batches of polymer, which had degraded while stored in the freezer for months, were repolymerized. For repolymerization, the SAA was dissolved in acetic anhydride, then stirred using an overhead stirrer and oil bath. This mixture was heated to 70 ^{o}C first under vacuum to distill off excess acetic anhydride, then polymerized at 180 ^{o}C. This method was performed multiple times and while it yielded 10-15 kDa polymer, the integration ratios were far too low, often 1: < 1, and the product was a dark brown. Thus, while repolymerization does increase the polymer M_w, it alters the SAPAE chemical formula to contain too many SA units.

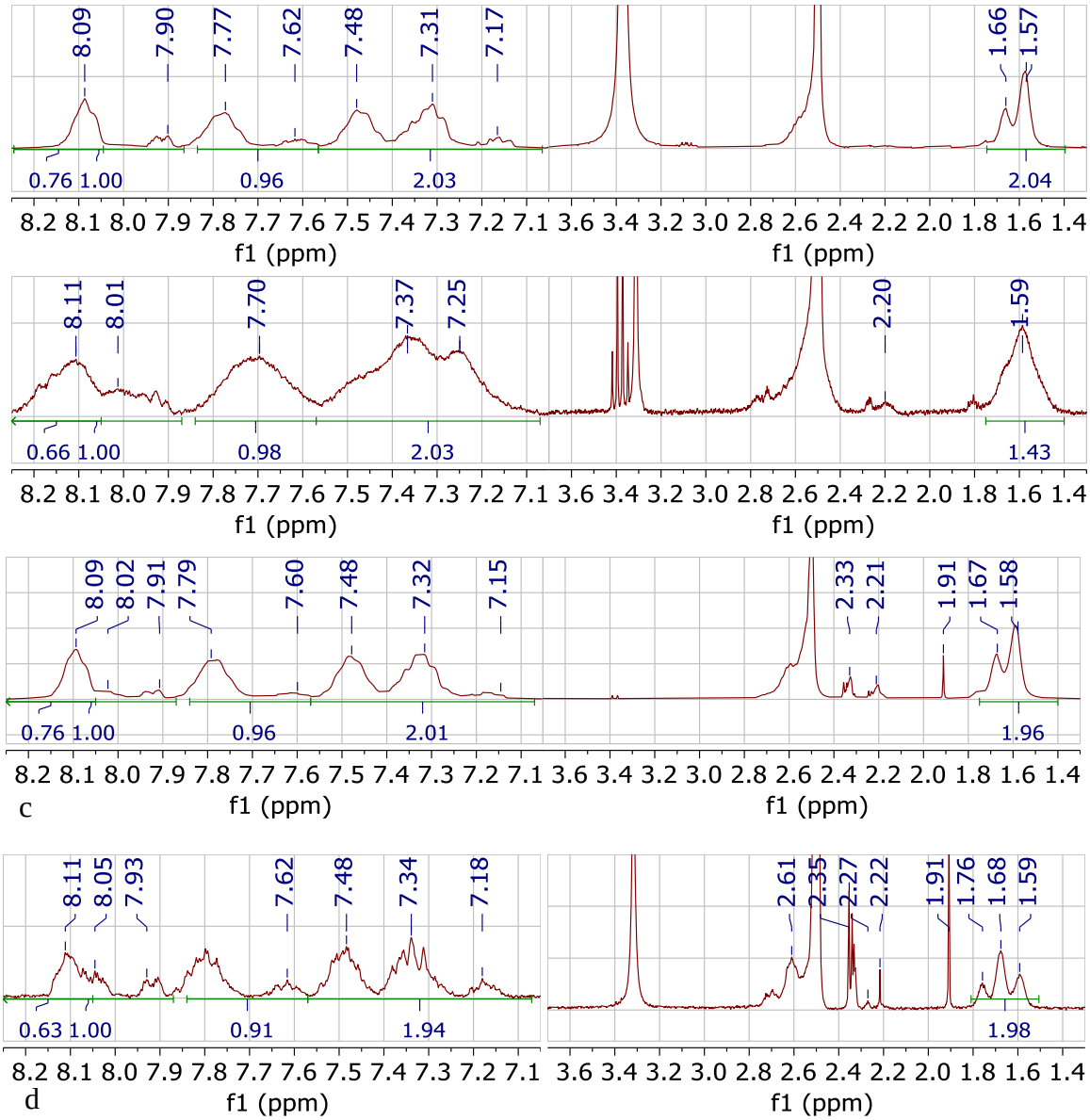

Figure 4.7: ^{1}H-NMR in DMSO-d_6 comparing SAA at different stages of polymerization. a) 100 ^{o}C 0h b) 125 ^{o}C 0h, c) 180 ^{o}C 2h, and d) ideal polymer. a-c were made from diacid EBTD 2-13-21, which had less water than the diacid used for the polymer in d (9/10/20).

Polymers made on 2/1 and 2/9/21 illustrate the effect of polymerization time. If the polymerization goes past a certain point, the aromatic:aliphatic integration ratio decreases and the M_w can as well. A similar, but not perfect, trend exists in the polymers

made after 2/9/21. To intentionally make low M_w polymer, the polymerization temperature and time were decreased to 0 h, when the reaction flask was removed from the oil bath as soon as it reached the set temperature. Early in the polymerization process, the aromatic peak coupling patterns are more distinct since only oligomers have formed (Fig 4.7). Peaks from the monomer at 1.76 and 2.35 ppm are also present, as is a small amount of acetic acid, acetic anhydride, and adipic acid. These data could mean the adipic acid is cleaved from the diacid or polymer during the anhydride exchange or vacuum distillation, as adipic acid peaks were also present in the monomer. It is undetectable during the anhydride exchange, however, since it is overshadowed by the large acetic anhydride peak.

The acetic acid and aromatic impurities persist as the polymerization proceeds (Fig 4.7), although the aromatic impurities initially decrease in breadth and number (Fig 4.7a-b) before increasing (Fig 4.7c). The ideal SAA (Fig 4.7d) looks more similar to the polymer during the early stages of polymerization (Fig 4.7b), including two aliphatic peaks at 1.57 and 1.66 ppm when only one peak at 1.6 ppm has been reported by previous studies. These results show that while it is possible to obtain SAA with a high M_w and the correct structure, the process parameters required to do so vary per batch of diacid.

4.3 SAPAE-coated Magnesium

4.3.1 Methods

Polymer solution (100 μL of 0.8 g/mL SAA/DCM; 6-8 kDa Yue Batch III) was pipetted onto glass coverslips and Mg alloy plates that were sanded using 600-1200-1800 grit sandpaper to achieve a uniform surface. Spin coating parameters of 3 and 6 $krpm^2$

acceleration to speeds of 3 and 6 krpm for 1 minute were used to coat the Mg in thick and thin SAPAE films, respectively. Much of the SAPAE solution was flung off the Mg substrate during coating, but using lower solution volumes resulted in less uniform coatings. After coating, the films were dried in air for 24 h, then under vacuum for 48 h at 50 ^{o}C to remove residual cytotoxic DCM. ^{1}H NMR spectroscopy was used on one sample per batch dedicated for this purpose to confirm the DCM was removed. The films were characterized or further processed immediately after heating, as they degraded rapidly.

Adhesion testing was performed using a direct pull method [22,23]. An aluminum bar was glued to the film and an aluminum sheet to the bottom of the substrate and the assembly was placed in an Instron mechanical testing frame (Fig 4.8). To prevent the bar from breaking off through misalignment-induced shear when the grips were tightened, the grips were used to adhere the bar to the substrate, the glue was allowed to dry for 30 minutes, and then the bar was pulled at 0.1 mm/min to delaminate the film. The cross-sectional area of the bar was used to calculate stress.

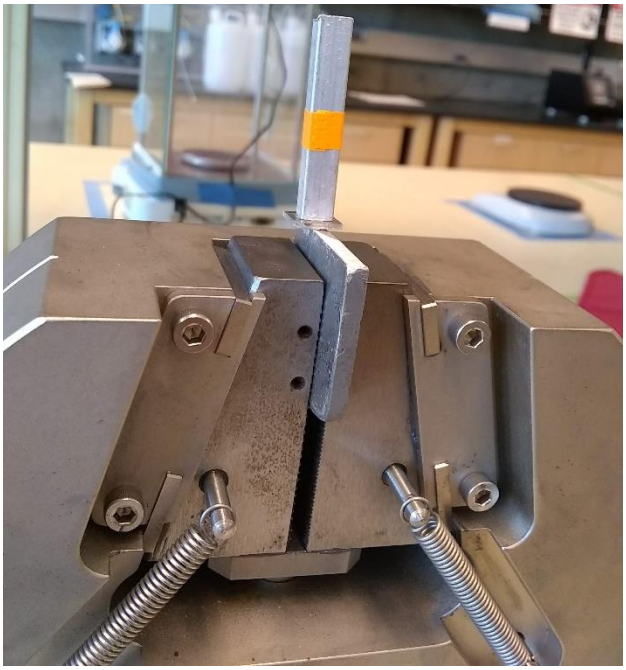

Figure 4.8: Photograph of the direct pull adhesion test setup used for SAA-coated Mg.

Degradation studies were performed in Dulbecco's Modified Eagle Medium (DMEM), which was also used for cytotoxicity studies with Bone marrow-derived Mesenchymal Stem Cells (BMSCs). The following samples were tested for SAA degradation in 3 mL media at 37 ^{o}C and 100 rpm shaking: thick and thin films on Mg and glass, SAA powder at 1, 0.5, 0.1, and 0 mg/mL concentrations. SAA was initially dissolved in DMSO, then 30 μL of that solution was added to the degradation media to eliminate particle size effects on the SA release. SA release was quantified using UV-Vis spectroscopy to determine the absorbance of the SA peak at 295 nm. A baseline subtraction was performed using pure degradation media, then a calibration curve made from standards with known SA concentrations in each type of degradation media was used to calculate the SA concentration for each sample. Cumulative release was

determined by adding the SA mass from time point *n* to that of time point *n-1* and determined the theoretical maximum SA release using the SAA film mass before degradation. Dongwei Sun performed additional tests to evaluate the ability of the SAA coating to prevent the Mg from corroding and analyze corrosion mechanisms, which will be published along with the cell culture and degradation results in an upcoming report.

4.3.2 Results

Uniform, smooth, debris-free SAPAE films were coated on Mg and glass substrates using both parameters (Fig 4.9). Adhesion testing was difficult, as the glue in half the samples fractured through shear instead of tension (e.g. from bumping the grips or adjusting them), and the aluminum rods often slipped in the Instron grips. Successful tests showed an average adhesion strength of 1.20 ± 0.912 MPa with a range from 0.380-3.21 MPa (Fig 4.10). These values are lower than other biodegradable polymers tested using the same method [23]. However, microscopy of the fracture surfaces showed 25-75% of the SAPAE film was still adhered to the Mg substrate even after failure. These data suggest the majority of the samples failed cohesively instead of adhesively, meaning that the polymer binding to the Mg substrate was stronger than the internal polymer bonds. Given the difficulties with direct pull adhesion testing, micro- or nano-indentation are better methods to determine the SAA film adhesion testing.

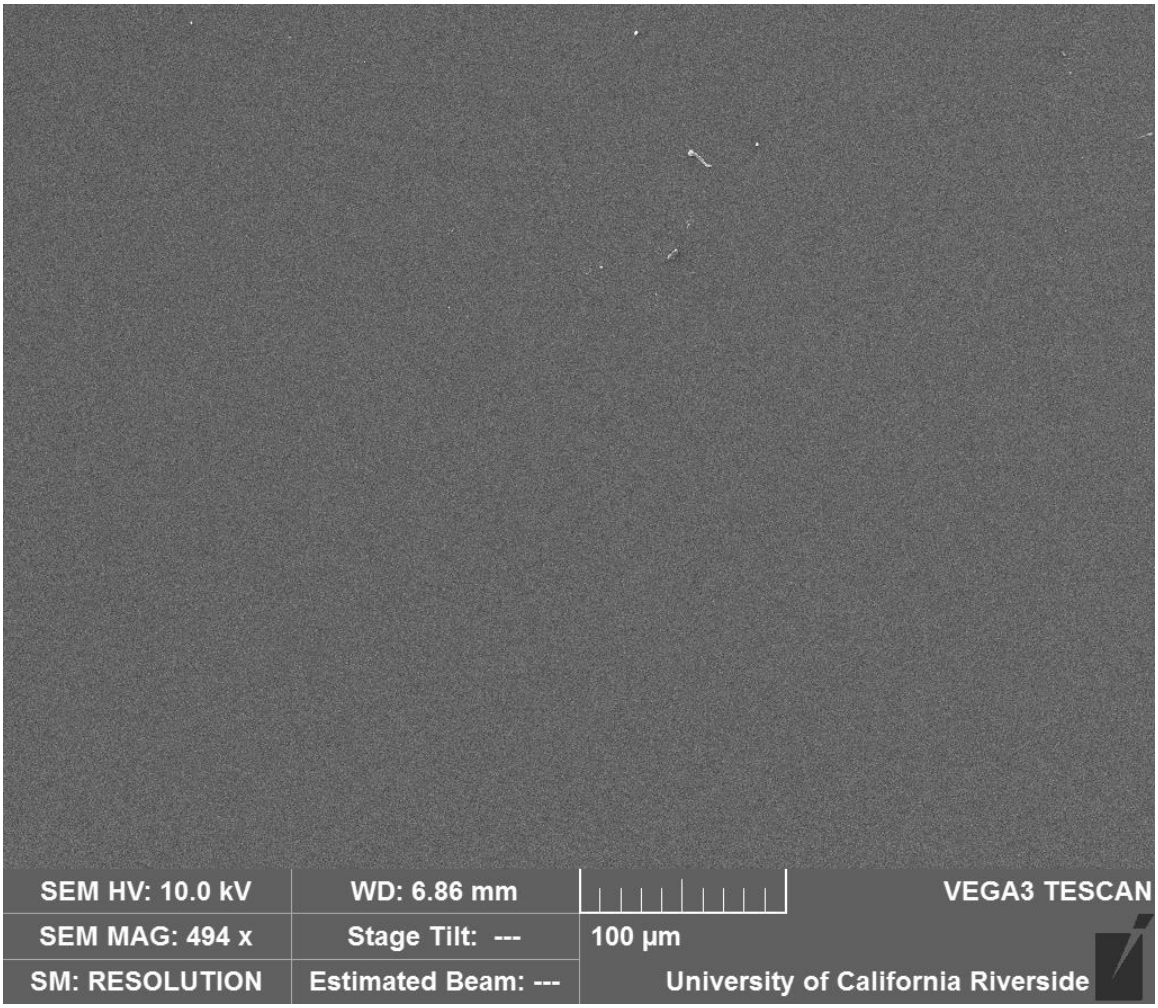

Figure 4.9: Uniform, mostly defect-free SAA coating on Mg.

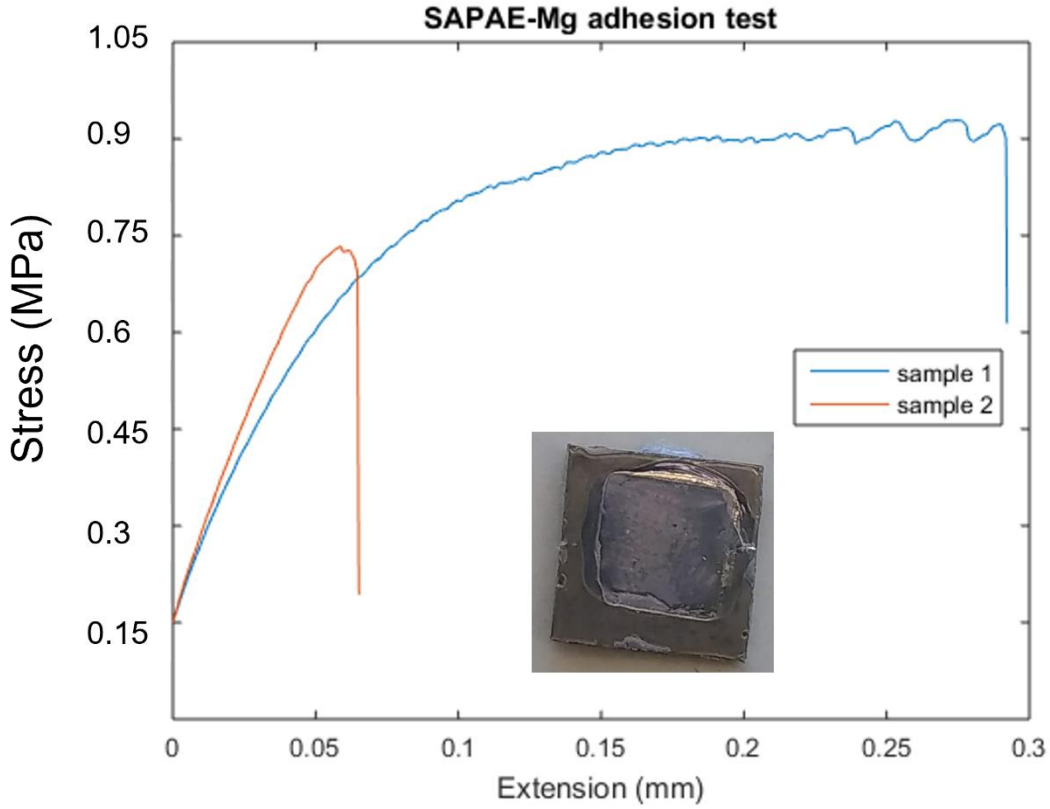

Figure 4.10: stress vs extension curves of select SAA films on Mg using the direct pull method. The inset shows a photograph of a 1 cm square sample after testing.

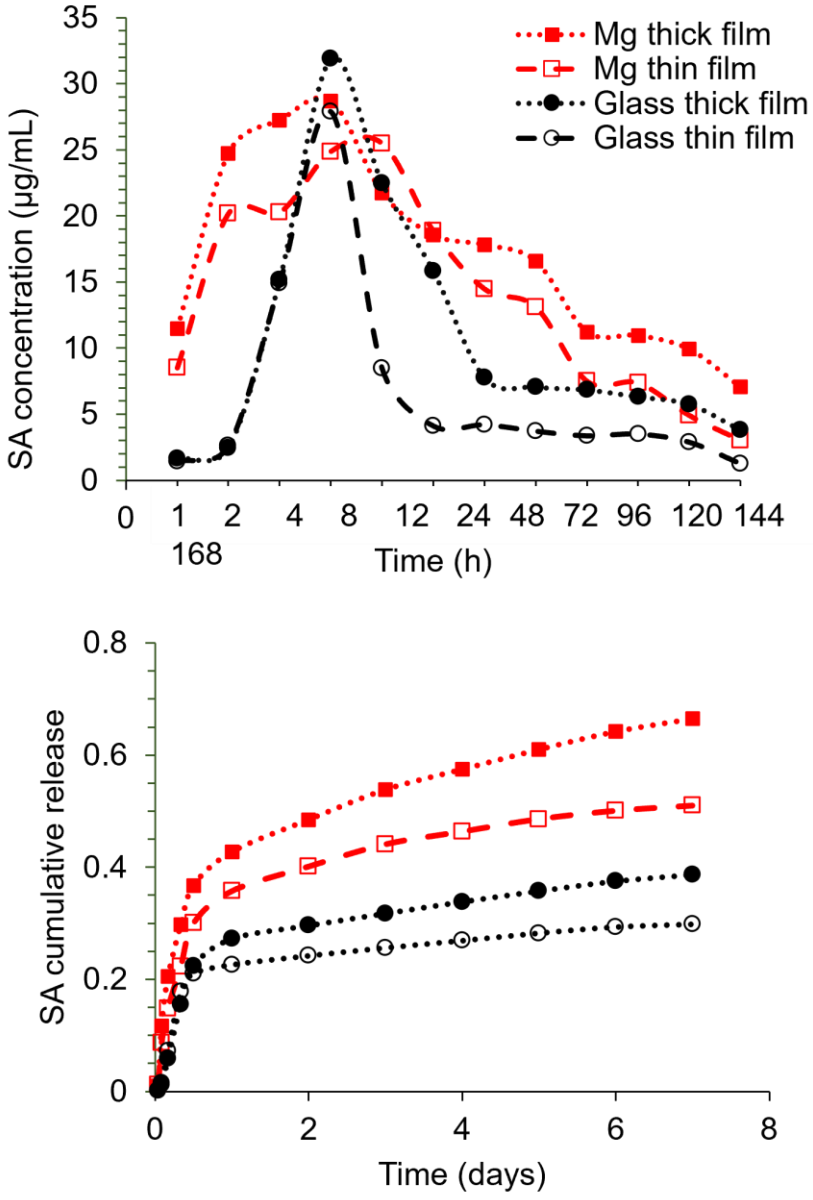

Figure 4.11: Hourly and cumulative SA release from SAA coated samples.

SAA films on Mg showed a faster burst release than those on glass, suggesting the magnesium catalyzes SAA degradation (Fig 4.11). As expected, due to their larger mass, thick films released more SA than thin ones. SAA coated on glass had a delayed

burst release after 4 hours, but the release slowed considerably after 2 days while the SA release from coated Mg decreased more gradually. The SA release for both samples was faster than SAA in solution and previous reports of SA release, likely because the thin films have a higher surface area to volume ratio than the SAA discs used in most previous degradation studies. Overall, this release is too quick to meet the needs for this application and while the polymers slowed Mg corrosion, they did not slow it enough. Based on these results, a slower-degrading SAPAE should be tested for this application.

4.4 Protein-Encapsulated SAPAE Microspheres

4.4.1 Methods

4.4.1.1 Microsphere Synthesis

SAA was evaluated as the initial polymer to use in microsphere synthesis, as SAA microspheres are stable through multiple processing conditions and well characterized. For a typical SAA microsphere synthesis at a 20-200 mg scale, a 1% w/v (10 mg/mL) PVA/DI water solution was first prepared in a beaker. The PVA can take up to an hour to dissolve, accelerated by heating the solution to 50-80 ^{o}C. Next, a 100 mg/mL SAA/DCM solution was prepared at a 1:50 volume ratio with the PVA solution. This solution was added all at once to the PVA solution while homogenizing (IKA I10 basic ultra-turrax, Wilmington, NC) at 10 krpm for 2-5 minutes. No difference was observed between adding the SAA solution dropwise or all at once or based on the homogenization durations used. MEK can be substituted as a solvent for DCM, but these microspheres required drying using a commercial lyophilizer (Labconco FreeZone Triad, Kansas City, MO) to remove this high-boiling solvent. After homogenization, the solution stirred at

500 rpm for 2 hours to remove residual DCM. The emulsion was sampled at this point, pipetted onto a glass slide, and secured with a coverslip for optical microscopy to ensure microspheres had formed. ^{1}H NMR spectroscopy was performed on this solution at 20 mg scale and showed the DCM evaporated after 15 minutes.

After evaporating the DCM, the microspheres were washed 2-5 times with pH 2 DI water, centrifuged, and decanted after each wash to remove residual PVA. The capped centrifuge tube was shaken each time water was added to ensure the microspheres were dispersed. More washes were needed at larger scales. Neutral water can also be used, but may require an extra wash. If there was residual PVA, bubbles formed on top of the solution, it was more difficult to disperse the microspheres, and the microspheres continued to stick together as the solution is decanted. Three drying techniques were used on the microspheres after washing was complete: lyophilization, either using a commercial instrument or by freezing the centrifuge tube containing the microspheres in liquid nitrogen; washing with 100 % ethanol; or vacuum filtration. All of these techniques were followed by drying under < 29 -in Hg vacuum. Vacuum filtration was easier, but had a lower average yield (46%) than that of lyophilization (65%).

To encapsulate BSA, the same procedure was followed with an additional homogenization step. Protein solution (100 mg/mL BSA/PBS) was added to the SAA/DCM solution at a 1:20-1:40 volume ratio (1 mL SAA/DCM minimum), homogenized at 15 krpm for 1 minute, and transferred immediately to the PVA/DI water solution and homogenized at 10 krpm for 2 minutes. The PBS/DCM emulsion was also

sampled and verified with optical microscopy. The same DCM evaporation, washing, and drying procedures were used as with unencapsulated SAA microspheres.

To achieve faster-degrading microspheres, Dr. Shuang Song synthesized the following different SAPAEs (Scheme 4.7): Solution polymerized SAPAE using a glycolic linker (SGA) and a copolymer of 1:1 SAA:SGA; 1:1 SAA-co-fumaric acid (SAA:FA); 4:1 SAA-co-Adipic Acid (SAA:AA); and 4:1 SAA-co-phenyldiacetic acid (SAA:PA). These SAPAE polymers and copolymers required adjustments to the microsphere synthesis process, such as shorter stirring times for DCM evaporation, as they degraded more quickly or did not form stable emulsions. The final standard process used a 2-minute homogenization, 3x acidic water wash, 15-30 min stirring to evaporate DCM, and vacuum filtration for drying.

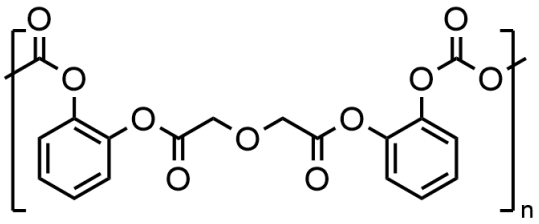

Glycolic SAPAE (SGA)

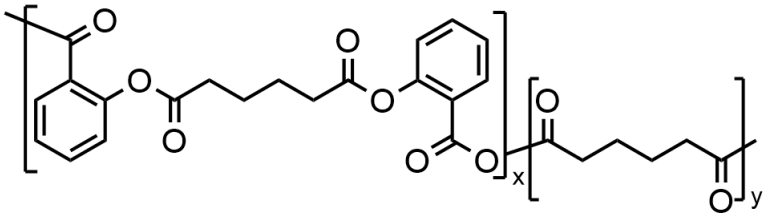

SAA-co-Adipic Acid (SAA-AA)

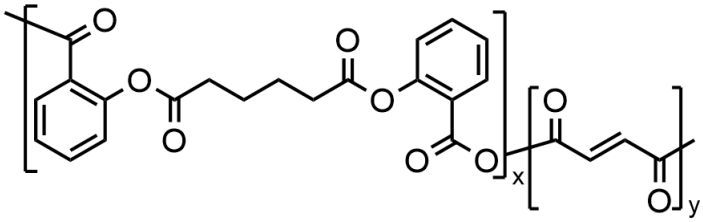

SAA-co-Ferulic Acid (SAA-FA)

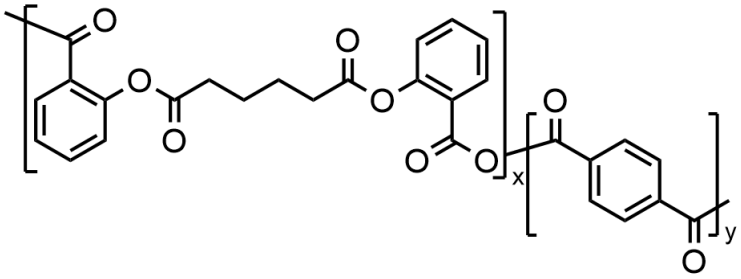

(SAA-PA)

Scheme 4.6: Structures of faster-degrading SAPAEs.

4.4.1.2 Characterization

After drying the microspheres overnight, a small amount were placed onto an SEM sample holder to evaluate their size and surface morphology, sputter coated with gold (Cressington, 30 mA, 20s), and imaged at 10 kV (Tescan Vega). GPC and NMR

spectroscopy were performed on the microspheres using the parameters and instruments previously described in this chapter, and FTIR spectroscopy (ThermoFisher Nicolet iS10) was performed to check for residual PVA. For degradation studies (N = 1-3), 15 mg microspheres were added to 15 mL PBS in a centrifuge tube, and then incubated at room temperature and 200 rpm shaking. The centrifuge tubes were placed on their side to agitate the microspheres; if placed upright, the microspheres aggregated at the bottom of the tube. Sometimes it was difficult to disperse the microspheres in the media, so sonication was investigated as a solution. If the microspheres remained aggregated in chunks in the degradation media, many microsphere surfaces were not exposed to the degradation media, slowing degradation and increasing variance.

At certain time intervals, the tubes were centrifuged, 1 mL of supernatant was sampled, replenished with 1 mL fresh PBS, and the centrifuge tubes were shaken by hand to re-disperse the microspheres. UV-Vis spectroscopy was used to determine the SA content in each sample as described earlier in this chapter. BSA release from these same samples was measured using a bicinchoninic acid (BCA) assay. 50 μL sample was added to 200 μL BCA working solution (ThermoFisher) and incubated in a water bath at 60 ^{o}C for 30 minutes. The working solution is alkaline and contains BCA and copper ions, giving it a green color. Proteins reduce Cu^{2+} to Cu^{1+} in an alkaline solution, which complexes with the BCA. This change is detectable through a color change to blue or purple and a UV-Vis absorbance peak at 562 nm. As described in section 4.3.1, the absorbance from a blank sample was subtracted and a calibration curve was used to determine the SA and BSA release. The maximum theoretical release was calculated

from the initial SAA and BSA masses in the sample. Residue was noticed on the micropipette tip and the centrifuge tube cap after sampling. This residue could be SA, diacid, or SAA that escapes the centrifuge tube. Thus, it is possible the maximum SA release is lower than its theoretical value. To mitigate leakage, the threads and cap of the centrifuge tube were greased with silicone.

This degradation protocol was similar to previously published studies using SAPAE microspheres, but differed from most previously published studies which used pressed SAPAE pellets, as only a portion of the supernatant was removed. To simulate *in vivo* conditions for the "pellet method," supernatant was fully removed from the polymer being evaluated and the media replenished to establish "sink conditions," such that the media is far above the solubility limit of the degradation products. Notably, SA is soluble at 2 mg/mL in PBS at room temperature, which is 2-3 times the concentration that would be present if the polymer completely degraded, so the protocol outlined here should not approach the solubility limit.

Because this protocol was different than that described in section 4.3, the cumulative release was calculated differently. If no samples were taken, the SA concentration measured at each time point would represent the cumulative release, which can be multiplied by the degradation media volume to determine the mass of SA present in the system. However, some SA was removed from the system each time a sample is collected. Consequently, the SA mass measured at each time point did not represent the cumulative release until the mass lost during sampling was accounted for. The calculation of the cumulative mass removed was similar to the calculation of cumulative release

described in section 4.3.1. For each time point, the cumulative mass removed = cumulative mass removed at time point *n-1* + mass removed at time point *n*. The corrected cumulative SA release at time point *n* was then equal to measured SA mass in the degradation media at time point *n* + the cumulative mass removed at time point *n-1*.

4.4.2 Results

4.4.2.1 Microsphere Morphology

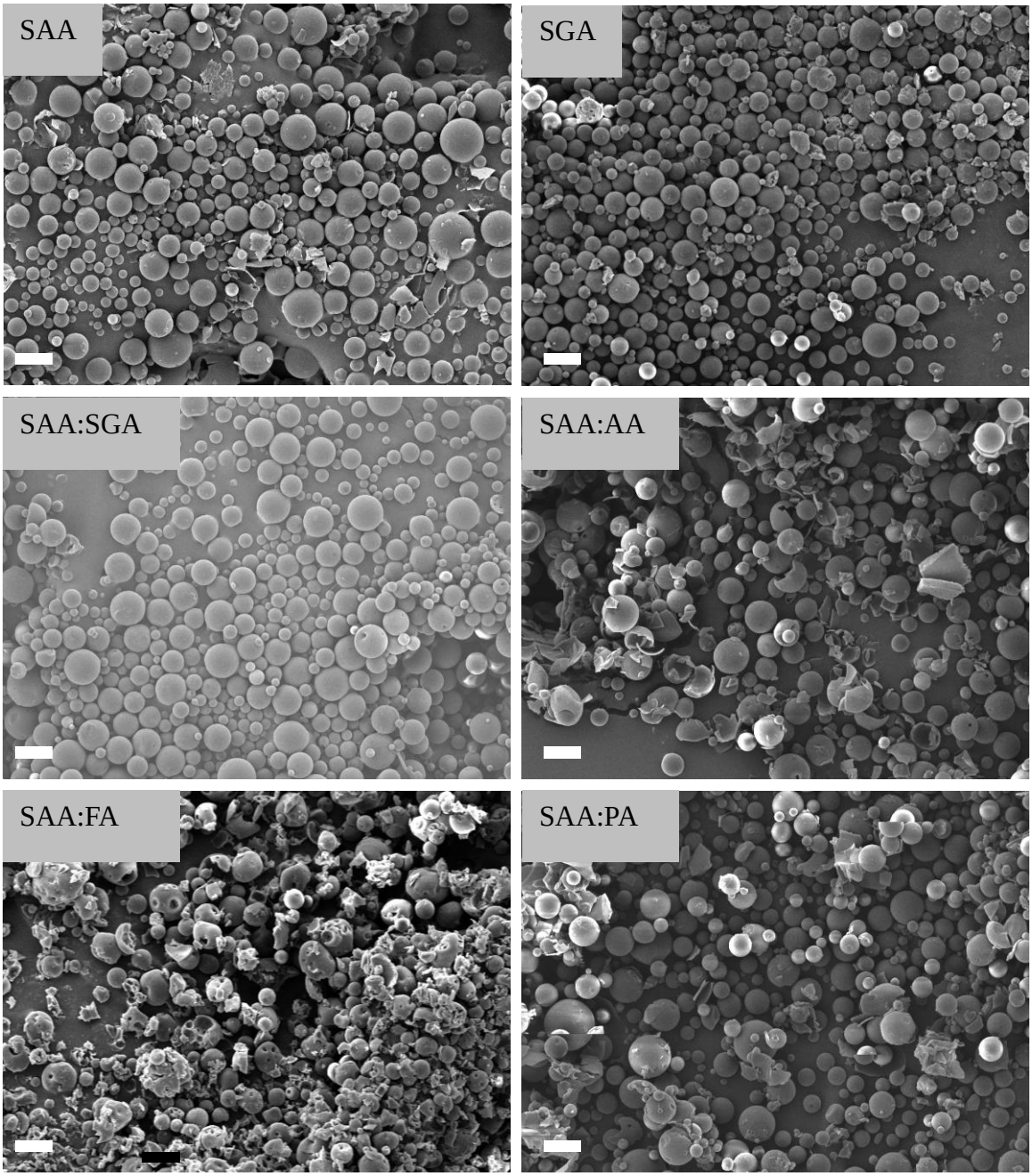

Figure 4.12: Microspheres made from different SAPAEs. Scale bar is 20 μm.

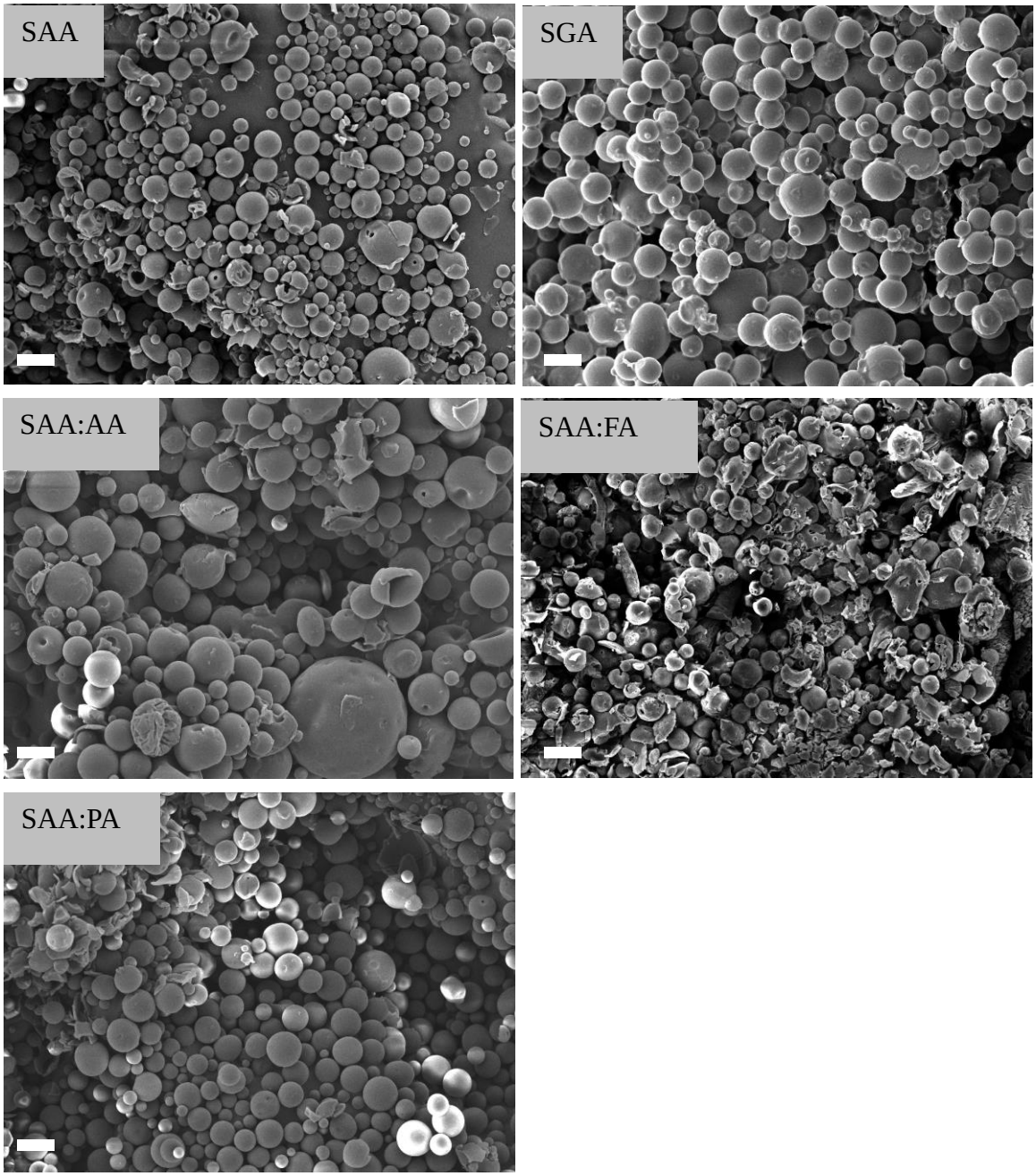

Figure 4.13: BSA-encapsulated microspheres made from different SAPAEs. Scale bar is 20 μm.

Microspheres and BSA-encapsulated microspheres were successfully synthesized from each polymer studied (Fig 4.12, 4.13). Many of the SAA-FA microspheres were broken, which could be due to the low polymer M_w or the microsphere synthesis process.

About 5-15% of the BSA encapsulated microspheres for the other polymer compositions appeared to be broken, but this value is likely low enough to not drastically affect degradation and BSA release. Microspheres of each polymer had a wide diameter range, but their average diameters were consistently within 1 standard deviation of each other (Table 4.2). Sonicating unencapsulated and encapsulated SAA microspheres for 5 seconds in isopropanol caused no noticeable damage (Fig 4.14). Isopropanol is a better solvent for SAA microspheres than water (though SAA has low solubility in both), so SAA microspheres should be stable after sonication in PBS as well. Similar tests should be done for other SAPAEs before using sonication to disperse them in degradation media.

BSA encapsulated microspheres were more difficult to synthesize. Three acidic water washes were used, and the microspheres were dried by vacuum filtration; the main process change was the stirring duration to evaporate DCM. The SGA, SAA-FA, and SAA-PA microspheres aggregated at the bottom of the beaker if stirred for over 30 minutes. Remarkably, the aggregated SGA microspheres held their form, but the synthesis was repeated to ensure consistency. BSA encapsulated microspheres generally had larger diameters than unencapsulated microspheres (7-12 μm vs 9-16 μm). If the SAPAE microspheres are too small, the thin walls caused by their core-shell structure after encapsulation could collapse during stirring to evaporate DCM or drying.

Table 4.2: SAPAE microsphere summary

Polymer	Scale (mg)	washes	Drying technique	Approximate Mw (kDa)	Microsphere diameter (μm, N = 30)
SAA solution	200	3, DI water	lyophilize	5	9.3 ± 3.7
SAA melt	200	3, DI water	lyophilize	10	9.5 ± 5.1
	50	3, acidic water	Lyophilize	Did not measure	12.4 ± 4.4
	50	3, acidic water	lyophilize	Did not measure	10.2 ± 3.8
	200	3, acidic water	Vacuum filtration	4.7	9.2 ± 4.7
SGA	200	3, DI water	lyophilize	5	7.6 ± 3.14
	200	3, acidic water	Vacuum filtration	18	10.6 ± 4.4
	200	3, acidic water	Vacuum filtration	5.4	8.0 ± 3.5
SGA:SAA 1:1	200	3, DI water	lyophilize	5	9.7 ± 4.8
SAA-FA	200	3, acidic water	Vacuum filtration	0.4	6.7 ± 2.4
SAA-AA	200	3, acidic water	Vacuum filtration	2.6	8.7 ± 4.1
SAA-PA	200	3, acidic water	Vacuum filtration	3.8	7.5 ± 3.9

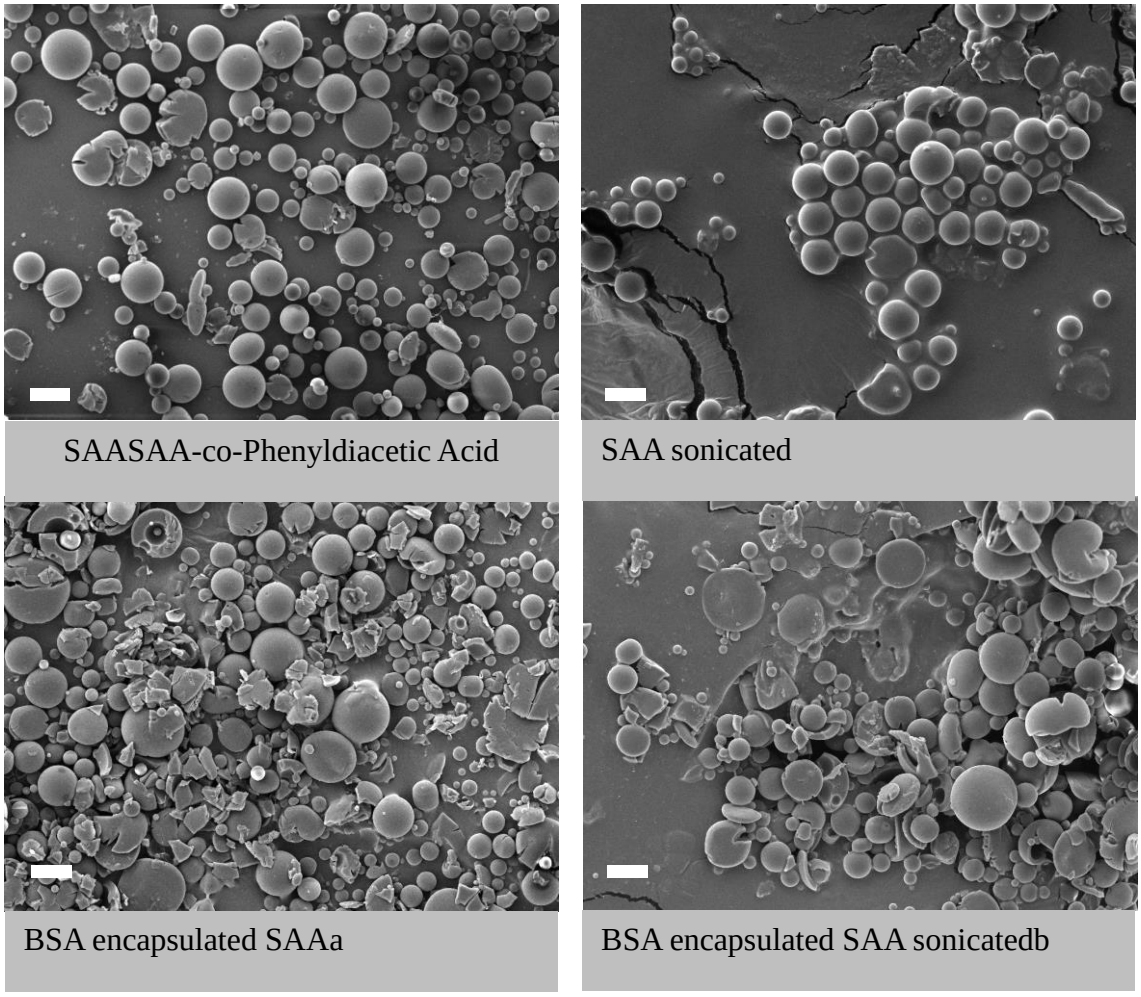

Figure 4.14: Unencapsulated and BSA encapsulated SAA microspheres before and after sonication. Scale bar is 20 μm

Table 4.3: BSA encapsulated SAPAE microsphere summary

Polymer	Scale (mg)	DCM evaporation stir time (min)	Microsphere diameter (μm, N = 30)
SAA	200	120	10.2 ± 3.8
SGA	200	45	9.7 ± 5.0
SGA	200	30	11.6 ± 4,6
SAA-FA	20	30	11.4 ± 4.8
SAA-FA	20	15	8.8 ± 2.3
SAA-AA	20	120	12.3 ± 6.2
SAA-AA	200	30	16.1 ± 14.9
SAA-PA	20	30	12.1 ± 3.8

Dichloromethane is becoming increasingly restricted in the European Union and to a lesser extent the US, so less carcinogenic solvents were evaluated for SAA microsphere synthesis. SAA must be soluble in high concentrations, and the solvent must be mostly immiscible with water. Chloroform and acetone are known solvents for SAA, but chloroform is just as toxic as DCM and acetone is water miscible. The solubility of SAA in THF, ethyl acetate, ethanol, methanol, and isopropanol at room temperature was observed to be less than 0.05 mg/mL. However, the polymer is soluble in MEK at concentrations > 100 mg/mL, thus, MEK was substituted for DCM and used to synthesize SAA microspheres (Fig 4.15). The microspheres were more likely to degrade during the synthesis process than SAA microspheres made using DCM, and their diameters were lower, at 4.39 ± 2.64 μm. They will likely degrade more quickly than SAA microspheres made using DCM. Water is more miscible with MEK than DCM, so it is possible there were water impurities in the MEK, or nanoscopic water droplets which penetrated the SAA/MEK droplets during emulsification. This effect would increase porosity in the SAA microspheres, leading to a lower stability in water and quicker degradation times.

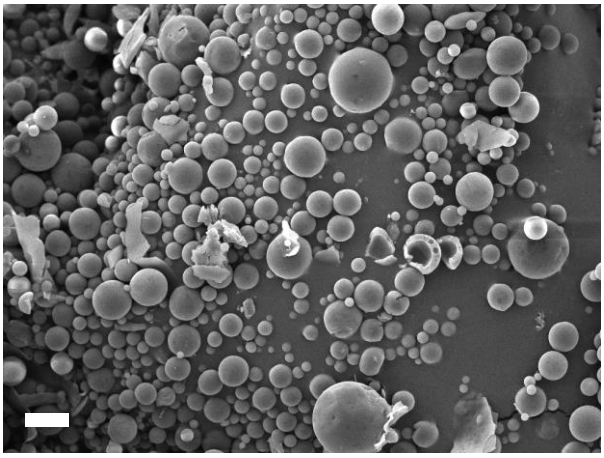

Figure 4.15: SAA microspheres synthesized using methyl ethyl ketone as a solvent. Scale bar is 20 μm.

4.4.2.2 Microsphere Degradation and BSA Release

SAA microspheres showed a constant degradation rate through 1-7 days of incubation, after which degradation plateaued for 3 weeks (Fig 4.16a). The degradation rate was similar to previous studies, although in those studies SA release continued at a constant rate for 3 weeks. SAA microspheres at a lower concentration expectedly degraded more quickly, but had the same plateau behavior. BSA encapsulated SAA microspheres degraded even more quickly. As the microsphere surfaces eroded and the BSA was released, this exposed pockets inside the microspheres to the degradation media, further increasing the surface area in contact with the degradation media and accelerating degradation. SAA-AA and SAA-FA degraded even more quickly, as expected due to their higher hydrophilicity. The cumulative release follows the same trend (Fig 4.16b), and 100% SA release occurred after 6 weeks. Despite accounting for mass removed from the system during sampling, there were still points where the cumulative release appeared to decrease (SAA-BSA 17 and 21 days). This effect is likely

due to degradation media leaking or SA precipitating onto the micropipette tip as mentioned earlier.

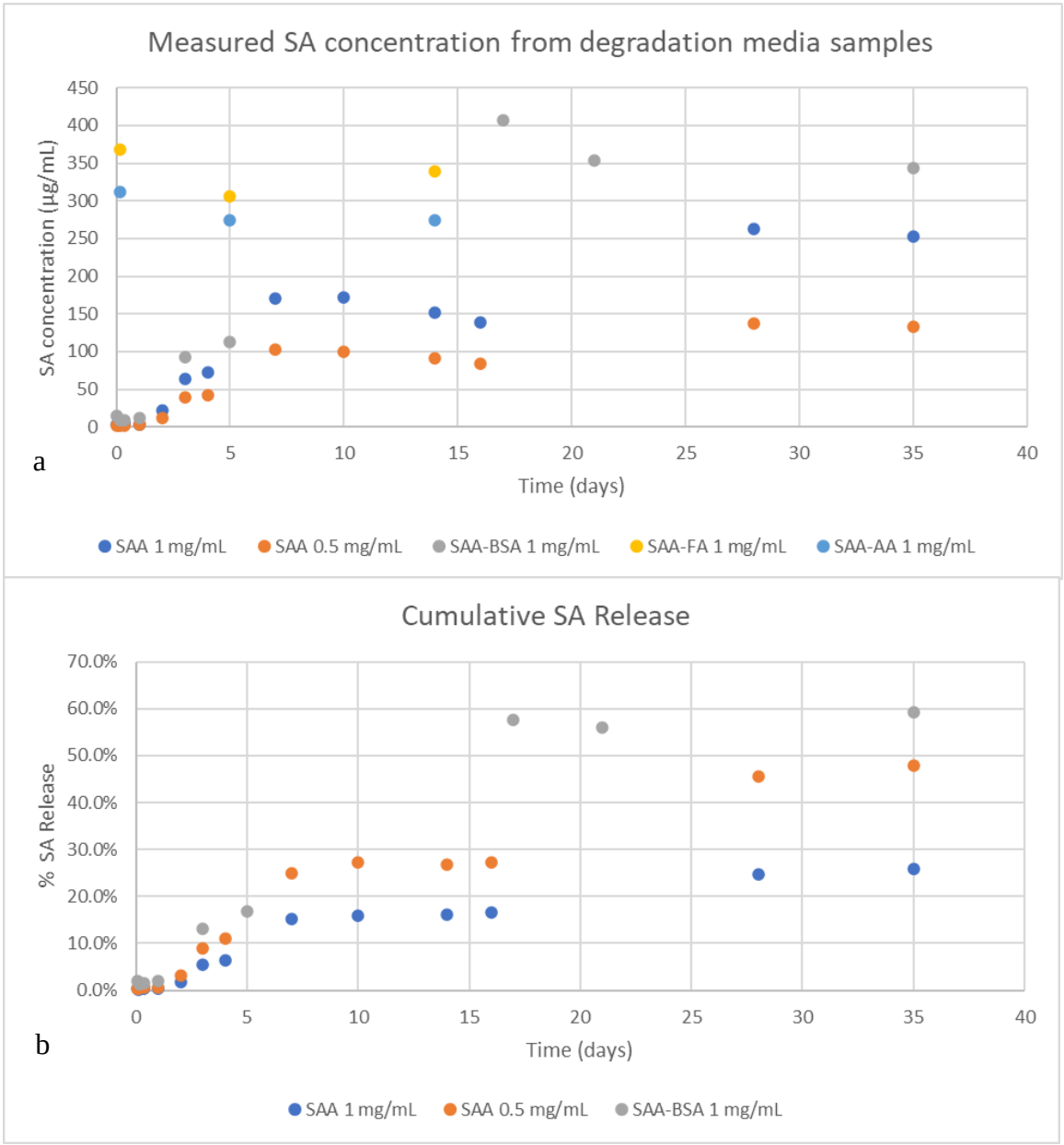

Figure 4.16: Measured and cumulative SA release from select SAPAE with concentrations listed in the legend.

During SAPAE degradation, the anhydride bonds are less stable in water and will hydrolyze first relative to the ester bonds, and SA will be released upon hydrolysis of the ester bonds. Initial SA release in these studies likely came from low-M_w polymer, residual SA, or residual diacid. The plateaus are likely periods where higher M_w SAA breaks down into oligomers or water is being imbibed into the microspheres. This process should occur faster in the SAA copolymers, since there is a lower SA mass fraction and an increase in the relative mass fraction of ester and anhydride groups, which makes these polymers more hydrophilic. Adding NaOH to the degradation media to a concentration of 1 M will hydrolyze any remaining SAPAE and diacid. These data can be used to determine the actual SA mass at 100% release.

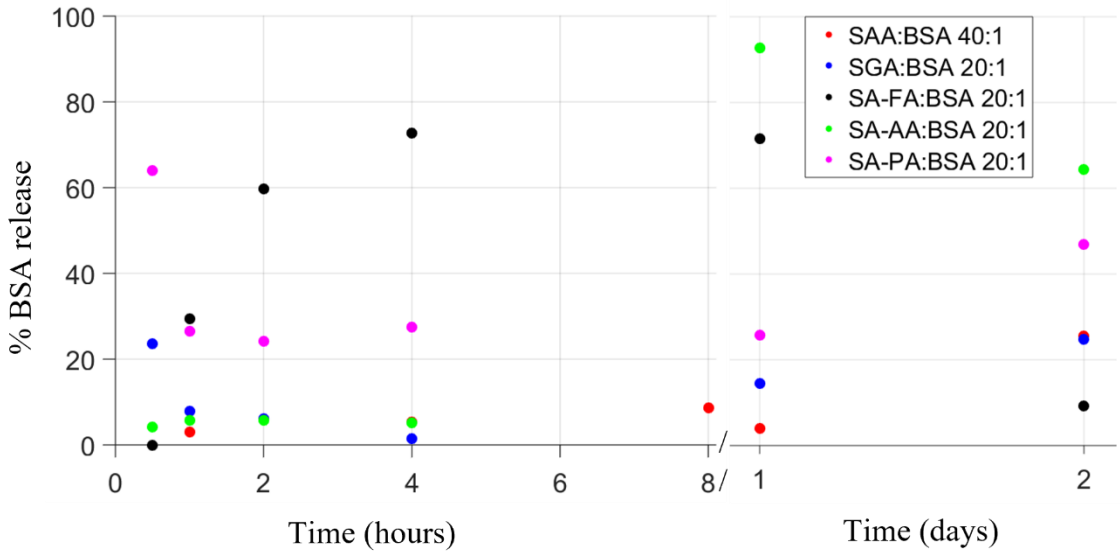

Figure 4.17: BSA release from SAPAE polymers and copolymers. The x-axis is split to better show the early stages of BSA release.

BSA release began within 30 minutes for SAA-FA and SAA-PA (Fig 4.17). SGA showed an initial burst release, then a gradual increase in BSA release through 1-2 days.

SAA-AA had a delayed release of 1 day, but then had a higher BSA release than any other polymer. SAA had a slow release until 2 days had passed. Attempts were made to study SA release from 0.5-4 hours in PBS for the fast-degrading polymers, but the measured SA content varied dramatically per time point (Table 4.4), even decreasing significantly as time passed despite corrections for the SA mass removed from the system. No degradation media was observed leaking from the centrifuge tubes, so these results could be due to poor SA distribution in the degradation media when sampled.

Table 4.4 SA mass released from fast-degrading SAPAEs

Cumulative SA mass released (μm)						
Time (hours):	0.5	1	2	4	24	48
SA-AA	53	77	323	1220	117	177
SA-FA	675	164	114	120	509	497
SGA	803	822	1270	203	234	251
SGAE	66	94	394	600	527	319
SA-PA	897	262	206	398	926	1310
SA-PAE	1050	1360	1190	1670	918	1280

4.5 Conclusions and Future Work

Although SAPAEs have been synthesized for over 20 years, there remain unknowns and inconsistencies in their synthesis procedure. Sources of variation could arise from the different pieces of equipment, precursor chemicals, and environments (building temperature, humidity, air quality, etc.) that have been used over this time frame, or from structure-processing relationships of these polymers. Impurities in the precursor compounds can persist and cause unknown effects throughout the polymerization. For SAPAEs, water is a significant concern. My studies on SAPAE

synthesis show that the water content of the diacid significantly affects the required polymerization times. The polymer and diacid can also break down during the process, forming adipic acid that persists through the polymerization. This breakdown results in a polymer that, as a result of processing conditions, has a different structure than intended.

The SAPAE synthesis process needs to be systematically studied to identify why the adipic acid is cleaved (Table 4.5). For example, multiple diacid batches can be mixed and recrystallized together to get > 50 g of diacid with the same amount of water, thus holding that variable constant. As another example, the temperatures and times used during vacuum distillation step should be varied to determine their effects. Finally, lower polymerization temperatures could be investigated as results showed that SAPAE can be polymerized quickly at low temperatures.

Table 4.5 Example experimental plan to evaluate SAPAE polymerization parameters

SAPAE polymerization step	Parameters to vary
Anhydride Exchange	Diacid:acetic anhydride ratio. 25, 50, 100 mL anhydride per 5 g diacid Temperature: room temperature, 50, 100 ^{o}C
Vacuum distillation	Duration: 30 min, 1h, 2h Temperature: 50, 70, 90 ^{o}C or combinations of two temperatures
Polymerization	Temperature: 140, 160 ^{o}C
Characterize monomer after distillation by ^{1}H NMR and polymer by ^{1}H NMR and GPC	

Using the microsphere synthesis and degradation study procedures described herein, future researchers should collect enough data for statistical analysis on the degradation and BSA release of different SAPAE polymers and copolymers. Introducing

new polymers may necessitate slight modifications to these procedures. Similarly, longer-degrading SAPAEs should be investigated as protective coatings for Mg bone implants. Slower SA release should lead to better cytocompatibility and slow the Mg corrosion.

By synthesizing and characterizing SAPAEs, the full range of SPPP relationships was explored. Changing the SAPAE molecular formula through copolymerization or by changing the linker controls how these polymers must be processed, their properties, and their performance for a desired application. Problems in the SAPAE synthesis process result in a polymer structure different than the target structure, which will change the properties and performance of SAPAEs. Specific applications require SAPAEs with different properties. Protective coatings for Mg bone implants require slow-degrading SAPAEs, while other applications require fast degradation and the release of encapsulated proteins. The flexibility of SAPAEs, with tailorable structures, processing, and properties to meet desired applications, exemplifies this fundamental tenet of polymer materials science. As more manufacturers look towards green alternatives to traditional products, SAPAEs will become more widely used.

4.6 References

(1) Paterson, J. R. Salicylic Acid: A Link between Aspirin, Diet and the Prevention of Colorectal Cancer. *QJM* **2001**, *94* (8), 445–448. https://doi.org/10.1093/qjmed/94.8.445.

(2) Vane, J. R.; Botting, R. M. Mechanism of Action of Nonsteroidal Anti-Inflammatory Drugs. *The American Journal of Medicine.* **1998**, *104* (3A), 2S-8S.

(3) Arif, T. Salicylic Acid as a Peeling Agent: A Comprehensive Review. *CCID* **2015**, 455. https://doi.org/10.2147/CCID.S84765.

(4) Prudencio, A.; Schmeltzer, R. C.; Uhrich, K. E. Effect of Linker Structure on Salicylic Acid-Derived Poly(Anhydride−esters). *Macromolecules* **2005**, *38* (16), 6895–6901. https://doi.org/10.1021/ma048051u.

(5) Schmeltzer, R. C.; Schmalenberg, K. E.; Uhrich, K. E. Synthesis and Cytotoxicity of Salicylate-Based Poly(Anhydride Esters). *Biomacromolecules*. **2005**, *6*, 359-367.

(6) Mitchell, A.; Kim, B.; Cottrell, J.; Snyder, S.; Witek, L.; Ricci, J.; Uhrich, K. E.; Patrick O'Connor, J. Development of a Guided Bone Regeneration Device Using Salicylic Acid-Poly(Anhydride-Ester) Polymers and Osteoconductive Scaffolds: Guided Bone Regeneration Device Development. *J. Biomed. Mater. Res.* **2014**, *102* (3), 655–664. https://doi.org/10.1002/jbm.a.34728.

(7) Yu, W.; Bien-Aime, S.; Mattos, M.; Alsadun, S.; Wada, K.; Rogado, S.; Fiorellini, J.; Graves, D.; Uhrich, K. Sustained, Localized Salicylic Acid Delivery Enhances Diabetic Bone Regeneration via Prolonged Mitigation of Inflammation. *J. Biomed. Mater. Res.* **2016**, *104* (10), 2595–2603. https://doi.org/10.1002/jbm.a.35781.

(8) Wada, K.; Yu, W.; Elazizi, M.; Barakat, S.; Ouimet, M. A.; Rosario-Meléndez, R.; Fiorellini, J. P.; Graves, D. T.; Uhrich, K. E. Locally Delivered Salicylic Acid from a Poly(Anhydride-Ester): Impact on Diabetic Bone Regeneration. *Journal of Controlled Release* **2013**, *171* (1), 33–37. https://doi.org/10.1016/j.jconrel.2013.06.024.

(9) Bryers, J. D.; Jarvis, R. A.; Lebo, J.; Prudencio, A.; Kyriakides, T. R.; Uhrich, K. Biodegradation of Poly(Anhydride-Esters) into Non-Steroidal Anti-Inflammatory Drugs and Their Effect on Pseudomonas Aeruginosa Biofilms in Vitro and on the Foreign-Body Response in Vivo. *Biomaterials* **2006**, *27* (29), 5039–5048. https://doi.org/10.1016/j.biomaterials.2006.05.034.

(10) Harten, R. D.; Svach, D. J.; Schmeltzer, R.; Uhrich, K. E. Salicylic Acid-Derived Poly(Anhydride-Esters) Inhibit Bone Resorption and Formationin Vivo. *J. Biomed. Mater. Res.* **2005**, *72A* (4), 354–362. https://doi.org/10.1002/jbm.a.30184.

(11) Johnson, I.; Wang, S. M.; Silken, C.; Liu, H. A Systemic Study on Key Parameters Affecting Nanocomposite Coatings on Magnesium Substrates. *Acta Biomaterialia* **2016**, *36*, 332–349. https://doi.org/10.1016/j.actbio.2016.03.026.

(12) Carbone, A. L.; Song, M.; Uhrich, K. E. Iodinated Salicylate-Based Poly(Anhydride-Esters) as Radiopaque Biomaterials. *Biomacromolecules* **2008**, *9* (6), 1604–1612. https://doi.org/10.1021/bm8000759.

(13) Yeagy, B. A.; Prudencio, A.; Schmeltzer, R. C.; Uhrich, K. E.; Cook, T. J. Characterization and ***in Vitro*** Degradation of Salicylate-Derived Poly(Anhydride-Ester Microspheres). *Journal of Microencapsulation* **2006**, *23* (6), 643–653. https://doi.org/10.1080/02652040600776481.

(14) Whitaker-Brothers, K.; Uhrich, K. Poly(Anhydride-Ester) Fibers: Role of Copolymer Composition on Hydrolytic Degradation and Mechanical Properties. *J. Biomed. Mater. Res.* **2004**, *70A* (2), 309–318. https://doi.org/10.1002/jbm.a.30083.

(15) Whitaker-Brothers, K.; Uhrich, K. Investigation into the Erosion Mechanism of Salicylate-Based Poly(Anhydride-Esters). *J. Biomed. Mater. Res.* **2006**, *76A* (3), 470–479. https://doi.org/10.1002/jbm.a.30356.

(16) deRonde, B. M.; Carbone, A. L.; Uhrich, K. Storage Stability Study of Salicylate-Based Poly(Anhydride-Esters). *Polymer Degradation and Stability* **2010**, *95* (9), 1778–1782. https://doi.org/10.1016/j.polymdegradstab.2010.05.008.

(17) Snyder, S. S.; Anastasiou, T. J.; Uhrich, K. E. In Vitro Degradation of an Aromatic Polyanhydride with Enhanced Thermal Properties. *Polymer Degradation and Stability* **2015**, *115*, 70–76. https://doi.org/10.1016/j.polymdegradstab.2015.02.002.

(18) Delgado-Rivera, R.; Rosario-Meléndez, R.; Yu, W.; Uhrich, K. E. Biodegradable Salicylate-Based Poly(Anhydride-Ester) Microspheres for Controlled Insulin Delivery: Biodegradable Salicylate-Based Paes Microspheres. *J. Biomed. Mater. Res.* **2014**, *102* (8), 2736–2742. https://doi.org/10.1002/jbm.a.34949.

(19) Yu, W.; Bien-Aime, S.; Li, J.; Zhang, L.; McCormack, E. S.; Goldberg, I. D.; Narayan, P.; Uhrich, K. E. Injectable Microspheres for Extended Delivery of Bioactive Insulin and Salicylic Acid. *Journal of Bioactive and Compatible Polymers* **2015**, *30* (3), 340–346. https://doi.org/10.1177/0883911515569919.

(20) Faig, J. J.; Smith, K.; Moretti, A.; Yu, W.; Uhrich, K. E. One-Pot Polymerization Syntheses: Incorporating Bioactives into Poly(Anhydride-Esters). *Macromol. Chem. Phys.* **2016**, *217* (16), 1842–1850. https://doi.org/10.1002/macp.201600115.

(21) Schmeltzer, R. C.; Johnson, M.; Griffin, J.; Uhrich, K. Comparison of Salicylate-Based Poly(Anhydride-Esters) Formed via Melt-Condensation versus Solution Polymerization. *Journal of Biomaterials Science, Polymer Edition* **2008**, *19* (10), 1295–1306. https://doi.org/10.1163/156856208786052362.

(22) Mittal, K. L. Adhesion Measurement of Thin Films. *Electrocomponent Science and Technology*. **1976,** *3*, 21-42.

(23) Xu, L.; Yamamoto, A. Characteristics and Cytocompatibility of Biodegradable Polymer Film on Magnesium by Spin Coating. *Colloids and Surfaces B: Biointerfaces* **2012**, *93*, 67–74. https://doi.org/10.1016/j.colsurfb.2011.12.009.

Chapter 5: Conclusions and Future Work

A material's behavior (performance) can always be traced back to its structure, processing, or properties. Changes in polyacrylonitrile molecular structure like acidic copolymers make processing easier, and changing the temperature, tension, and atmosphere of the oxidative stabilization process affects the properties and performance of carbon fiber made from PAN precursors. Spider silk is one of the strongest natural fibers due to its protein structure and spiders' ability to fold silk proteins during fiber spinning (processing). Regrettably, the stabilization and carbonization processes used to make carbon fiber disrupt the hydrogen bonds in silk, making it lose its inherent strength even though it does graphitize. SAPAEs have tailorable structures to control degradation rate, but impurities which form during polymerization could change the behavior of the resulting polymers.

My dissertation studies have mostly failed. Yet as scientists, we often learn more from failure than we do from success. Although my WAXS experiments on PAN failed, I performed a thorough literature review and can advise the next generation of students to better calibrate their *in-situ* system and perform complementary *ex-situ* studies. Despite the PAN fibers not reaching the desired stabilization temperature, the diffraction data collected was quantifiable using methods which should be applied to future studies. Although I was unable to understand how spiders fold spidroins into silk proteins, my results suggest that pH and shear are the main factors and the salt ion gradient along the MA gland duct is a product of proton pumps. While spider silk itself is not an ideal natural carbon fiber precursor, the polyalanine repeat sections of the protein structure do

graphitize and thus could be incorporated into a synthetic or hybrid peptide. With the data I have collected and improvements I have made to SAPAE polymerization, future students are on the path towards identifying the ideal process parameters for a more reliable polymerization. Similarly, future students can use the microsphere synthesis and characterization procedures I developed to create a library of SAPAE microspheres for protein encapsulation and controlled release. Finally, these studies have enlightened certain design principles for sustainable materials.

If natural materials or polymers made from natural precursors are used in processes designed for synthetic materials, they must fit the mold of the material they are trying to replace. For example, oxidative stabilization is designed for polyacrylonitrile. Heat gives enough energy for cyclization and dehydrogenation to occur, and the air provides oxygen to catalyze carbonization. Natural precursors to replace PAN should behave similarly if used in the same process, ideally with a direct crystalline transition from the native structure to graphite. Alternatively, different processes should be developed that better adapt to the structures of natural materials. Perhaps certain polysaccharides can be annealed in inert atmospheres or irradiated to catalyze graphitization. Finally, the limitations of natural materials in synthetic processes could be considered. In the case of spider silk, it should not be processed in a way that disrupts hydrogen bonding within the spidroins.

Following the 12 principles of green chemistry, using renewable feedstocks is the first step towards making sustainable materials. Nature inherently creates materials through non-toxic processes, lest the organisms creating those materials die during

synthesis. With SAPAEs as an example, polymers made using natural materials have the necessary building blocks for non-toxic, efficient synthesis procedures. Future polymers should be intelligently designed from natural or renewable precursors based on the end application. Conductive polymers should use highly aromaticized precursors. Structural polymers should use semicrystalline, structural natural precursors. While many attempts to replace synthetic materials with natural ones consist of throwing a natural material like spider silk in a process meant for synthetic polymers, this is not the way. Instead, natural precursors should be used to make new materials and processes to create sustainable polymers. This includes synthesizing natural materials through genetic engineering, making synthetic natural materials like peptoids, or combining natural and synthetic precursors.

5.1 Complete Bibliography

Agnarsson, I.; Boutry, C.; Blackledge, T. A. Spider Silk Aging: Initial Improvement in a High Performance Material Followed by Slow Degradation. *J. Exp. Zool. Part Ecol. Genet. Physiol.* **2008**, *309A* (8), 494–504. https://doi.org/10.1002/jez.480.

Alexander, L. *X-Ray Diffractio Methods in Polymer Science*; John Wiley & Sons, Inc.: New York, 1969.

Andersson, M.; Jia, Q.; Abella, A.; Lee, X.-Y.; Landreh, M.; Purhonen, P.; Hebert, H.; Tenje, M.; Robinson, C. V.; Meng, Q.; Plaza, G. R.; Johansson, J.; Rising, A. Biomimetic Spinning of Artificial Spider Silk from a Chimeric Minispidroin. *Nat. Chem. Biol.* **2017**, *13* (3), 262–264. https://doi.org/10.1038/nchembio.2269.

Arif, T. Salicylic Acid as a Peeling Agent: A Comprehensive Review. *CCID* **2015**, 455. https://doi.org/10.2147/CCID.S84765.

Babb, P. L.; Lahens, N. F.; Correa-Garhwal, S. M.; Nicholson, D. N.; Kim, E. J.; Hogenesch, J. B.; Kuntner, M.; Higgins, L.; Hayashi, C. Y.; Agnarsson, I.; Voight, B. F. The Nephila Clavipes Genome Highlights the Diversity of Spider Silk Genes and Their Complex Expression. *Nat. Genet.* **2017**, *49* (6), 895–903.

Bacon, R. Filamentary Graphite and Method for Producing the Same. 2957756, October 15, 1960.

Bang, Y. H.; Lee, S.; Cho, H. H. Effect of Methyl Acrylate Composition on the Microstructure Changes of High Molecular Weight Polyacrylonitrile for Heat Treatment. *J. Appl. Polym. Sci.* **1998**, *68*, 2205–2213.

Bashir, Z. A Critical Review of the Stabilisation of Polyacrylonitrile. *Carbon* **1991**, *29* (8), 1081–1090. https://doi.org/10.1016/0008-6223(91)90024-D.
Bell, F. A.; Lehrle, R. S.; Robb, J. C. Polyacrylonitrile Degradation Kinetics Studied by the Micropyrolysis—g.l.c. Technique. *Polymer* **1971**, *12* (9), 579–599. https://doi.org/10.1016/0032-3861(71)90039-5.

Belyaev, S. S.; Arkhangelsky, I. V.; Makarenko, I. V. Non-Isothermal Kinetic Analysis of Oxidative Stabilization Processes in PAN Fibers. *Thermochim. Acta* **2010**, *507–508*, 9–14. https://doi.org/10.1016/j.tca.2010.04.022.

Blackledge, T. A.; Boutry, C.; Wong, S.-C.; Baji, A.; Dhinojwala, A.; Sahni, V.; Agnarsson, I. How Super Is Supercontraction? Persistent versus Cyclic Responses to Humidity in Spider Dragline Silk. *J. Exp. Biol.* **2009**, *212* (13), 1981–1989. https://doi.org/10.1242/jeb.028944.

Blackledge, T. A.; Cardullo, R. A.; Hayashi, C. Y. Polarized Light Microscopy, Variability in Spider Silk Diameters, and the Mechanical Characterization of Spider Silk: Polarized Light Microscopy of Spider Silk. *Invertebr. Biol.* **2005**, *124* (2), 165–173. https://doi.org/10.1111/j.1744-7410.2005.00016.x.

Bohn, C. R.; Schaefgen, J. R.; Statton, W. O. Laterally Ordered Polymers: Polyacrylonitrile and Poly(Vinyl Trifluoroacetate). *J. Polym. Sci.* **1961**, *55* (162), 531–549.

Boutry, C.; Blackledge, T. A. Wet Webs Work Better: Humidity, Supercontraction and the Performance of Spider Orb Webs. *J. Exp. Biol.* **2013**, *216* (19), 3606–3610. https://doi.org/10.1242/jeb.084236.

Brooks, A. Distinct Contributions of Model MaSp1 and MaSp2 like Peptides to the Mechanical Properties of Synthetic Major Ampullate Silk Fibers as Revealed in Silico. *Nanotechnol. Sci. Appl.* **2008**, *Volume 1*, 9–16. https://doi.org/10.2147/NSA.S3961.

Brown, C. P.; Whaite, A. D.; MacLeod, J. M.; Macdonald, J.; Rosei, F. With Great Structure Comes Great Functionality: Understanding and Emulating Spider Silk. *J. Mater. Res.* **2015**, *30* (1), 108–120. https://doi.org/10.1557/jmr.2014.365.

Bryers, J. D.; Jarvis, R. A.; Lebo, J.; Prudencio, A.; Kyriakides, T. R.; Uhrich, K. Biodegradation of Poly(Anhydride-Esters) into Non-Steroidal Anti-Inflammatory Drugs and Their Effect on Pseudomonas Aeruginosa Biofilms in Vitro and on the Foreign-Body Response in Vivo. *Biomaterials* **2006**, *27* (29), 5039–5048. https://doi.org/10.1016/j.biomaterials.2006.05.034.

Carbone, A. L.; Song, M.; Uhrich, K. E. Iodinated Salicylate-Based Poly(Anhydride-Esters) as Radiopaque Biomaterials. *Biomacromolecules* **2008**, *9* (6), 1604–1612. https://doi.org/10.1021/bm8000759.

Cardoso dos Santos, L. G.; Kawano, Y. Degradation of Polyacrylonitrile by X-Ray Radiation. *Polym. Degrad. Stab.* **1994**, *44*, 27–32.

Casem, M. L.; Tran, L. P. P.; Moore, A. M. F. Ultrastructure of the Major Ampullate Gland of the Black Widow Spider, Latrodectus Hesperus. *Tissue Cell* **2002**, *34* (6), 427–436. https://doi.org/10.1016/S0040816602000836.

Chae, H. G.; Choi, Y. H.; Minus, M. L.; Kumar, S. Carbon Nanotube Reinforced Small Diameter Polyacrylonitrile Based Carbon Fiber. *Compos. Sci. Technol.* **2009**, *69* (3–4), 406–413. https://doi.org/10.1016/j.compscitech.2008.11.008.

Chae, H. G.; Minus, M. L.; Rasheed, A.; Kumar, S. Stabilization and Carbonization of Gel Spun Polyacrylonitrile/Single Wall Carbon Nanotube Composite Fibers. *Polymer* **2007**, *48* (13), 3781–3789. https://doi.org/10.1016/j.polymer.2007.04.072.

Chaw, R. C.; Correa-Garhwal, S. M.; Clarke, T. H.; Ayoub, N. A.; Hayashi, C. Y. Proteomic Evidence for Components of Spider Silk Synthesis from Black Widow Silk Glands and Fibers. *J. Proteome Res.* **2015**, *14* (10), 4223–4231. https://doi.org/10.1021/acs.jproteome.5b00353.

Cho, D. W.; Hong, S. C. Synergistic Effect of Comonomers on the Thermal Oxidative Stabilization of Polyacrylonitrile Copolymers for Carbon Materials. *Polym. Degrad. Stab.* **2019**, *161*, 191–197. https://doi.org/10.1016/j.polymdegradstab.2019.01.027.

Cho, S. Y.; Yun, Y. S.; Lee, S.; Jang, D.; Park, K.-Y.; Kim, J. K.; Kim, B. H.; Kang, K.; Kaplan, D. L.; Jin, H.-J. Carbonization of a Stable β-Sheet-Rich Silk Protein into a Pseudographitic Pyroprotein. *Nat. Commun.* **2015**, *6* (1). https://doi.org/10.1038/ncomms8145.

Choi, J.; Kim, S.-S.; Chung, Y.-S.; Lee, S. Evolution of Structural Inhomogeneity in Polyacrylonitrile Fibers by Oxidative Stabilization. *Carbon* **2020**, *165*, 225–237. https://doi.org/10.1016/j.carbon.2020.04.027.

Chu, P. K.; Li, L. Characterization of Amorphous and Nanocrystalline Carbon Films. *Mater. Chem. Phys.* **2006**, *96* (2–3), 253–277.

Cipriani, E.; Zanetti, M.; Bracco, P.; Brunella, V.; Luda, M. P.; Costa, L. Crosslinking and Carbonization Processes in PAN Films and Nanofibers. *Polym. Degrad. Stab.* **2016**, *123*, 178–188.

Colvin, B. G.; Storr, P. The Crystal Structure of Polyacrylonitrile. *Eur. Polym. J.* **1974**, *10* (4), 337–340.

Correa-Garhwal, S. M.; Chaw, R. C.; Dugger, T.; Clarke, T. H.; Chea, K. H.; Kisailus, D.; Hayashi, C. Y. Semi-aquatic Spider Silks: Transcripts, Proteins, and Silk Fibres of the Fishing Spider, *Dolomedes Triton* (Pisauridae). *Insect Mol. Biol.* **2019**, *28* (1), 35–51. https://doi.org/10.1111/imb.12527.

Creager, M. S.; Jenkins, J. E.; Thagard-Yeaman, L. A.; Brooks, A. E.; Jones, J. A.; Lewis, R. V.; Holland, G. P.; Yarger, J. L. Solid-State NMR Comparison of Various Spiders' Dragline Silk Fiber. *Biomacromolecules* **2010**, *11* (8), 2039–2043. https://doi.org/10.1021/bm100399x.

Dalton, S.; Heatley, F.; Budd, P. M. Thermal Stabilization of Polyacrylonitrile Fibres. *Polymer* **1999**, *40* (20), 5531–5543. https://doi.org/10.1016/S0032-3861(98)00778-2.

Delgado-Rivera, R.; Rosario-Meléndez, R.; Yu, W.; Uhrich, K. E. Biodegradable Salicylate-Based Poly(Anhydride-Ester) Microspheres for Controlled Insulin Delivery: Biodegradable Salicylate-Based Paes Microspheres. *J. Biomed. Mater. Res.* **2014**, *102* (8), 2736–2742. https://doi.org/10.1002/jbm.a.34949.

deRonde, B. M.; Carbone, A. L.; Uhrich, K. Storage Stability Study of Salicylate-Based Poly(Anhydride-Esters). *Polymer Degradation and Stability* **2010**, *95* (9), 1778–1782. https://doi.org/10.1016/j.polymdegradstab.2010.05.008.

Devasia, R.; Nair, C. P. R.; Sivadasan, P.; Katherine, B. K.; Ninan, K. N. Cyclization Reaction in Poly(Acrylonitrile/Itaconic Acid) Copolymer: An Isothermal Differential Scanning Calorimetry Kinetic Study. *J. Appl. Polym. Sci.* **2003**, *88* (4), 915–920. https://doi.org/10.1002/app.11706.

Dicko, C.; Kenney, J. M.; Knight, D.; Vollrath, F. Transition to a β-Sheet-Rich Structure in Spidroin in Vitro: The Effects of PH and Cations †. *Biochemistry* **2004**, *43* (44), 14080–14087. https://doi.org/10.1021/bi0483413.

Dietrich, J.; Hirt, P.; Herlinger, H. Electron-Beam-Induced Cyclisation to Obtain C-Fibre Precursors from Polyacrylonitrile Homopolymers. *Eur. Polym. J.* **1996**, *32* (5), 617–623. https://doi.org/10.1016/0014-3057(95)00185-9.

Dong, Z.; Lewis, R. V.; Middaugh, C. R. Molecular Mechanism of Spider Silk Elasticity. *Arch. Biochem. Biophys.* **1991**, *284* (1), 53–57. https://doi.org/10.1016/0003-9861(91)90262-H.

Dugger, T. W.; Sarkar, S.; Correa-Garhwal, S. M.; Zhernenkov, M.; Zhang, Y.; Kolhatkar, G.; Mohan, R.; Cruz, L.; Lubio, A. D.; Ruediger, A.; Hayashi, C. Y.; Uhrich, K. E.; Kisailus, D. J. Ultrastructures and Mechanics of Annealed *Nephila Clavipes* Major Ampullate Silk. *Biomacromolecules* **2020**, *21* (3), 1186–1194. https://doi.org/10.1021/acs.biomac.9b01615.

Edison, T. Electric Lamp. US Patent No. 223898, January 27, 1880.

Elices, M.; Pérez-Rigueiro, J.; Plaza, G.; Guinea, G. V. Recovery in Spider Silk Fibers: Recovery in Spider Silk Fibers. *J. Appl. Polym. Sci.* **2004**, *92* (6), 3537–3541. https://doi.org/10.1002/app.20383.

Ene, R.; Papadopoulos, P.; Kremer, F. Supercontraction in Nephila Spider Dragline Silk – Relaxation into Equilibrium State. *Polymer* **2011**, *52* (26), 6056–6060. https://doi.org/10.1016/j.polymer.2011.10.056.

Ezekiel, H. M.; Spain, R. G. Preparation of Graphite Fibers from Polymeric Fibers. *J. Polym. Sci. Part C Polym. Symp.* **2007**, *19* (1), 249–265. https://doi.org/10.1002/polc.5070190120.

Faber, K. T.; Evans, A. G. Crack Deflection Processes—I. Theory. *Acta Metall.* **1983**, *31* (4), 565–576.

Faber, K. T.; Evans, A. G. Crack Deflection Processes—II. Experiment. *Acta Metall.* **1983**, *31* (4), 577–584.

Faig, J. J.; Smith, K.; Moretti, A.; Yu, W.; Uhrich, K. E. One-Pot Polymerization Syntheses: Incorporating Bioactives into Poly(Anhydride-Esters). *Macromol. Chem. Phys.* **2016**, *217* (16), 1842–1850. https://doi.org/10.1002/macp.201600115.

Ferrari, A. C. Raman Spectroscopy of Graphene and Graphite: Disorder, Electron–Phonon Coupling, Doping and Nonadiabatic Effects. *Solid State Commun.* **2007**, *143* (1–2), 47–57.

Ferrari, A. C.; Robertson, J. Interpretation of Raman Spectra of Disordered and Amorphous Carbon. *Phys. Rev. B* **2000**, *61* (20), 14095–14107.

Fitzer, E. Pan-Based Carbon Fibers—Present State and Trend of the Technology from the Viewpoint of Possibilities and Limits to Influence and to Control the Fiber Properties by the Process Parameters. *Carbon* **1989**, *27* (5), 621–645.

Fitzer, E.; Müller, D. J. The Influence of Oxygen on the Chemical Reactions during Stabilization of Pan as Carbon Fiber Precursor. *Carbon* **1975**, *13* (1), 63–69. https://doi.org/10.1016/0008-6223(75)90259-6.

Foelix, R. *Biology of Spiders*, 3rd ed.; Oxford University Press: New York, 2011.

Ford, C. Fibrous Graphite. US Patent No. 3107152, October 15, 1963.

Fu, Z.; Gui, Y.; Cao, C.; Liu, B.; Zhou, C.; Zhang, H. Structure Evolution and Mechanism of Polyacrylonitrile and Related Copolymers during the Stabilization. *J. Mater. Sci.* **2014**, *49* (7), 2864–2874. https://doi.org/10.1007/s10853-013-7992-3.

Fu, Z.; Liu, B.; Sun, L.; Zhang, H. Study on the Thermal Oxidative Stabilization Reactions and the Formed Structures in Polyacrylonitrile during Thermal Treatment. *Polym. Degrad. Stab.* **2017**, *140*, 104–113. https://doi.org/10.1016/j.polymdegradstab.2017.04.018.

Ge, J. J.; Hou, H.; Li, Q.; Graham, M. J.; Greiner, A.; Reneker, D. H.; Harris, F. W.; Cheng, S. Z. D. Assembly of Well-Aligned Multiwalled Carbon Nanotubes in Confined

Polyacrylonitrile Environments: Electrospun Composite Nanofiber Sheets. *J. Am. Chem. Soc.* **2004**, *126* (48), 15754–15761. https://doi.org/10.1021/ja048648p.

Glišović, A.; Salditt, T. Temperature Dependent Structure of Spider Silk by X-Ray Diffraction. *Appl. Phys. A* **2007**, *87* (1), 63–69. https://doi.org/10.1007/s00339-006-3849-9.

Gosline, J. M.; Guerette, P. A.; Ortlepp, C. S.; Savage, K. N. The Mechanical Design of Spider Silks: From Fibroin Sequence to Mechanical Function. *J. Exp. Biol.* **1999**, *202* (23), 3295–3303.

Grassie, N.; McGuchan, R. Pyrolysis of Polyacrylonitrile and Related Polymers-I: Thermal Analysis of Polyacrylonitrile. *Eur. Polym. J.* **1970**, *6*, 1277–1291.

Grassie, N.; McGuchan, R. Pyrolysis of Polyacrylonitrile and Related Polymers—IX. *Eur. Polym. J.* **1973**, *9* (6), 507–517. https://doi.org/10.1016/0014-3057(73)90034-7.

Grassie, N.; McGuchan, R. Pyrolysis of Polyacrylonitrile and Related Polymers—VI. Acrylonitrile Copolymers Containing Carboxylic Acid and Amide Structures. *Eur. Polym. J.* **1972**, *8* (2), 257–269. https://doi.org/10.1016/0014-3057(72)90032-8.

Grassie, N.; McGuchan, R. Pyrolysis of Polyacrylonitrile and Related Polymers—VII. *Eur. Polym. J.* **1972**, *8* (7), 865–878. https://doi.org/10.1016/0014-3057(72)90046-8.

Grassie, N.; McGuchan, R. Pyrolysis of Polyacrylonitrile and Related Polymers—VIII. Copolymers of Acrylonitrile with Vinyl Acetate, Vinyl Formate, Acrolein and Methyl Vinyl Ketone. *Eur. Polym. J.* **1973**, *9* (2), 113–124. https://doi.org/10.1016/0014-3057(73)90134-1.

Grubb, D. T.; Jelinski, L. W. Fiber Morphology of Spider Silk: The Effects of Tensile Deformation. *Macromolecules* **1997**, *30* (10), 2860–2867. https://doi.org/10.1021/ma961293c.

Guinea, G. V.; Elices, M.; Pérez-Rigueiro, J.; Plaza, G. R. Stretching of Supercontracted Fibers: A Link between Spinning and the Variability of Spider Silk. *J. Exp. Biol.* **2005**, *208* (1), 25–30. https://doi.org/10.1242/jeb.01344.

Guinea, G. V.; Elices, M.; Pérez-Rigueiro, J.; Plaza, G. Self-Tightening of Spider Silk Fibers Induced by Moisture. *Polymer* **2003**, *44* (19), 5785–5788. https://doi.org/10.1016/S0032-3861(03)00625-6.

Gupta, A. K.; Paliwal, D. K.; Bajaj, P. Acrylic Precursors for Carbon Fibers. *Polym. Rev.* **1991**, *31* (1), 1–89. https://doi.org/10.1080/15321799108021557.

Gupta, A.; Harrison, I. R. New Aspects in the Oxidative Stabilization of PAN-Based Carbon Fibers. *Carbon* **1996**, *34* (11), 1427–1445. https://doi.org/10.1016/S0008-6223(96)00094-2.

Gupta, A.; Harrison, I. R. New Aspects in the Oxidative Stabilization of PAN-Based Carbon Fibers: II. *Carbon* **1997**, *35* (6), 809–818. https://doi.org/10.1016/S0008-6223(97)00025-0.

Gupta, A.; Harrison, I. R.; Lahijani, J. Small-Angle X-Ray Scattering in Carbon Fibers. *J. Appl. Crystallogr.* **1994**, *27* (4), 627–636. https://doi.org/10.1107/S002188989400227X.
Hajir Bahrami, S.; Bajaj, P.; Sen, K. Thermal Behavior of Acrylonitrile Carboxylic Acid Copolymers. *J. Appl. Polym. Sci.* **2003**, *88* (3), 685–698. https://doi.org/10.1002/app.11637.

Harten, R. D.; Svach, D. J.; Schmeltzer, R.; Uhrich, K. E. Salicylic Acid-Derived Poly(Anhydride-Esters) Inhibit Bone Resorption and Formationin Vivo. *J. Biomed. Mater. Res.* **2005**, *72A* (4), 354–362. https://doi.org/10.1002/jbm.a.30184.

Hayashi, C. Y.; Shipley, N. H.; Lewis, R. V. Hypotheses That Correlate the Sequence, Structure, and Mechanical Properties of Spider Silk Proteins. *Int. J. Biol. Macromol.* **1999**, *24* (2–3), 271–275. https://doi.org/10.1016/S0141-8130(98)00089-0.

He, J.-H.; Liu, Y.; Xu, L.; Yu, J.-Y.; Sun, G. BioMimic Fabrication of Electrospun Nanofibers with High-Throughput. *Chaos Solitons Fractals* **2008**, *37* (3), 643–651. https://doi.org/10.1016/j.chaos.2007.11.028.

Hermans, P. H. *Contribution to the Physics of Cellulose Fibers*; Elsevier Publishing Company, INC: Amsterdam, 1946.

Hexemer, A.; Bras, W.; Glossinger, J.; Schaible, E.; Gann, E.; Kirian, R.; MacDowell, A.; Church, M.; Rude, B.; Padmore, H. A SAXS/WAXS/GISAXS Beamline with Multilayer Monochromator. *J. Phys. Conf. Ser.* **2010**, *247*, 012007. https://doi.org/10.1088/1742-6596/247/1/012007.

Hijirida, D. H.; Do, K. G.; Michal, C.; Wong, S.; Zax, D.; Jelinski, L. W. 13C NMR of Nephila Clavipes Major Ampullate Silk Gland. *Biophys. J.* **1996**, *71* (6), 3442–3447. https://doi.org/10.1016/S0006-3495(96)79539-5.

Hiremath, N.; Mays, J.; Bhat, G. Recent Developments in Carbon Fibers and Carbon Nanotube-Based Fibers: A Review. *Polym. Rev.* **2017**, *57* (2), 339–368. https://doi.org/10.1080/15583724.2016.1169546.

Holcomb, Griffin. Carbon Fiber & Graphene Manufacturing in the US. *IBISWorld Ind. Rep. OD4649* **2019**.

Hou, H.; Ge, J. J.; Zeng, J.; Li, Q.; Reneker, D. H.; Greiner, A.; Cheng, S. Z. D. Electrospun Polyacrylonitrile Nanofibers Containing a High Concentration of Well-Aligned Multiwall Carbon Nanotubes. *Chem. Mater.* **2005**, *17* (5), 967–973. https://doi.org/10.1021/cm0484955.

Huang, X. Fabrication and Properties of Carbon Fibers. *Materials* **2009**, *2* (4), 2369–2403. https://doi.org/10.3390/ma2042369.

Jain, M. K.; Abhiraman, A. S. Conversion of Acrylonitrile-Based Precursor Fibres to Carbon Fibres: Part 1 A Review of the Physical and Morphological Aspects. *J. Mater. Sci.* **1987**, *22* (1), 278–300. https://doi.org/10.1007/BF01160584.

Jin, H.-J.; Fridrikh, S. V.; Rutledge, G. C.; Kaplan, D. L. Electrospinning *Bombyx Mori* Silk with Poly(Ethylene Oxide). *Biomacromolecules* **2002**, *3* (6), 1233–1239. https://doi.org/10.1021/bm025581u.

Jin, H.-J.; Kaplan, D. L. Mechanism of Silk Processing in Insects and Spiders. *Nature* **2003**, *424* (6952), 1057–1061. https://doi.org/10.1038/nature01809.

Jing, M.; Wang, C.; Wang, Q.; Bai, Y.; Zhu, B. Chemical Structure Evolution and Mechanism during Pre-Carbonization of PAN-Based Stabilized Fiber in the Temperature Range of 350–600°C. *Polym. Degrad. Stab.* **2007**, *92* (9), 1737–1742. https://doi.org/10.1016/j.polymdegradstab.2007.05.020.

Johnson, I.; Wang, S. M.; Silken, C.; Liu, H. A Systemic Study on Key Parameters Affecting Nanocomposite Coatings on Magnesium Substrates. *Acta Biomaterialia* **2016**, *36*, 332–349. https://doi.org/10.1016/j.actbio.2016.03.026.

Johnson, W.; Phillips, L.; Watt, W. Production of Carbon Fibres and Compositions Containing Said Fibres. 3412062, November 19, 1968.

Jones, B.; Duncan, R. The Effect of Fibre Diameter on the Mechanical Properties of Graphite Fibres Manufactured from Polyacrylonitrile and Rayon. *J. Mater. Sci.* **1971**, *6*, 289–293.

Jones, J. A.; Harris, T. I.; Tucker, C. L.; Berg, K. R.; Christy, S. Y.; Day, B. A.; Gaztambide, D. A.; Needham, N. J. C.; Ruben, A. L.; Oliveira, P. F.; Decker, R. E.; Lewis, R. V. More Than Just Fibers: An Aqueous Method for the Production of Innovative Recombinant Spider Silk Protein Materials. *Biomacromolecules* **2015**, *16* (4), 1418–1425. https://doi.org/10.1021/acs.biomac.5b00226.

Jones, J.; Harris, T.; Oliveira, P.; Bell, B.; Alhabib, A.; Lewis, R. Importance of Heat and Pressure for Solubilization of Recombinant Spider Silk Proteins in Aqueous Solution. *Int. J. Mol. Sci.* **2016**, *17* (11), 1955. https://doi.org/10.3390/ijms17111955.

Ju, A.; Guang, S.; Xu, H. Effect of Comonomer Structure on the Stabilization and Spinnability of Polyacrylonitrile Copolymers. *Carbon* **2013**, *54*, 323–335. https://doi.org/10.1016/j.carbon.2012.11.044.

Kakida, H.; Tashiro, K. Mechanism and Kinetics of Stabilization Reaction of Polyacrylonitrile and Related Copolymers II. Relationships between Isothermal DSC Thermograms and FT-IR Spectral Changes of Polyacrylonitrile in Comparison with the Case of Acrylonitrile/Methacrylic Acid Copolymer. *Polym. J.* **1997**, *29* (4), 353–357. https://doi.org/10.1295/polymj.29.353.

Kakida, H.; Tashiro, K.; Kobayashi, M. Mechanism and Kinetics of Stabilization Reaction of Polyacrylonitrile and Related Copolymers I. Relationship between Isothermal DSC Thermogram and FT/IR Spectral Change of an Acrylonitrile/Methacrylic Acid Copolymer. *Polym. J.* **1996**, *28* (1), 30–34. https://doi.org/10.1295/polymj.28.30.

Karacan, İ.; Erdoğan, G. An Investigation on Structure Characterization of Thermally Stabilized Polyacrylonitrile Precursor Fibers Pretreated with Guanidine Carbonate Prior to Carbonization. *Polym. Eng. Sci.* **2012**, *52* (5), 937–952. https://doi.org/10.1002/pen.22160.

Karbownik, I.; Fiedot, M.; Rac, O.; Suchorska-Woźniak, P.; Rybicki, T.; Teterycz, H. Effect of Doping Polyacrylonitrile Fibers on Their Structural and Mechanical Properties. *Polymer* **2015**, *75*, 97–108. https://doi.org/10.1016/j.polymer.2015.08.015.

Kenney, J. M.; Knight, D.; Wise, M. J.; Vollrath, F. Amyloidogenic Nature of Spider Silk: Amyloidogenic Nature of Spider Silk. *Eur. J. Biochem.* **2002**, *269* (16), 4159–4163. https://doi.org/10.1046/j.1432-1033.2002.03112.x.

Keten, S.; Buehler, M. J. Nanostructure and Molecular Mechanics of Spider Dragline Silk Protein Assemblies. *J. R. Soc. Interface* **2010**, *7* (53), 1709–1721. https://doi.org/10.1098/rsif.2010.0149.

Keten, S.; Xu, Z.; Ihle, B.; Buehler, M. J. Nanoconfinement Controls Stiffness, Strength and Mechanical Toughness of β-Sheet Crystals in Silk. *Nat. Mater.* **2010**, *9* (4), 359–367. https://doi.org/10.1038/nmat2704.

Knight, D. P.; Knight, M. M.; Vollrath, F. Beta Transition and Stress-Induced Phase Separation in the Spinning of Spider Dragline Silk. *Int. J. Biol. Macromol.* **2000**, *27* (3), 205–210. https://doi.org/10.1016/S0141-8130(00)00124-0.

Knight, D. P.; Vollrath, F. Liquid Crystals and ¯ow Elongation in a Spider's Silk Production Line. **1999**, 6.

Knight, D. S.; White, W. B. Characterization of Diamond Films by Raman Spectroscopy. *J. Mater. Res.* **1989**, *4* (2), 385–393. https://doi.org/10.1557/JMR.1989.0385.

Knight, D.; Vollrath, F. Changes in Element Composition along the Spinning Duct in a Nephila Spider. *Naturwissenschaften* **2001**, *88* (4), 179–182. https://doi.org/10.1007/s001140100220.

Knight, D.; Vollrath, F. Hexagonal Columnar Liquid Crystal in the Cells Secreting Spider Silk. *Tissue Cell* **1999**, *31* (6), 617–620. https://doi.org/10.1054/tice.1999.0076.

Ko, F.; Gogotsi, Y.; Ali, A.; Naguib, N.; Ye, H.; Yang, G. L.; Li, C.; Willis, P. Electrospinning of Continuous Carbon Nanotube-Filled Nanofiber Yarns. *Adv. Mater.* **2003**, *15* (14), 1161–1165. https://doi.org/10.1002/adma.200304955.

Ko, T.-H.; Ting, H.-Y.; Lin, C.-H.; Chen, J.-C. The Microstructure of Stabilized Fibers. *J. Appl. Polym. Sci.* **1988**, *35* (4), 863–874. https://doi.org/10.1002/app.1988.070350402.

Kumar, S. *Polyacrylonitrile/Carbon Nanotube Composite: Precursor for Next Generation Carbon Fiber*; FA9550-07-1–0233; Georgia Institute of Technology: Air Force office of Scientific Research, 2010.

Langford, J. I.; Wilson, A. J. C. Scherrer after Sixty Years: A Survey and Some New Results in the Determination of Crystallite Size. *J. Appl. Crystallogr.* **1978**, *11,* 102-113.

Lee, J. K.; Shim, H. J.; Lim, J. C.; Choi, G. J.; Kim, Y. dae; Min, B. G.; Park, D. Influence of Tension during Oxidative Stabilization on SO2 Adsorption Characteristics of Polyacrylonitrile (PAN) Based Activated Carbon Fibers. *Carbon* **1997**, *35* (6), 837–843. https://doi.org/10.1016/S0008-6223(97)00040-7.

Lee, S. *Amazing Fantasy*; Marvel Comics, 1962; Vol. 15.

Lee, S.; Kim, J.; Ku, B.-C.; Kim, J.; Joh, H.-I. Structural Evolution of Polyacrylonitrile Fibers in Stabilization and Carbonization. *Adv. Chem. Eng. Sci.* **2012**, *02* (02), 275–282. https://doi.org/10.4236/aces.2012.22032.

Lefèvre, T.; Paquet-Mercier, F.; Rioux-Dubé, J.-F.; Pézolet, M. Structure of Silk by Raman Spectromicroscopy: From the Spinning Glands to the Fibers. *Biopolymers* **2012**, *97* (6), 322–336. https://doi.org/10.1002/bip.21712.

Lewis, R. V. Spider Silk: Ancient Ideas for New Biomaterials. *Chem. Rev.* **2006**, *106* (9), 3762–3774. https://doi.org/10.1021/cr010194g.

Li, L. L.; Liu, J.; Liang, J. Y. Influence of Cuprous Chloride Treatment on Pre-Oxidized PAN Tow. *Adv. Mater. Res.* **2006**, *11–12*, 453–456. https://doi.org/10.4028/www.scientific.net/AMR.11-12.453.

Li, X.; Meng, L.; Lin, Y.; Chen, X.; Zhang, Q.; Zhang, R.; Wu, L.; Zhang, W.; Li, L. Preparation of Highly Oriented Polyethylene Precursor Film with Fibril and Its Influence on Microporous Membrane Formation. *Macromol. Chem. Phys.* **2016**, *217* (8), 974–986. https://doi.org/10.1002/macp.201500471.

Li, Z. Q.; Lu, C. J.; Xia, Z. P.; Zhou, Y.; Luo, Z. X-Ray Diffraction Patterns of Graphite and Turbostratic Carbon. *Carbon* **2007**, *45* (8), 1686–1695. https://doi.org/10.1016/j.carbon.2007.03.038.

Lian, F.; Liu, J.; Ma, Z.; Liang, J. Stretching-Induced Deformation of Polyacrylonitrile Chains Both in Quasicrystals and in Amorphous Regions during the in Situ Thermal Modification of Fibers Prior to Oxidative Stabilization. *Carbon* **2012**, *50* (2), 488–499. https://doi.org/10.1016/j.carbon.2011.09.003.

Liu, H. C.; Chien, A.-T.; Newcomb, B. A.; Bakhtiary Davijani, A. A.; Kumar, S. Stabilization Kinetics of Gel Spun Polyacrylonitrile/Lignin Blend Fiber. *Carbon* **2016**, *101*, 382–389. https://doi.org/10.1016/j.carbon.2016.01.096.

Liu, J.; He, L.; Ma, S.; Liang, J.; Zhao, Y.; Fong, H. Effects of Chemical Composition and Post-Spinning Stretching Process on the Morphological, Structural, and Thermo-Chemical Properties of Electrospun Polyacrylonitrile Copolymer Precursor Nanofibers. *Polymer* **2015**, *61*, 20–28. https://doi.org/10.1016/j.polymer.2015.01.063.

Liu, J.; Zhou, P.; Zhang, L.; Ma, Z.; Liang, J.; Fong, H. Thermo-Chemical Reactions Occurring during the Oxidative Stabilization of Electrospun Polyacrylonitrile Precursor Nanofibers and the Resulting Structural Conversions. *Carbon* **2009**, *47* (4), 1087–1095. https://doi.org/10.1016/j.carbon.2008.12.033.

Liu, S.; Han, K.; Chen, L.; Zheng, Y.; Yu, M.; Li, J.; Yang, Z. Influence of External Tension on the Structure and Properties of Melt-Spun PAN Precursor Fibers during Thermal Oxidation: Influence of External Tension on Performances of Pre-Oxidized Melt-Spun Fibers. *Macromol. Mater. Eng.* **2015**, *300* (10), 1001–1009. https://doi.org/10.1002/mame.201500104.

Liu, Y.; Kumar, S. Polymer/Carbon Nanotube Nano Composite Fibers–A Review. *ACS Appl. Mater. Interfaces* **2014**, *6* (9), 6069–6087. https://doi.org/10.1021/am405136s.

Lombardi, S., J.; Kaplan, D. L. The Amino Acid Composition of Major Ampullate Gland Silk (Dragline) of Nephila Clavipes (Araneae, Tetragnathidae). *J. Arachnol.* **1990**, *18*, 297–306.

Lv, M.; Ge, H.; Chen, J. Study on the Chemical Structure and Skin-Core Structure of Polyacrylonitrile-Based Fibers during Stabilization. *J. Polym. Res.* **2009**, *16* (5), 513–517. https://doi.org/10.1007/s10965-008-9254-7.

Mack, J. J.; Viculis, L. M.; Ali, A.; Luoh, R.; Yang, G.; Hahn, H. T.; Ko, F. K.; Kaner, R. B. Graphite Nanoplatelet Reinforcement of Electrospun Polyacrylonitrile Nanofibers. *Adv. Mater.* **2005**, *17* (1), 77–80. https://doi.org/10.1002/adma.200400133.

Mair, W. N.; Mansfield, E. H. William Watt. 14 April 1912 to 11 August 1985. In *Biographical Memoirs of Fellows of the Royal Society*; The Royal Society, 1987; Vol. 33, pp 642–667.

Mascia, L.; Paxton, E. G. Physical Changes during Thermal Oxidation of PAN Fibres and Effects of Y-Radiation Pre-Treatment. *Thermochimica Acta.* **1991** *184*, 251-267.

Matthews, M. J.; Pimenta, M. A.; Dresselhaus, G.; Dresselhaus, M. S.; Endo, M. Origin of Dispersive Effects of the Raman ***D*** Band in Carbon Materials. *Phys. Rev. B* **1999**, *59* (10), R6585–R6588. https://doi.org/10.1103/PhysRevB.59.R6585.

Merlen, A.; Buijnsters, J.; Pardanaud, C. A Guide to and Review of the Use of Multiwavelength Raman Spectroscopy for Characterizing Defective Aromatic Carbon Solids: From Graphene to Amorphous Carbons. *Coatings* **2017**, *7* (10), 153. https://doi.org/10.3390/coatings7100153.

Merlen, A.; Buijnsters, J.; Pardanaud, C. A Guide to and Review of the Use of Multiwavelength Raman Spectroscopy for Characterizing Defective Aromatic Carbon Solids: From Graphene to Amorphous Carbons. *Coatings* **2017**, *7* (10), 153. https://doi.org/10.3390/coatings7100153.

Mitchell, A.; Kim, B.; Cottrell, J.; Snyder, S.; Witek, L.; Ricci, J.; Uhrich, K. E.; Patrick O'Connor, J. Development of a Guided Bone Regeneration Device Using Salicylic Acid-Poly(Anhydride-Ester) Polymers and Osteoconductive Scaffolds: Guided Bone Regeneration Device Development. *J. Biomed. Mater. Res.* **2014**, *102* (3), 655–664. https://doi.org/10.1002/jbm.a.34728.

Mittal, J.; Bahl, O. P.; Mathur, R. B.; Sandle, N. K. IR Studies of PAN Fibres Thermally Stabilized at Elevated Temperatures. *Carbon* **1994**, *32* (6), 1133–1136. https://doi.org/10.1016/0008-6223(94)90222-4.

Mittal, K. L. Adhesion Measurement of Thin Films. *Electrocomponent Science and Technology*. **1976,** *3*, 21-42.

Moon, M.; Tillinghast, E. K. Fine Structure of the Glandular Epithelium during Secretory Silk Production in the Black Widow Spider *Latrodectus Mactans*. *Korean J. Biol. Sci.* **2002**, *6* (4), 327–333. https://doi.org/10.1080/12265071.2002.9647672.

Moon, M.; Townley, M. A.; Tillinghast, E. K. Fine Structural Analysis of Secretory Silk Production in the Black Widow Spider, *Latrodectus Mactans*. *Korean J. Biol. Sci.* **1998**, *2* (1), 145–152. https://doi.org/10.1080/12265071.1998.9647401.

Morales, M. S.; Ogale, A. A. Wet-Spun, Photoinitiator-Modified Polyacrylonitrile Precursor Fibers: UV-Assisted Stabilization. *J. Appl. Polym. Sci.* **2013**, *130* (4), 2494–2503. https://doi.org/10.1002/app.39442.

Mukhopadhyay, S. K.; Zhu, Y. Structure-Property Relationships of PAN Precursor Fibers During Thermo-Oxidative Stabilization. *Text. Res. J.* **1995**, *65* (1), 25–31. https://doi.org/10.1177/004051759506500104.

Murthy, M. R.; Radhakrishna, S. Radiation Damage in Polyacrylonitrile. *Pramana* **1983**, *20* (1), 85–90. https://doi.org/10.1007/BF02846184.

Naskar, A. K.; Walker, R. A.; Proulx, S.; Edie, D. D.; Ogale, A. A. UV Assisted Stabilization Routes for Carbon Fiber Precursors Produced from Melt-Processible Polyacrylonitrile Terpolymer. *Carbon* **2005**, *43* (5), 1065–1072. https://doi.org/10.1016/j.carbon.2004.11.047.

Newcomb, B. A. Processing, Structure, and Properties of Carbon Fibers. *Compos. Part Appl. Sci. Manuf.* **2016**, *91*, 262–282. https://doi.org/10.1016/j.compositesa.2016.10.018.

Ogawa, H.; Saito, K. Oxidation Behavior of Polyacrylonitrile Fibers Evaluated by New Stabilization Index. *Carbon* **1995**, *33* (6), 783–788.

Ortlepp, C. S.; Gosline, J. M. Consequences of Forced Silking. *Biomacromolecules* **2004**, *5* (3), 727–731. https://doi.org/10.1021/bm034269x.

Ouyang, Q.; Cheng, L.; Wang, H.; Li, K. Mechanism and Kinetics of the Stabilization Reactions of Itaconic Acid-Modified Polyacrylonitrile. *Polym. Degrad. Stab.* **2008**, *93* (8), 1415–1421. https://doi.org/10.1016/j.polymdegradstab.2008.05.021.

Paiva, M. C.; Kotasthane, P.; Edie, D. D.; Ogale, A. A. UV Stabilization Route for Melt-Processible PAN-Based Carbon Fibers. *Carbon* **2003**, *41* (7), 1399–1409. https://doi.org/10.1016/S0008-6223(03)00041-1.

Park, S.-J.; Heo, G.-Y. Precursors and Manufacturing of Carbon Fibers. In *Carbon Fibers*; Springer Netherlands: Dordrecht, 2015; Vol. 210, pp 31–66. https://doi.org/10.1007/978-94-017-9478-7_2.

Park, Su-Jin. A Review of the Preparation and Properties of Carbon Nanotubes-Reinforced Polymer Compositess. *Carbon Lett.* **2011**, *12* (2), 57–69. https://doi.org/10.5714/CL.2011.12.2.057.

Paterson, J. R. Salicylic Acid: A Link between Aspirin, Diet and the Prevention of Colorectal Cancer. *QJM* **2001**, *94* (8), 445–448. https://doi.org/10.1093/qjmed/94.8.445.

Peebles, L. H.; Peyser, P.; Snow, A. W.; Peters, W. C. On the Exotherm of Polyacrylonitrile Pyrolysis of the Homopolymer under Inert Conditions. *Carbon* **1990**, *28* (5), 707–715.

Plaza, G. R.; Guinea, G. V.; Pérez-Rigueiro, J.; Elices, M. Thermo-Hygro-Mechanical Behavior of Spider Dragline Silk: Glassy and Rubbery States. *J. Polym. Sci. Part B Polym. Phys.* **2006**, *44* (6), 994–999. https://doi.org/10.1002/polb.20751.

Prudencio, A.; Schmeltzer, R. C.; Uhrich, K. E. Effect of Linker Structure on Salicylic Acid-Derived Poly(Anhydride−esters). *Macromolecules* **2005**, *38* (16), 6895–6901. https://doi.org/10.1021/ma048051u.

Qin, X.; Lu, Y.; Xiao, H.; Zhao, W. Effect of Heating and Stretching Polyacrylonitrile Precursor Fibers in Steam on the Properties of Stabilized Fibers and Carbon Fibers. *Polym. Eng. Sci.* **2013**, *53* (4), 827–832. https://doi.org/10.1002/pen.23328.

Rahaman, M. S. A.; Ismail, A. F.; Mustafa, A. A Review of Heat Treatment on Polyacrylonitrile Fiber. *Polym. Degrad. Stab.* **2007**, *92* (8), 1421–1432. https://doi.org/10.1016/j.polymdegradstab.2007.03.023.

Rising, A.; Nimmervoll, H.; Grip, S.; Fernandez-Arias, A.; Storckenfeldt, E.; Knight, D. P.; Vollrath, F.; Engström, W. Spider Silk Proteins – Mechanical Property and Gene Sequence. *Zoolog. Sci.* **2005**, *22* (3), 273–281. https://doi.org/10.2108/zsj.22.273.

Ross, S. E. Observations Concerning the Carbonization of Viscose Rayon Yarn. *Text. Res. J.* **1968**, *38* (9), 906–913. https://doi.org/10.1177/004051756803800905.

Sabet, E. N.; Nourpanah, P.; Arbab, S. Quantitative Analysis of Entropic Stress Effect on the Structural Rearrangement during Pre-Stabilization of PAN Precursor Fibers. *Polymer* **2016**, *90*, 138–146. https://doi.org/10.1016/j.polymer.2016.03.001.

Şahin, K.; Fasanella, N. A.; Chasiotis, I.; Lyons, K. M.; Newcomb, B. A.; Kamath, M. G.; Chae, H. G.; Kumar, S. High Strength Micron Size Carbon Fibers from

Polyacrylonitrile–Carbon Nanotube Precursors. *Carbon* **2014**, *77*, 442–453. https://doi.org/10.1016/j.carbon.2014.05.049.

Salim, N. V.; Blight, S.; Creighton, C.; Nunna, S.; Atkiss, S.; Razal, J. M. The Role of Tension and Temperature for Efficient Carbonization of Polyacrylonitrile Fibers: Toward Low Cost Carbon Fibers. *Ind. Eng. Chem. Res.* **2018**, *57* (12), 4268–4276. https://doi.org/10.1021/acs.iecr.7b05336.

Sampath, S.; Isdebski, T.; Jenkins, J. E.; Ayon, J. V.; Henning, R. W.; Orgel, J. P. R. O.; Antipoa, O.; Yarger, J. L. X-Ray Diffraction Study of Nanocrystalline and Amorphous Structure within Major and Minor Ampullate Dragline Spider Silks. *Soft Matter* **2012**, *8* (25), 6713. https://doi.org/10.1039/c2sm25373a.

Sampath, S.; Yarger, Jeffery. L. Structural Hysteresis in Dragline Spider Silks Induced by Supercontraction: An X-Ray Fiber Micro-Diffraction Study. *RSC Adv* **2015**, *5* (2), 1462–1473. https://doi.org/10.1039/C4RA13936D.

Schalamon, W.; Bacon, R. Process for Producing Carbon Fibers Having a High Young's Modulus of Elasticity. US Patent No. 3716331, February 13, 1973.

Schmeltzer, R. C.; Johnson, M.; Griffin, J.; Uhrich, K. Comparison of Salicylate-Based Poly(Anhydride-Esters) Formed via Melt-Condensation versus Solution Polymerization. *Journal of Biomaterials Science, Polymer Edition* **2008**, *19* (10), 1295–1306. https://doi.org/10.1163/156856208786052362.

Schmeltzer, R. C.; Schmalenberg, K. E.; Uhrich, K. E. Synthesis and Cytotoxicity of Salicylate-Based Poly(Anhydride Esters). *Biomacromolecules*. **2005**, *6*, 359-367.

Shao, Z.; Young, R. J.; Vollrath, F. The Effect of Solvents on Spider Silk Studied by Mechanical Testing and Single-Fibre Raman Spectroscopy. *Int. J. Biol. Macromol.* **1999**, *24* (2), 295–300.

Shin, H. K.; Park, M.; Kim, H.-Y.; Park, S.-J. An Overview of New Oxidation Methods for Polyacrylonitrile-Based Carbon Fibers. *Carbon Lett.* **2015**, *16* (1), 11–18. https://doi.org/10.5714/CL.2015.16.1.011.

Shindo, A. Process for the Preparation of Carbon Fibers. US Patent No. 3529934, February 20, 1967.

Shindo, A. Producing Method of Carbon or Carbonaceous Material. US Patent No. 3427120, February 11, 1969.

Shindo, A.; Nakanishi, Y.; Sawada, Y. Method for Manufacture of Heat-Resistant Fibers. US Patent No. 3886263, May 27, 1975.

Simmons, A. H.; Michal, C. A.; Jelinski, L. W. Molecular Orientation and Two-Component Nature of the Crystalline Fraction of Spider Dragline Silk. *Science* **1996**, *271* (5245), 84–87. https://doi.org/10.2307/2890379.

Snyder, S. S.; Anastasiou, T. J.; Uhrich, K. E. In Vitro Degradation of an Aromatic Polyanhydride with Enhanced Thermal Properties. *Polymer Degradation and Stability* **2015**, *115*, 70–76. https://doi.org/10.1016/j.polymdegradstab.2015.02.002.

Soutis, C. Carbon Fiber Reinforced Plastics in Aircraft Construction. *Mater. Sci. Eng. A* **2005**, *412* (1–2), 171–176. https://doi.org/10.1016/j.msea.2005.08.064.

Souto, F.; Calado, V.; Pereira, N. Lignin-Based Carbon Fiber: A Current Overview. *Mater. Res. Express* **2018**, *5* (7), 072001. https://doi.org/10.1088/2053-1591/aaba00.

Sponner, A.; Schlott, B.; Vollrath, F.; Unger, E.; Grosse, F.; Weisshart, K. Characterization of the Protein Components of *Nephila Clavipes* Dragline Silk †. *Biochemistry* **2005**, *44* (12), 4727–4736. https://doi.org/10.1021/bi047671k.

Sponner, A.; Vater, W.; Monajembashi, S.; Unger, E.; Grosse, F.; Weisshart, K. Composition and Hierarchical Organisation of a Spider Silk. *PLoS ONE* **2007**, *2* (10), e998. https://doi.org/10.1371/journal.pone.0000998.

Stéfani, R.; Chevreton, M.; Garnier, M.; Eyraud, C. Les Structures Cristallines Du Polyacrylonitrile. In *Comptes rendus Hebdomadaires des Séances de l'Académie des Sciences*; Académie des Sciences, **1960,** *251*, 2174–2176.

Stephens, J. S.; Fahnestock, S. R.; Farmer, R. S.; Kiick, K. L.; Chase, D. B.; Rabolt, J. F. Effects of Electrospinning and Solution Casting Protocols on the Secondary Structure of a Genetically Engineered Dragline Spider Silk Analogue Investigated via Fourier Transform Raman Spectroscopy. *Biomacromolecules* **2005**, *6* (3), 1405–1413. https://doi.org/10.1021/bm049296h.

Sun, T.; Hou, Y.; Wang, H. Mass DSC/TG and IR Ascertained Structure and Color Change of Polyacrylonitrile Fibers in Air/Nitrogen during Thermal Stabilization. *J. Appl. Polym. Sci.* **2010**, *118* (1), 462–468. https://doi.org/10.1002/app.32175.

Surianarayanan, M.; Uchida, T.; Wakakura, M. Evolved Gases by Simultaneous TG–MS Technique and Associated Thermal Hazard in Drying of Polyacrylonitrile. *J. Loss Prev. Process Ind.* **1998**, *11* (2), 99–108. https://doi.org/10.1016/S0950-4230(97)00032-6.

Takahagi, T.; Shimada, I.; Fukuhara, M.; Morita, K.; Ishitani, A. XPS Studies on the Chemical Structure of the Stabilized Polyacrylonitrile Fiber in the Carbon Fiber

Production Process. *J. Polym. Sci. Part Polym. Chem.* **1986**, *24* (11), 3101–3107. https://doi.org/10.1002/pola.1986.080241134.

Tang, M. M.; Bacon, R. Carbonization of Cellulose Fibers-I Low Temperature Pyrolysis. *Carbon* **1964**, *2*, 211–200.

Tang, M.; Rice, G. G.; Fellers, J. F.; Lin, J. S. X-ray Scattering Studies of Graphite Fibers. *J. Appl. Phys.* **1986**, *60* (2), 803–810. https://doi.org/10.1063/1.337378.

Tedford, H. W.; Sollod, B. L.; Maggio, F.; King, G. F. Australian Funnel-Web Spiders: Master Insecticide Chemists. *Toxicon* **2004**, *43* (5), 601–618. https://doi.org/10.1016/j.toxicon.2004.02.010.

Thomas, L. C. Use of Multiple Heating Rate DSC and Modulated Temperature DSC to Detect and Analyze Temperature-Time-Dependent Transitions in Materials. *Ameriacan Laboratory.* **2001**.

Tokareva, O.; Michalczechen-Lacerda, V. A.; Rech, E. L.; Kaplan, D. L. Recombinant DNA Production of Spider Silk Proteins: Recombinant Spider Silks. *Microb. Biotechnol.* **2013**, *6* (6), 651–663. https://doi.org/10.1111/1751-7915.12081.

Trancik, J. E.; Czernuszka, J. T.; Bell, F. I.; Viney, C. Nanostructural Features of a Spider Dragline Silk as Revealed by Electron and X-Ray Diffraction Studies. *Polymer* **2006**, *47* (15), 5633–5642. https://doi.org/10.1016/j.polymer.2005.01.110.

Tsai, J.-S. Effect of Drawing Ratio during Spinning and Oxidation on the Properties of Polyacrylonitrile Precursor and Resulting Carbon Fibre. *J. Mater. Sci. Lett.* **1992**, *11* (3), 140–142. https://doi.org/10.1007/BF00724670.

Tsai, J.-S. Tension Effects on the Properties of Oxidized Polyacrylonitrile and Carbon Fibers during Continuous Oxidation. *Polym. Eng. Sci.* **1995**, *35* (16), 1313–1316. https://doi.org/10.1002/pen.760351607.

Tsai, J.-S.; Lin, C.-H. Effect of Comonomer Composition on the Properties of Polyacrylonitrile Precursor and Resulting Carbon Fiber. *J. Appl. Polym. Sci.* **1991**, *43* (4), 679–685. https://doi.org/10.1002/app.1991.070430405.

Tuinstra, F.; Koenig, J. L. Raman Spectrum of Graphite. *J. Chem. Phys.* **1970**, *53* (3), 1126–1130. https://doi.org/10.1063/1.1674108.

Usami, T.; Itoh, T.; Ohtani, H.; Tsuge, S. Structural Study of Polyacrylonitrile Fibers during Oxidative Thermal Degradation by Pyrolysis-Gas Chromatography, Solid-State Carbon-13 NMR, and Fourier-Transform Infrared Spectroscopy. *Macromolecules* **1990**, *23* (9), 2460–2465. https://doi.org/10.1021/ma00211a009.

Vane, J. R.; Botting, R. M. Mechanism of Action of Nonsteroidal Anti-Inflammatory Drugs. *The American Journal of Medicine.* **1998**, *104* (3A), 2S-8S.

Vehoff, T.; Glišović, A.; Schollmeyer, H.; Zippelius, A.; Salditt, T. Mechanical Properties of Spider Dragline Silk: Humidity, Hysteresis, and Relaxation. *Biophys. J.* **2007**, *93* (12), 4425–4432. https://doi.org/10.1529/biophysj.106.099309.

Vollrath, F.; Holtet, T.; Thogersen, H. C.; Frische, S. Structural Organization of Spider Silk. In *Proceedings: Biological Sciences*; The Royal Society, 1996; Vol. 263, pp 147–151.

Vollrath, F.; Knight, D. P. Liquid Crystalline Spinning of Spider Silk. *Nature* **2001**, *410* (6828), 541–548. https://doi.org/10.1038/35069000.

Vollrath, F.; Knight, D. P. Structure and Function of the Silk Production Pathway in the Spider Nephila Edulis. *Int. J. Biol. Macromol.* **1999**, *24* (2–3), 243–249. https://doi.org/10.1016/S0141-8130(98)00095-6.

Vollrath, F.; Knight, D. P.; Hu, X. W. Silk Production in a Spider Involves Acid Bath Treatment. *Proc. R. Soc. Lond. B Biol. Sci.* **1998**, *265* (1398), 817–820. https://doi.org/10.1098/rspb.1998.0365.

Vollrath, F.; Porter, D. Spider Silk as Archetypal Protein Elastomer. *Soft Matter* **2006**, *2* (5), 377. https://doi.org/10.1039/b600098n.

Wada, K.; Yu, W.; Elazizi, M.; Barakat, S.; Ouimet, M. A.; Rosario-Meléndez, R.; Fiorellini, J. P.; Graves, D. T.; Uhrich, K. E. Locally Delivered Salicylic Acid from a Poly(Anhydride-Ester): Impact on Diabetic Bone Regeneration. *Journal of Controlled Release* **2013**, *171* (1), 33–37. https://doi.org/10.1016/j.jconrel.2013.06.024.

Wang, P.; Liu, J.; Yue, Z.; Li, R. Thermal Oxidative Stabilization of Polyacrylonitrile Precursor Fiber—Progression of Morphological Structure and Mechanical Properties. *Carbon* **1992**, *30* (1), 113–120. https://doi.org/10.1016/0008-6223(92)90114-C.

Wang, X.; Zhao, P.; Li, Y.; Yi, Q.; Ma, S.; Xie, K.; Chen, H.; Xia, Q. Modifying the Mechanical Properties of Silk Fiber by Genetically Disrupting the Ionic Environment for Silk Formation. *Biomacromolecules* **2015**, *16* (10), 3119–3125. https://doi.org/10.1021/acs.biomac.5b00724.

Wang, Y.; Xu, L.; Wang, M.; Pang, W.; Ge, X. Structural Identification of Polyacrylonitrile during Thermal Treatment by Selective ^{13}C Labeling and Solid-State ^{13}C NMR Spectroscopy. *Macromolecules* **2014**, *47* (12), 3901–3908. https://doi.org/10.1021/ma500727n.

Warner, S. B.; Peebles, L. H.; Uhlmann, D. R. Oxidative Stabilization of Acrylic Fibres. *J. Mater. Sci.* **1979**, *14*, 556–564.

Whitaker-Brothers, K.; Uhrich, K. Investigation into the Erosion Mechanism of Salicylate-Based Poly(Anhydride-Esters). *J. Biomed. Mater. Res.* **2006**, *76A* (3), 470–479. https://doi.org/10.1002/jbm.a.30356.

Whitaker-Brothers, K.; Uhrich, K. Poly(Anhydride-Ester) Fibers: Role of Copolymer Composition on Hydrolytic Degradation and Mechanical Properties. *J. Biomed. Mater. Res.* **2004**, *70A* (2), 309–318. https://doi.org/10.1002/jbm.a.30083.

White, E. B. *Charlotte's Web*; Harper & Brothers: New York, 1952.

Willcox, P. J.; Gido, S. P.; Muller, W.; Kaplan, D. L. Evidence of a Cholesteric Liquid Crystalline Phase in Natural Silk Spinning Processes. *Macromolecules* **1996**, *29* (15), 5106–5110. https://doi.org/10.1021/ma960588n.

Wu, G.; Lu, C.; Ling, L.; Hao, A.; He, F. Influence of Tension on the Oxidative Stabilization Process of Polyacrylonitrile Fibers. *J. Appl. Polym. Sci.* **2005**, *96* (4), 1029–1034. https://doi.org/10.1002/app.21388.

Wu, X.; Zhang, X.; Lu, C.; Ling, L. Thermo-Chemical Reactions and Structural Evolution of Acrylamide-Modified Polyacrylonitrile. *Chin. J. Polym. Sci.* **2010**, *28* (3), 367–376. https://doi.org/10.1007/s10118-010-9026-9.

Xu, D.; Guo, C.; Holland, G. P. Probing the Impact of Acidification on Spider Silk Assembly Kinetics. *Biomacromolecules* **2015**, *16* (7), 2072–2079. https://doi.org/10.1021/acs.biomac.5b00487.

Xu, G.; Gong, L.; Yang, Z.; Liu, X. Y. What Makes Spider Silk Fibers Stronger: From Molecular-Crystallite Network to Hierarchical Structure. **2014**, 6.

Xu, L.; Yamamoto, A. Characteristics and Cytocompatibility of Biodegradable Polymer Film on Magnesium by Spin Coating. *Colloids and Surfaces B: Biointerfaces* **2012**, *93*, 67–74. https://doi.org/10.1016/j.colsurfb.2011.12.009.

Xue, T. J.; McKinney, M. A.; Wilkie, C. A. The Thermal Degradation of Polyacrylonitrile. *Polym. Degrad. Stab.* **1997**, *58*, 193–202.

Xue, Y.; Liu, J.; Lian, F.; Liang, J. Effect of the Oxygen-Induced Modification of Polyacrylonitrile Fibers during Thermal-Oxidative Stabilization on the Radial Microcrystalline Structure of the Resulting Carbon Fibers. *Polym. Degrad. Stab.* **2013**, *98* (11), 2259–2267. https://doi.org/10.1016/j.polymdegradstab.2013.08.016.

Xue, Y.; Liu, J.; Liang, J. Correlative Study of Critical Reactions in Polyacrylonitrile Based Carbon Fiber Precursors during Thermal-Oxidative Stabilization. *Polym. Degrad. Stab.* **2013**, *98* (1), 219–229. https://doi.org/10.1016/j.polymdegradstab.2012.10.018.

Yeagy, B. A.; Prudencio, A.; Schmeltzer, R. C.; Uhrich, K. E.; Cook, T. J. Characterization and ***in Vitro*** Degradation of Salicylate-Derived Poly(Anhydride-Ester Microspheres). *Journal of Microencapsulation* **2006**, *23* (6), 643–653. https://doi.org/10.1080/02652040600776481.

Yu, M.; Wang, C.; Bai, Y.; Wang, Y.; Wang, Q.; Liu, H. Combined Effect of Processing Parameters on Thermal Stabilization of PAN Fibers. *Polym. Bull.* **2006**, *57* (4), 525–533. https://doi.org/10.1007/s00289-006-0581-8.

Yu, M.; Wang, C.; Bai, Y.; Zhu, B.; Ji, M.; Xu, Y. Microstructural Evolution in Polyacrylonitrile Fibers during Oxidative Stabilization: Microstructural Evolution in PAN Fibers. *J. Polym. Sci. Part B Polym. Phys.* **2008**, *46* (7), 759–765. https://doi.org/10.1002/polb.21410.

Yu, M.; Wang, C.; Zhao, Y.; Zhang, M.; Wang, W. Thermal Properties of Acrylonitrile/Itaconic Acid Polymers in Oxidative and Nonoxidative Atmospheres. *J. Appl. Polym. Sci.* **2009**, n/a-n/a. https://doi.org/10.1002/app.31664.

Yu, M.-J.; Wang, C.-G.; Bai, Y.-J.; Ji, M.-X.; Xu, Y. SEM and OM Study on the Microstructure of Oxidative Stabilized Polyacrylonitrile Fibers. *Polym. Bull.* **2007**, *58* (5–6), 933–940. https://doi.org/10.1007/s00289-007-0737-1.

Yu, W.; Bien-Aime, S.; Li, J.; Zhang, L.; McCormack, E. S.; Goldberg, I. D.; Narayan, P.; Uhrich, K. E. Injectable Microspheres for Extended Delivery of Bioactive Insulin and Salicylic Acid. *Journal of Bioactive and Compatible Polymers* **2015**, *30* (3), 340–346. https://doi.org/10.1177/0883911515569919.

Yu, W.; Bien-Aime, S.; Mattos, M.; Alsadun, S.; Wada, K.; Rogado, S.; Fiorellini, J.; Graves, D.; Uhrich, K. Sustained, Localized Salicylic Acid Delivery Enhances Diabetic Bone Regeneration via Prolonged Mitigation of Inflammation. *J. Biomed. Mater. Res.* **2016**, *104* (10), 2595–2603. https://doi.org/10.1002/jbm.a.35781.

Yuan, H.; Wang, Y.; Yu, H.; Wei, Z.; Ge, B.; Mei, Y. Effect of UV Irradiation on PAN Precursor Fibers and Stabilization Process. *J. Wuhan Univ. Technol.-Mater Sci Ed* **2011**, *26* (3), 449–454. https://doi.org/10.1007/s11595-011-0247-8.

Zhang, F.; Zuo, B.; Fan, Z.; Xie, Z.; Lu, Q.; Zhang, X.; Kaplan, D. L. Mechanisms and Control of Silk-Based Electrospinning. *Biomacromolecules* **2012**, *13* (3), 798–804. https://doi.org/10.1021/bm201719s.

Zhang, W.; Wang, Y.; Sun, C. Characterization on Oxidative Stabilization of Polyacrylonitrile Nanofibers Prepared by Electrospinning. *J. Polym. Res.* **2007**, *14* (6), 467–474. https://doi.org/10.1007/s10965-007-9130-x.

Zhang, Y.; Tajaddod, N.; Song, K.; Minus, M. L. Low Temperature Graphitization of Interphase Polyacrylonitrile (PAN). *Carbon* **2015**, *91*, 479–493. https://doi.org/10.1016/j.carbon.2015.04.088.

Zhao, J.; Zhang, J.; Zhou, T.; Liu, X.; Yuan, Q.; Zhang, A. New Understanding on the Reaction Pathways of the Polyacrylonitrile Copolymer Fiber Pre-Oxidation: Online Tracking by Two-Dimensional Correlation FTIR Spectroscopy. *RSC Adv.* **2016**, *6* (6), 4397–4409. https://doi.org/10.1039/C5RA24320C.

Zhao, W.; Yamamoto, Y.; Tagawa, S. Regulation of the Thermal Reactions of Polyacrylonitrile by γ-Irradiation. *Chem. Mater.* **1999**, *11* (4), 1030–1034. https://doi.org/10.1021/cm9806836.

Zhernenkov, Mikhail. Soft Matter Interfaces Beamline at NSLS-II: Geometrical Ray-Tracing vs. Wavefront Propagation Simulations. In *Advances in Computational Methods for X-Ray Optics III*; Sanchez del Rio, M., Chubar, O., Eds.; 2014; Vol. 9209.

Zhou, S.; Peng, H.; Yu, X.; Zheng, X.; Cui, W.; Zhang, Z.; Li, X.; Wang, J.; Weng, J.; Jia, W.; Li, F. Preparation and Characterization of a Novel Electrospun Spider Silk Fibroin/Poly(d , l -Lactide) Composite Fiber. *J. Phys. Chem. B* **2008**, *112* (36), 11209–11216. https://doi.org/10.1021/jp800913k.

Zhou, Z.; Liu, K.; Lai, C.; Zhang, L.; Li, J.; Hou, H.; Reneker, D. H.; Fong, H. Graphitic Carbon Nanofibers Developed from Bundles of Aligned Electrospun Polyacrylonitrile Nanofibers Containing Phosphoric Acid. *Polymer* **2010**, *51* (11), 2360–2367. https://doi.org/10.1016/j.polymer.2010.03.044.

Zhu, Y.; Wilding, M. A.; Mukhopadhyay, S. K. Estimation, Using Infrared Spectroscopy, of the Cyclization of Poly(Acrylonitrile) during the Stabilization Stage of Carbon Fibre Production. *J. Mater. Sci.* **1996**, *31* (14), 3831–3837. https://doi.org/10.1007/BF00352799.

Zickler, G. A.; Smarsly, B.; Gierlinger, N.; Peterlik, H.; Paris, O. A Reconsideration of the Relationship between the Crystallite Size La of Carbons Determined by X-Ray Diffraction and Raman Spectroscopy. *Carbon* **2006**, *44* (15), 3239–3246. https://doi.org/10.1016/j.carbon.2006.06.029.

Zweben, C. In *Mechanical Engineers' Handbook*; Kutz, M., Ed.; Wiley:

Appendix 1: SAPAE polymerization notes

SA Diacid

Monosubstituted diacid is another potential impurity, but it was unable to be identified through TLC or ^{1}H NMR. Water present during the reaction can react with adipoyl chloride to form adipic acid as a terminal product.

There are impurity peaks corresponding to cyclohexanone, and that's a feasible byproduct from the diacid synthesis, but its existence isn't confirmed and its effects aren't known.

Despite our best efforts, there will always be some water in the reaction vessel. Since the SA and adipoyl chloride are added stoichiometrically (2:1), any adipoyl chloride which reacts with water means there will be residual SA. A monosubstituted diacid would form when one end of the adipoyl chloride reacts with SA while the other end is poisoned by water or rendered unreactive by some other means. A good way to identify or remove monosubstituted diacid has not yet been identified. It's possible that no monosubstituted diacid is present, but it could explain other problems with the polymerization we encounter.

Drying diacids under vacuum doesn't remove water and drying them under vacuum at elevated temperatures also hasn't been successful, but those experiments were done on Diacids with large amounts of water.

Monomer Isolation

Previous protocols suggested the diacid could be dissolved at room temperature after stirring overnight, but this was found to be unreliable based on the volume of acetic anhydride used. A higher anhydride:diacid ratio could be successful in dissolving and acetylating the anhydride without heating.

Other protocols suggest vacuum distillation for 2 h at 70 ^{o}C, but we found that unnecessary. Oligomers can form during distillation, but this isn't known to hinder polymerization.

The few NMR spectra I collected on the monomer showed the cleaved adipic acid present in the monomer. More careful characterization of the monomer will help figure out the issues in the polymerization.

Polymerization

Effectiveness of polymerization temperature on removing water hasn't been studied.

Purification

Other protocols suggest chilling the ether before workup, but this hasn't impacted polymer yield or Mw

Characterization

For NMR of anhydride exchange solution, 1.75 ppm peak is missing, possibly because of the large amount of acetic anhydride present.

The anhydride exchange is itself an equilibrium between diacid and monomer, but the excess acetic anhydride favors the monomer as a product. However, water and acetic anhydride aren't azeotropic based on experimental evidence, so it's impossible to fully remove any water from the system.

Watch the integration of the monomer CH3 peak to make sure there is enough acetylation.

Sometimes the Ch2 peaks from 1.6-1.8 ppm look like a triplet, but the coupling is too broad for this to be the case.

Microsphere synthesis

Different stirring speeds during DCM evaporation haven't been investigated.

SA release and microsphere characterization

The vacuum grease doesn't have an absorbance peak in any range studied for SA release (290-500 nm).

Increasing the scale may have led to a decrease in microsphere diameter, exemplified by the SAA microspheres. Other processing parameters had no other noticeable effect on microsphere diameters.

Cumulative SA release can't be calculated for copolymers unless the exact copolymer ratio is known and used to calculate the molar mass.